NUMERICAL MODELLING OF FREE-SURFACE FLOWS

BY

TIMOTHY TAYLOR MAXWELL

THESIS SUBMITTED FOR THE DEGREE OF
DOCTOR OF PHILOSOPHY
IN THE FACULTY OF ENGINEERING
UNIVERSITY OF LONDON
AND
FOR THE DIPLOMA OF MEMBERSHIP OF
IMPERIAL COLLEGE

MECHANICAL ENGINEERING DEPARTMENT
IMPERIAL COLLEGE
LONDON
ENGLAND

AUGUST 1977

TO

MY WIFE, SUSAN

MY CHILDREN, WENDY AND ROBIN

AND

MY PARENTS, MR. AND MRS. L O MAXWELL, JR.

ABSTRACT

This thesis describes a numerical model for predicting the behaviour of free-surface flows. An Eulerian finite-difference procedure is used to compute the hydrodynamics; and the free-surface is defined by the motion of a set of "Lagrangean particles". The conventional mass continuity equation is rearranged to form a volumetric or bulk-continuity equation. The use of this bulk-continuity relation allows the hydrodynamic variables to be computed over the entire flow domain. Thus, the free-surface boundary conditions are imposed implicitly and the problem formulation is greatly simplified. The gas regions of the flow can be treated as compressible or incompressible, and multiple free-surfaces can be simulated. Both two-dimensional plane flows and axisymmetric flows can be predicted.

An experimental study of wave motions generated in a perspex tank is also reported. The effects of the initial water depth and vertical barriers on the movement of waves across the tank are recorded photographically. The primary objective of this experimental work is to provide data with which to validate the numerical model.

The numerical procedure is validated by comparing predicted results of a wide range of problems with analytical solutions, experimental data from the literature and the results of the current experimental work. The procedure is shown to produce numerically accurate and physically realistic predictions of free-surface flows.

PREFACE

I have been a research student in the Heat Transfer Section of the Mechanical Engineering Department of the Imperial College of Science and Technology since September 1974. During these past three years I have been involved in the development of numerical procedures for the prediction of fluid-dynamic and heat-transfer problems. The primary objective of my work has been to produce better and more economical computational procedures which can be used to solve industrial problems.

During the first year of my studies I became familiar with the SIMPLE (Semi-Implicit Method for Pressure-Linked Equations), finite-difference procedure (Caretto, et al, 1972) being used by the Heat Transfer Section to solve elliptic flows. The EASI (Elliptic Axi-Symmetric Integrator) Program (Markatos, 1974) and the TRIC (Three-dimensional Recirculating Integrator in Cartesian coordinates) Program (Markatos, 1974), which embody SIMPLE, were used to analyse the steady-state flow in shell-and-tube heat exchangers and steam generators. This early work provided a basic understanding of the finite-difference procedures.

For the last two years, my research activities have been focussed on the development and validation of a numerical procedure to predict free-surface flows. The results of this work will be described in this thesis.

I would like to express my gratitude to all those who have contributed to my studies at Imperial College. First, I am most grateful to my supervisor, Professor D.B. Spalding, for his skilful guidance, sincere interest, and continual encouragement. The work presented in this thesis is built upon his ideas and suggestions. I have indeed been fortunate to have had the opportunity and privilege of working with him.

Dr. David Dyer and Dr. Glennon Maples introduced me to Professor Spalding and helped enormously in making arrangements for me to study at Imperial College. For this and for their continuing friendship and support, I am deeply grateful.

Discussions with Dr. Said Elghobashi, Dr. E. Ioannides, Dr. V.S. Pratap and others at CHAM (Concentration, Heat and Momentum Limited) have been most helpful in resolving the technical difficulties which have been encountered.

The friendship and close association with George Carroll has been particularly valuable. I have very much enjoyed knowing Ashok Singhal and have appreciated his helpful suggestions.

The day-to-day exchange of ideas, concerning both technical and non-technical matters, with other students, post-doctoral fellows and visiting professors

has been most beneficial. These include Andrew Pollard, Alaeldin Gamal Awn, Amr Serag-ElDin, Amin Baghdadi, Mohamed Elhadidy, Vinoth Ramachandra, Ayodeji Demuren, Madhuban Nilmani, Yogeshwhr Sahai, Dr. Gordon Mallinson, Dr. V. Ganesan, Dr. A.K. Majumdar, Dr. S. Kanbour, Dr. Kenjiro Suzuki, Dr. David Pratt, and Professor G. de Vahl Davis.

I would like to thank Dr. A.S.C. Ma, John Pilmer and Bob King for their help in conducting the experimental portion of my work.

Thanks are due to Colleen King, Sue Farmiloe and Marguerite Farrell for their assistance in administrative matters. I would also like to thank Miss E.M. Archer and Mrs. S. Boot for providing very efficient library services.

I am grateful to Christine MacKenzie for her excellent typing of the thesis.

Finally, I wish to thank Combustion, Heat and Mass Transfer Limited, London, England, Fluid Mechanics and Thermal Systems, Inc., Waverly, Alabama, USA, and the Science Research Council, for providing financial support during my studies.

London
August 1977 TIMOTHY T. MAXWELL

NUMERICAL MODELLING OF FREE-SURFACE FLOWS

ERRATA

Page 2

In 5th line from top:

replace Lagrangean
by Lagrangian

Page 10

In 7th line from top:

replace VOLUME
by VOLUMES

Page 11

In 4th line from bottom:

replace FOR COLLAPSING COLUMN
by FOR RECTANGULAR COLLAPSING COLUMN

Page 12

In 1st and 3rd lines from top:

replace FOR COLLAPSING COLUMN
by FOR RECTANGULAR COLLAPSING COLUMN

Page 14

In 4th line from bottom:
replace CIRCULAR
by SEMI-CIRCULAR

Page 15

In 9th line from bottom:
replace Lagrangean
by Lagrangian

Page 41

In 11th line from bottom:
replace volume
by volumes

Page 49

In 2nd line from top:
replace $(p'_W - p_p)$
by $(p'_W - p'_p)$
In 8th line from top:
replace (2-11)
by (2-6)

Page 54

In 8th line from top:
replace density in
by density is

Page 94

In 3rd line from bottom:
replace Chapter 7
by Chapter 6

Page 101

Ordinate label for Figure 5-3
replace PLUG VELOCITY (M/SEC)
by PLUG-FACE LOCATION (M)

Page 138

In 13th line from top:
replace (from Chan Street
by (from Chan, Street

Page 143

In 6th line from top:
replace Daily & Stephen
by ● Daily & Stephen

Page 173

In 2nd line from bottom:

replace	14 12
by	14 by 12

TABLE OF CONTENTS

PAGE NUMBER

LIST OF FIGURES

LIST OF TABLES

CHAPTER 1

INTRODUCTION

1.1 THE PROBLEM CONSIDERED

Free-surface flows are characterised by the interaction of two fluids which are separated by a distinct interface. The fluids differ in phase and density; thus, free-surface flows are two-phase flows in which the phases are completely separated. Typical examples of free-surface flows include the movement of slugs or bubbles through a liquid, the motion of surface waves on a body of water and the distortion of the surface of a liquid as it is being drained from a tank.

This thesis describes the development and validation of a numerical model for predicting transient, free-surface flows. Embodied in the model are an Eulerian finite-difference scheme to solve the hydrodynamic equations and a set of Lagrangean particles to mark the free surface. In general, the model is applicable to fully three-dimensional flows; however, for simplicity the work presented here is restricted to two-dimensional or axially-symmetric flows. The fluid properties are assumed constant within each fluid, and both surface-tension and mass transfer between the fluids are neglected. A typical flow arrangement is shown in Figure 1-1.

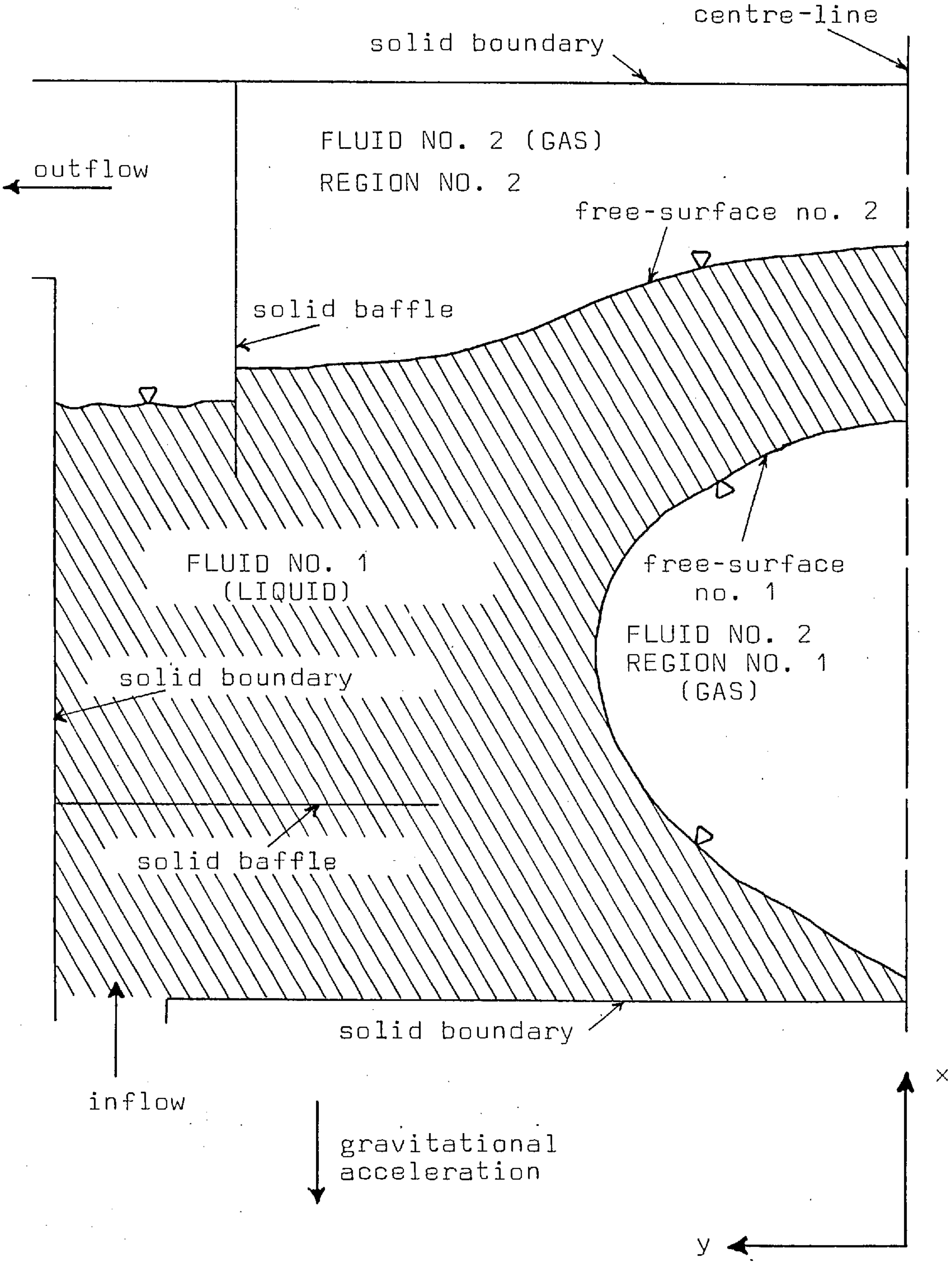

FIGURE 1-1 : TYPICAL FLOW CONFIGURATION

1.2 PRACTICAL RELEVANCE

Free-surface flows abound in nature, they are present in industrial equipment and processes, they occur in nuclear reactors and they may be found in spacecraft. Typical free-surface flows include:

(a) the interaction of surface waves with structures, i.e. wave loading on an offshore oil platform;

(b) the rapid expansion of a vapour bubble trapped in a nuclear reactor core;

(c) the sloshing of a liquid in a container;

(d) the filling or draining of a tank with a liquid, especially under low gravity conditions;

(e) the movement of gas and liquid slugs through a pipeline.

(f) the flow of smoke in a corridor.

Some of these flows are illustrated in Figure 1-2.

To adequately design equipment and structures which must operate in a free-surface flow environment, industry must possess detailed information about free-surface flow phenomena. Analytical methods cannot

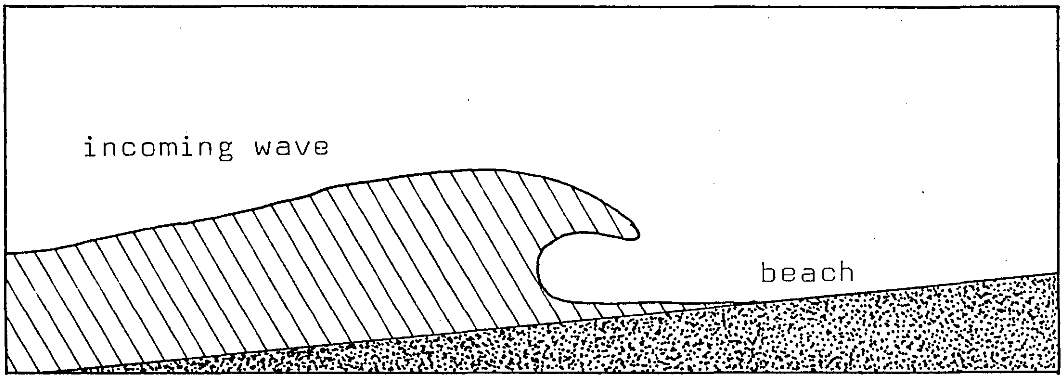

(a) Wave breaking on a beach

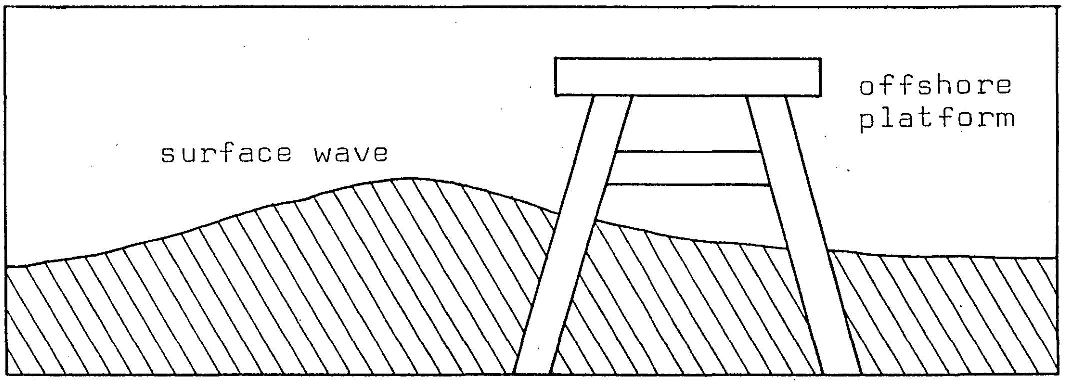

(b) Impact of waves on structures and walls

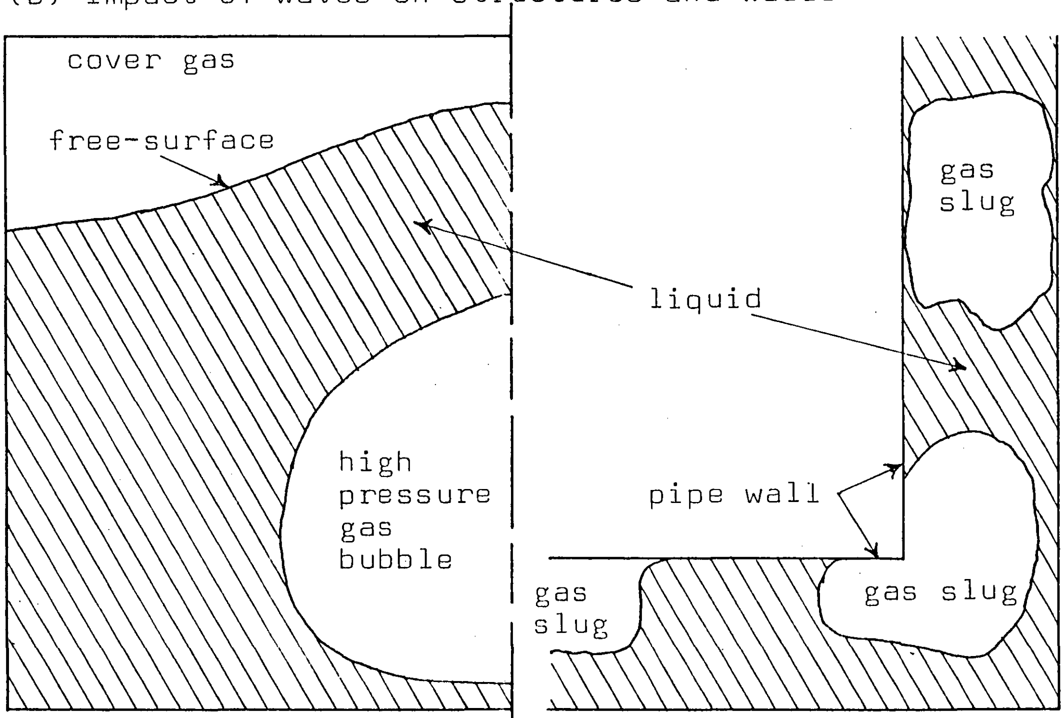

(c) Expansion of a high pressure gas bubble

(d) Slug flow around a pipe bend (2-D pipe)

FIGURE 1-2 : SOME TYPICAL FREE-SURFACE FLOWS produce solutions for viscous, free-surface flows in complex geometrical configurations, and experimental studies are expensive if not impractical. Thus, the ability to accurately predict the behaviour of free-surface flows will provide a valuable design tool.

A second use of a numerical procedure for analysing free-surface flows is the study of fundamental aspects of two-phase flow. Such a procedure would allow attention to be focussed on the interaction of two fluids near their common interface. For instance, the distortion of a gas slug moving in a pipe or the formation of a vapour bubble can be analysed in detail. The effects of various physical phenomena, such as gravity or gas compressibility, on the bubble or slug can be compared computationally much more easily than experimentally.

1.3 REVIEW OF PREVIOUS WORK

Numerous works emphasising various aspects of free-surface flows have been published in the literature. Most texts on fluid mechanics or hydraulics include discussion on wave motions, i.e. Lamb (1975), Wiegel (1964) and Ippen (1966). More complex analytical methods for predicting free-surface flows have been developed and reported; however, these are usually limited to relatively-simple geometrical configurations. In recent years, several numerical procedures, which are less restricted than analytical methods, have been developed and applied to free-surface flows. This section will point out some significant numerical methods and some typical experimental studies of free-surface flows.

Numerical Methods

Development of the MAC (Marker and Cell) Method at the Los Alamos Scientific Laboratory by Welch, Harlow, Shannon and Daly (1965) was the first extensive use of a numerical procedure to solve free-surface flows. The MAC method employs an explicit finite-difference scheme to solve the time-dependent Navier-Stokes equations for a viscous, incompressible fluid. Special features of the MAC method include the use of a staggered grid, the use of conservative forms of the equations of motion and the use of marker particles to denote the location of the liquid phase. The free-surface boundary conditions are expressed by requiring $\frac{\partial u}{\partial x}$ and $\frac{\partial v}{\partial y}$ to vanish at the surface, and the external or gas pressure is applied directly to the free-surface.

Chan and Street (1970) modified the MAC method by improving the free-surface boundary condition. In the original MAC procedure, the free-surface boundary conditions are applied at the centres of the surface cells; however, Chan and Street found that this practice could produce a "ragged" surface. By applying the free-surface boundary conditions at the surface itself rather than at the centre of the cells, they reduced some of the calculational instabilities and increased the accuracy of the computations. They produced very good predictions of solitary-wave motions.

MAC was superceded by the SMAC (Simplified Marker and Cell) Method, (Amsden and Harlow, 1970). There are two basic differences between MAC and SMAC. First, SMAC does not solve for the pressure field directly, as does MAC; hence, the boundary conditions are greatly simplified. Secondly, the resulting Poisson equation for mass conservation needs only homogeneous boundary conditions, and thus, is easier to solve.

Moody (1970) developed a method for predicting free-surface flows in which the pressure and body forces dominate. He assumed the fluid to be inviscid, incompressible and irrotational and used a finite-difference scheme to solve for the velocity potential. Where the MAC and SMAC methods employed particles to locate the entire liquid phase, Moody places markers only on the free-surface. The hydrodynamic variables are computed only in the liquid region.

Bradshaw, Kramer and Zich (1976) used the SMAC method to predict liquid reorientation in space-vehicle fuel tanks. They enhanced the method to allow a variable grid and incorporated surface-tension effects.

A method for predicting low-speed, single-component, two-phase flow was developed by Ramshaw and Trapp (1976). In order to maintain the steep gradients in density and enthalpy at the liquid-vapour interface, they rearranged the energy equation so as to remove the convective derivatives and used a modified donor-acceptor differencing technique. Finally, noting that the spatial variation of momentum density, $\rho\bar{u}$, is much greater than that of velocity, they chose to employ non-conservative forms of the momentum equations. This method is not suitable for problems in which an accurate description of the free-surface shape is required.

Experimental Work

Street and Camfield (1966) studied the deformation of two-dimensional, solitary waves approaching a sloping beach. The phase shift and amplitude of solitary waves undergoing a head-on collision was measured by Maxworthy (1976).

The collapse of liquid columns was studied by Martin and Moyce (1951). They presented data for the velocity and location of the wave front.

The space program has generated much interest in the areas of sloshing and low-gravity flows. Abramson (1966) provides a very useful summary of both analytical and experimental work related to the dynamic behaviour of liquids in moving containers. Nussle, Derdul and

Petrash (1965), Otto (1966), Gluck, Gille, Simkin and Zukoski (1966), Symons and Staskas (1971) and Aydelott (1976) all present data for the draining or filling of tanks of various shapes under low gravity conditions.

The effects of containing walls on the rise of large gas bubbles through a liquid were reported by Collins (1967).

1.4 CALCULATIONAL PROCEDURES USED IN THE PRESENT STUDY

The theoretical prediction of transient, two-dimensional, elliptic flows necessitates the simultaneous solution of the set of non-linear, partial-differential equations which govern the conservation of mass and momentum. If the transport of other flow properties, such as energy, is to be accounted for, an additional equation for each additional property must be included. This system of equations is very complex, and in general, no closed-form analytical solution has been discovered. Therefore, the need for accurate and reliable predictions of real flow systems necessitates the development of numerical solution procedures.

The work reported in this thesis is based on an implicit finite-difference scheme referred to as SIMPLE (Semi-Implicit Method for Pressure-Linked Equations) (Caretto, et al, 1972, and Patankar and Spalding, 1972). SIMPLE is an iterative procedure in which the velocity fields are calculated from a "guessed" pressure field, and then, "pressure-corrections" are computed from the continuity relations. These "pressure-corrections" are used to adjust both the pressure and velocity fields. The new fields are then used as "guesses" for the next iteration; after several iterations, the hydrodynamic fields are obtained. In the case of a transient flow, this iterative procedure is repeated at each "step" in time and the "guessed" values are taken as the results of the previous step.

To compute free-surface flows, two modifications to the SIMPLE procedure are necessary. The first modification is the introduction of GALA (Gas And Liquid Analyser) (Spalding, 1974, and Spalding, 1976). The central concept of GALA is the replacement of the conventional mass-continuity equation with a volumetric continuity equation. The use of GALA permits the computation of the hydrodynamic variables over the entire flow domain (throughout the gas and liquid regions), so that the pressure and velocity fields are continuous across the free surface. Thus, because the free surface is not a boundary of the computation, the complex free-surface boundary conditions are imposed implicitly. The second modification is the addition of a set of massless particles to "track" the free surface. These particles are moved, at the end of each step in time, with the local fluid velocities and the particle locations are then used to determine the local fluid densities.

1.5 OBJECTIVES OF THE STUDY

The objectives of this study are listed below:

(a) to develop a mathematical model and solution procedure capable of predicting the details of free-surface flows;

(b) to validate the numerical accuracy of the solution procedure by comparing predictions with known or analytical solutions;

(c) to conduct an experimental investigation of wave motions on the surface of a liquid and compare these experimental results with predictions to validate the physical reality simulated by the model;

(d) to demonstrate the potential of the model by presenting predictions of several additional free-surface flows.

CHAPTER 2

MATHEMATICAL FORMULATION

2.1 INTRODUCTION

The first step in analysing a fluid-dynamics problem is to write down, in mathematical form, the physical laws which govern the flow. These physical laws include the conservation of mass, momentum and scalar properties and any auxiliary relations necessary to complete the system of equations. The physical laws are very general in nature; however, when a particular flow is being studied, it is sometimes reasonable to neglect some of the mechanisms described by the general laws. This chapter presents the equations necessary to describe free-surface flows and states the assumptions that are necessary to obtain these equations.

2.2 BASIC EQUATIONS

The partial-differential equations which govern the transient, three-dimensional motion of a fluid are expressed below in vector notation.

Conservation of Mass

$$\frac{\partial \rho}{\partial t} + \nabla \cdot (\rho \overline{V}) = 0 \qquad (2\text{-}1)$$

Conservation of Momentum

$$\begin{aligned}\rho \frac{\partial \overline{V}}{\partial t} + \rho(\overline{V}.\nabla)\ \overline{V} &= -\nabla\ p + \rho\ \overline{B} \\ &\quad - \nabla \times \left[\mu(\nabla \times \overline{V})\right] \\ &\quad + \nabla\left[(\lambda + 2\mu)\ \nabla.\overline{V}\right] + S_{\overline{V}}\end{aligned} \qquad (2\text{-}2)$$

Transport of a Scalar, ϕ

$$\rho \frac{\partial \phi}{\partial t} + \rho(\overline{V}.\nabla)\ \phi = \nabla\ .\ (\Gamma_\phi\ \nabla\phi) + S_\phi \qquad (2\text{-}3)$$

The symbols in the above equations represent:

$\overline{V}$	the velocity vector,
p	the static pressure,
$\overline{B}$	the body-force vector,
ϕ	any scalar property,
ρ	the fluid density,
μ	the dynamic viscosity,
λ	the second coefficient of viscosity,
Γ_ϕ	the transport coefficient for the scalar property, ϕ,
t	time,
$S_{\overline{V}}$, S_ϕ	any additional sources (or sinks) of the respective quantity,
∇	the vector differential operator.

2.3 COORDINATE SYSTEMS

Predictions are presented in later chapters for both plane flows and axisymmetric flows. Figure 2-1 illustrates the cartesian coordinate system (x,y,z)

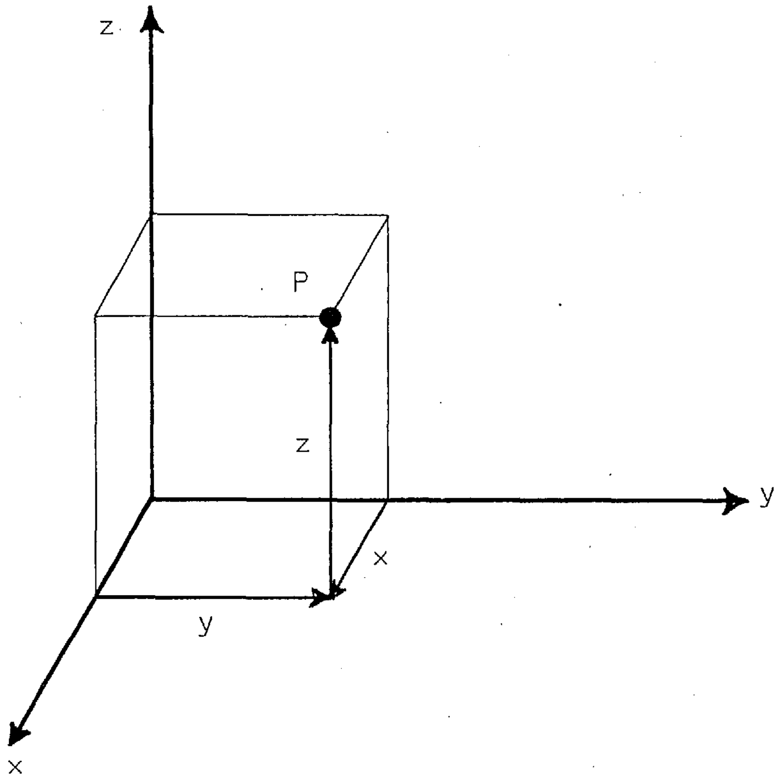

Cartesian coordinates (x, y, z)

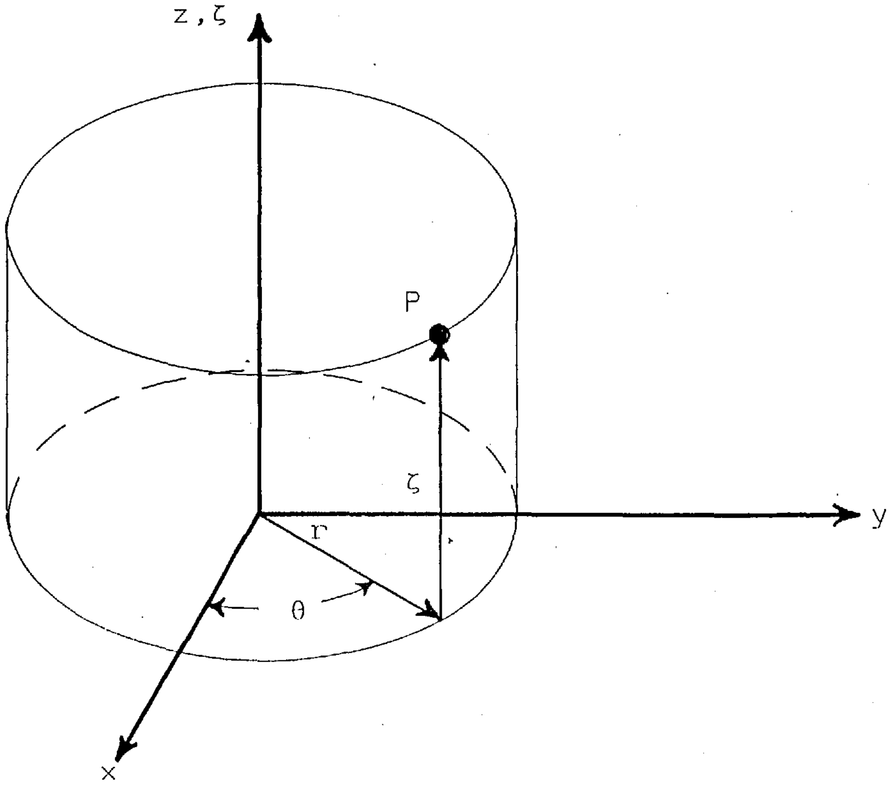

Cylindrical polar coordinates (r, θ, ζ)

FIGURE 2-1 : COORDINATE SYSTEMS

and the cylindrical polar coordinate system (r,θ,ζ). The mathematical model will be developed in cylindrical polar coordinates. It should be noted that equations written in cylindrical polar coordinates reduce to their cartesian counterparts at large radii. To simplify the notation, the symbols (r,θ,ζ) are replaced by (y,z,x) and the new symbols rearranged as (x,y,z). Thus, x denotes the axial direction, y the radial direction and z the circumferential direction, and u, v and w are the respective velocity components.

2.4 ASSUMPTIONS AND MODIFICATIONS

The equations (2-1, 2-2 and 2-3) must be simplified and arranged in a form suitable for numerical solution. The most obvious simplification is the limitation of the model to two space dimensions. Two-dimensionality implies that there is no variation of fluid properties or flow parameters in one of the coordinate directions. Neglecting variations in the circumferential direction for the cylindrical coordinate system yields an axisymmetric configuration. It makes no difference which direction is neglected in the cartesian system.

In general, no other assumptions are necessary. However, many of the terms in equations (2-1, 2-2 and 2-3) are not important in free-surface flows and they will be removed in the interests of computational efficiency and convenience. The remaining assumptions and modifications will be discussed in relation to the particular equations to which they apply.

Continuity Equation

The continuity equation may be rearranged as

$$\frac{D\rho}{Dt} + \rho(\nabla.\overline{V}) = 0$$

or

$$\nabla.\overline{V} = -\frac{1}{\rho}\frac{D\rho}{Dt} \qquad (2\text{-}4)$$

where $\frac{D(\ )}{Dt}$ is the "substantial" derivative and is defined as

$$\frac{D(\ )}{Dt} = \frac{\partial(\ )}{\partial t} + \overline{V} \cdot (\nabla(\ )) \quad . \qquad (2\text{-}5)$$

Rearrangement of the continuity equation from (2-1) to (2-4) is the GALA concept. There are two important differences between (2-1) and (2-4). First, the density does not appear on the left-hand side of (2-4), and second, (2-4) is written in terms of "volumetric" continuity rather than mass continuity. The substantial derivative of ρ is always zero for flows of incompressible fluids, and very often, both of the fluids can be considered incompressible. For instance, the compressibility of air is not important to the motion of surface waves on a body of water. When the compressibility of one fluid is important, as in the expansion of a high-pressure gas bubble, the right-hand side of (2-4) can be treated as a "source" of volume and computed approximately from a suitable relation, such as

$$p\rho^{-k} = \text{constant}. \tag{2-5}$$

Details of how the right-hand side of equation (2-4) may be approximated will be discussed in the chapter on solution procedure. Thus, the continuity equation can be written as

$$\frac{\partial u}{\partial x} + \frac{1}{y}\frac{\partial(yv)}{\partial y} = R\ , \tag{2-6}$$

where R is the rate of reduction of fluid volume,

$$-\frac{1}{\rho}\frac{D\rho}{Dt}\ .$$

Conservation of Momentum

The majority of free-surface flows involve the interaction of a gas and a liquid. The liquid can always be assumed incompressible, thus, $\nabla.\overline{V}$ is zero in the liquid regions. Frequently, the gas can also be assumed incompressible and $\nabla.\overline{V}$ is zero throughout the flow domain. Since the momentum of the gas is very small with respect to the liquid momentum, and the viscous terms are not greatly important in free-surface flows, the terms containing $\nabla.\overline{V}$ can be neglected throughout the flow domain even if the gas is being considered compressible. It is also assumed that the fluid properties remain constant within each fluid. Subject to the above assumptions, the momentum equations can be written in Eulerian formulation as:

x-direction

$$\frac{\partial(\rho u)}{\partial t} + \frac{\partial(\rho uu)}{\partial x} + \frac{1}{y}\frac{\partial(y\rho uv)}{\partial y} = -\frac{\partial p}{\partial x}$$

$$+ \mu\left[\frac{\partial^2 u}{\partial x^2} + \frac{\partial^2 u}{\partial y^2}\right] + \frac{\mu}{y}\frac{\partial u}{\partial y}$$

$$+ \rho\, B_u + S_u \quad , \qquad (2\text{-}7)$$

y-direction

$$\frac{\partial(\rho v)}{\partial t} + \frac{\partial(\rho uv)}{\partial x} + \frac{1}{y}\frac{\partial(y\rho vv)}{\partial y} = -\frac{\partial p}{\partial y}$$

$$+ \mu\left[\frac{\partial^2 v}{\partial x^2} + \frac{\partial^2 v}{\partial y^2}\right] + \frac{\mu}{y}\left[\frac{\partial v}{\partial y} - \frac{v}{y}\right]$$

$$+ \rho\frac{w^2}{y} + S_v \quad , \qquad (2\text{-}8)$$

z-direction

$$\frac{\partial(\rho w)}{\partial t} + \frac{\partial(\rho uw)}{\partial x} + \frac{1}{y}\frac{\partial(y\rho vw)}{\partial y} =$$

$$\mu\left[\frac{\partial^2 w}{\partial x^2} + \frac{\partial^2 w}{\partial y^2}\right] + \frac{\mu}{y}\left[\frac{\partial w}{\partial y} - \frac{w}{y}\right]$$

$$+ \rho\frac{vw}{y} + S_w \quad . \qquad (2\text{-}9)$$

The left-hand side of equation (2-7) contains the transient and convective flux terms for the u-velocity component, while the pressure gradient term, the viscous terms, the body-force term and the source term appear on the right-hand side. The y-direction equation,(2-8),is of the same form as equation (2-7) with the exception of the body-force term. In an axisymmetric system only axial body forces are allowed; however, for a cartesian system there may also be a y-direction body force. The z-direction or swirl-velocity equation,(2-9),is not linked to x- or y-direction equations by the pressure field. For plane flow, the z-direction momentum equation is trivial.

Transport of the scalar, ϕ

It is only necessary to apply the assumptions that the fluid properties are constant within each fluid. The equation can then be written in Eulerian formulation as

$$\frac{\partial(\rho\phi)}{\partial t} + \frac{\partial(\rho u\phi)}{\partial x} + \frac{1}{y}\frac{\partial(y\rho v\phi)}{\partial y}$$

$$= \Gamma_\phi \left[\frac{\partial^2\phi}{\partial x^2} + \frac{\partial^2\phi}{\partial y^2}\right] + S_\phi \qquad (2\text{-}10)$$

2.5 THE GENERAL TRANSPORT EQUATION

Inspection of equations (2-7, 2-8, 2-9 and 2-10) reveals that they can all be written in the same form as equation (2-10). In vector notation this form is

$$\frac{\partial(\rho\phi)}{\partial t} + \nabla \cdot (\rho \, \overline{V} \, \phi) = \Gamma_\phi \nabla^2 \phi + S_\phi \quad . \qquad (2\text{-}11)$$

Equation (2-11) is the standard form of the general transport equation that can be solved by the solution procedure to be described in the next chapter.

There are four terms in equation (2-11); on the left-hand side are the transient and convective terms and on the right are the gradient-diffusion and source terms. The source term is used to force all the equations into the standard form. Not only real sources of ϕ, but all additional terms in the equation are contained in the source term. For instance, the body-force term, the pressure-gradient term and all viscous terms that are not included in the gradient diffusion terms have been absorbed in S_ϕ.

2.6 AUXILIARY INFORMATION

To mark the free-surface a set of massless particles is spread along the interface. It is assumed that if the particles are placed on the free-surface initially, they will remain on the free-surface throughout the calculation. The particles move in accordance with the equation

$$\frac{D\bar{r}}{Dt} = \bar{u}_p \qquad (2\text{-}12)$$

where $\bar{r}$ is the position vector of the particle and $\bar{u}_p$ is the particle velocity. The set, or string, of particles is connected by straight-line segments to form the free-surface.

To complete the specification of the mathematical formulation both initial conditions and boundary conditions are needed. The necessary initial conditions include the initial value of the flow variables, ϕ's, and the initial position of the free-surface marker particles. The necessary boundary conditions are the values of the ϕ's along the boundary of the calculation domain as functions of time. Details of how the auxiliary information is implemented in the solution procedure will be discussed in the next chapter.

2.7 SUMMARY

The information presented in this chapter is summarised below.

(a) The basic equations of transient, three-dimensional flow are presented.

(b) The coordinate systems, Cartesian and cylindrical polar, to be used in the work reported in this thesis are defined.

(c) The assumptions made in modifying the equation set for transient, two-dimension, free-surface flow are stated and the resulting equations are presented.

(d) A standard transport equation is developed.

(e) The auxiliary information necessary to complete the mathematical model is speciifed.

CHAPTER 3

SOLUTION PROCEDURE

3.1 INTRODUCTION

After the mathematical model has been defined, a solution procedure capable of extracting quantitative predictions from the model must be developed. An implicit finite-difference scheme has been selected to form the basis of the solution procedure presented in this thesis. The solution procedure may be divided into three parts.

1 - Sub-dividing the flow domain into small, discrete regions by constructing a finite-difference "grid".

2 - Integrating the differential equations over the grid "cells", and then, solving the resulting finite-difference equations for the hydrodynamic variables.

3 - Tracking the free surface.

The details of the solution procedure are described below.

3.2 THE FINITE-DIFFERENCE GRID

3.2.1 General Concept

The finite-difference grid is composed of intersecting, orthogonal grid lines which are spread over the calculation domain parallel to the coordinate axes. Intersections of the grid lines are called grid nodes. These grid nodes provide reference locations for specifying the flow parameters. The grid lines may be spread non-uniformly to allow more grid nodes in regions where large gradients in the flow parameters are expected. However, once the grid spacings have been set they remain fixed during the solution processes. The grid is so chosen that the predictions will be as independent of grid spacing as is possible.

3.2.2 Location of the Flow Variables

Figure 3-1 shows a typical grid configuration and identifies the locations at which the flow variables are "stored". The pressure and other scalar properties are stored at the grid nodes, but the velocity components are stored midway between the grid nodes. This "staggered-grid" configuration has three advantages.

1 - The calculation of a continuity balance over the region surrounding a grid node is simple because the velocities normal to the boundaries of this region are located on the boundaries.

2 - The pressures are located such that calculation of the pressure gradients that affect the velocity components is

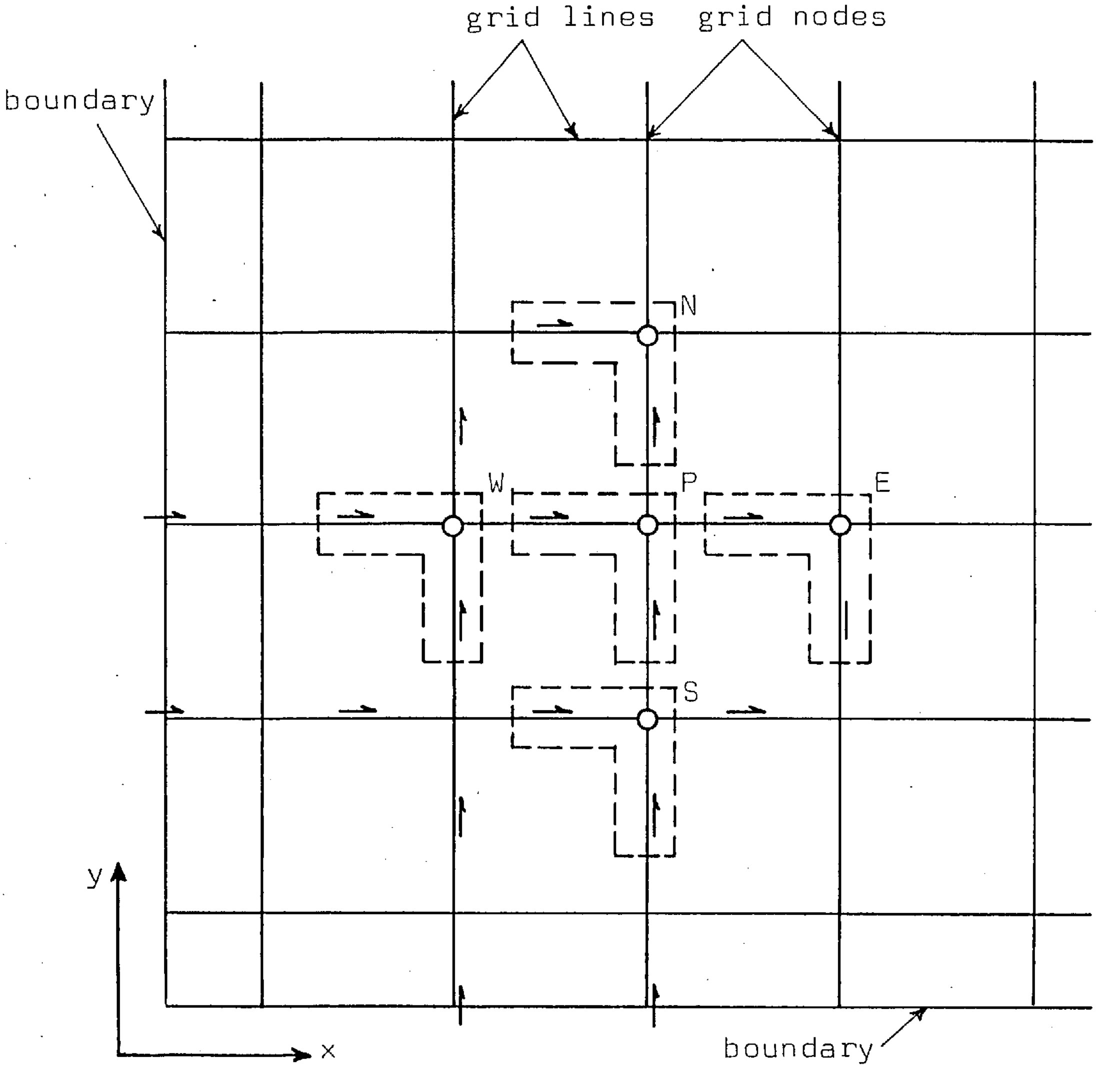

LOCATION	VARIABLE
o	ϕ, p
→	u
↑	v

FIGURE 3-1 : LOCATION OF THE VARIABLES ON THE FINITE-DIFFERENCE GRID convenient.

3 - The velocity components are located so as to simplify the calculation of convective fluxes for the scalar properties stored at the grid nodes.

The dashed enclosures in Figure 3-1 show the manner in which the variable locations have been grouped for identification.

3.2.3 Control Volumes for Integration

The differential equations are integrated over discrete regions of space to yield the finite-difference equations. These regions of space are called "control volumes". Because there are three different types of locations for the variables on the staggered-grid, there are three types of control volumes; "main" or grid node control volumes for the variables stored at each grid node, u-velocity control volumes for the u-velocity storage locations and v-velocity control volumes for the v-velocity storage locations. Examples of each of these control volumes are shown in Figure 3-2. The boundaries of the grid-node control volumes lie half-way between the grid nodes; thus, the surfaces of these control volumes pass through the locations where the normal velocities are stored. The velocity control volumes are bounded in a similar way on the side perpendicular to the velocity

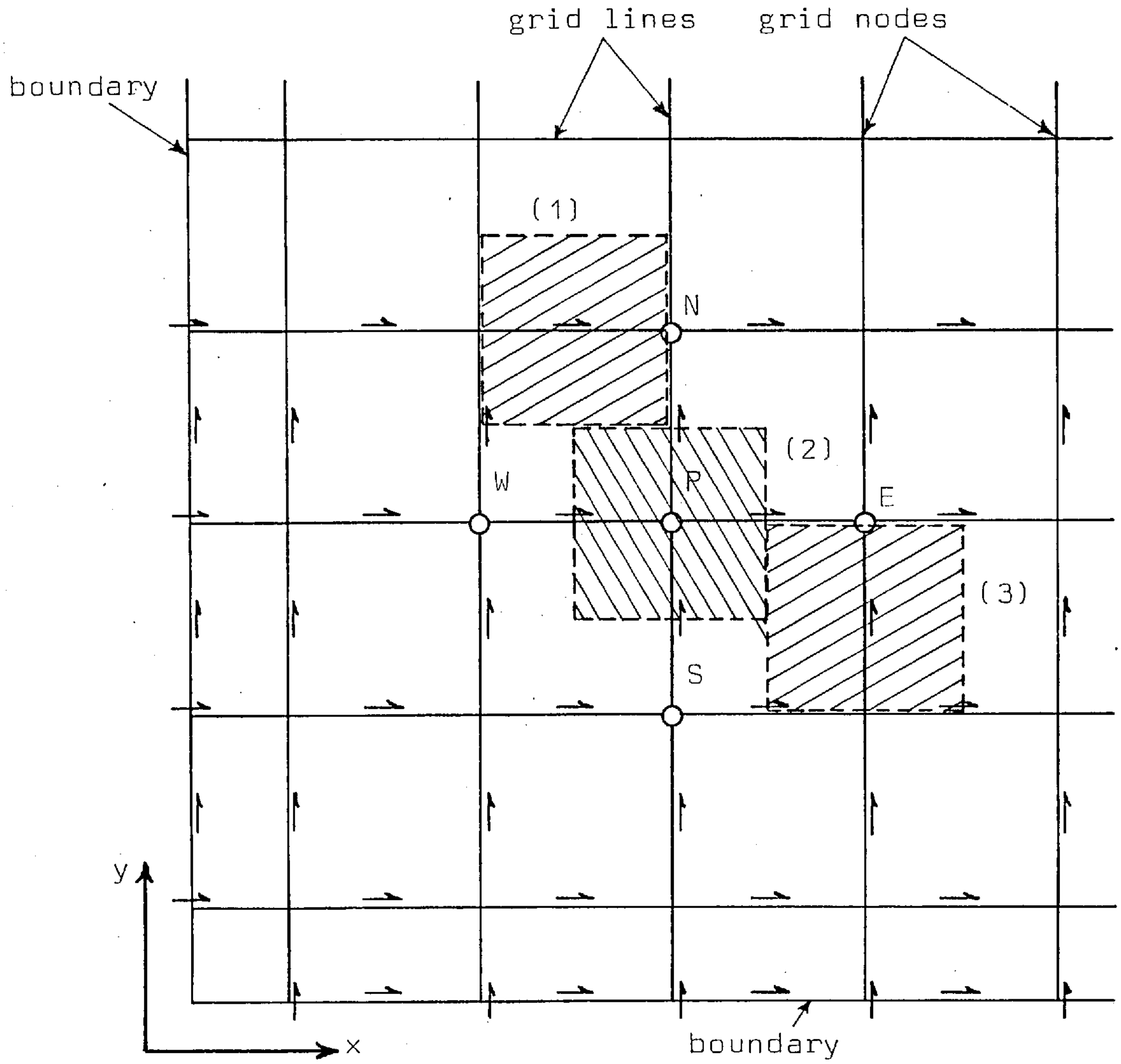

SYMBOL	CONTROL VOLUME	VARIABLE
(1)	u-velocity	u_N
(2)	grid node	ϕ_P, p_P
(3)	v-velocity	v_E

FIGURE 3-2 : DEFINITION OF THE CONTROL VOLUMES component, but in the direction of the velocity component, the boundaries of the control volume pass through the grid nodes in front of and behind the velocity location. For an axisymmetric grid all of the control volumes are one radian "thick" in the circumferential direction and all cartesian control volumes are one length unit "thick".

3.2.4 Grid Boundaries

Due to the staggered-grid configuration, two modifications to the near-boundary portions of the grid are necessary. First, the normal velocities near the grid boundary are stored on the boundary rather than in the normal staggered location. These boundary locations are shown in Figure 3-1. As a result of this modified location of the boundary velocities, the near boundary normal veloicty control volume must be modified. The near-boundary control volumes are illustrated in Figure 3-3.

3.3 THE HYDRODYNAMIC CALCULATIONS

3.3.1 The General Finite-Difference Equation

The differential equations have been formulated by invoking the conservation laws over an infinitesimal control volume. The finite-difference equations will be developed by integrating the differential equations over a finite-control volume. In this section the general finite-difference equation for the transport

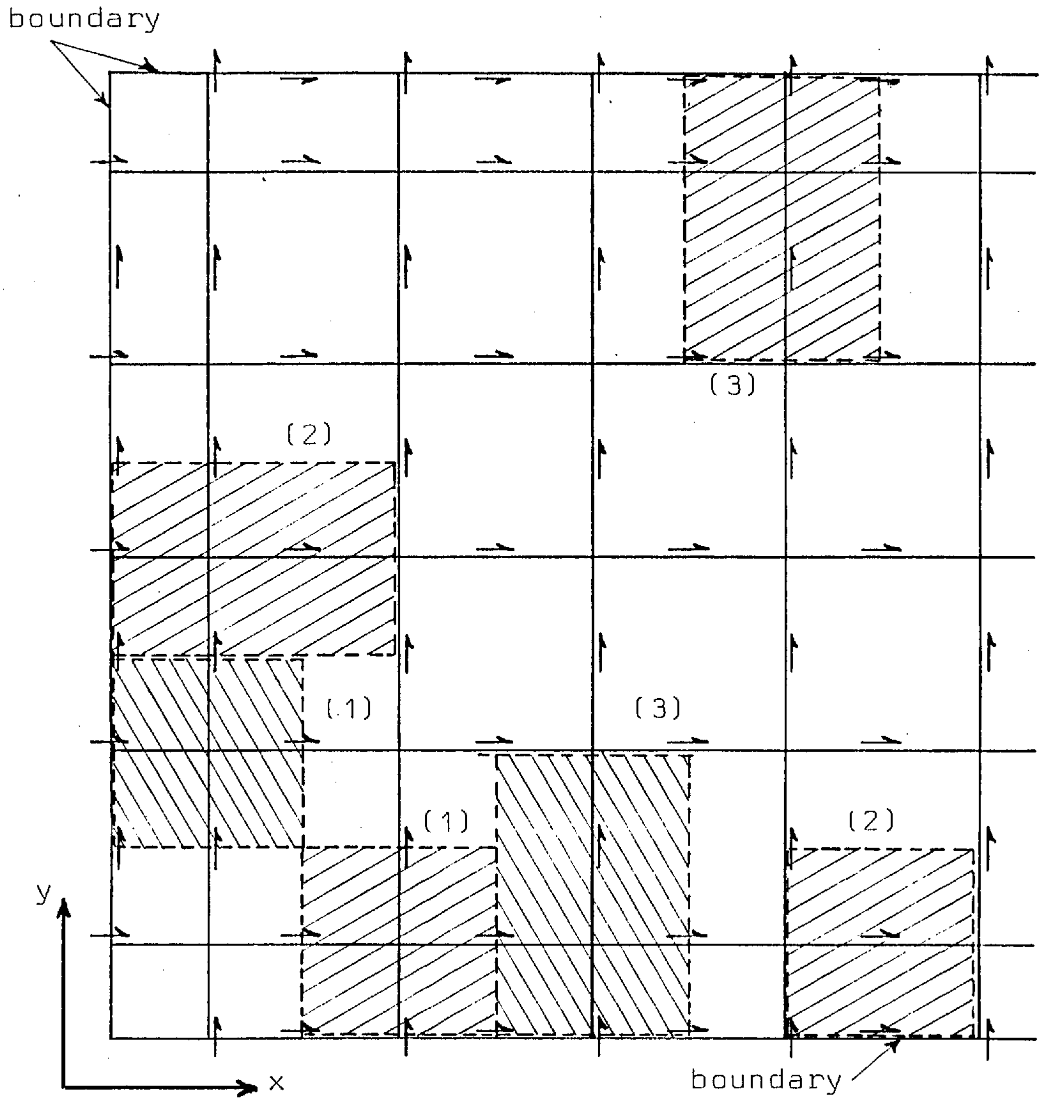

SYMBOL	CONTROL VOLUME
(1)	ϕ, p
(2)	u-velocity
(3)	v-velocity

FIGURE 3-3 : NEAR-BOUNDARY CONTROL VOLUMES of ϕ is derived by integrating equation (2-10).

Figure 3-4 shows the ϕ-location P, its neighbouring locations N, S, E and W and its control volume. The quantities a_n, u_n, ρ_n, ϕ_n are taken as the prevailing values at the control volume face n (Figure 3-4) and similarly for the other three faces. The areas of the control volume faces are:

$$a_n = r_n \, \Delta y \, \Delta\theta \qquad \text{(north face),}$$
$$a_s = r_s \, \Delta y \, \Delta\theta \qquad \text{(south face),} \qquad (3\text{-}1)$$

$$a_e = r_P \, \Delta x \, \Delta\theta \qquad \text{(east face),}$$

and

$$a_w = r_P \, \Delta x \, \Delta\theta \qquad \text{(west face).}$$

The volume of the control volume is

$$V = r_P \, \Delta x \, \Delta y \, \Delta\theta \quad . \qquad (3\text{-}2)$$

The r's in equations (3-1 and 3-2) are the radial distances from the coordinate centre-line to the location denoted by the subscript. For cartesian co-ordinates the r's are set to unity. $\Delta\theta$ is either one radian or a unit length, depending on the choice of coordinate systems.

Transient Term

To express the time-dependent term, $\frac{\partial(\rho\phi)}{\partial t}$, in finite-difference form, it is assumed that the value of ϕ at P prevails throughout the control volume.

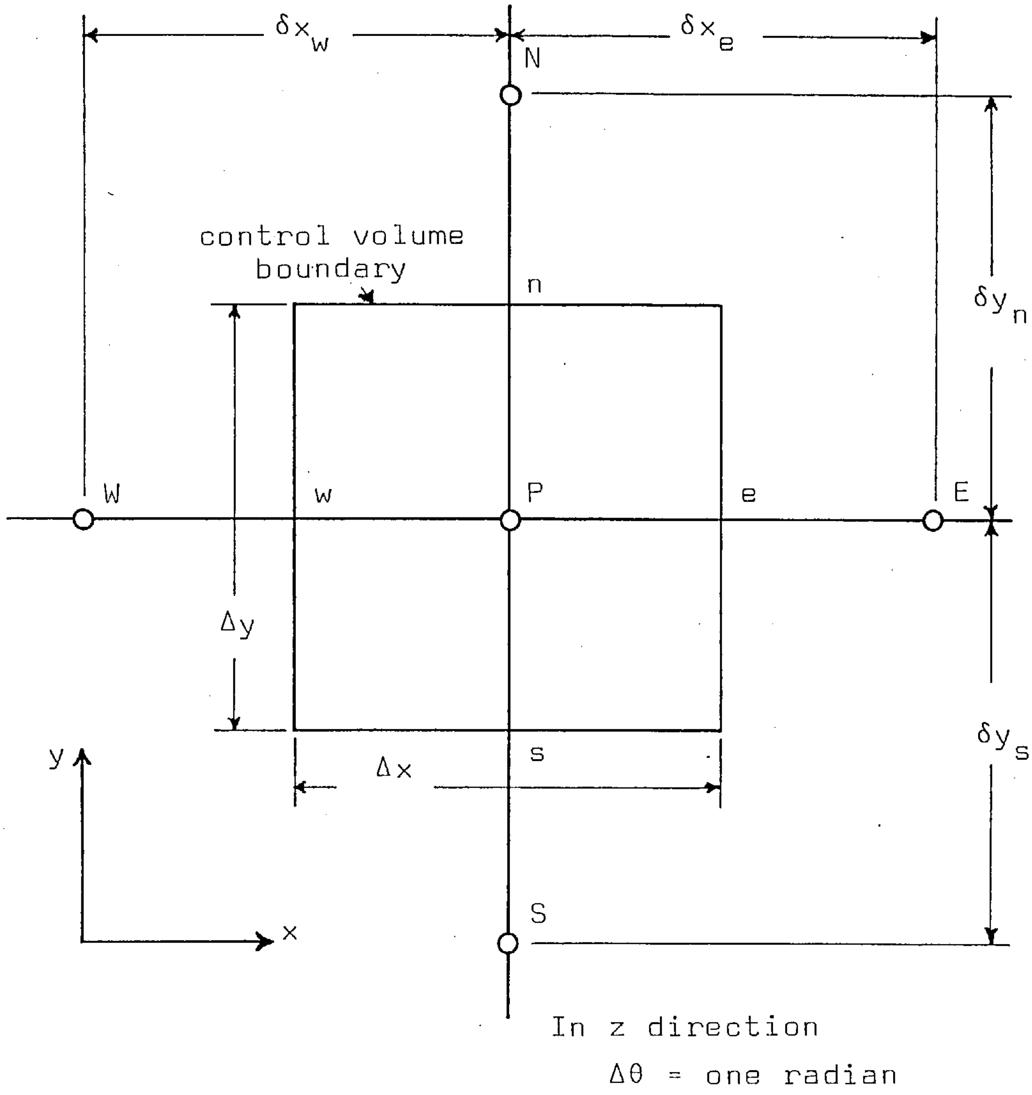

FIGURE 3-4 : GRID NOMENCLATURE USED TO DEVELOP THE FINITE-DIFFERENCE EQUATIONS

Integration of the time-dependent term over the control volume yields

$$\frac{\partial(\rho\phi)}{\partial t} \approx M\,\phi_P - M_o\,\phi_{P,o} \qquad (3\text{-}3)$$

where

$M = \rho\, V/\Delta t$

and the subscript o implies values from the beginning of the time step.

Convection and Diffusion Terms

If it is assumed that ϕ, ρ and Γ vary linearly between grid nodes, then the convective and diffusive fluxes across the west, w, face of the control volume are

$$\text{convective flux} = a_w\,\rho_w\,\phi_w \;,$$

$$\text{diffusive flux} = -a_w\,\Gamma_{\phi,w}\,\frac{(\phi_P - \phi_W)}{\delta x_w} \;. \qquad (3\text{-}4)$$

The way in which ϕ_w is evaluated determines the type of "differencing" used for the convective term. The most obvious way to calculate ϕ_w is to linearly interpolate the values ϕ_P and ϕ_W; this is commonly referred to as the "central-difference" formulation. However, because in the flows to be considered, the local Peclet number, $\frac{\rho_w\, U_w\, \delta x_w}{\Gamma_{\phi,w}}$, will be much larger than unity; the "upwind-difference" formulation will be used. Thus, ϕ_w is specified as

$$\phi_w = \phi_W \quad \text{if } u_w > 0 \quad ,$$
$$\phi_w = \phi_P \quad \text{if } u_w < 0 \quad . \qquad (3\text{-}5)$$

The total convective and diffusive flux across the west face of the control volume is expressed below.

$$A_W \, \phi_W - (A_W - (a\rho u)_w) \, \phi_P \qquad (3\text{-}6)$$

where

$$A_W = \frac{a_w \, \Gamma_{\phi w}}{\delta x_w} + \frac{\rho_w u_w}{2} \quad \text{(central difference)}$$

or

$$\left.\begin{array}{ll} A_W = \dfrac{a_w \, \Gamma_{\phi,w}}{\delta x_w} + \rho_w u_w \, , & u_w > 0 \\[2ex] A_W = \dfrac{a_w \, \Gamma_{\phi,w}}{\delta x_w} \, , & u_w < 0 \end{array}\right\} \text{(upwind difference)}$$

Of course, similar expressions exist for the e, s and n faces of the control volume.

Source Terms

Sources of ϕ are linearised so that they may be written in the form

$$S_\phi = S_U + S_P \, \phi_P \quad , \qquad (3\text{-}7)$$

The Complete Equation

The finite-difference form of equation (2-10) can now be assembled from equations (3-3, 3-6 and 3-7).

$$
\begin{aligned}
M\,\phi_P - M_o\,\phi_{P,o} = {} & A_W\,\phi_W - (A_W - (a\rho u)_w)\,\phi_P \\
& + A_E\,\phi_E - (A_E - (a\rho u)_e)\,\phi_P \\
& + A_N\,\phi_N - (A_N - (a\rho u)_n)\,\phi_P \\
& + A_S\,\phi_S - (A_S - (a\rho u)_s)\,\phi_P \\
& + S_U + S_P\,\phi_P \qquad (3\text{-}8)
\end{aligned}
$$

Equation (3-8) may be rearranged and simplified to yield the general finite-difference equation,

$$A_P\,\phi_P = A_W\,\phi_W + A_E\,\phi_E + A_N\,\phi_N + A_S\,\phi_S + M_o\,\phi_{P,o} + S_U\,, \qquad (3\text{-}9)$$

where

$$A_P = A_N + A_E + A_N + A_S + M_o - S_P\,.$$

3.3.2 The Momentum Equations

The finite-difference equations for momentum are of the same form as equation (3-9); however, there are two differences. First, because the velocities are stored at the "staggered" locations (Figure 3-1), the momentum equations are formulated for the velocity-control volumes (Figure 3-2). This simply means that the points P, N, S, E and W in Figure 3-4 represent velocity locations rather than grid nodes. The other difference is the presence of the special source term, the pressure gradient. If the pressure field was known, the momentum equations would be coupled only to each other, and thus, they could be solved independently of the other equations. However, the pressure field is not known in advance; therefore, the momentum equations are solved by using a guessed pressure field. This guessed pressure field, p*, is usually taken to be the pressure field of the last time step. The velocity fields, u* and v*, that result do not satisfy continuity, but u*, v* and p* are corrected later in the solution procedure.

3.3.3 The Pressure-Correction Equation

The u* and v* velocity fields, which were obtained from the solution of the momentum equations, must be corrected to account for the error introduced by the guessed pressure field, p*. Also, if the correct solution is to be reached, the p* field must be corrected during each cycle of the iterative procedure and the corrected pressures used as the guesses for the next iteration. These corrections are computed from the continuity equation.

First, it is assumed that the corrected pressure is defined by

$$p = p^* + p' \qquad (3\text{-}10)$$

where p' is the "pressure-correction". It then follows that the velocity fields are equal to the solutions from the momentum equations, u* and v*, plus a term to account for the pressure gradient imposed by the pressure-corrections. Thus, the velocities on the faces of the control volume for grid node P are:

$$
\begin{aligned}
u_e &= u_e^* + D_e^u\,(p'_P - p'_E)\\
u_w &= u_w^* + D_w^u\,(p'_W - p'_P)\\
v_n &= v_n^* + D_n^v\,(p'_P - p'_N)\\
v_s &= v_s^* + D_s^v\,(p'_S - p'_P)
\end{aligned}
\qquad (3\text{-}11)
$$

4/

where the D's are the pressure gradient coefficients from the respective momentum equations[†].

The pressure-correction equation is formulated from the GALA or volumetric continuity equation (2-~~11~~). It is convenient to consider for the moment a one-dimensional problem in which the volume source, R, is zero. Then, the finite-difference continuity equation is

6/

$$a_e u_e - a_w u_w = 0 \quad . \qquad (3\text{-}12)$$

Substitution of equations (3-11) into (3-12) yields

$$
\begin{aligned}
(a_e D_e^u + a_w D_w^u)\; p'_P &= (a_e D_e^u)\; p'_E\\
&\quad + (a_w D_w^u)\; p'_W + (a_w u_w^* - a_e u_e^*) \quad . \qquad (3\text{-}13)
\end{aligned}
$$

The complete two-dimensional pressure-correction equation can now be written in the form

$$A_P\, p'_P = A_E\, p'_E + A_W\, p'_W + A_N\, p'_N + A_S\, p'_S + S_u \qquad (3\text{-}14)$$

[†] Equations (3-11) are truncated forms of the momentum equations. The complete form is

$$u_w = u_w^* + D_w^u\,(p'_W - p'_P) + \sum_i A_i\,(u_i - u_i^*)$$

where i indicates the summation over the neighbouring velocity locations and the A_i's are the coefficients from the momentum equations. It is permissible to use these truncated equations because the pressure-corrections tend to zero as convergence is approached.

where

$$A_P = A_E + A_W + A_N + A_S - S_P \quad ,$$

$$A_E = a_e D_e^u \quad ,$$

$$A_W = a_w D_w^u \quad ,$$

$$A_N = a_n D_n^v \quad ,$$

$$A_S = a_s D_s^v \quad ,$$

and

$$S_U = a_w u_w^* - a_e u_e^* + a_s v_s^* - a_n v_n^* + S_V \quad .$$

The S_V and S_P terms are used to include the additional volume sources when R in equation (2-11) is not zero. These source terms are linearised in the form

$$R = S_V + S_P \, p'_P \quad . \qquad (3\text{-}15)$$

R is zero for incompressible fluids; however, if either fluid is compressible, $\frac{1}{(t-t_o)} \int_{t_o}^{t} (-\frac{1}{\rho}\frac{D\rho}{Dt}) \, V \, dt$, which is the rate of reduction of fluid volume within the control volume, must be represented in the R term. The substantial derivative of the density describes the density of the <u>moving</u> fluid elements, but it is being integrated over a fixed control volume. This practice is not entirely consistent; however, the important contribution of this term is the net expansion of the fluid in the vicinity of the control volume. If the location of this expansion is displaced a small amount from its true location, the effect will be secondary.

Any reasonable $p \sim \rho$ relationship can be used to evaluate R. A simple, but very useful, example is the relationship expressed in equation (2-5) for a reversible, adiabatic process.

3.3.4 Solution of the Difference Equations

The tri-diagonal matrix algorithm (TDMA), which is described in most numerical analysis texts (i.e., Roache, 1976), solves systems of equations of the form

$$D_i \phi_i = A_i \phi_{i+1} + B_i \phi_{i-1} + C_i \quad . \tag{3-15}$$

Equation (3-15) can be rearranged to produce

$$\phi_i = A_i' \phi_{i+1} + B_i' \tag{3-16}$$

where

$$A_i' = \frac{A_i}{D_i - B_i A_{i-1}'}$$

$$B_i' = \frac{C_i + B_{i-1}' B_i}{D_i - B_i A_{i-1}'}$$

and back substitution then yields the ϕ's.

In the difference equations like equation (3-9), ϕ_P is related to its four unknown neighbours ϕ_N, ϕ_S, ϕ_E and ϕ_W. However, if attention is restricted to the control volumes along one grid line and the best available values are substituted for the ϕ's on the neighbouring grid lines, the equations for the ϕ's along the grid line in question will be of the form of equation (3-15), and may be solved by application of the TDMA. In this manner a TDMA solution can be obtained for each x-direction grid line and then for each y-direction grid line. The equations for a "sweep" of the x-direction grid lines are

$$A_P\ \phi'_P = A_E\ \phi'_E + A_W\ \phi'_W + (A_N \phi_N + A_S \phi_S + S_U) \qquad (3\text{-}17)$$

where the terms in parentheses are known. The superscript ' denotes the values obtained from the first sweep. Then the equations for the y-direction lines are

$$A_P\ \phi''_P = A_N\ \phi''_N + A_S\ \phi''_S + (A_E \phi'_E + A_W \phi'_W + S_U)\ . \qquad (3\text{-}18)$$

To obtain the solution for a ϕ equation, several "sweeps" across the grid are necessary.

3.3.5 The Hydrodynamic-Solution Procedure

Because the finite-difference equations are implicit, a simultaneous solution is necessary at each step in time to obtain the hydrodynamic fields. The difference equations have been forced into a linear form, but, the coefficients are functions of the dependent variables. Thus, the simultaneous solution must be of an iterative nature; the coefficients being frequently recalculated with the "best" available values of the dependent variables. The steps of the hydrodynamic portion of the solution procedure, which is based on the SIMPLE Method (Caretto, et al, 1972), are described below.

(1) Step Forward in Time

The initial conditions are taken as the results of the previous time step. If the boundary conditions are time depedent, they must be updated.

(2) Guess the Pressure Field, p*

For the first iteration of a time step, p* is taken to be the previous time pressure field, p_o; otherwise, the pressure field from the previous iteration is used for p*.

(3) Calculate u* and v*

Coefficients computed from the most up-to-date values of the dependent variables and the guessed pressures are used to solve the momentum equations. The resulting u* and v* velocity fields do not, however, satisfy continuity.

(4) Calculate p'

The continuity errors produced by the u* and v* fields are used in equation (3-14) to calculate the pressure-corrections.

(5) Correct the Pressure and Velocity Fields

The pressure-corrections are used in equations (3-10 and 3-11) to adjust the pressure and velocity fields such that local continuity is satisfied in all control volumes.

(6) Complete the Iteration

If convergence has not been obtained, repeat steps 2 to 5.

The calculation of additional ϕ equations can be performed after the above sequence has been completed. Of course, if any of the additional ϕ equations are coupled to the momentum equations, as is the energy equation when the density in a function of temperature; then those ϕ's should be computed after step 5, inside the hydrodynamic iteration loop.

Finally, if the coefficients of the finite-difference equations incur large changes from one iteration to the next, the procedure can become unstable. The transient terms help to alleviate this problem by acting as a "natural" under-relaxation. However, in order to take larger steps in time, it is sometimes useful to directly under-relax the momentum equations.

3.3.6 Incorporation of Auxiliary Information

Boundary Conditions

The boundary conditions for the finite-difference equations are usually prescribed in one of two ways. Either the value of a variable or its normal gradient is specified at the grid boundary. For example, at stationary, impervious walls, the velocities are zero. However, at symmetry planes, the velocity gradients normal to the boundary are zero. The boundary conditions may be time dependent, in which case they must be modified appropriately before starting each time step.

Initial Conditions

The initial fields of pressure, velocities and all additional ϕ's must be specified before the calculational procedure can start. The initial conditions for the second and subsequent steps in time are taken as the results of the previous time step. Thus, the computation of each forward step is in essence a separate problem, and the solution procedure may be easily stopped and restarted.

Other Auxiliary Information

The fluid properties, densities and exchange coefficients, are assumed constant within each fluid region. In control volumes containing both fluids, suitable weighted averages of the gas and liquid properties are used. This calculation of these average properties will be discussed in Section 3.4.2.

Additional source terms for the individual equations must be incorporated as necessary. For instance, the buoyancy term must be in the axial-direction momentum equation for an axisymmetric geometry, but, in a plane flow, the gravitational vector may point in either coordinate direction or it may not be aligned with the axes. Other examples include the terms to represent the momentum loss incurred by flow through a distributed resistance and the simulation of walls internal to the flow geometry, either impermeable walls or "leaky" walls.

3.4 FREE-SURFACE CALCULATIONS

3.4.1 Particle Tracking

The free surface is marked by a "string" of massless particles. These particles are moved, according to equation (2-12), during each time step. The components of equation (2-12) in finite-difference form are

$$\begin{aligned} x_P &= x_{P,o} + u_P \Delta t \ , \\ y_P &= y_{P,o} + v_P \Delta t \ , \end{aligned} \qquad (3\text{-}19)$$

where (x_P, y_P) and $(x_{P,o}, y_{P,o})$ are respectively the new and old locations of the particle, and u_P and v_P are the instantaneous velocity components of the particle. The particle velocity components are evaluated at the old particle location $(x_{P,o}, y_{P,o})$ by linear interpolation of the four nearest velocities in the appropriate direction (see Figure 3-5).

3.4.2 Calculation of the Local Densities

Not only are the marker particles a convenient way to display the free-surface configuration in the output from the computations, but they also provide a means of calculating the densities for the control volumes intersected by the free surface. The densities of these

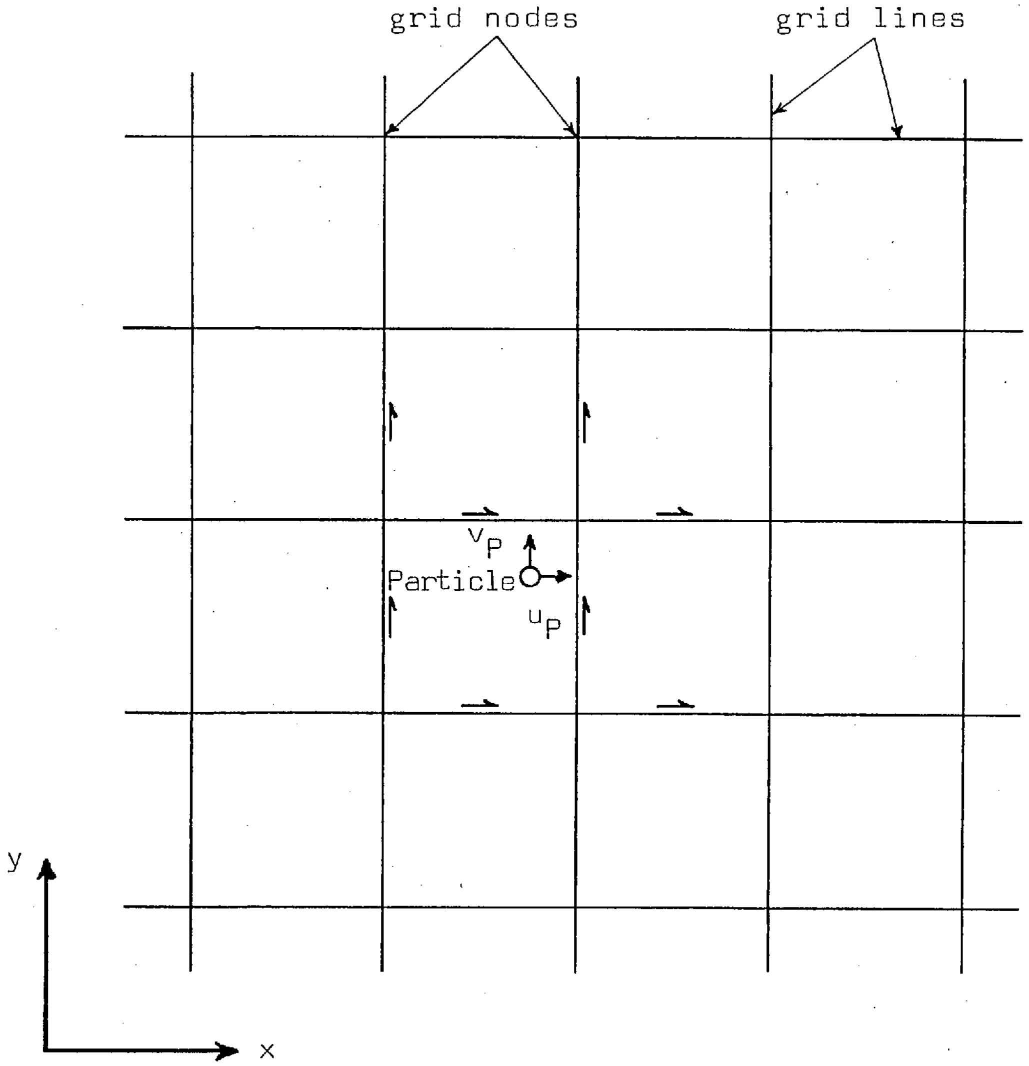

→ u-velocities used in interpolation procedure to obtain u_P.

↑ v-velocities used in interpolation procedure to obtain v_P.

FIGURE 3-5 : VELOCITIES USED IN THE INTERPOLATION OF THE PARTICLE VELOCITIES free-surface control volumes are calculated by averaging the gas and liquid densities with a weighting factor based on the relative amounts of each fluid within the control volume. Two types of average densities are calculated, those representative of the whole control volumes and those representative of the control volume faces. Both types of densities are computed for each of the three kinds of control volumes defined in Figure 3-2. These "local" densities are needed to solve the hydrodynamic equations; the control volume densities are used in the transient terms, the body-force terms, etc., and the densities for the control volume faces are used in the convective terms.

The free-surface marker particles are grouped into "strings", such that each string of particles begins and ends at a grid boundary. Hence, there are as many strings of particles as there are separate interfaces; only one or two strings are necessary to describe most flows of interest. Figure 3-6 shows an illustrative example of a free-surface flow composed of two strings. Note that both strings may pass through a single control volume and a string may pass through the same control volume several times. However, this flexibility is included to generalise the calculations, and it is important to keep in mind that details of the free-surface shape on a scale much smaller than the dimensions of the control volumes cannot be accurately predicted. Finally, the

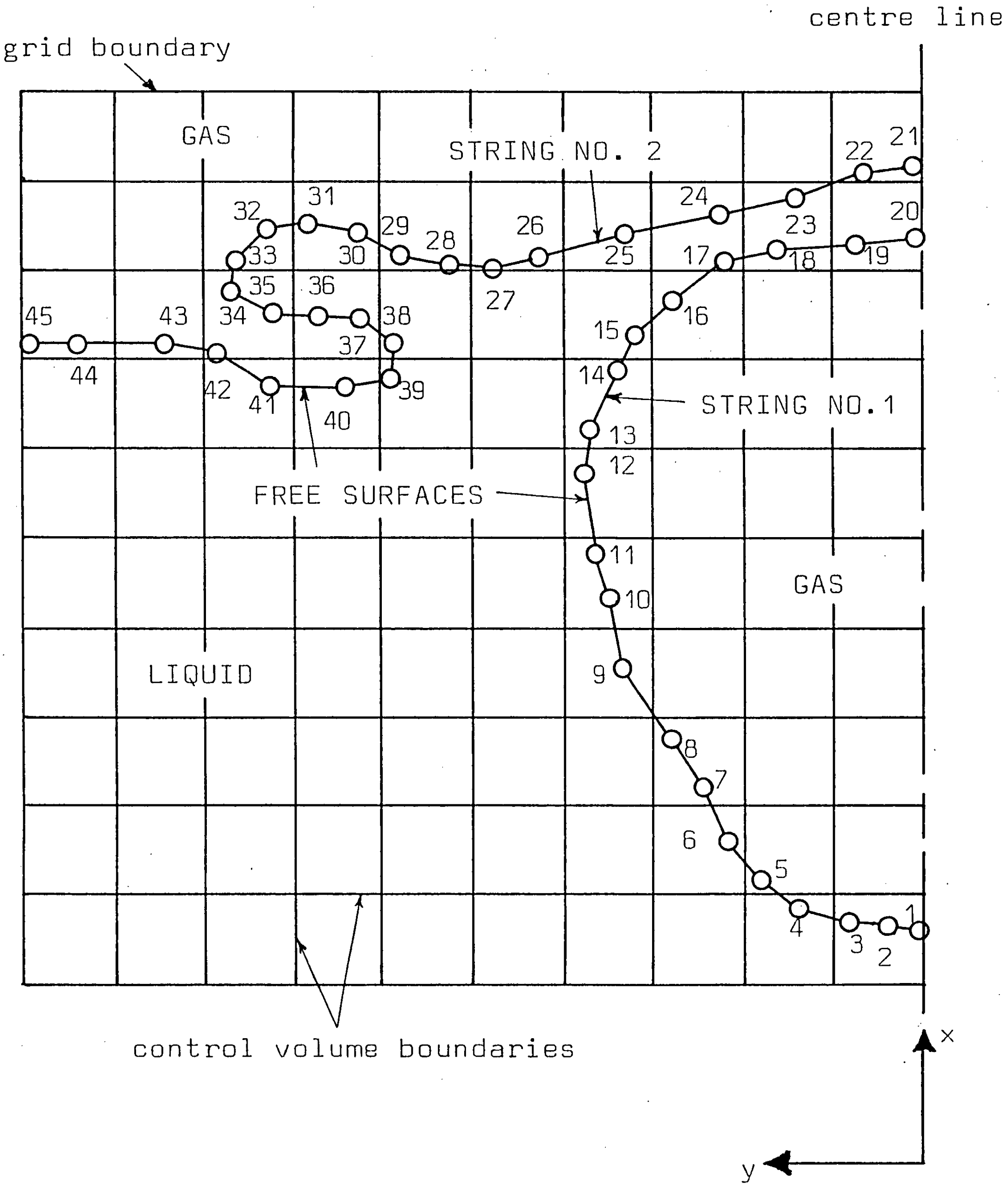

FIGURE 3-6 : TYPICAL FREE-SURFACE CONFIGURATION SHOWING THE PARTICLE NUMBERING CONVENTION strings of particles are not allowed to cross either themselves or other strings.

The particles are numbered consecutively along the strings such that an observer moving from particle k to particle k+1 (see Figure 3-6) always sees gas to his right and liquid to his left. Each time the particles are moved the calculational procedure inserts additional particles midway between any two consecutive particles that are separated by a distance greater than a prescribed maximum, δ_1 (see Figure 3-7(a)), and removes particles which are closer than a prescribed minimum, δ_2 (see Figure 3-7(b)). Also, the redundant particles in a configuration like the one depicted in Figure 3-7(c) are removed if ε is sufficiently small. As particles are deleted and inserted, the particle numbering is adjusted to maintain an orderly arrangement consistent with the example in Figure 3-6.

To calculate the local densities, the percentage of liquid present in each control volume and at each control volume face is computed from the particle locations. It is a straightforward procedure to determine which control volumes contain particles. Figure 3-8 illustrates a free-surface control volume and the particles along the portion of the string that passes through the control volume. The volume of fluid between the particle string and the face of the control volume nearest the y-axis is divided into

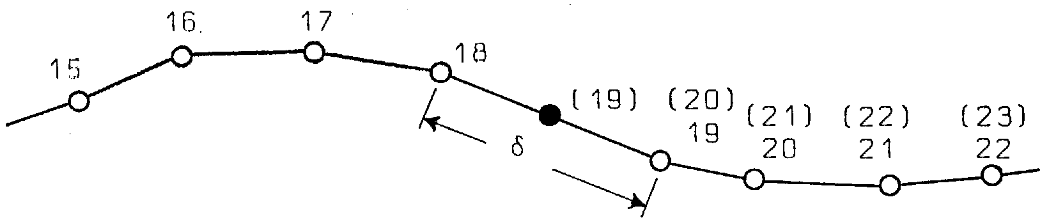

(a) A new particle is added midway between two particles (i.e. 18 and 19) if δ exceeds the maximum spacing, δ_1. The particles are then renumbered to account for the new particle.

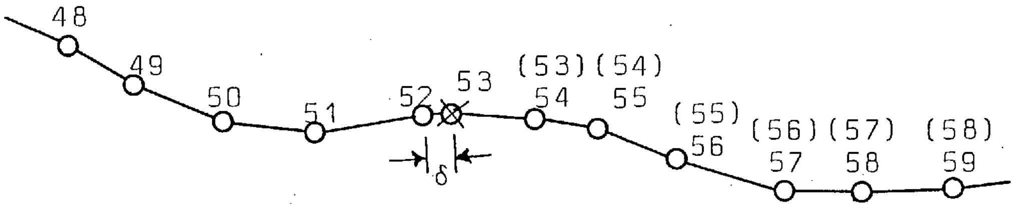

(b) Particle 53 is deleted if δ is less than the minimum spacing, δ_2. The particles are renumbered to account for the deleted particle.

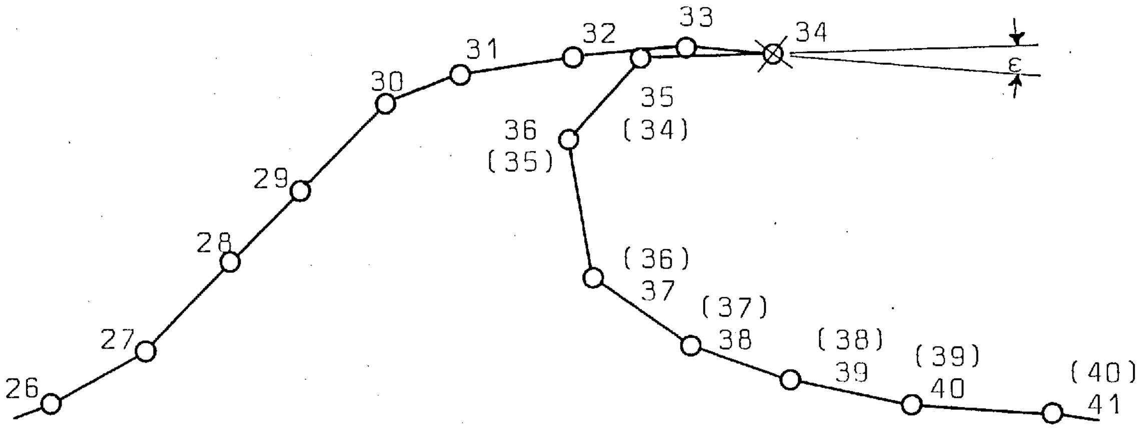

(c) Particle 34 is deleted if ε is smaller than a predetermined size. The particles are then renumbered to account for the deleted particle.

FIGURE 3-7 : PARTICLE DELETION AND ADDITION PROCEDURES

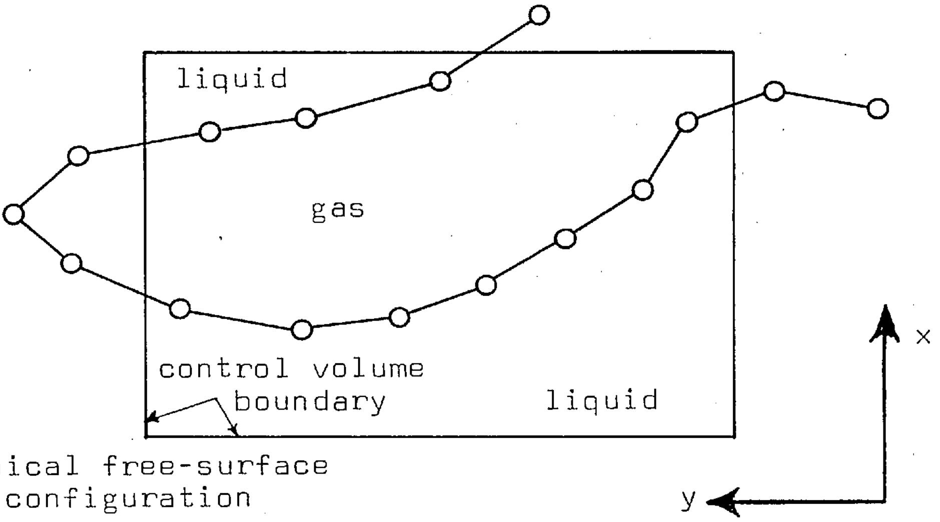

Typical free-surface configuration

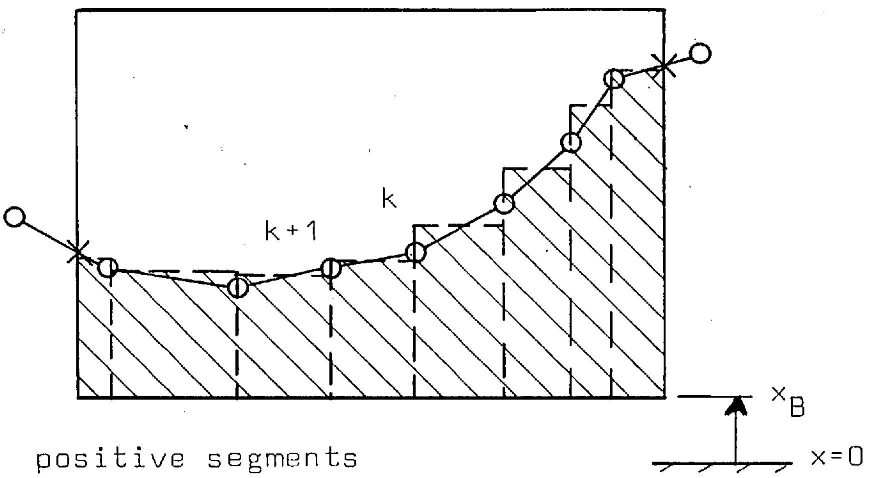

positive segments

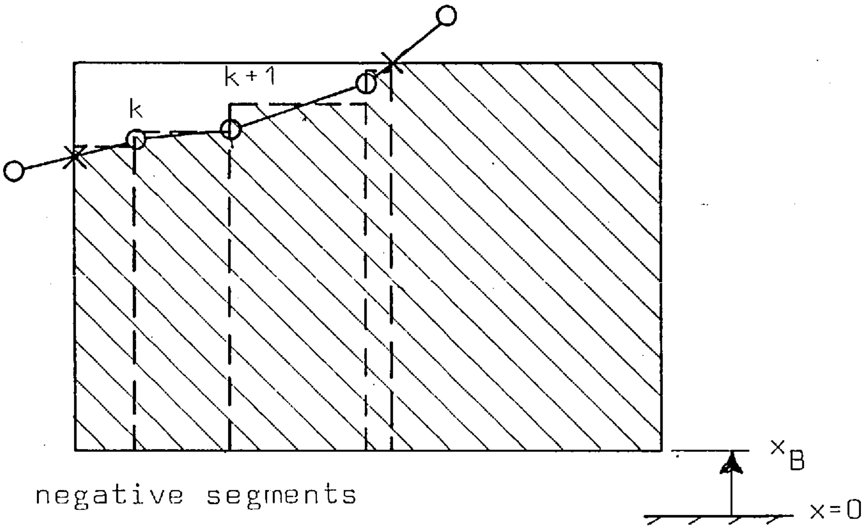

negative segments

Summation of all the segments gives (a) the volume of liquid in the control volume if the sum is positive, or (b) the volume gas in the control volume if the sum is negative.

FIGURE 3-8 : CALCULATION PROCEDURE FOR LOCAL DENSITIES segments as shown. The volume of these segments may be expressed as

$$V_{seg} = (y_{k+1} - y_k) \left(\frac{r_{k+1}+r_k}{2}\right) \left[\frac{(x_{k+1}+x_k)}{2}\right] - x_B \quad (3\text{-}21)$$

where the x's and y's are coordinate locations and the r's are radial distances for cylindrical coordinates and unity for cartesian coordinates. Obvious adjustments to equation (3-21) are necessary for the first and last segment in the control volume. The factor $(y_k - y_{k+1})$ will make V_{seg} positive when the segment is filled with liquid and negative when the segment is filled with gas. Thus, it is only necessary to algebraicly sum the segment volumes (the liquid segments add and the gas segments subtract) and divide the result by the total volume of the control volume to obtain the percentage of liquid present. If the result is positive, then it is the per cent liquid in the control volume; however, if the result is negative, the per cent liquid is produced by adding unity. This procedure can handle any free-surface configuration in which the particle strings do not intersect themselves or each other. The percentage of liquid on a control-volume face is calculated in a similar manner. Once the percentage of liquid is known the density can be computed from the simple relation

$$\rho_{avg} = \alpha\rho_{\ell} + (1-\alpha)\,\rho_g \quad (3\text{-}22)$$

where

$\alpha \equiv$ per cent liquid.

The effective viscosity needed to calculate the shear stresses may be averaged in the same manner as the control volume face densities.

Finally, the calculational procedure must be able to distinguish whether a control volume, which does not contain any particles, is filled with gas or liquid. The fluid region containing such a control volume is bounded by the nearest free surface. Hence, the particle nearest the control volume and its two neighbours form a segment of the bounding interface.† These particles are denoted a, b and c where a is the lowest numbered of the three particles, and c the highest. The control volume is identified by the geometrical centre, m. A set of coordinate axes $(x',y')_{pq}$ can be constructed so that the origin is located at a point p and the x' axis passes through the point q by translating and rotating the (x,y) coordinates.

$$x' = \frac{(x-y_p)(x_q-y_p) + (y-y_p)(y_q-y_p)}{\sqrt{(x_q-x_p)^2 + (y_q-y_p)^2}} \qquad (3\text{-}23)$$

---

†When the nearest particle is on the end of a string, the three particles at the end of the string are used.

$$y' = \frac{(y-y_p)(x_q-y_p) - (x-x_p)(y_q-y_p)}{\sqrt{(x_q-x_p)^2 - (y_q-y_p)^2}}$$

Then, to decide which fluid the control volume contains, it is sufficient to know the sign of $y'_{m_{ab}}$, $y'_{m_{bc}}$, $y'_{m_{ac}}$ and $y'_{b_{ac}}$. For instance, if $y'_{m_{ab}} < 0$, $y'_{m_{bc}} < 0$, $y'_{m_{ac}} < 0$ and $y'_{b_{ac}} > 0$ as in Figure 3-9, the control volume around m contains gas. There are sixteen possible combinations of the y''s which can be worked out easily.

3.5 SUMMARY OF THE SOLUTION PROCEDURE

The complete solution procedure is summarised below.

(1) Set the Initial Conditions

The necessary initial conditions include the hydrodynamic fields and any additional ϕ fields, as well as the initial locations of the free-surface marker particles. For the second and subsequent time steps, the results of the previous time step are the initial conditions.

(2) Step Forward in Time.

(3) Set the Boundary Conditions.

(4) Calculate the Local Densities.

The local densities are computed from the free-surface particle locations.

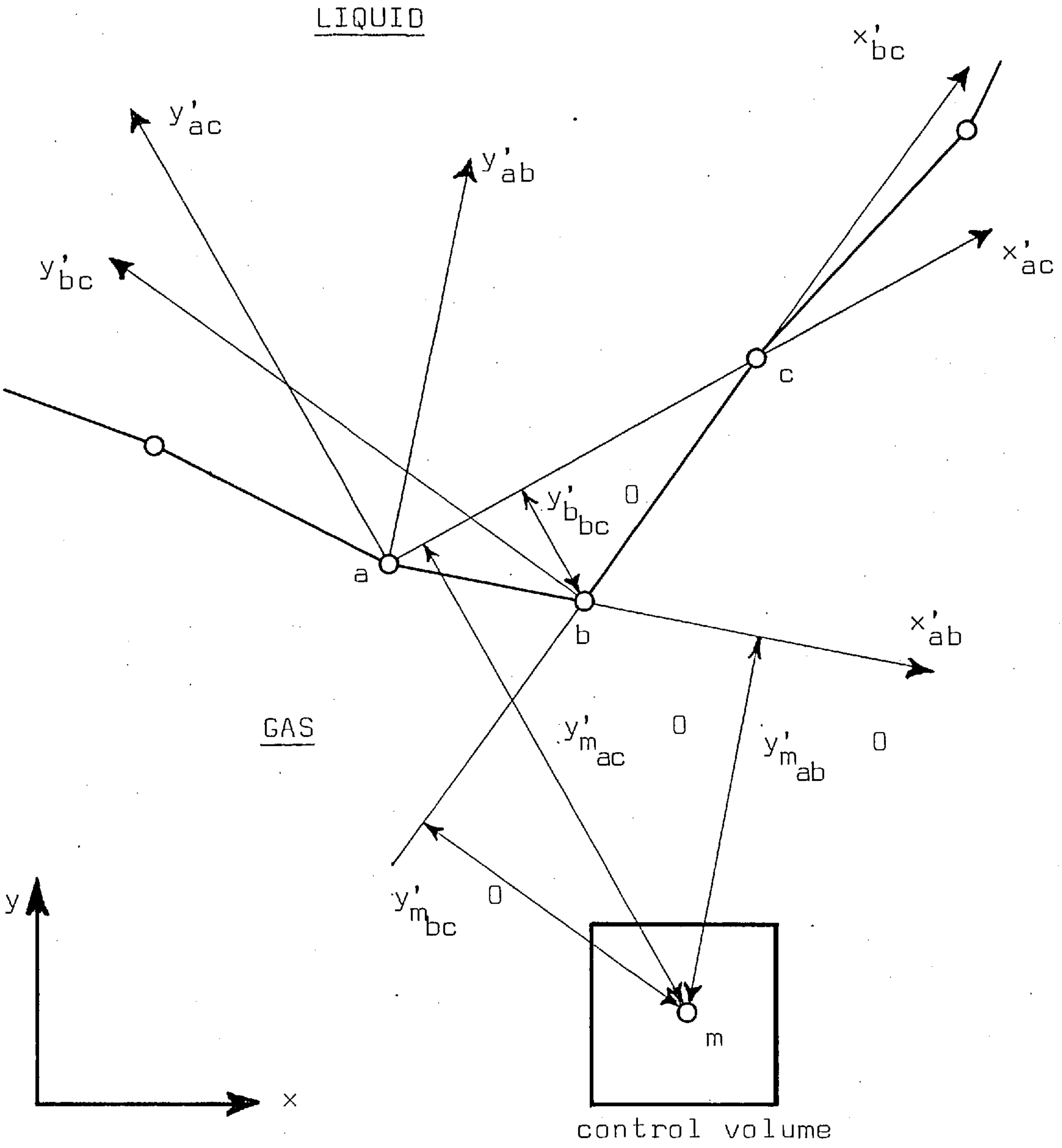

FIGURE 3-9 : PRIMED COORDINATE SYSTEMS USED TO DETERMINE DETERMINE WHICH FLUID IS PRESENT IN A CONTROL VOLUME WHICH CONTAINS NO PARTICLES

(5) Compute the Hydrodynamic Fields

The hydrodynamic fields are computed by the procedure outlined in Section 3.3.5.

(6) Move the Free-Surface Particles

The particles are moved with the new velocity fields.

(7) Output Results.

(8) Return to Step 1 and repeat for each additional time step.

CHAPTER 4

EXPERIMENTAL WORK

4.1 INTRODUCTION

Validation of the numerical model requires the comparison of predictions with experimental data. Some experimental results for free-surface flows are available in the literature; however, to complement the computational portion of this study, an experimental investigation of wave motions has been included. Waves generated in water contained in a perspex tank were filmed with a ciné camera. Prints of individual frames of the ciné film can be easily compared with the computed results for each time step. Comparisons with the experimental results can determine first, how well the model predicts the correct amplitude and forward speed of the wave, and secondly, how well the model can predict the wave shape.

4.2 EXPERIMENTAL APPARATUS

The experimental apparatus consists of a perspex tank and column arrangement as shown in Figures 4-1 and 4-2. The column is situated at one end of the tank so that there is a gap between the bottom of the column and the floor of the tank. The vertical position of the column can be adjusted to change the height of this gap. Near the top of the column is a 0.1016 M diameter hole which is fitted with a removable cover plate and

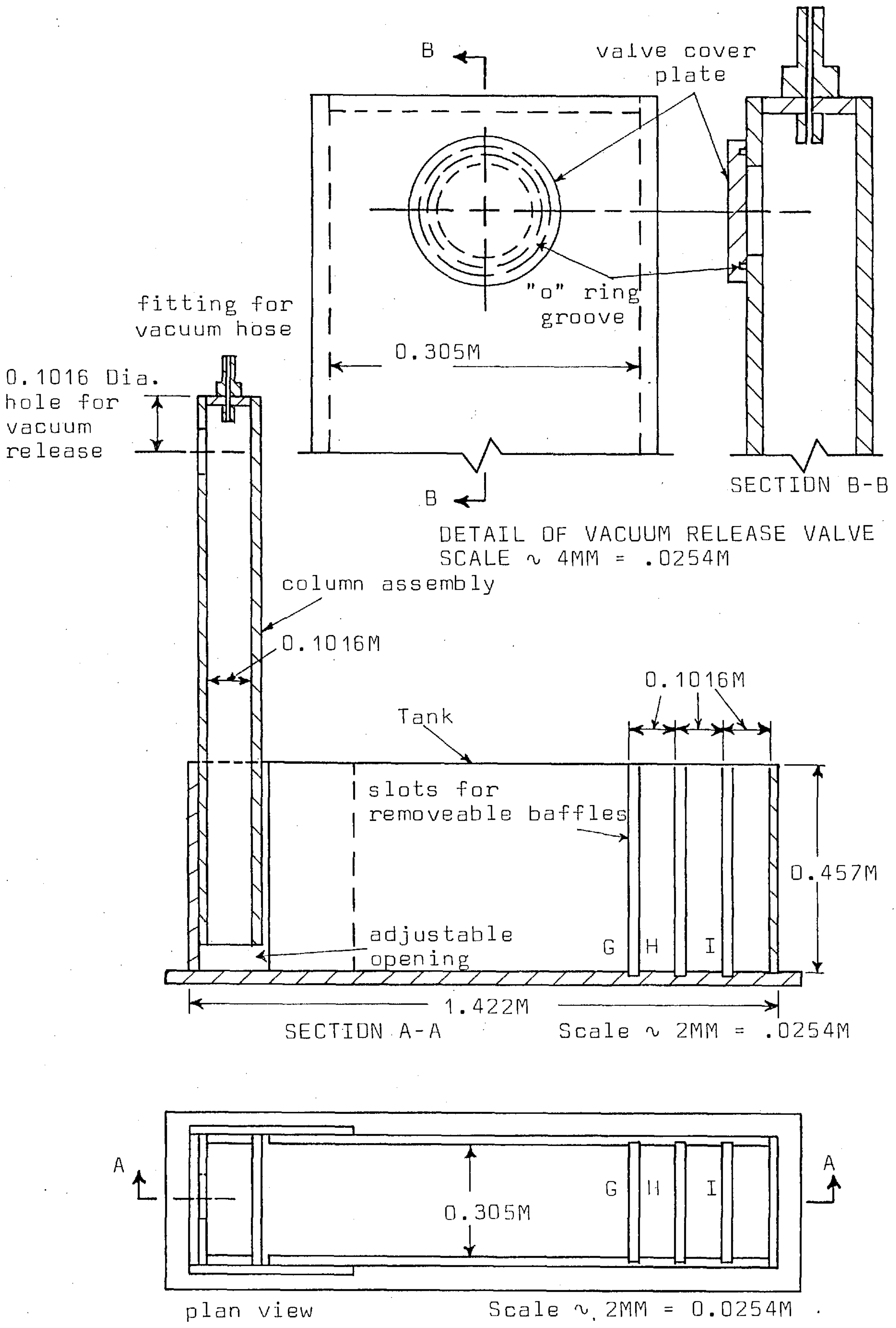

FIGURE 4-1 : DIAGRAM OF THE EXPERIMENTAL APPARATUS

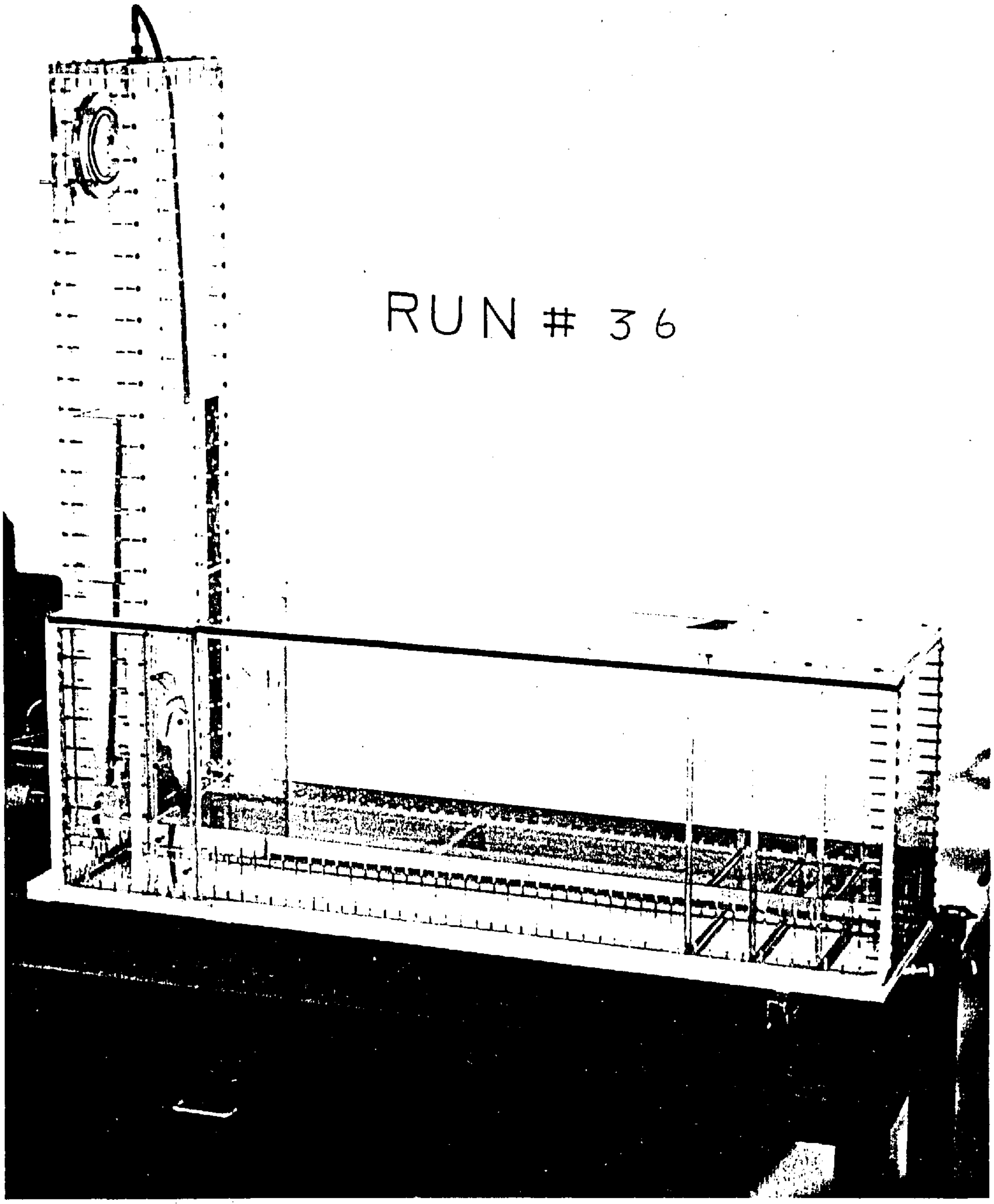

FIGURE 4-2 : OVERALL VIEW OF THE EXPERIMENTAL APPARATUS

"O" ring assembly. A vacuum line is connected to the top of the column, and finally, the tank is partially filled with water.

A wave can be generated in the tank quite easily. First, the air pressure above the water surface in the column is reduced via the vacuum line, and water is drawn up into the column. Then, removal of the cover plate and "O" ring assembly allows the air in the upper portion of the column to return to atmospheric pressure and gravitational acceleration causes the water stored in the column to rush down, through the gap at the bottom of the column and into the tank. The rush of water from the column produces a wave in the tank. The size and speed of the wave can be altered by adjusting the depth of water in the tank, the initial water level in the column and the size of the opening at the bottom of the column. Further, baffles can be inserted in the slots shown in Figure 4-1.

The experimental results were recorded with a Bolex 16H 16mm ciné camera. After the water levels in the tank and column had been adjusted for a particular run, the ciné camera was started and the wave was initiated by removing the cover plate from the hole at the top of the column. The camera was run until the initial wave had rebounded from the end of the tank. Blue dye was added to the water to improve the contrast between the water surface and the background.

Ideally, the experimental results should be free from all physical effects not modelled by the computational procedure described in the previous chapters. Thus, to ensure the two-dimensional nature of the waves, the tank was made 0.3048 meter wide. The curvature of the water surface is sufficiently large to remove the effects of surface tension. Finally, the Reynolds number of the flow through the opening at the bottom of the column is of the order of 10^5; however, it is assumed that turbulence will not significantly affect overall motion of the wave. Thus, the wave motion is dependent primarily on the inertial and gravitational forces.

Experimental errors may arise both when the ciné film is exposed, and when measurements are taken from the film. The time scale of the results is affected by the consistency of the film speed. Calibration of the camera showed that the actual film speed was 54 frames per second. To ensure a constant film speed, the camera was started approximately one second before the wave was initiated. The camera was placed 8 meters away from the tank and a 75mm, 1.9f auto lens was used in order to reduce the photographic distortion and to produce "two-dimensional" images on the film. The largest errors were introduced during the measurement of the quantities defined in Figure 4-3. These measurements were taken from the projected images of individual frames of the ciné film. The error incurred

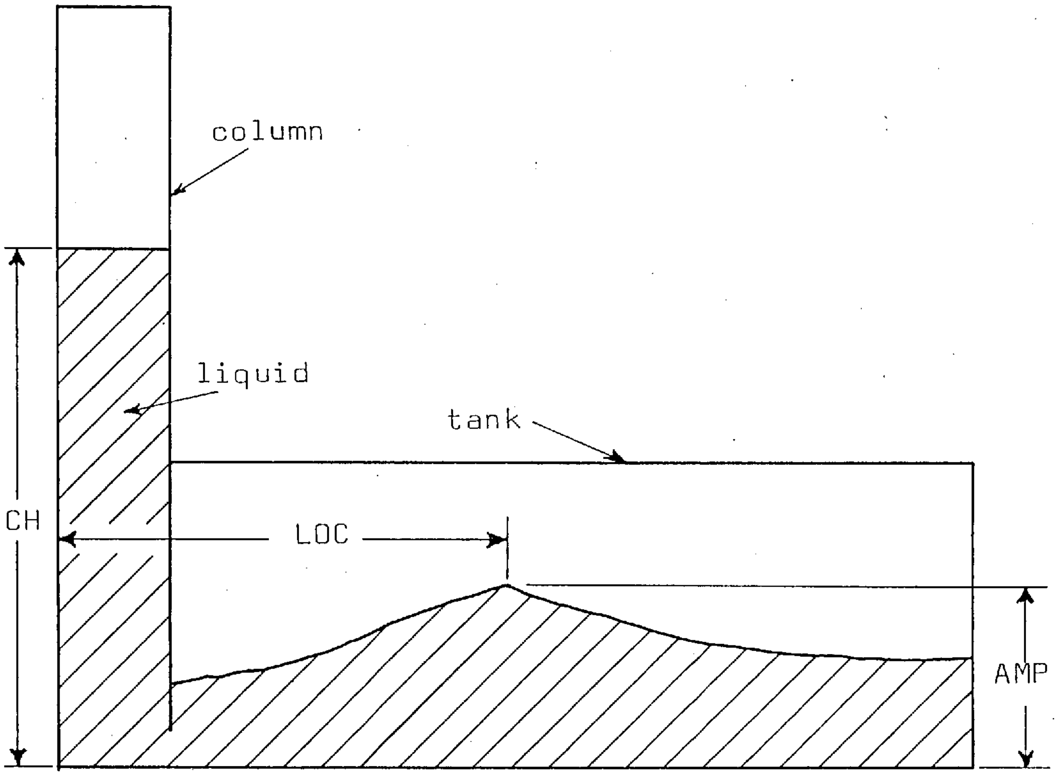

AMP	amplitude of the wave
LOC	location of the wave crest
CH	height of liquid in column

FIGURE 4-3 : DEFINITION SKETCH FOR THE MEASUREMENTS TAKEN FROM THE CINE FILM in these measurements is of the order of five to ten per cent.

4.3 EXPERIMENTAL RESULTS

More than thirty experimental runs were filmed. From these, four typical runs were selected for presentation and comparison with the computations. Details of these four runs are given in Table 4-1. Several frames from the ciné film of Run No. 4 are shown in Figure 4-4. As the wave moves across the tank, it first becomes very turbulent on the back side, and then it breaks forward very slightly. Impact of the wave on the end wall produces a run up of approximately twice the height of the approaching wave. Finally, a reflected wave forms and begins to move back across the tank. The measured data (as defined in Figure 4-3) for Run No. 4 are presented in Figure 4-5. A sequence of frames from Run No. 11 is shown in Figure 4-6. Run No. 11 has a greater initial depth of water in both the tank and the column than does Run No. 4; thus it produces a larger wave. Again, the wave is turbulent on the back side, but in Run No. 11 the wave does not break forward at all. Upon impact with the end wall the Run No.11 wave forms a tall, thin sheet of water up the end wall. The measured data for Run No. 11 are presented in Figure 4-7. For the other two typical runs a baffle 0.085 meters high was placed 1.08 meters from the column end of the tank (slot G in Figure 4-3). The initial water level in the tank for Run No. 8

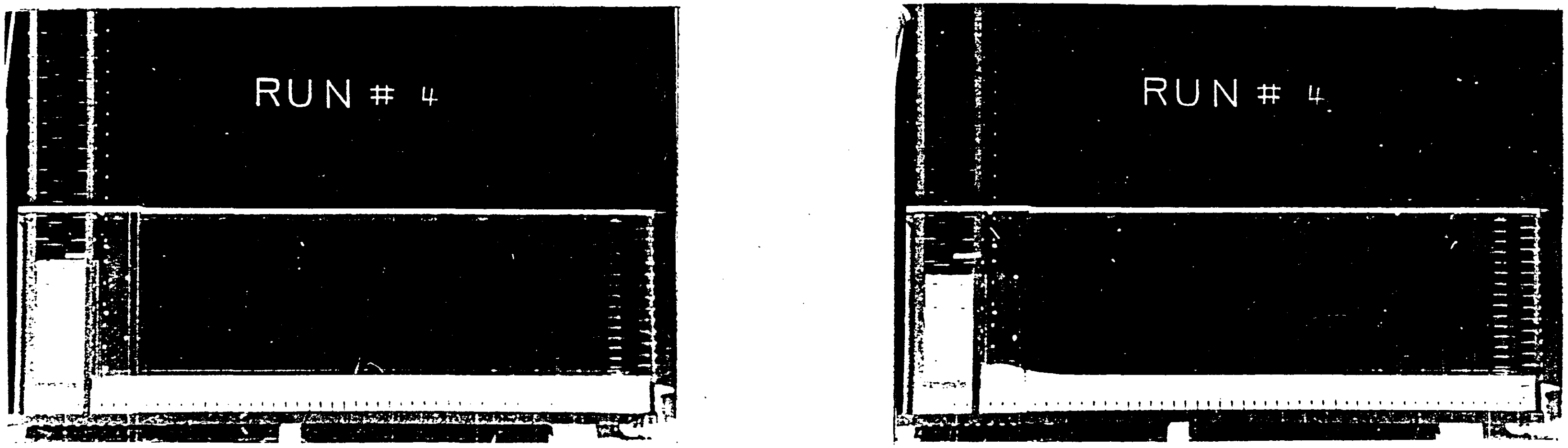

TIME = 0.000 SEC.   TIME = 0.111 SEC.

TIME = 0.222 SEC.   TIME = 0.333 SEC.

FIGURE 4-4: SEQUENCE OF FRAMES FOR RUN NO. 4

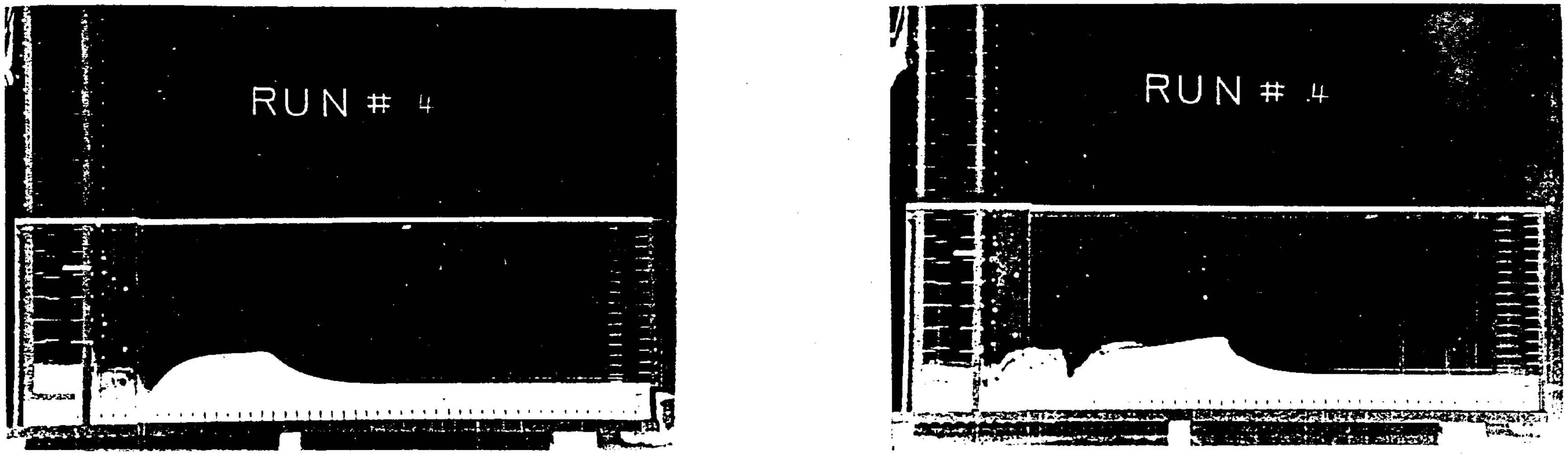

TIME = 0.444 SEC.

TIME = 0.555 SEC.

TIME = 0.666 SEC.

TIME = 0.777 SEC.

FIGURE 4-4 (CONTINUED)

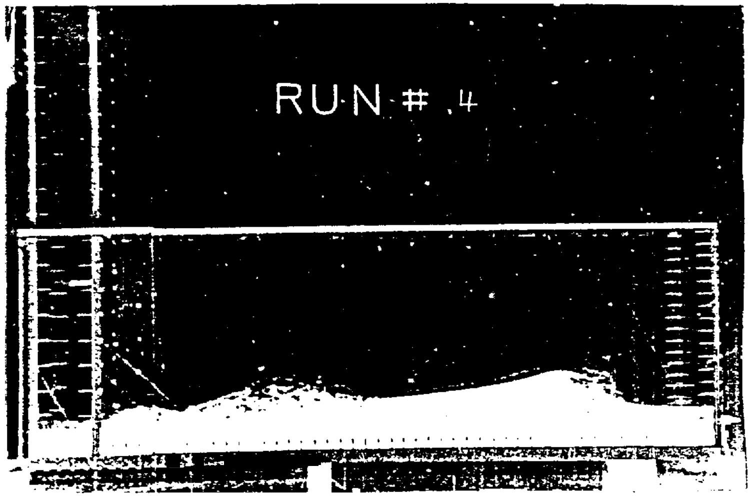

TIME = 0.888 SEC.

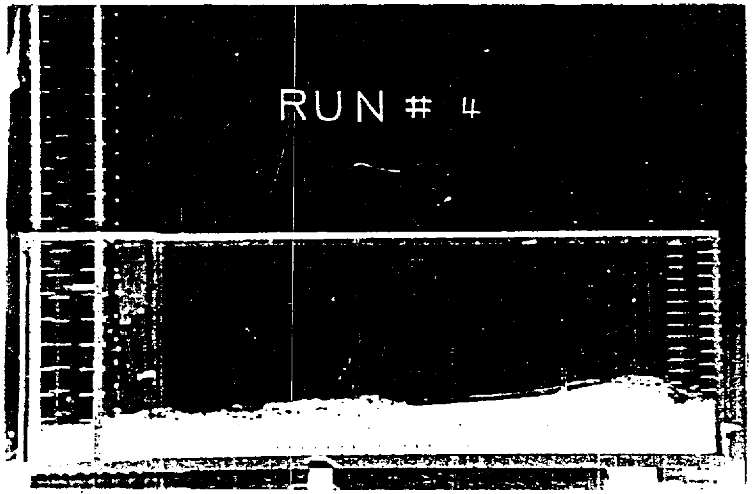

TIME = 0.999 SEC.

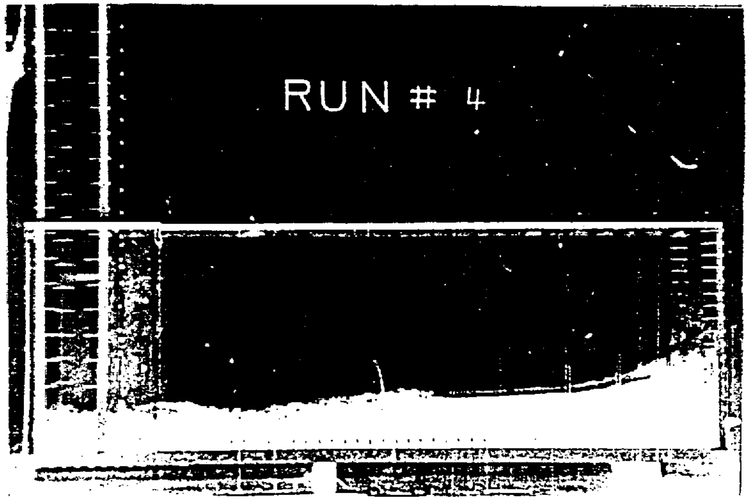

TIME = 1.111 SEC.

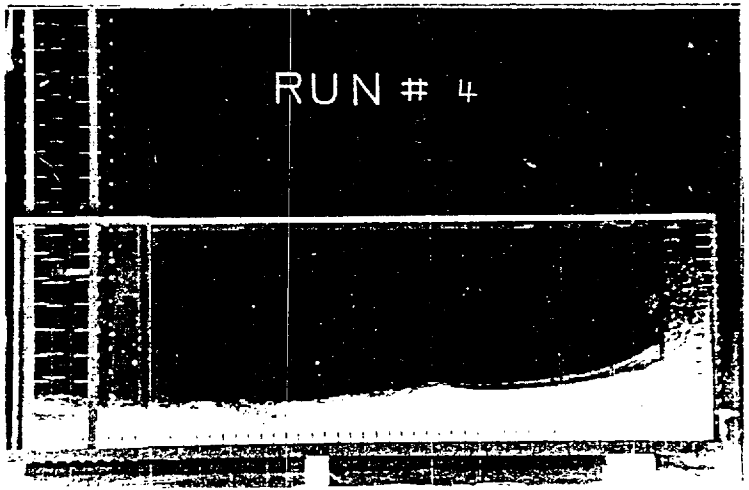

TIME = 1.222 SEC.

FIGURE 4-4 (CONTINUED)

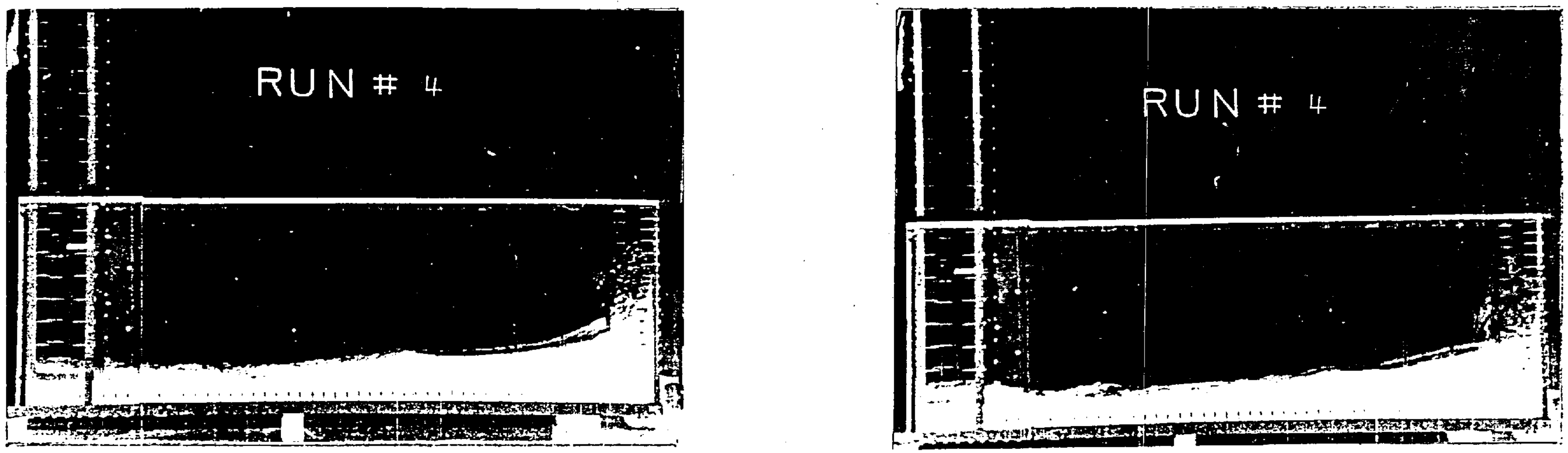

TIME = 1.333 SEC.

TIME = 1.444 SEC.

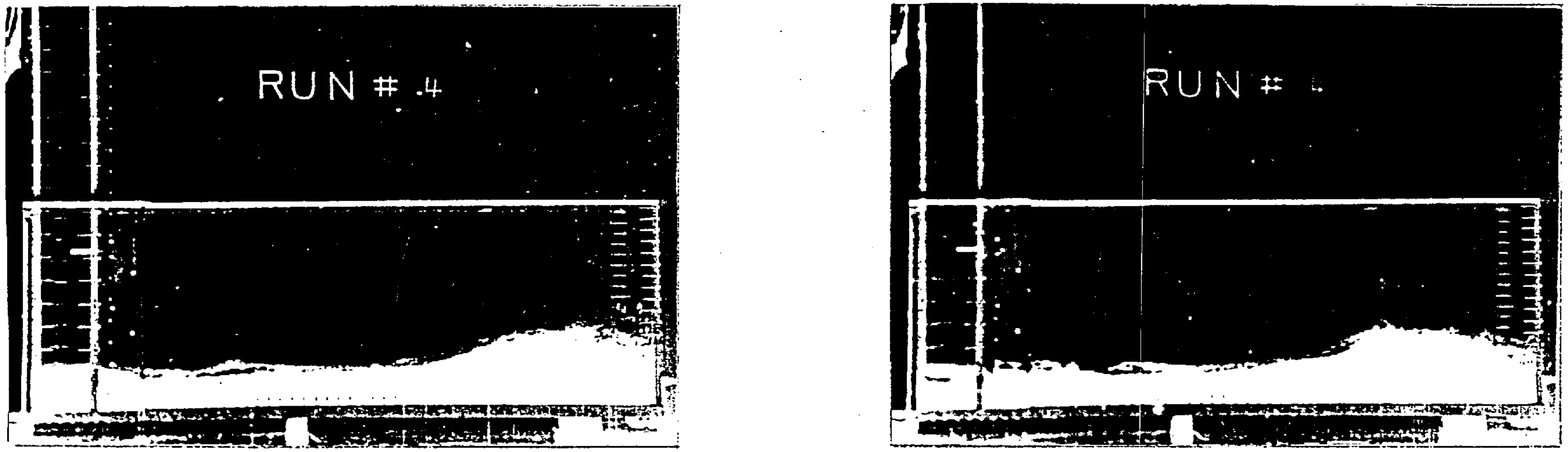

TIME = 1.555 SEC.

TIME = 1.666 SEC.

FIGURE 4-4 (CONTINUED)

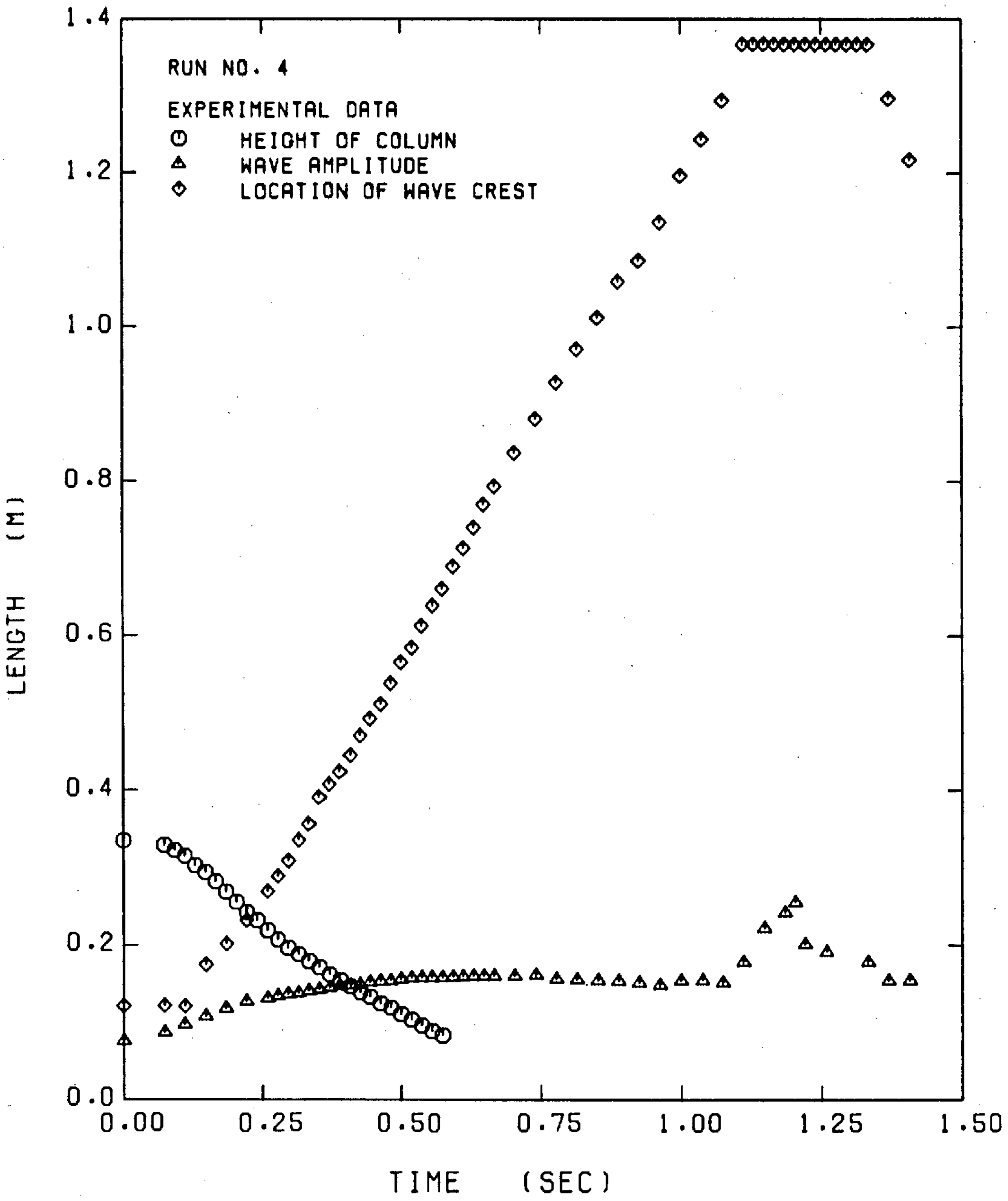

FIGURE 4-5 : MEASURED DATA FOR RUN NO. 4

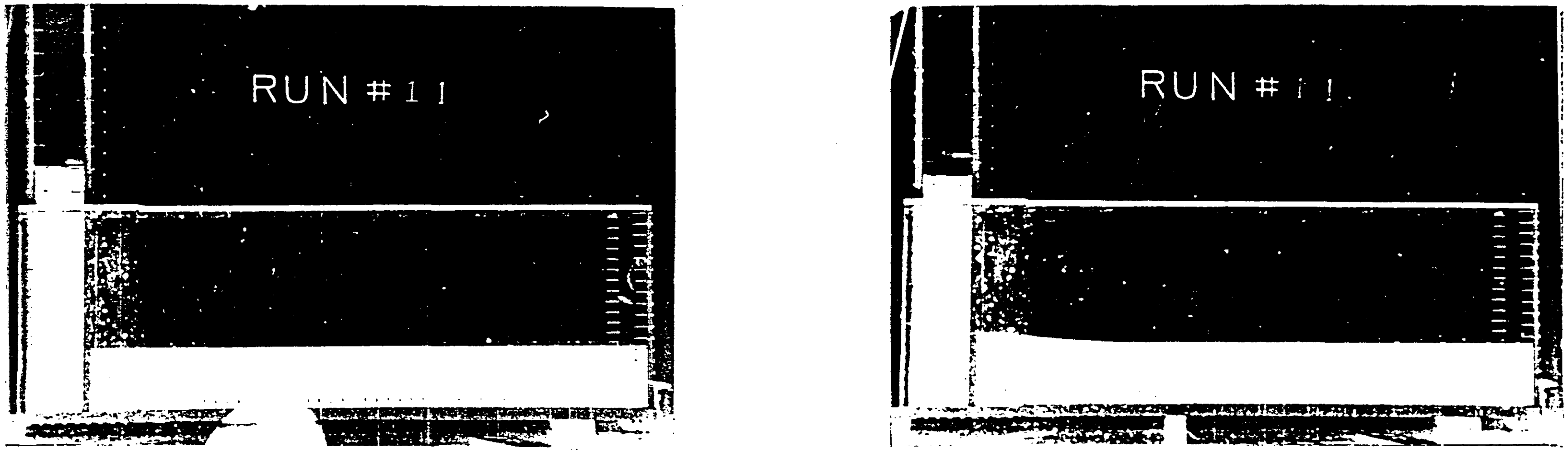

TIME = 0.000 SEC.

TIME = 0.111 SEC.

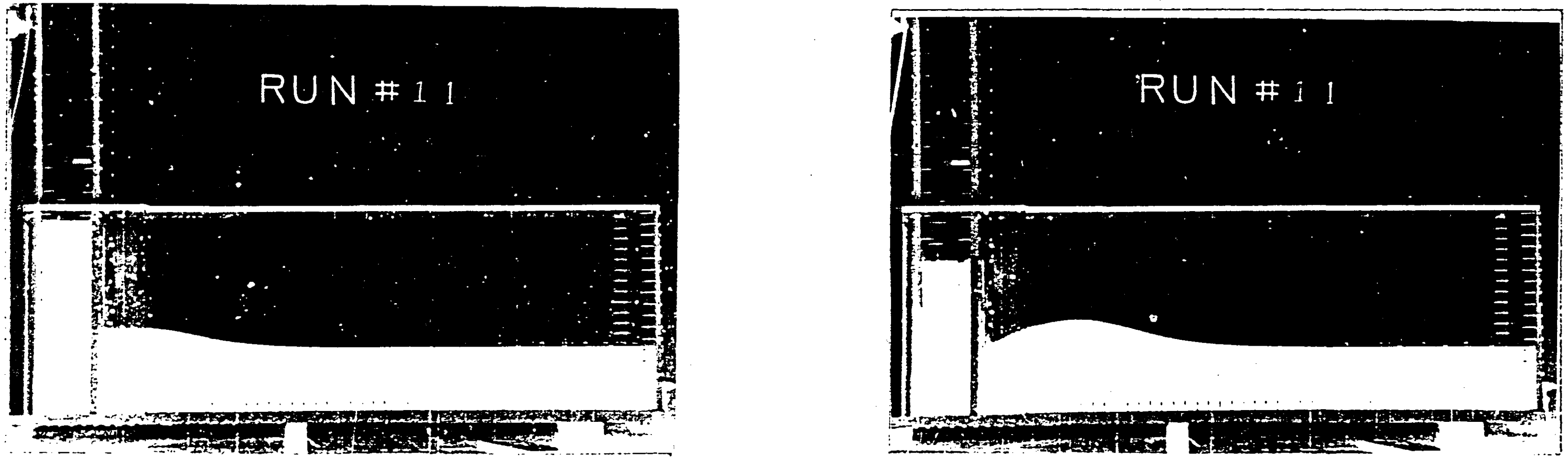

TIME = 0.222 SEC.

TIME = 0.333 SEC.

FIGURE 4-6: SEQUENCE OF FRAMES FOR RUN NO. 11

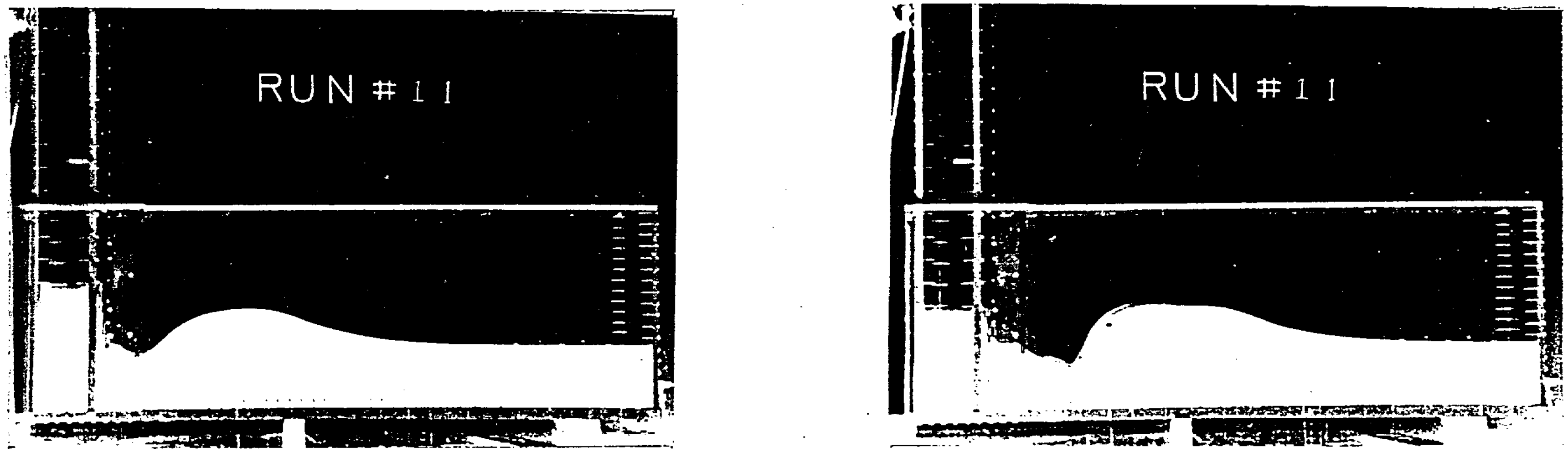

TIME = 0.444 SEC.

TIME = 0.555 SEC.

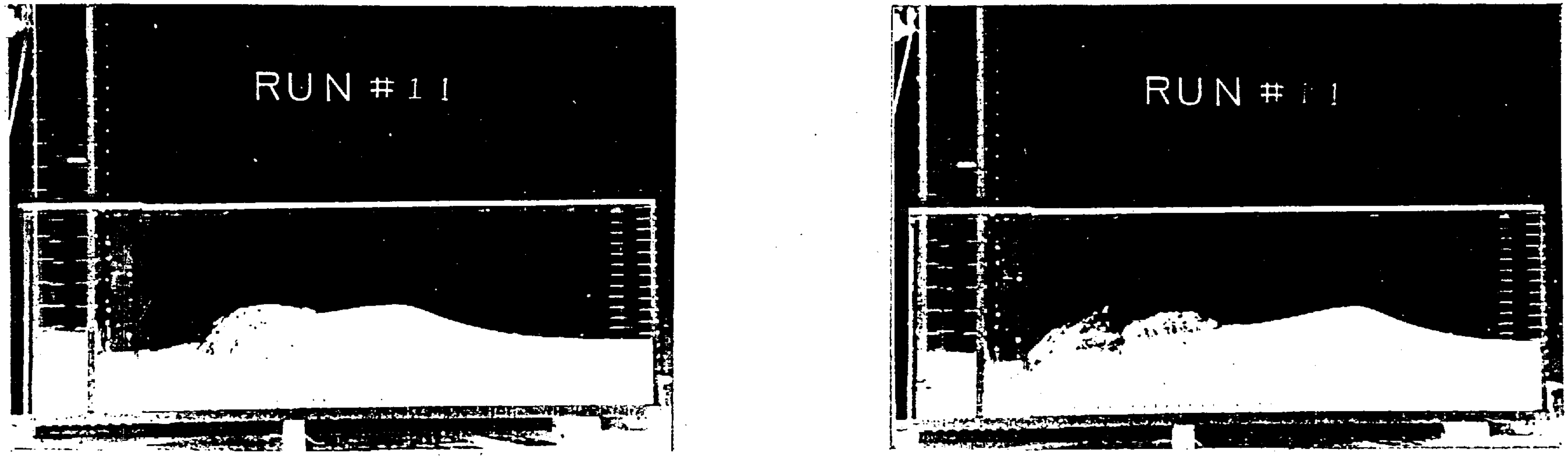

TIME = 0.666 SEC.

TIME = 0.777 SEC.

FIGURE 4-6 (CONTINUED)

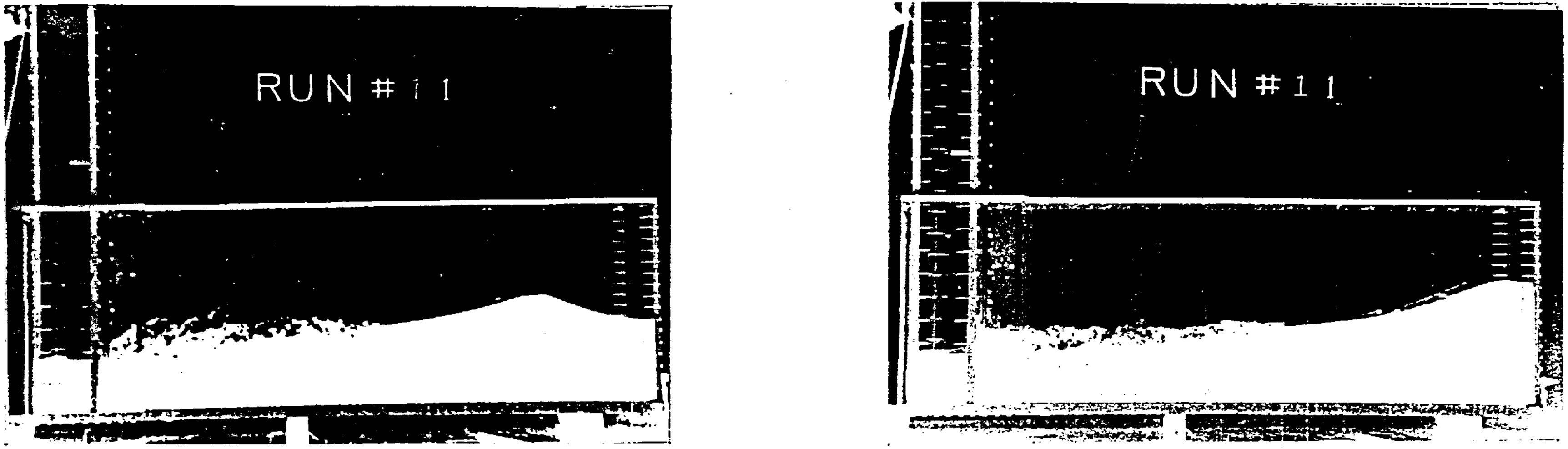

TIME = 0.888 SEC

TIME = 0.999 SEC.

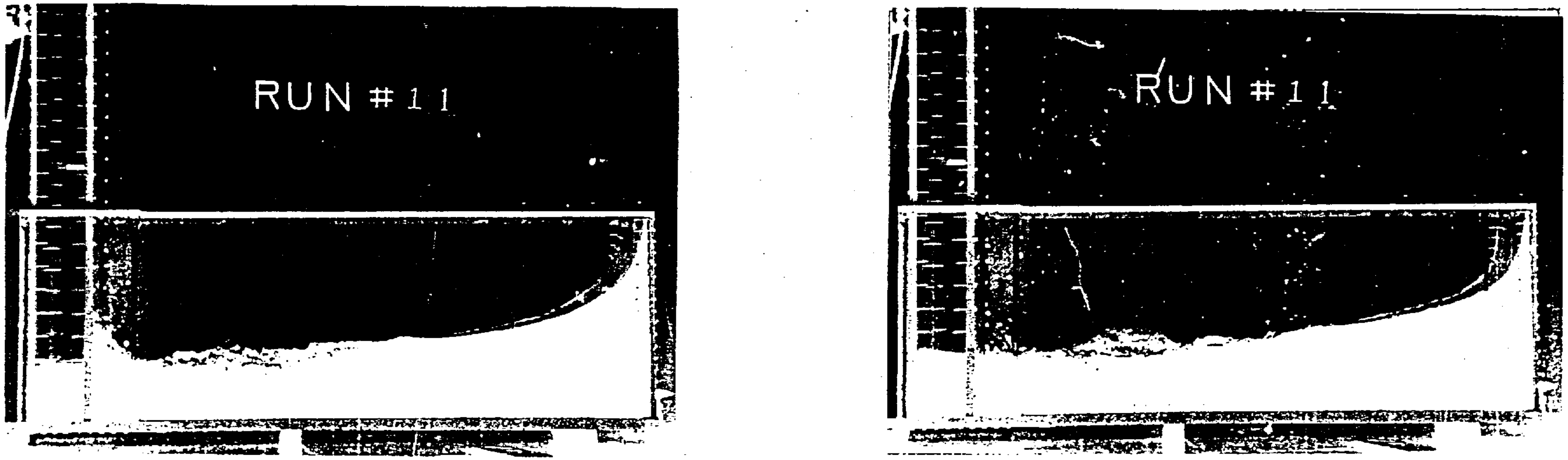

TIME = 1.111 SEC.

TIME = 1.222 SEC.

FIGURE 4-6 (CONTINUED)

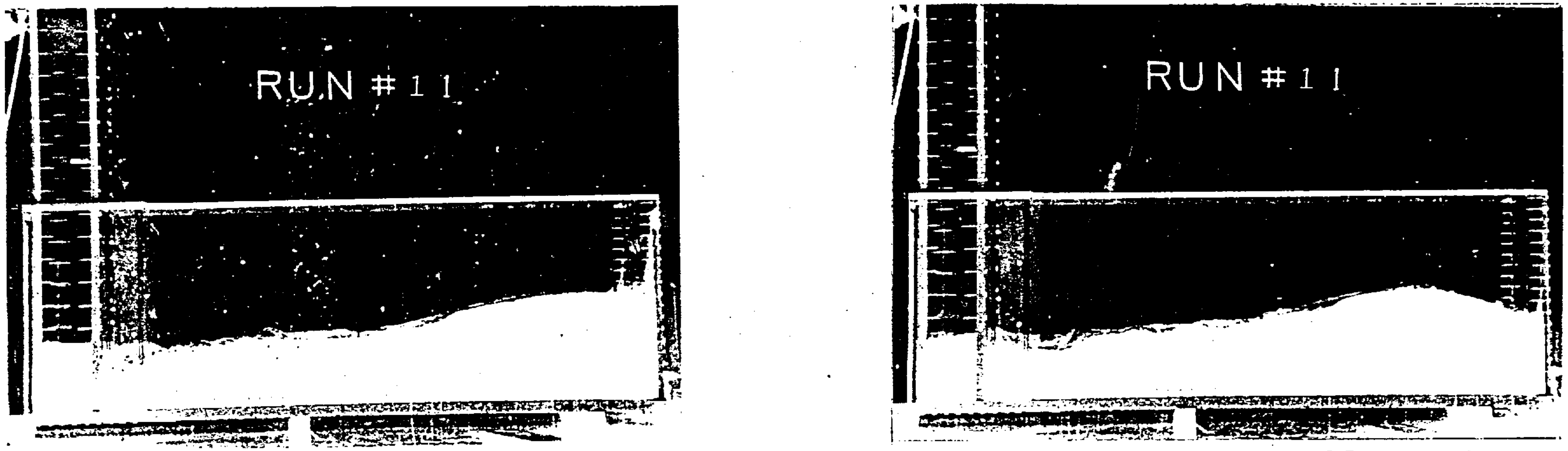

TIME = 1.333 SEC.

TIME = 1.444 SEC.

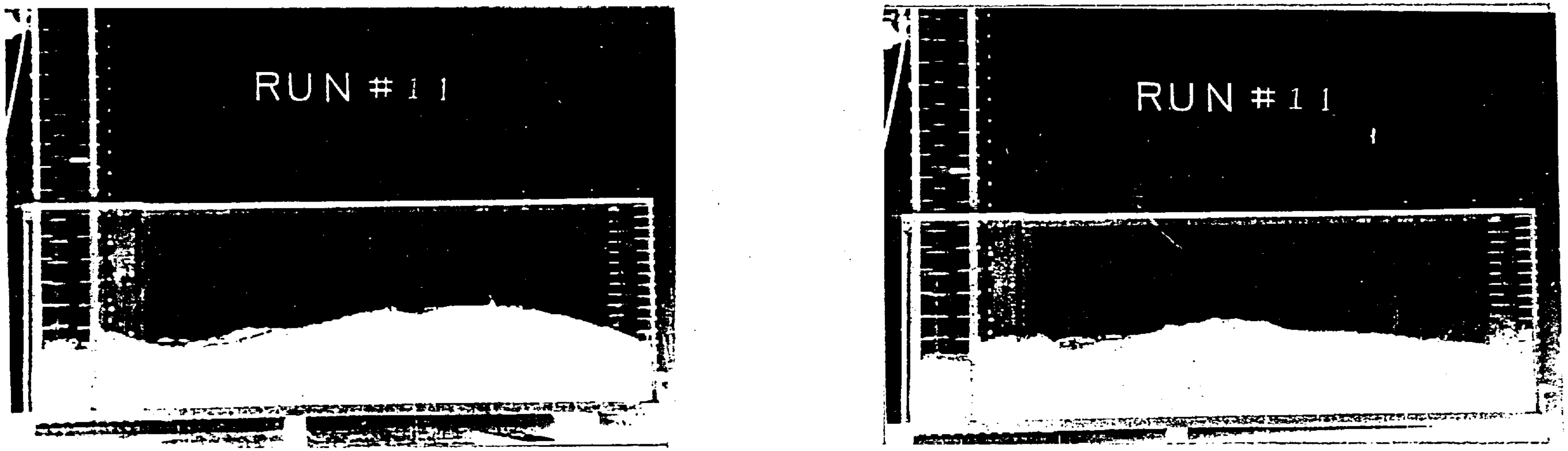

TIME = 1.555 SEC.

TIME = 1.666 SEC.

FIGURE 4-6 (CONTINUED)

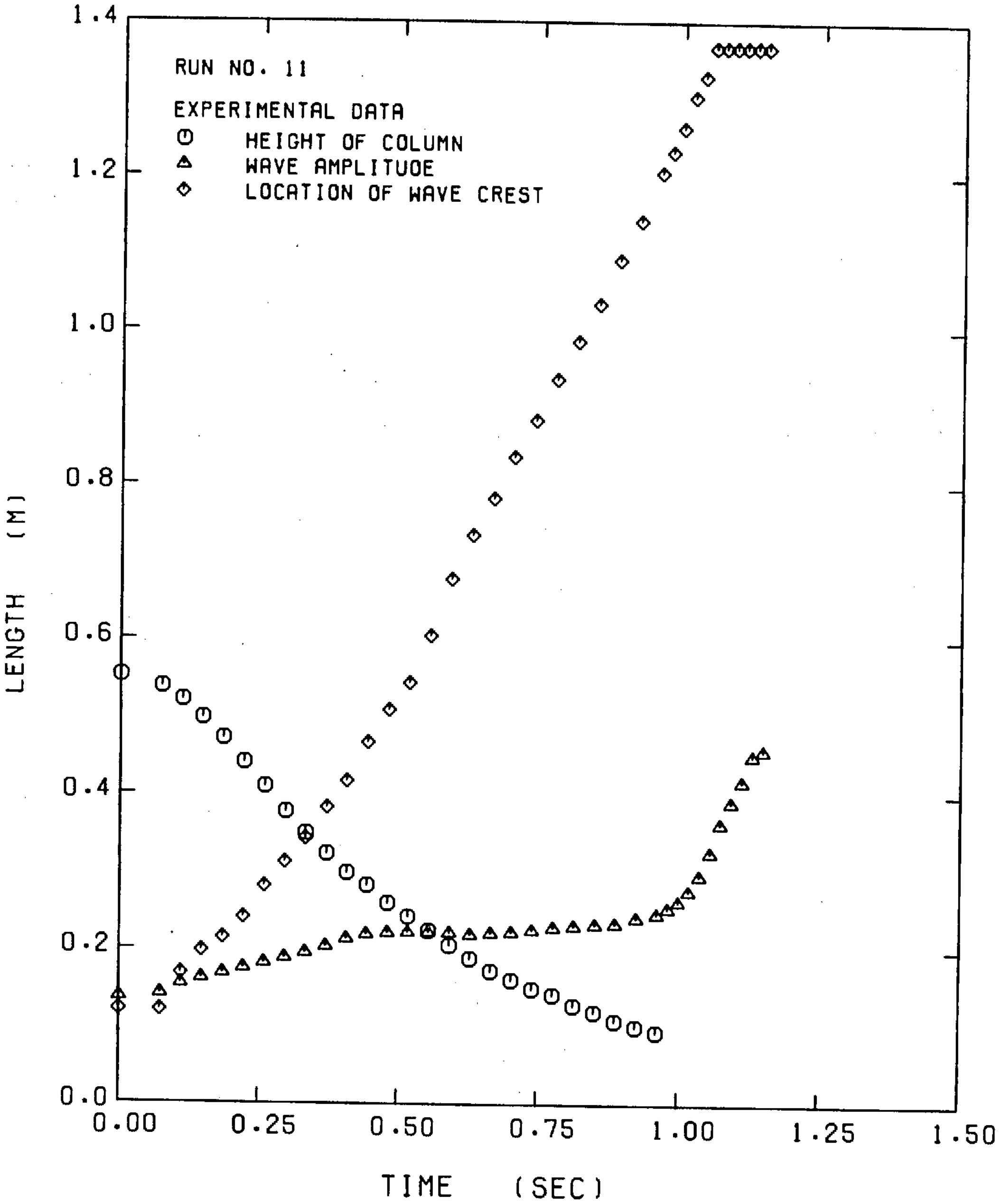

FIGURE 4-7 : MEASURED DATA FOR RUN NO. 11

(Figure 4-8) was just below the top of the baffle.

RUN NO.		4	8	11	13
Initial water height in column	(M)	.335	.302	.553	.591
Initial water depth in tank	(M)	.076	.076	.137	.135
Baffle location from column end of tank	(M)	-	1.08	-	1.08
Baffle height	(M)	-	.085	-	.085
Gap height (at bottom of column)	(M)	.523	.523	.523	.523

TABLE 4-1 : INITIAL CONDITIONS FOR THE EXPERIMENTAL RUNS

Run No. 8 is very similar to Run No. 4 before the wave approaches the baffle. Because the baffle is protruding above the water surface, the Run No. 8 wave breaks over the baffle and falls into the quiescent water behind the baffle. Figure 4-9 presents the measured data for Run No. 8. Run No. 13, shown in Figure 4-10, has an initial depth of water in the tank which is sufficient to submerge the baffle; hence, the wave does not break over the baffle. Instead it approaches the baffle with a constant amplitude and then rises to "climb" over the barrier. Behind the baffle the wave first loses amplitude and then impacts and runs up the end wall forming a thin, vertical sheet of water, as does Run No. 11. The measured data

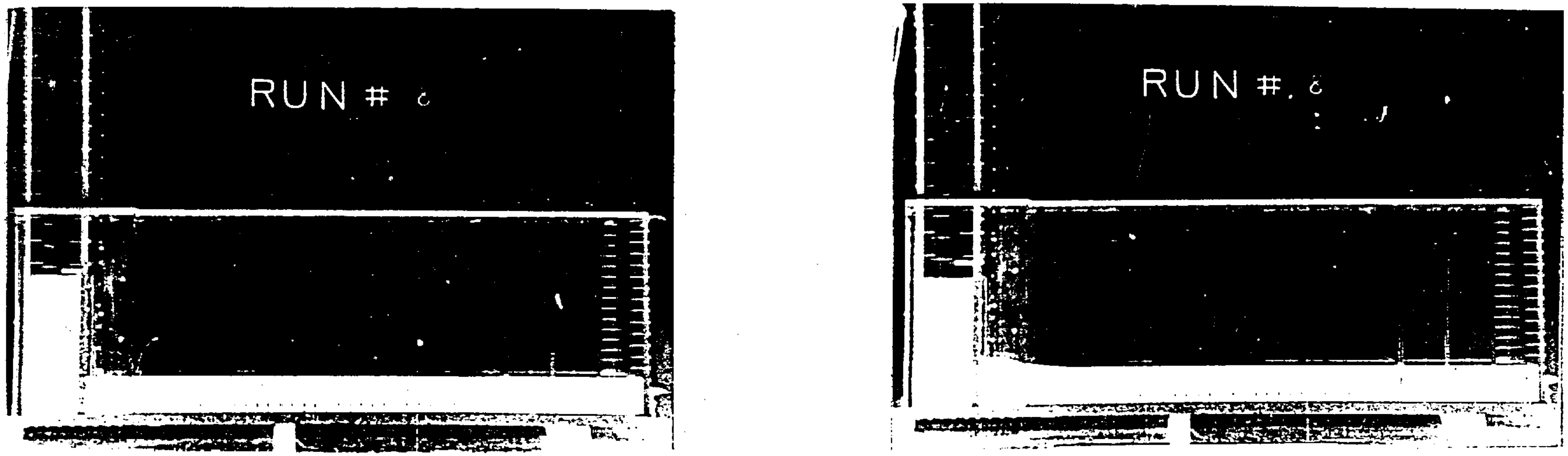

TIME = 0.000 SEC.

TIME = 0.111 SEC.

TIME = 0.222 SEC.

TIME = 0.333 SEC.

FIGURE 4-8: SEQUENCE OF FRAMES FOR RUN NO. 8

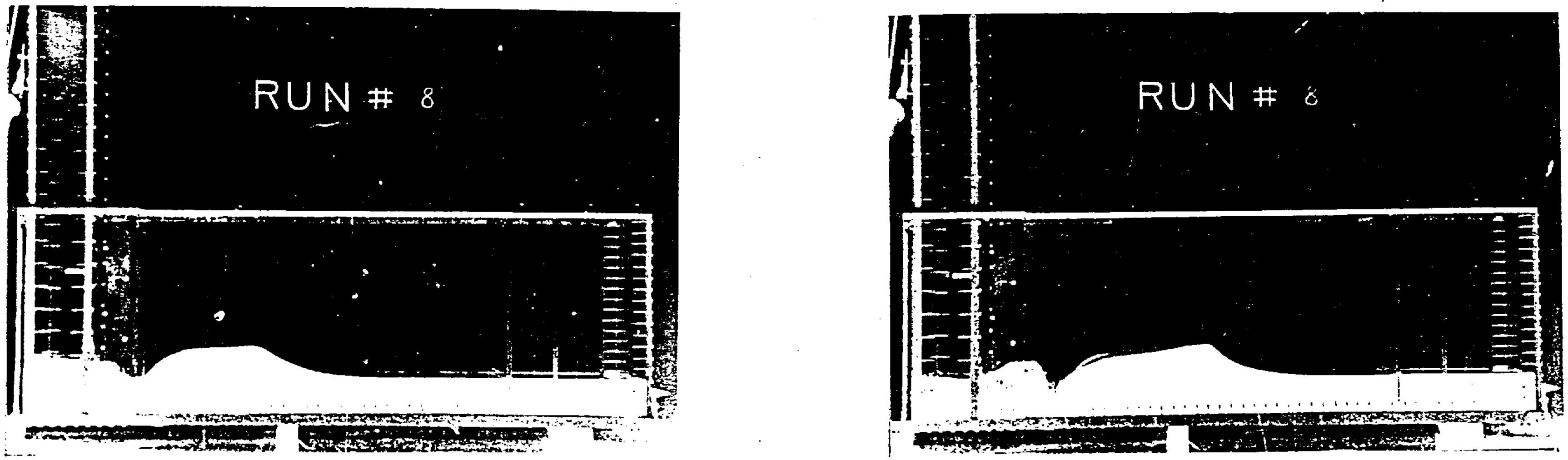

TIME = 0.444 SEC.

TIME = 0.555 SEC.

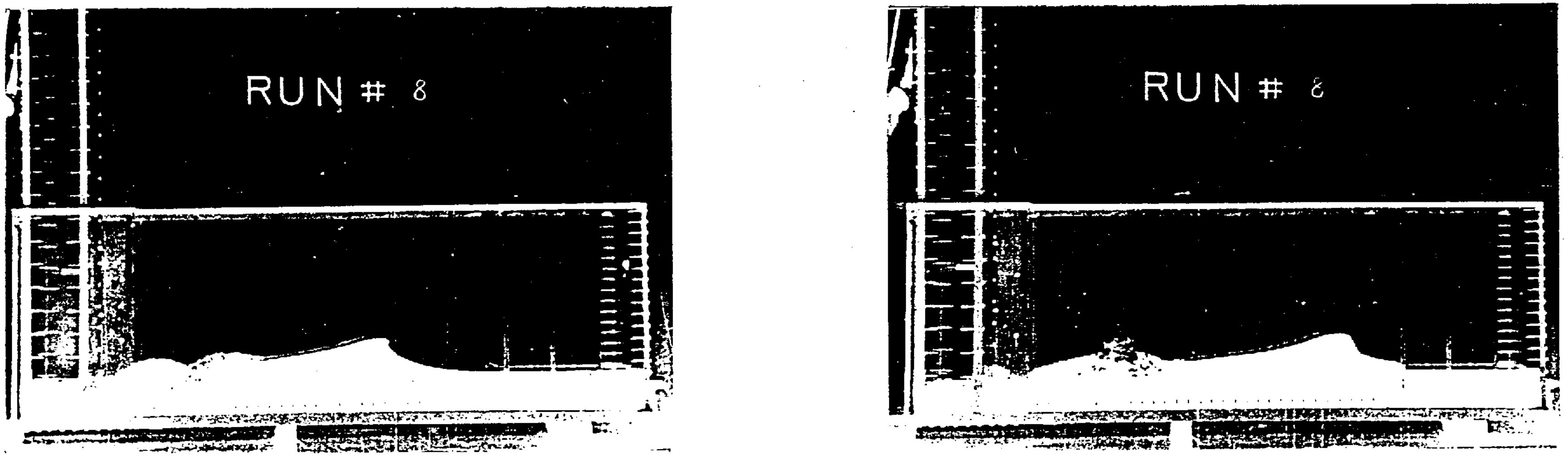

TIME = 0.666 SEC.

TIME = 0.777 SEC.

FIGURE 4-8 (CONTINUED)

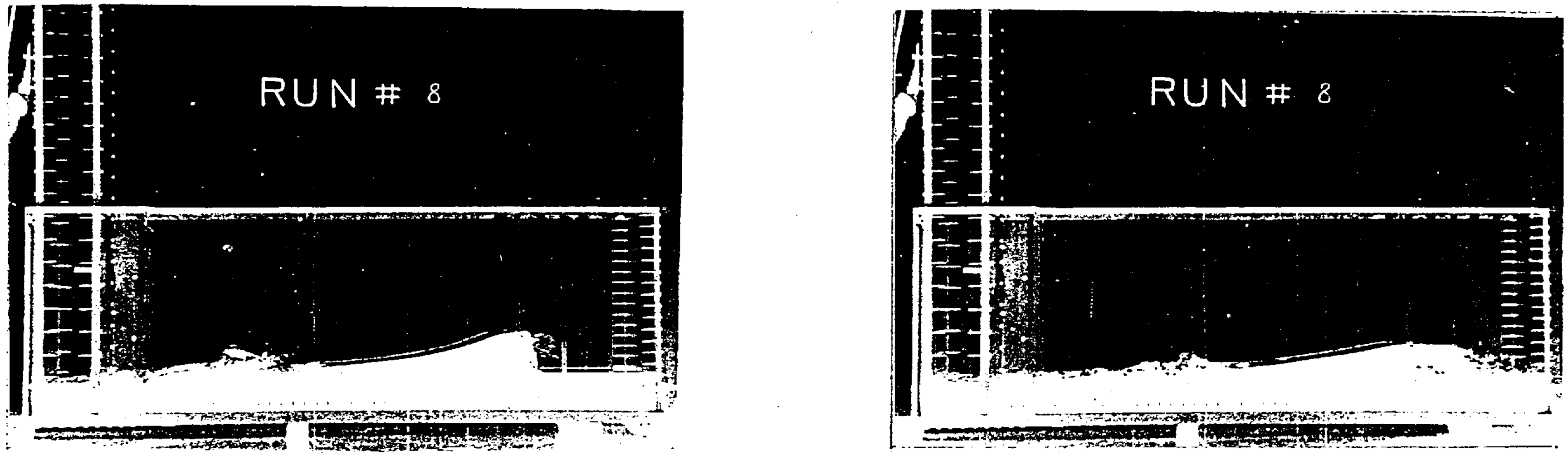

TIME = 0.888 SEC.

TIME = 0.999 SEC.

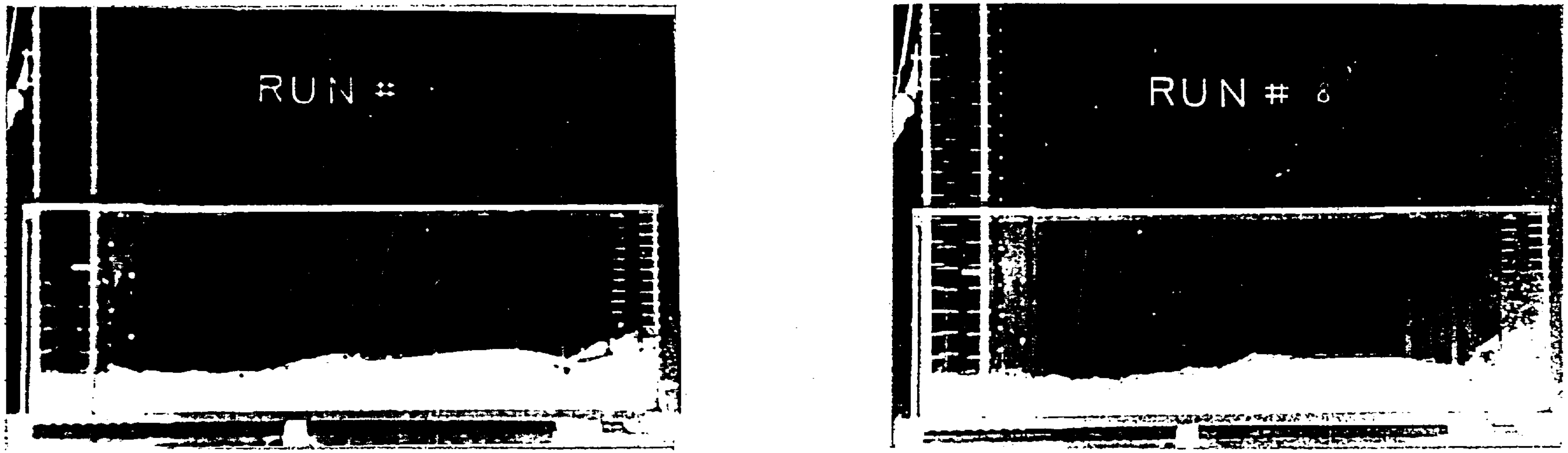

TIME = 1.111 SEC.

TIME = 1.222 SEC.

FIGURE 4.8 (CONTINUED)

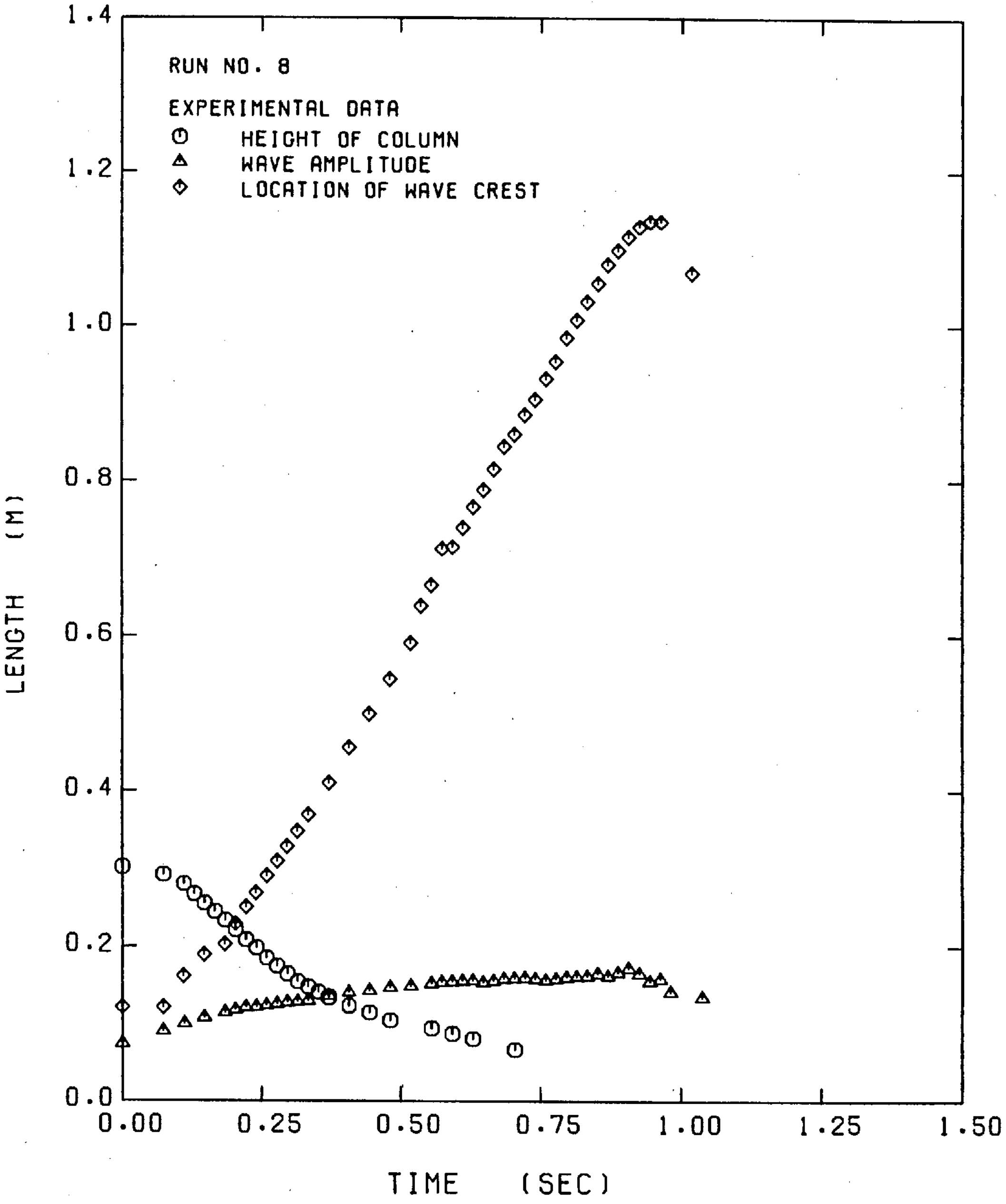

FIGURE 4-9 : MEASURED DATA FOR RUN NO. 8

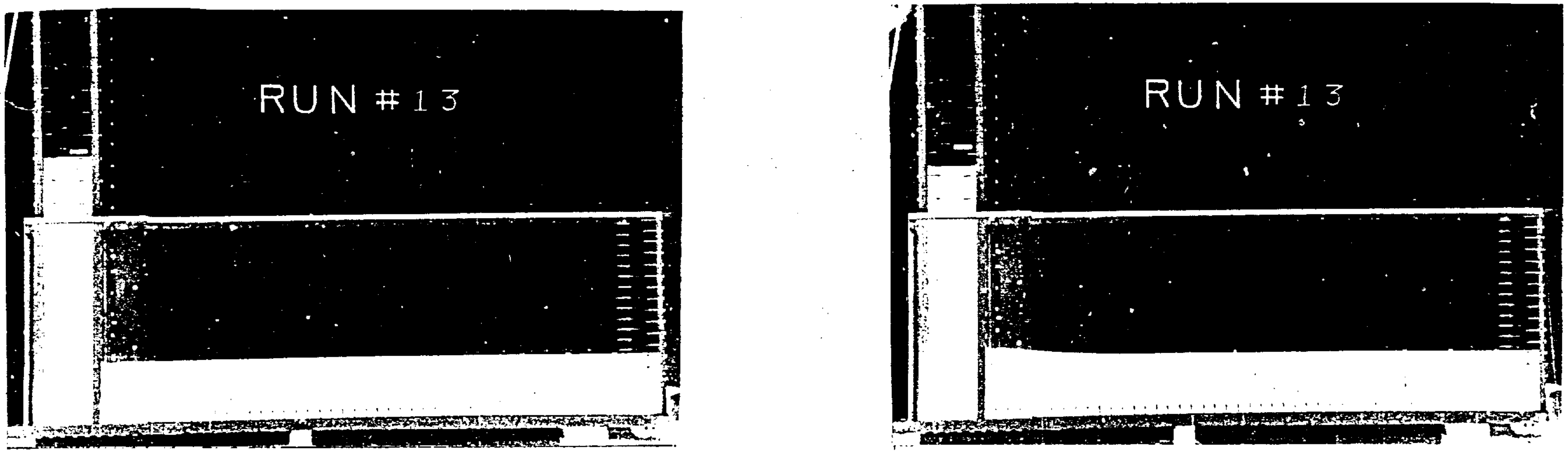

TIME = 0.000 SEC.

TIME = 0.111 SEC.

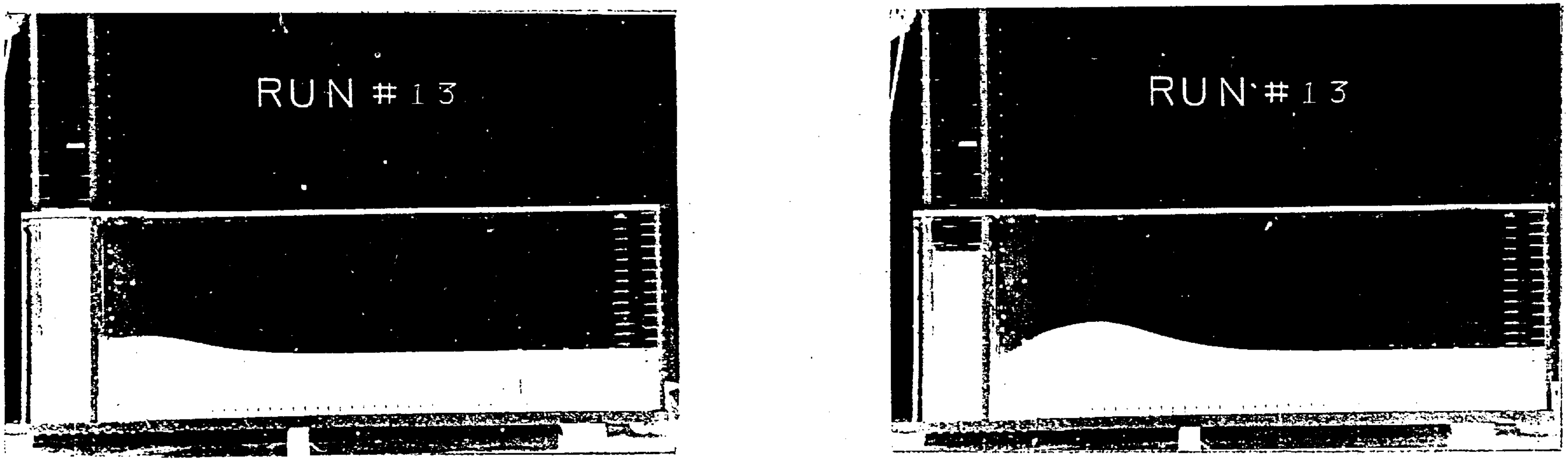

TIME = 0.222 SEC.

TIME = 0.333 SEC.

FIGURE 4-10: SEQUENCE OF FRAMES FOR RUN NO. 13

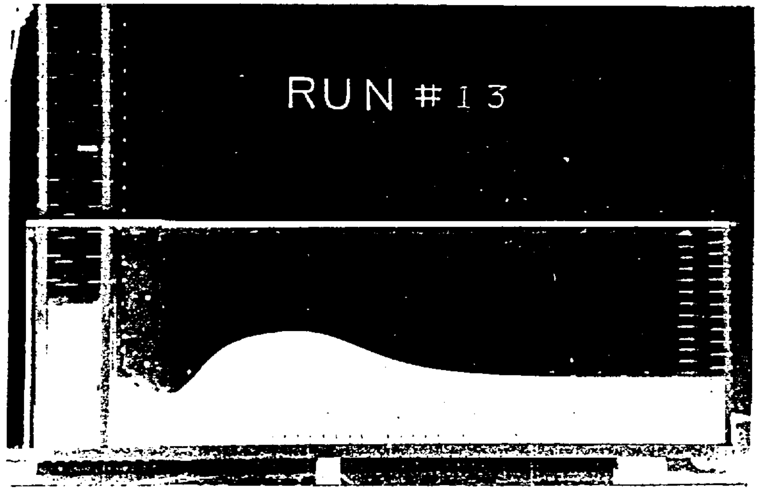

TIME = 0.444 SEC.

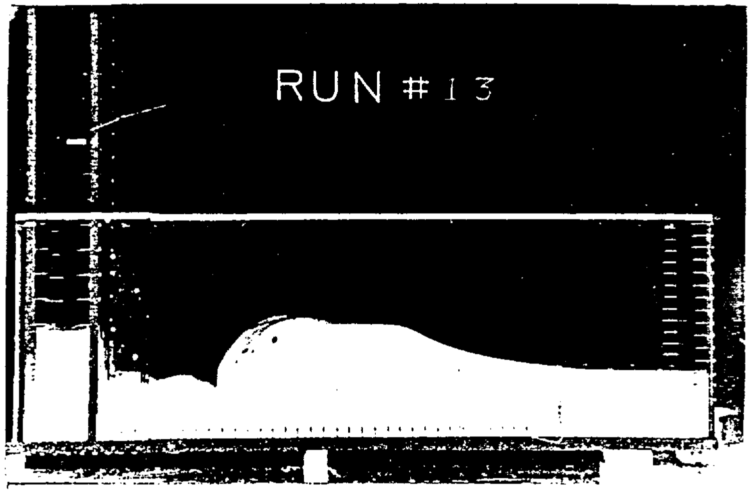

TIME = 0.555 SEC.

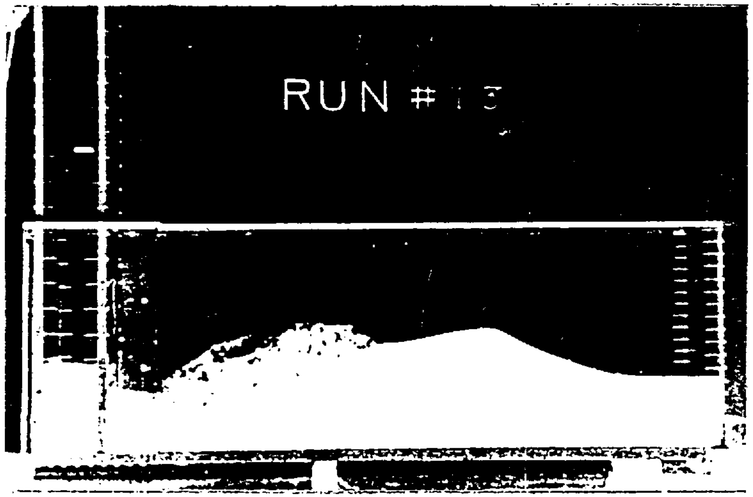

TIME = 0.666 SEC.

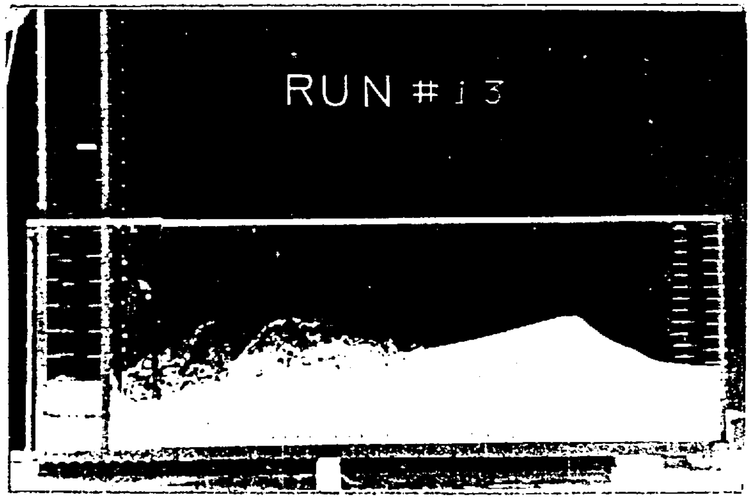

TIME = 0.777 SEC.

FIGURE 4-10 (CONTINUED)

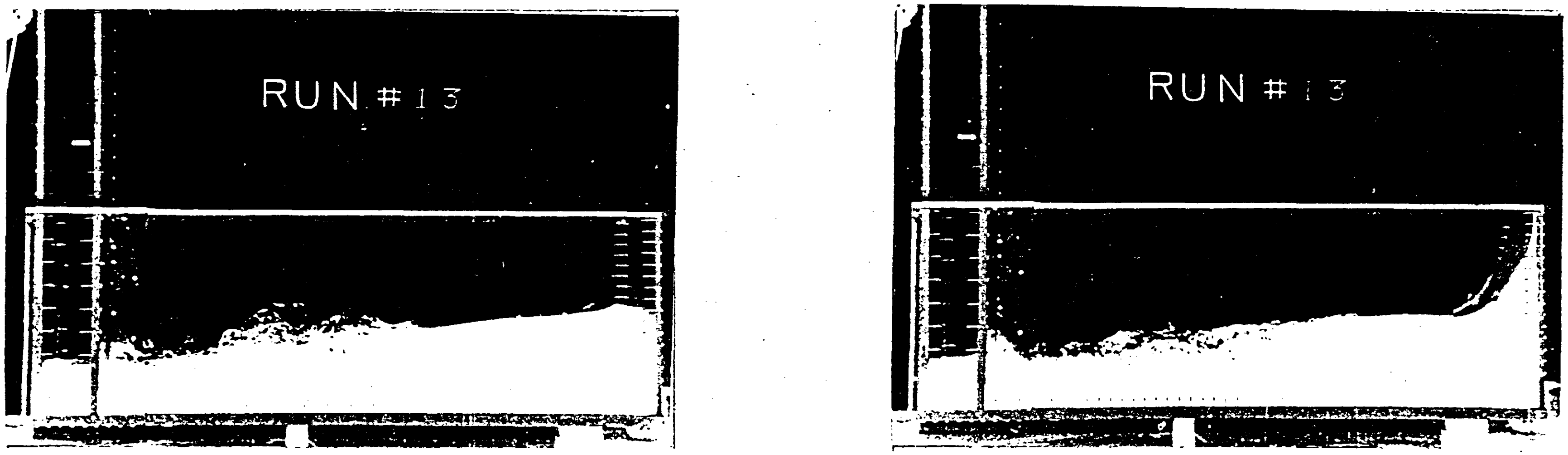

TIME = 0.888 SEC.

TIME = 0.999 SEC.

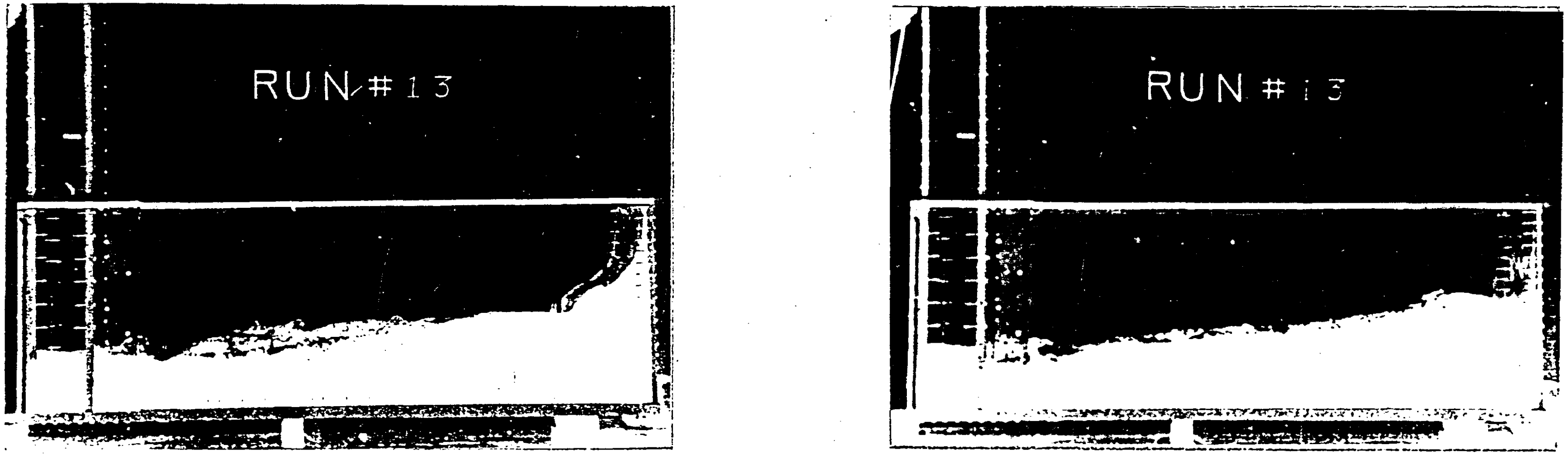

TIME = 1.111 SEC.

TIME = 1.222 SEC.

FIGURE 4-10 (CONTINUED)

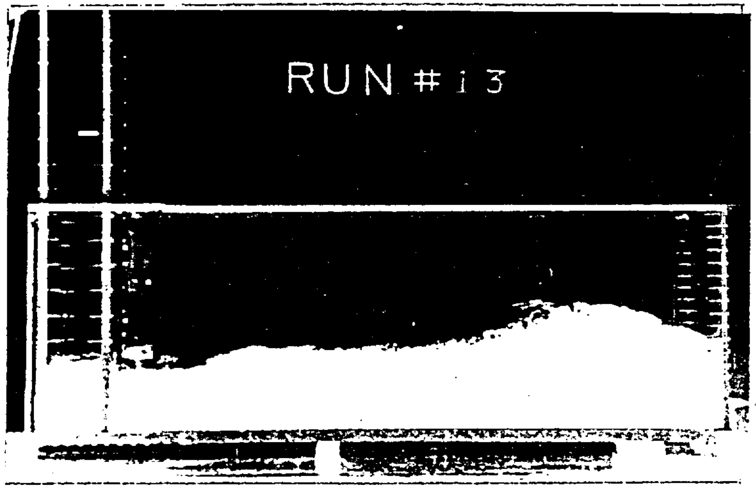

TIME = 1.333 SEC.

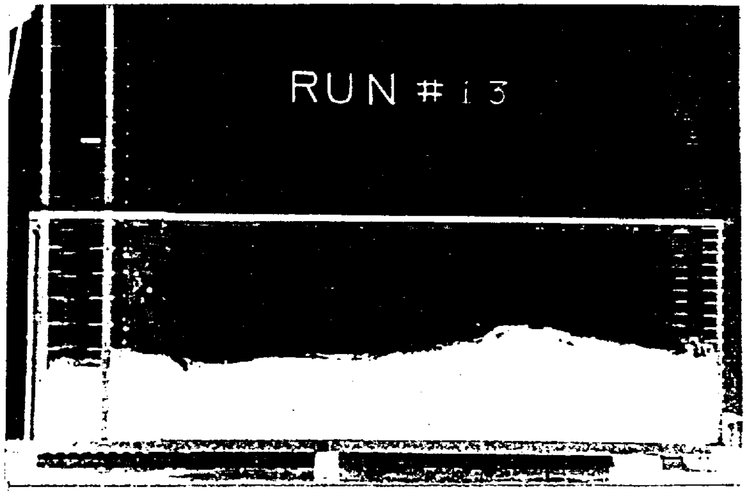

TIME = 1.444 SEC.

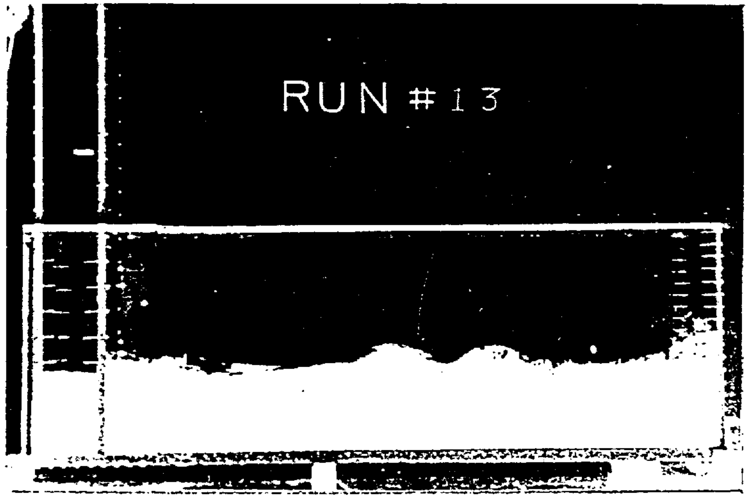

TIME = 1.555 SEC.

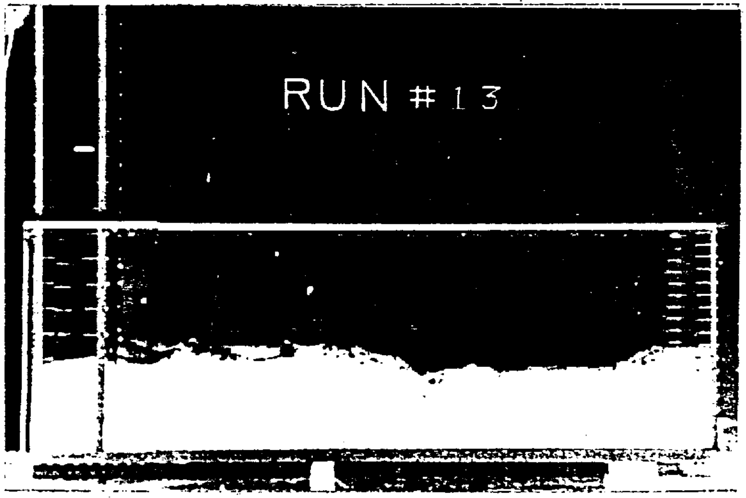

TIME = 1.666 SEC.

FIGURE 4-10 (CONTINUED)

for Run No. 13 are presented in Figure 4-11.

4.4 Summary

In this chapter the experimental investigation has been discussed. First, the equipment and experimental procedures were described. Then some typical experimental results were presented. In Chapter 7 these experimental results will be compared with predictions obtained from the numerical model.

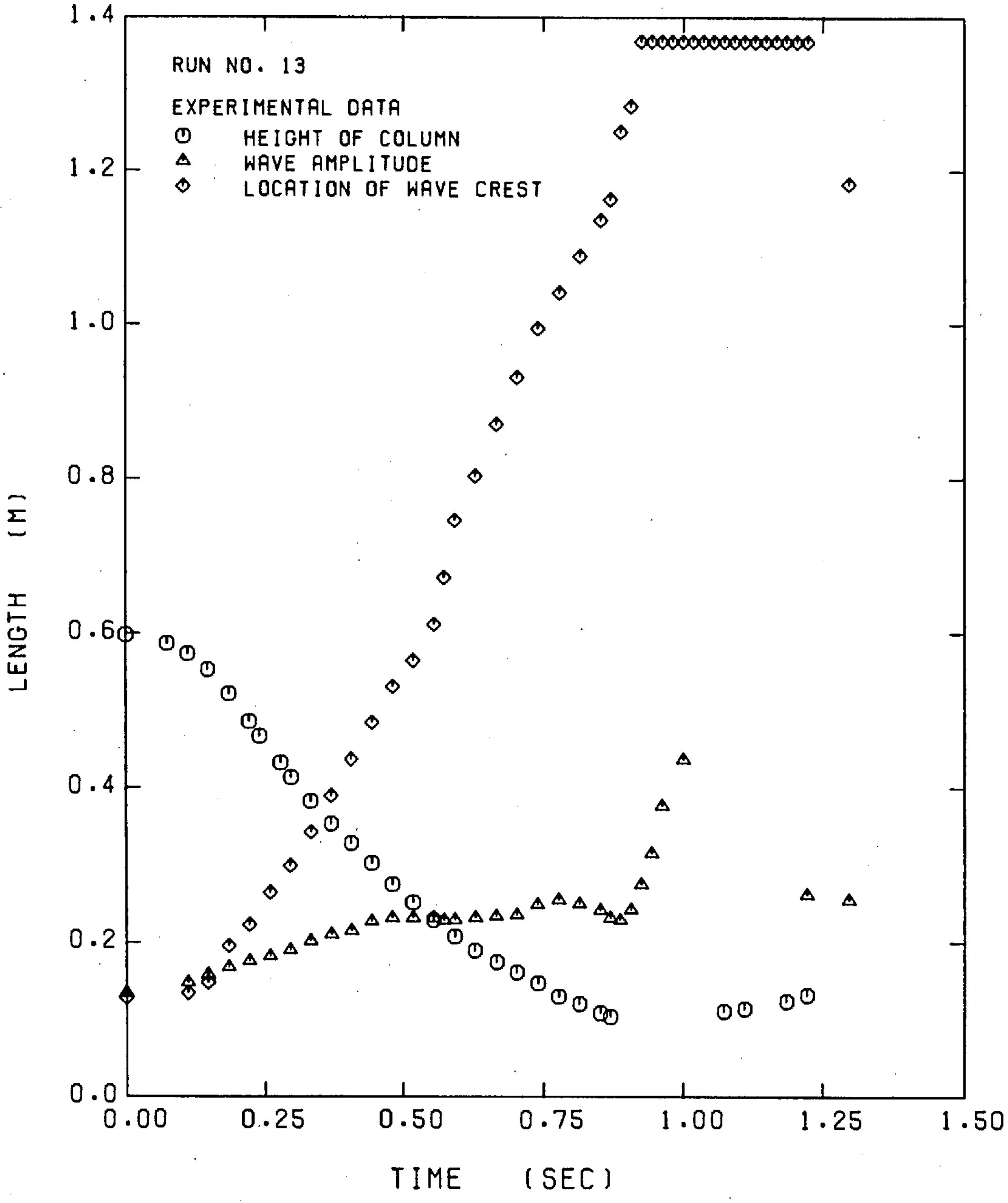

FIGURE 4-11 : MEASURED DATA FOR RUN NO. 13

CHAPTER 5

PREDICTIONS TO COMPARE WITH ANALYTICAL RESULTS

5.1 INTRODUCTION

A numerical solution procedure must possess three qualities. It should be capable of: (a) producing numerically accurate results, (b) realistically simulating physical processes, and (c) analysing flows of engineering and scientific interest. This and the following two chapters are devoted to evaluating how well the numerical model and solution procedure described in Chapters 2 and 3 accomplish these goals.

In this chapter the numerical accuracy of the solution procedure is checked by comparing predictions of four flows with analytical solutions. These flows are tabulated along with some pertinent data in Table 5-1. In Chapter 6 predicted results are compared with experimental data to test the physical reality of the computations and some additional flows of interest are presented in Chapter 7.

All of the computations presented were produced with the SPLASH (SIMPLE Program for Liquid and Air Systems Hydrodynamics) Computer Program, which embodies the solution procedure described in Chapter 3. SPLASH is written in standard FORTRAN and requires no special features of a particular computer. The amount of storage required by the program depends on the number

	WATER PLUG	U-TUBE	SPHERICAL BUBBLE	PERIODIC WAVE
Coordinate System	Cartesian	Cartesian	Cylindrical	Cartesian
Grid	22 × 3	22 × 3	17 × 17	22 × 17
Type of Grid Spacing	Uniform	Uniform	Uniform	Non-Uniform
Number of Particle Strings	2	2	1	1
Number of Particles at Start	6	6	100	100
Number of Particles at Finish	6	6	130	111
Maximum Time Sec	0.026	1.0	0.05	2.625
Time Step (Δt) Sec	0.0001	0.005	0.0005	0.025
Number of Time Steps	260	200	100	105
Number of Iterations per Time Step	10	10	12	10
Direction of Gravitational Acceleration	-	X	-	X
Density of Gas Kg/m^3	1.198	1.198	1.198	1.198
Density of Liquid Kg/m^3	1000.	1000.	1000.	1000.
Viscosity of Gas Nt Sec/m^2	0	0	10^{-3}	10^{-3}
Viscosity of Liquid Nt Sec/m^2	0	0	10^{-3}	10^{-3}
Computational Time CDC 6600 Sec	20	25	300	480

TABLE 5-1 : PERTINENT DATA FOR THE PREDICTIONS PRESENTED IN CHAPTER 5

of grid points allowed for; the storage requirement varies from 20000 words of memory for a 15 by 15 grid to 40000 words for a 37 by 22 grid. The predictions reported in this and the following chapters were computed on various CDC machines using the FTN optimization compiler. All computational times are quoted in terms of CDC 6600 seconds (or minutes).

5.2 ACCELERATION OF A LIQUID PLUG

Presentation

A "plug" of water confined to one-dimensional motion in a uniform channel behaves like a solid body. If a constant force (pressure drop) is applied to the plug (see Figure 5-1), it will accelerate at a constant rate. The conservation of mass and momentum require that

$$\frac{\partial u}{\partial x} = 0$$

and

$$\frac{\partial u}{\partial t} + \frac{u\partial u}{\partial x} = - \frac{1}{\rho} \frac{\partial p}{\partial x} \qquad (5-1)$$

The displacement and velocity of the water plug can be expressed as

$$x(t) = (p_L - p_R) \frac{t^2}{2\rho L} \qquad (5-2)$$

and

$$u(t) = (p_L - p_R) \frac{t}{\rho L} \quad . \qquad (5-3)$$

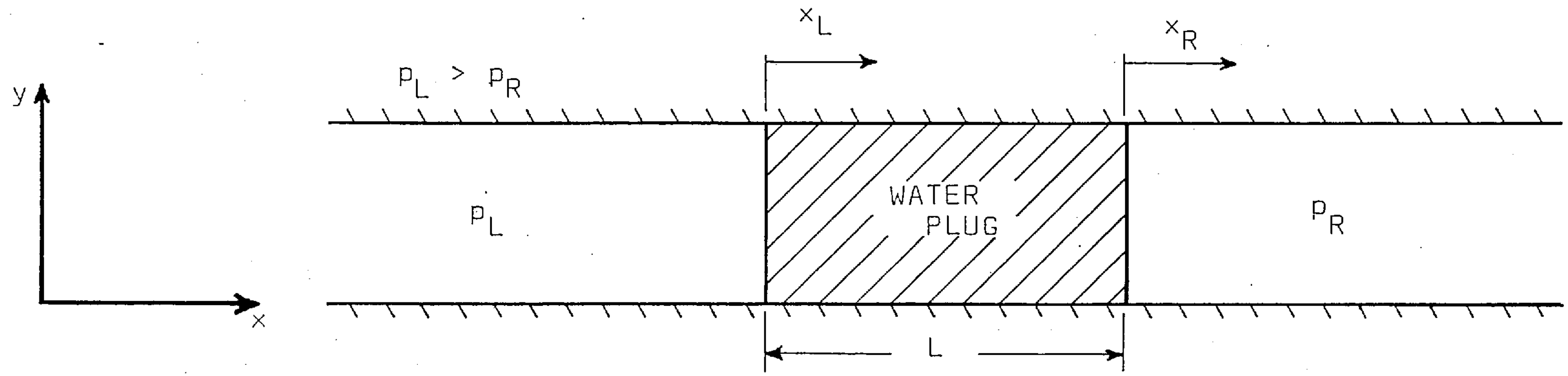

FIGURE 5-1 : DEFINITION OF THE WATER PLUG PROBLEM

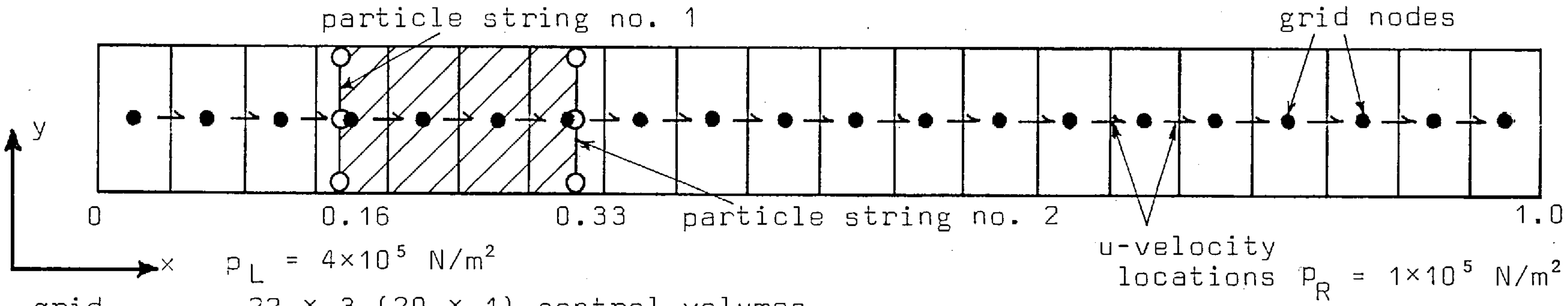

grid - 22 × 3 (20 × 1) control volumes
Δt - 0.0001 sec.
max. time - 0.026 sec.
L - 0.17 M

ρ liquid - 1000.0 kg/m^3
ρ gas - 1.198 kg/m^3
μ liquid - 0
μ gas - 0

FIGURE 5-2 : COMPUTATIONAL DETAILS FOR THE WATER PLUG PROBLEM

The grid and geometry used in predicting the motion of the water plug are shown in Figure 5-2. The solution was run for 260 time steps of .0001 seconds each, which required approximately 20 seconds of CDC 6600 time. The predicted velocity and displacement of the water plug are shown with the analytical solutions (equations 5-2 and 5-3) in Figures 5-3 and 5-4.

Discussion

Examination of Figures 5-3 and 5-4 confirms that the model can accurately predict the one-dimensional motion of the water plug. Of course this is a simple problem; however, the results verify the model and solution procedure in two ways. First, the solution procedure solved the simplified hydrodynamic equations correctly. Secondly, the particle-tracking procedure moved both faces of the water plug independently without deforming the plug.

5.3 LIQUID OSCILLATIONS IN A U-TUBE

Presentation

In the absence of friction, the oscillatory motion of a liquid in a U-tube, as shown in Figure 5-5, obeys the familiar equation for undamped, second-order motion,

$$a\rho L \frac{d^2x}{dt^2} = -\,2\,a\rho\,gx \quad . \qquad (5\text{-}4)$$

The symbols in equation (5-4) are defined in Figure 5-5.

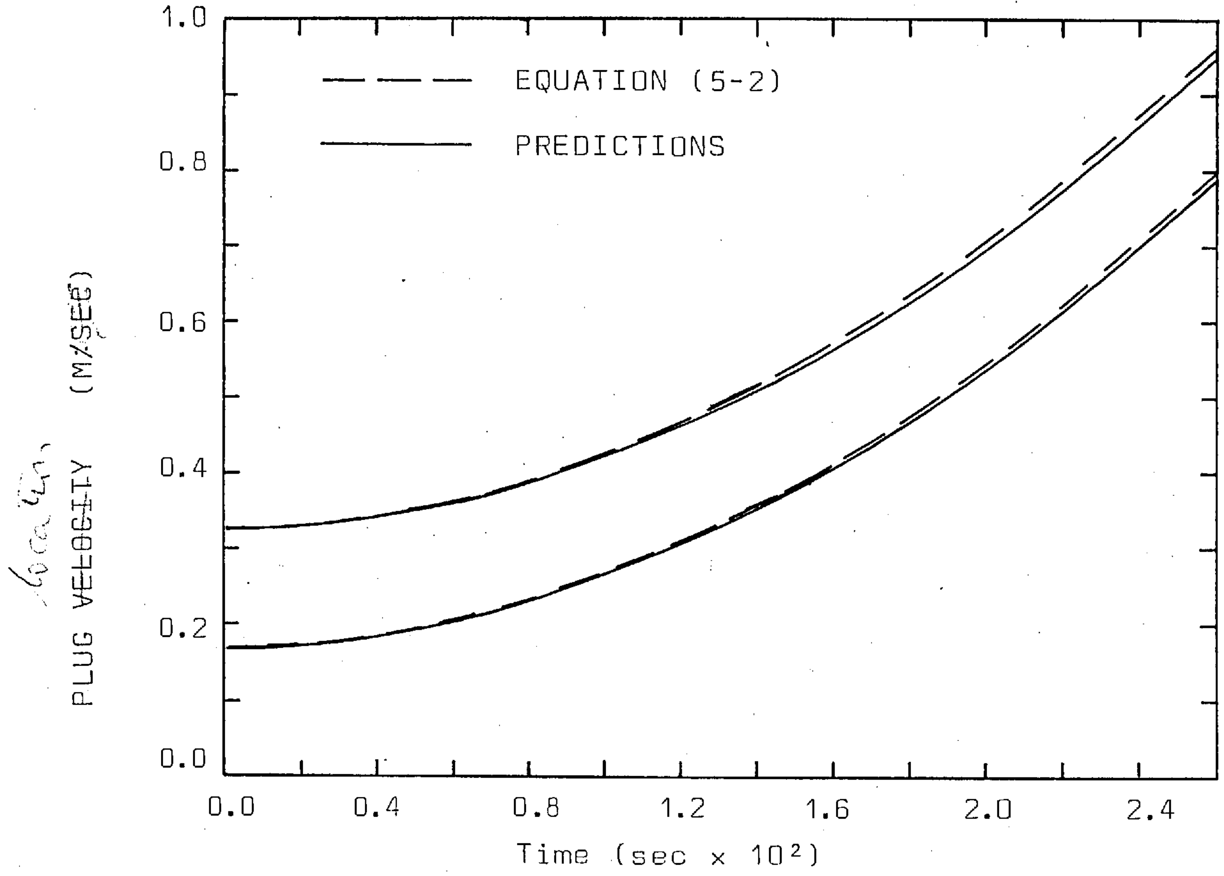

FIGURE 5-3 : DISPLACEMENT OF THE WATER PLUG

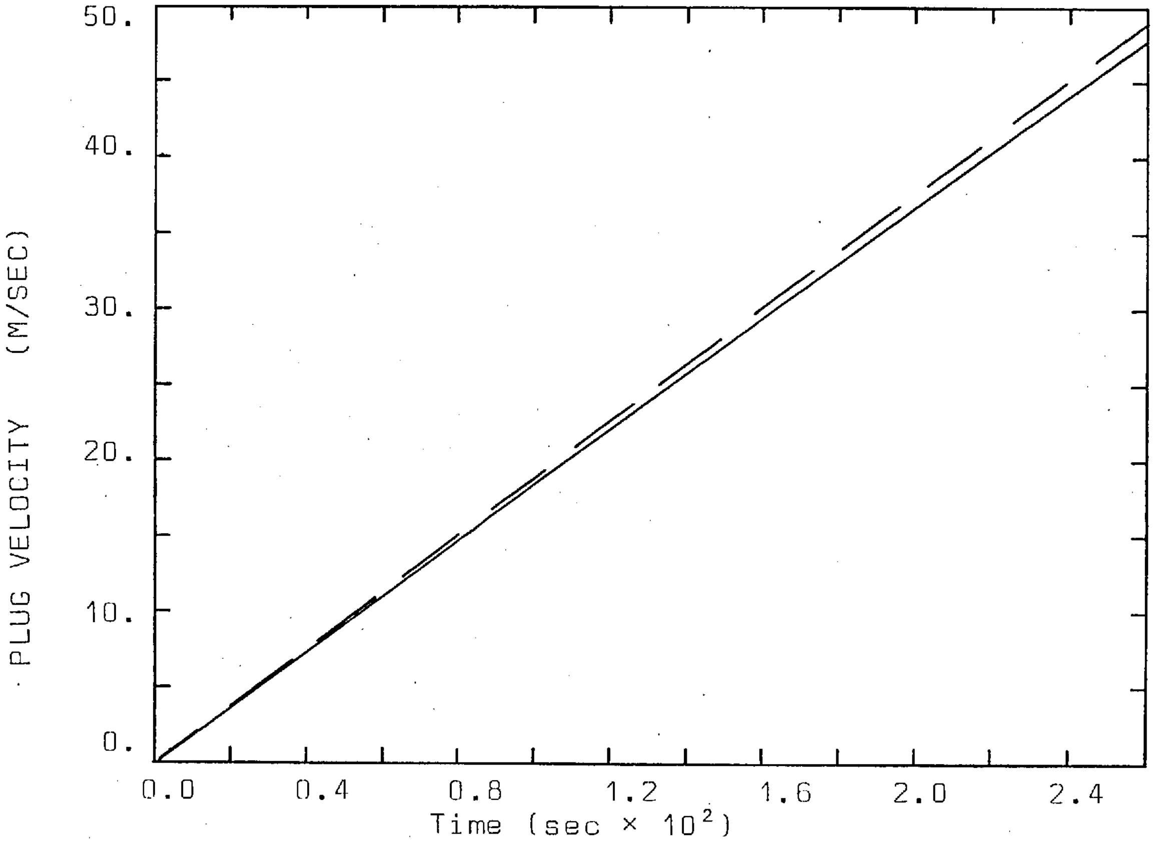

FIGURE 5-4 : VELOCITY OF THE WATER PLUG

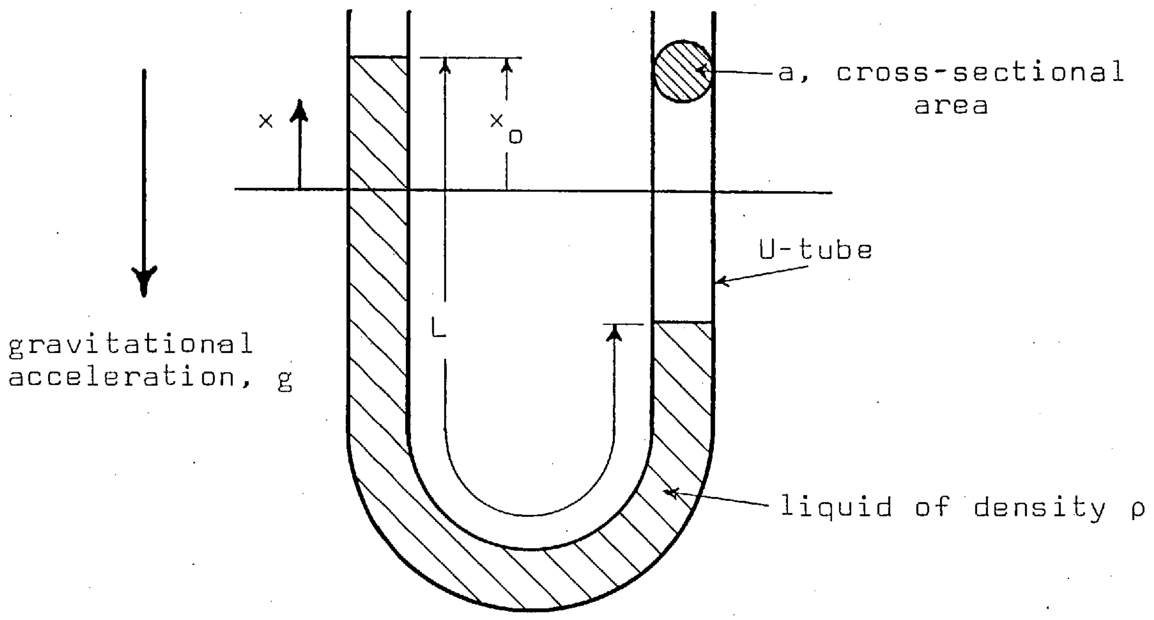

FIGURE 5-5 : DEFINITION OF THE U-TUBE PROBLEM

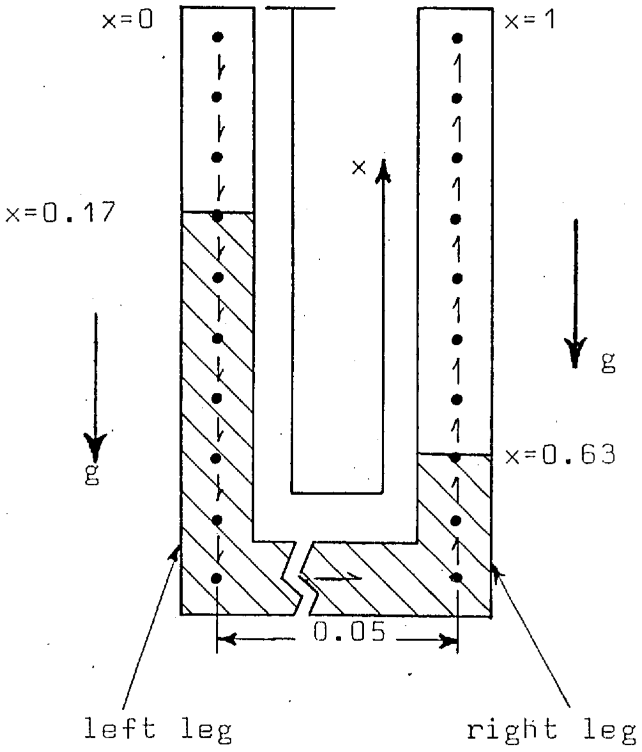

grid	-	22 × 3 (20 × 1)
t	-	0.005 sec
max. time	-	1.0 sec
ρ liquid	-	1000.0 kg/m^3
ρ gas	-	1.198 kg/m^3
μ liquid	-	0
μ gas	-	0
x_o	-	0.1M
L	-	0.46M

FIGURE 5-6 : COMPUTATIONAL DETAILS FOR THE U-TUBE PROBLEM

Subject to the initial conditions

$$x(0) = x_o \quad \text{and} \quad \left.\frac{dx}{dt}\right]_{t=0} = u = 0$$

the solution to equation (5-4) is

$$x(t) = x_o \cos\left[\frac{\sqrt{2g}}{L}\, t\right] \quad , \tag{5-5}$$

and it follows that the liquid velocity is

$$\frac{dx}{dt} = u(t) = \frac{\sqrt{2g}}{L}\, x_o \sin\left(\frac{\sqrt{2g}}{L}\, t\right) \quad . \tag{5-6}$$

The grid arrangement and coordinate system necessary to predict the U-tube oscillations are shown in Figure 5-6. The x-coordinate is "bent" so that it lies along the centre line of the U-tube. In the left leg the gravitational acceleration is in the positive x-direction, however, it is in the negative x-direction in the right leg. There are no gravitational effects in the lower section of the bend which connects the legs.

The computations were run for 200 time steps and required approximately 25 seconds on the CDC 6600. The computed displacements of the liquid surfaces are compared with equation (5-5) in Figure 5-7. Note that the displacements are relative to the x-coordinate defined in Figure 5-6. Figure 5-8 shows the variation of liquid velocity with time as computed compared with equation (5-6).

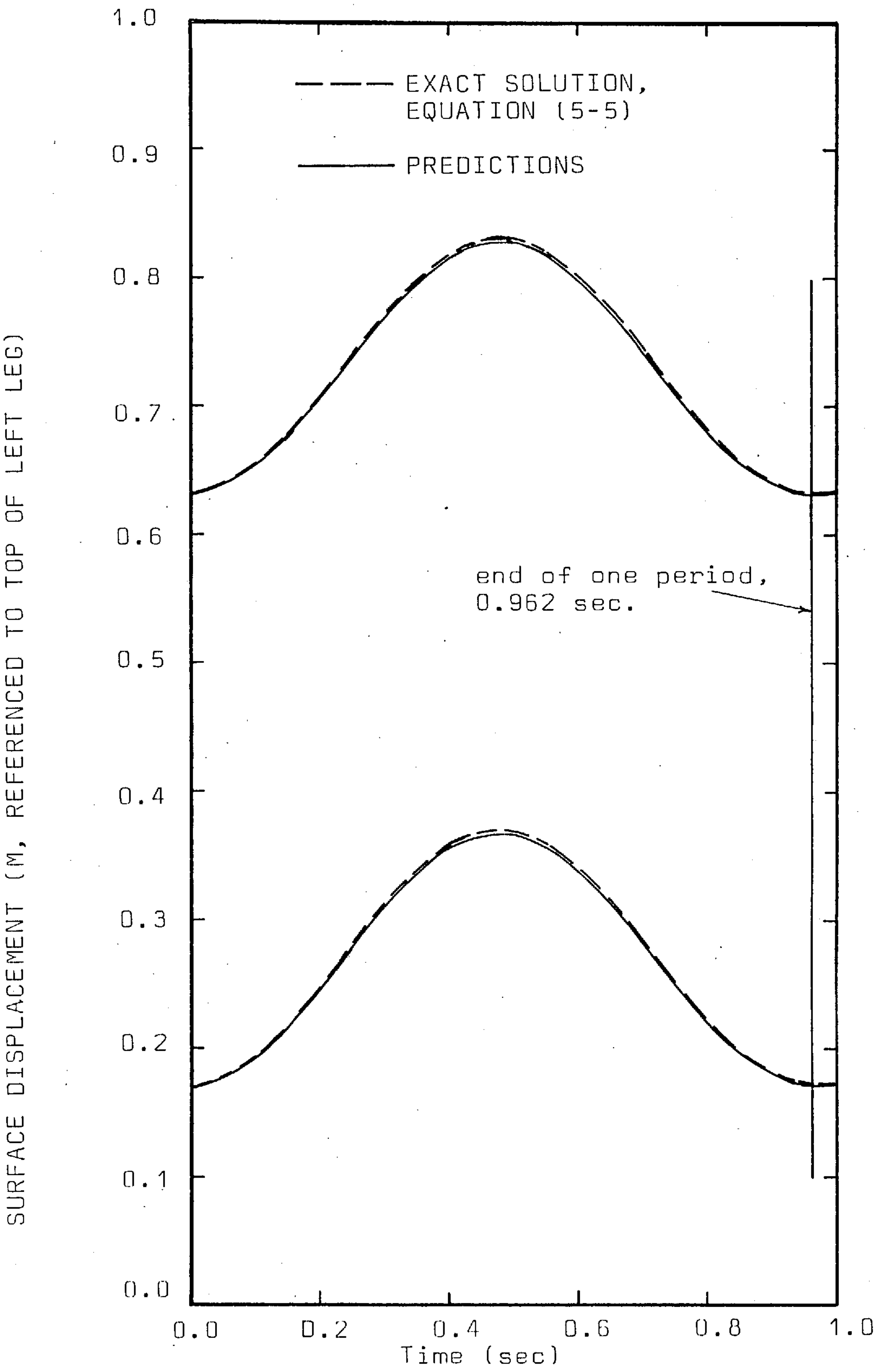

FIGURE 5-7 : SURFACE DISPLACEMENTS FOR THE U-TUBE PROBLEM

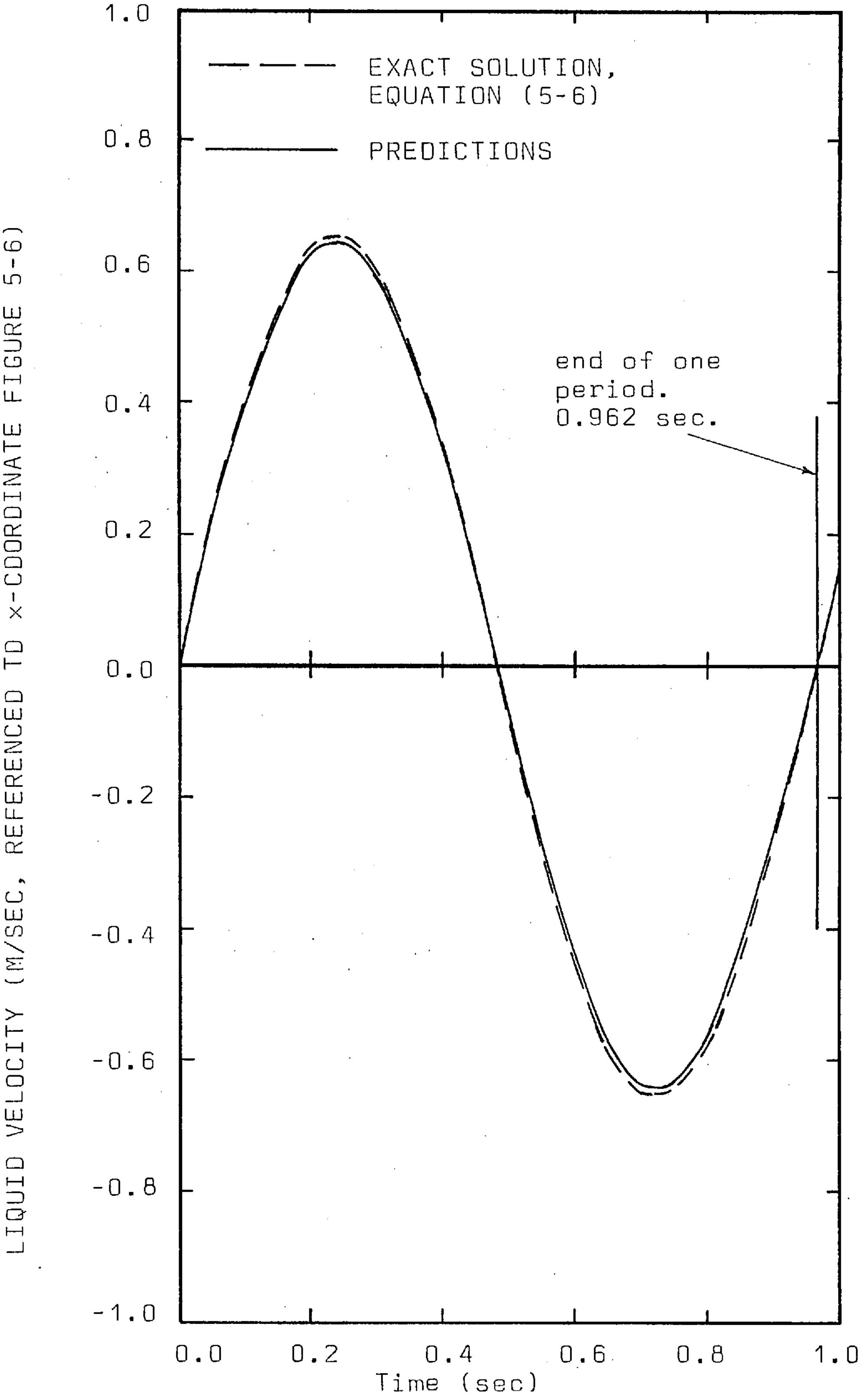

FIGURE 5-8 : LIQUID VELOCITY FOR THE U-TUBE PROBLEM

Discussion

The predictions agree well with the analytical solution. This agreement supports the results presented in the previous section, and thus, further validates the ability of the numerical model to correctly predict one-dimensional, free-surface flows. Additionally, the comparisons presented in Figures 5-7 and 5-8 demonstrate that the time scale of the periodic behaviour of the liquid is computed accurately.

5.4 GROWTH OF A SPHERICAL BUBBLE

Presentation

The growth of a spherical bubble in a liquid medium (i.e., a point source of gas or a perfectly symmetric explosion) is a one-dimensional flow in spherical coordinates. If q is the rate at which gas volume is created within the bubble, then from continuity, the bubble radius varies according to the relation

$$r^3(t) = r_o^3 + \frac{3}{4\pi} q \, \Delta t \quad . \qquad (5\text{-}7)$$

The growth of a spherical bubble was computed as a two-dimensional, axi-symmetric flow. A 17 by 17 uniform grid as shown in Figure 5-9 was used for the computations. Growth of the gas bubble was simulated by adding a source of gas volume in the main control volume at the centre of the bubble and specifying the appropriate velocity profiles along the outflow

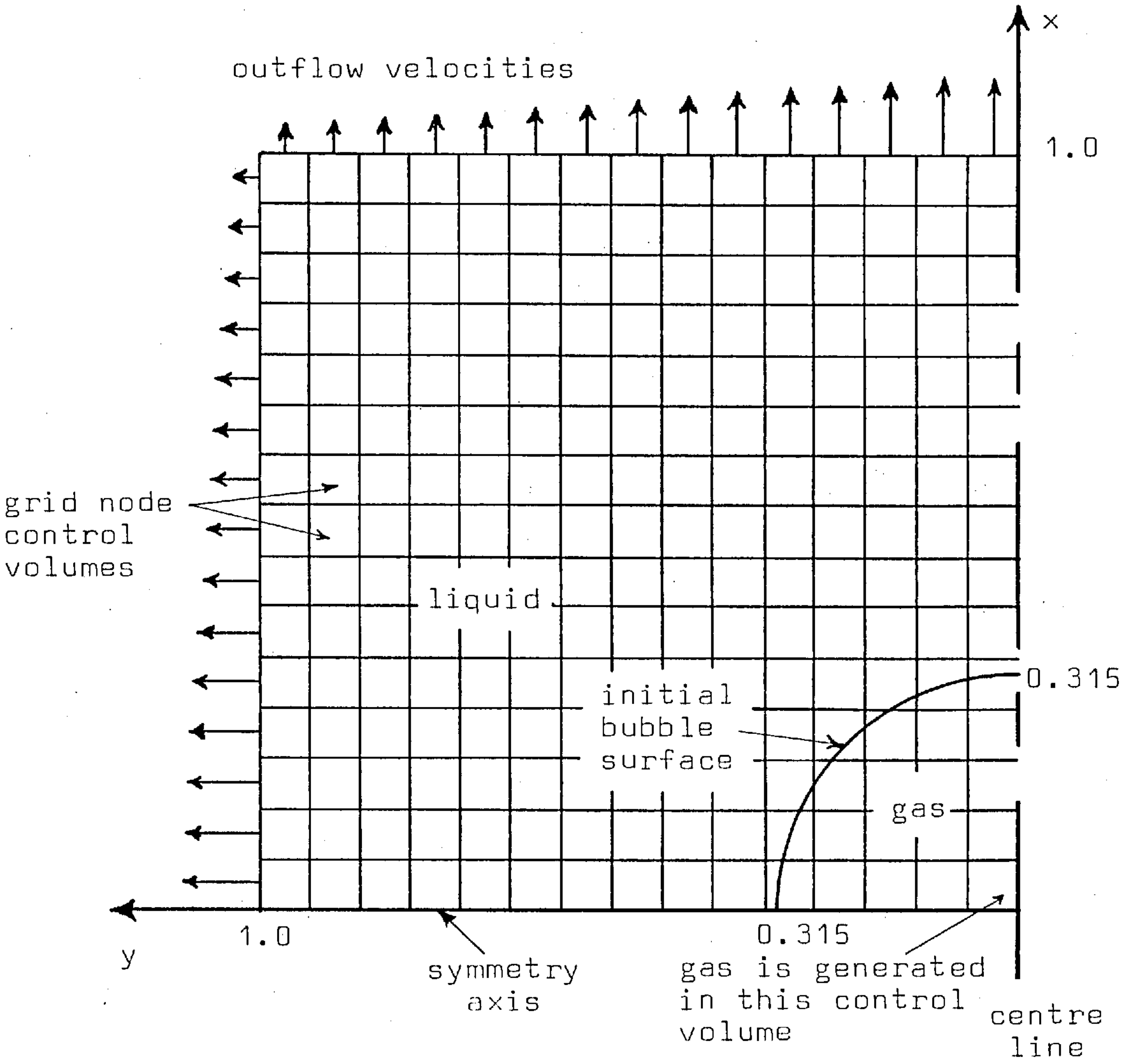

grid : 17×17 (15×15 main control volumes)
gas generation rate, $q/4\pi$: 1.0 m^3/sec
Δt : 0.005 sec
ρ liquid : 1000 kg/m^3
ρ gas : 1.198 kg/m^3

FIGURE 5-9 : DEFINITION SKETCH AND COMPUTATIONAL DETAILS FOR SPHERICAL BUBBLE PROBLEM boundaries. These outflow velocities were specified so as to represent the one-dimensional spherical motion of the fluid on the two-dimensional cylindrical grid and at the same time exactly balance the source of gas volume being generated within the bubble. The predictions were carried out for 100 time steps which required approximately 300 seconds of CDC 6600 time. Figure 5-10 shows the surface particle locations compared to the results of equation (5-7).

Discussion

This problem is included to demonstrate that the solution procedure can accurately predict the movement of a two-dimensional free-surface across the computational grid. Prediction of the bubble growth presents two problems. First, it is necessary to simulate the spherical nature of the bubble with cylindrical control volumes, and secondly, the gas created inside the bubble must push the denser liquid across the flow domain. As a result the predicted velocity fields exhibit recirculation zones inside the gas-bubble; however, Figure 5-10 shows that the bubble shape is predicted quite accurately. The effect of the automatic particle addition procedure can be seen by examining Figure 5-10. The string of particles is about twenty per cent longer after 100 time steps than it is after 50 time steps; but because particles were added, no gaps appear in the particle string.

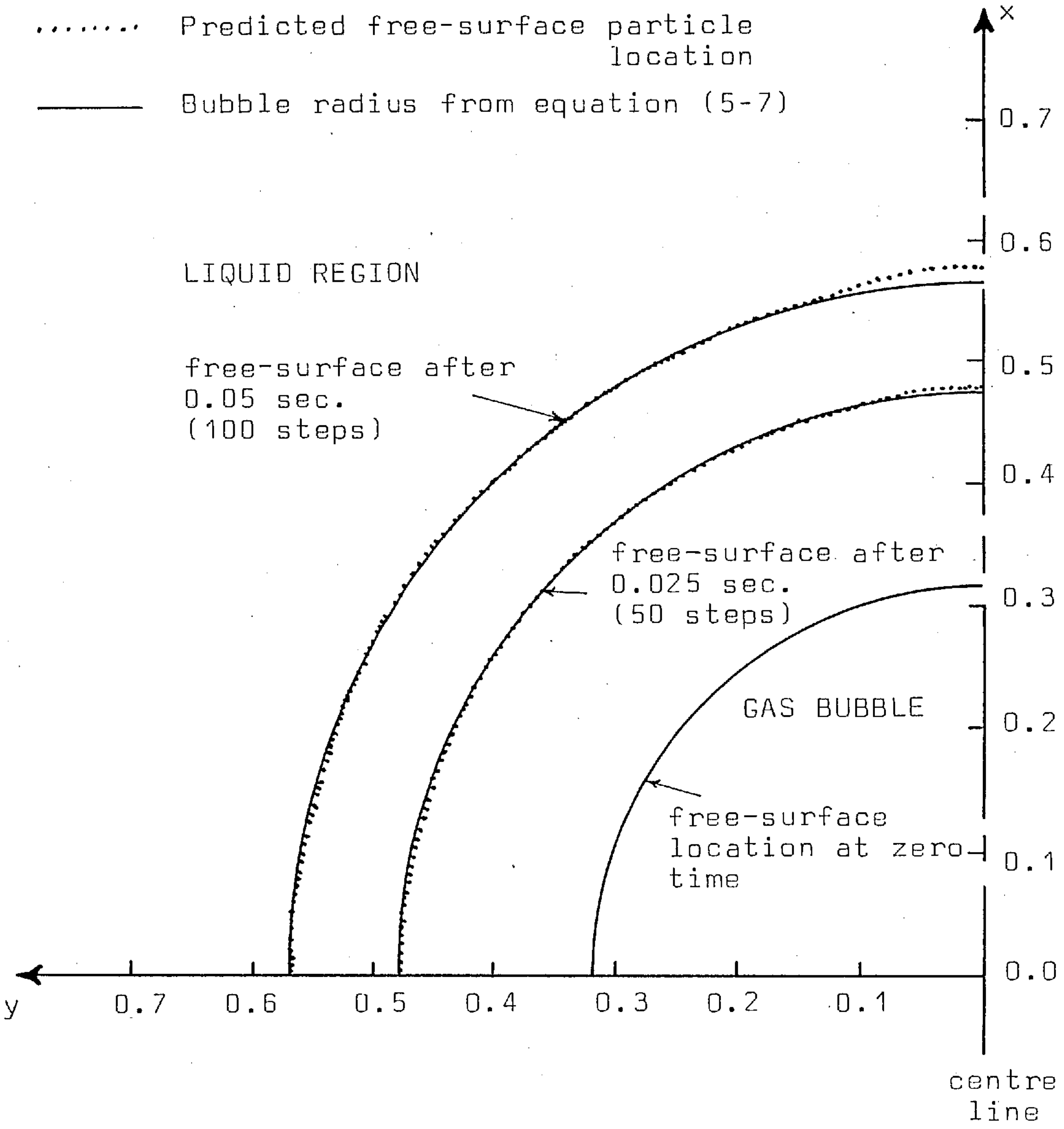

FIGURE 5-10 : PREDICTED FREE-SURFACE SHAPES FOR SPHERICAL BUBBLE

5.5 PERIODIC WAVE MOTION

Presentation

The last problem to be presented in this chapter is the periodic movement of a small amplitude wave in a deep tank; see Figure 5-11. If the tank is very deep with respect to the wave amplitude, the resulting wave motion can be described quite well by linear wave theory. The classic linear solution for the interface displacement, η, (Lamb, 1975, or Ippen, 1966) is

$$\eta(y,t) = a \sin(ky) \cos(\omega t) \quad , \qquad (5\text{-}8)$$

where

$\omega = [gk \tanh (k H)|^{\frac{1}{2}}$

$k = \dfrac{2\pi}{l}$

$l = 4L =$ wave length ,

and a, L and H are defined in Figure 5-11.

Figure 5-12 shows the 22 by 17 non-uniform grid used to compute the periodic wave motion. The grid lines have been concentrated near the free-surface to yield a more accurate prediction of the free-surface motion. The computations were run for one wave period, 2.5324 seconds. This required 105 time steps and consumed about 480 seconds of CDC 6600 time.

The computed shapes of the wave free-surface at approximately each fifth of a period are shown in

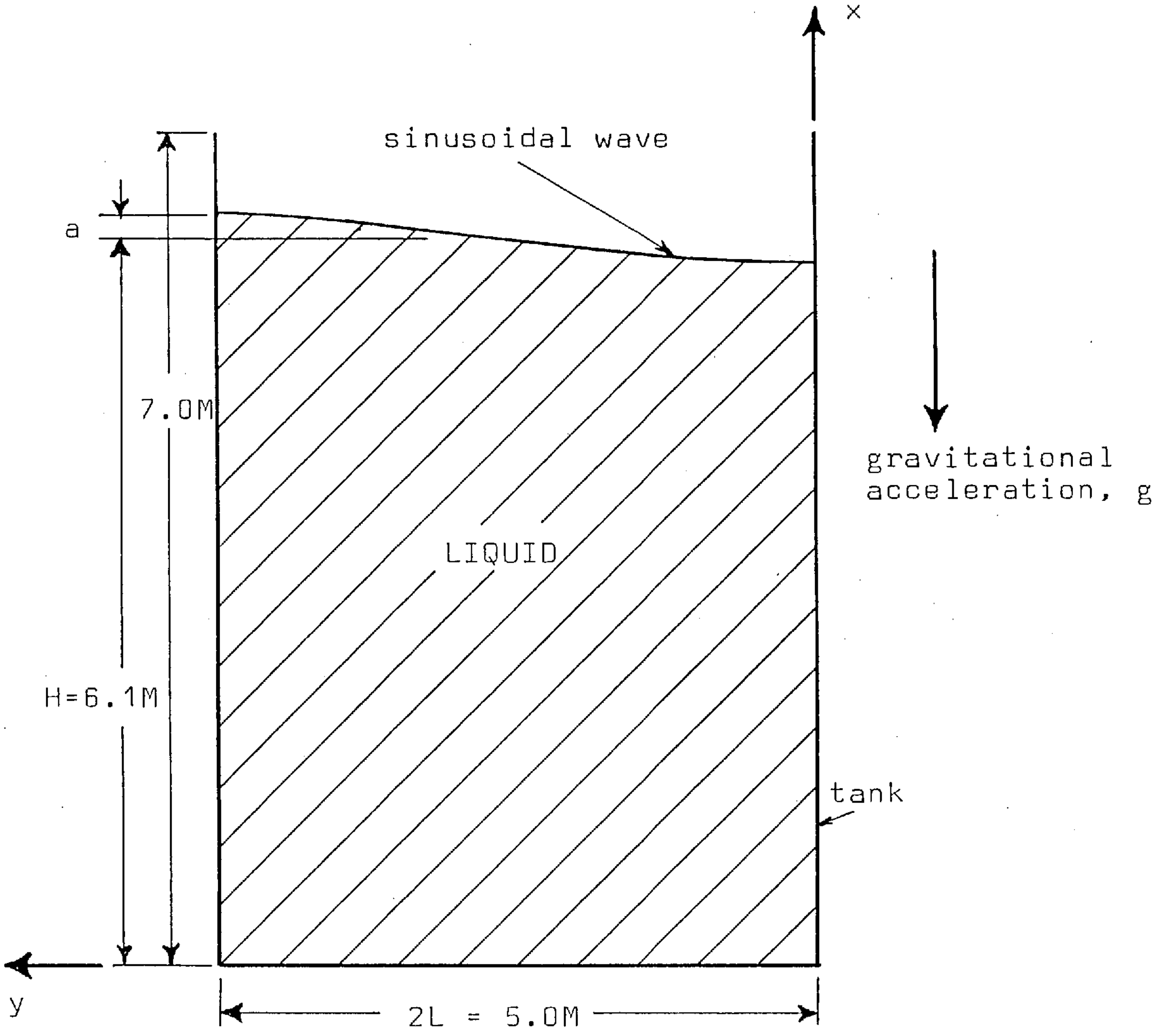

grid - 37 × 22
t - 0.025 sec.
max. time - 2.5 sec.
ρ liquid - 1000.0 kg/m^3
ρ gas - 1.198 kg/m^3
μ liquid - 10^{-3} Nt Sec/m^2
μ gas - 10^{-3} Nt Sec/m^2
g - 0.80665 M/sec^2

FIGURE 5-11 : DEFINITION SKETCH AND CIRCULATIONAL DETAILS FOR PERIODIC-WAVE PROBLEM

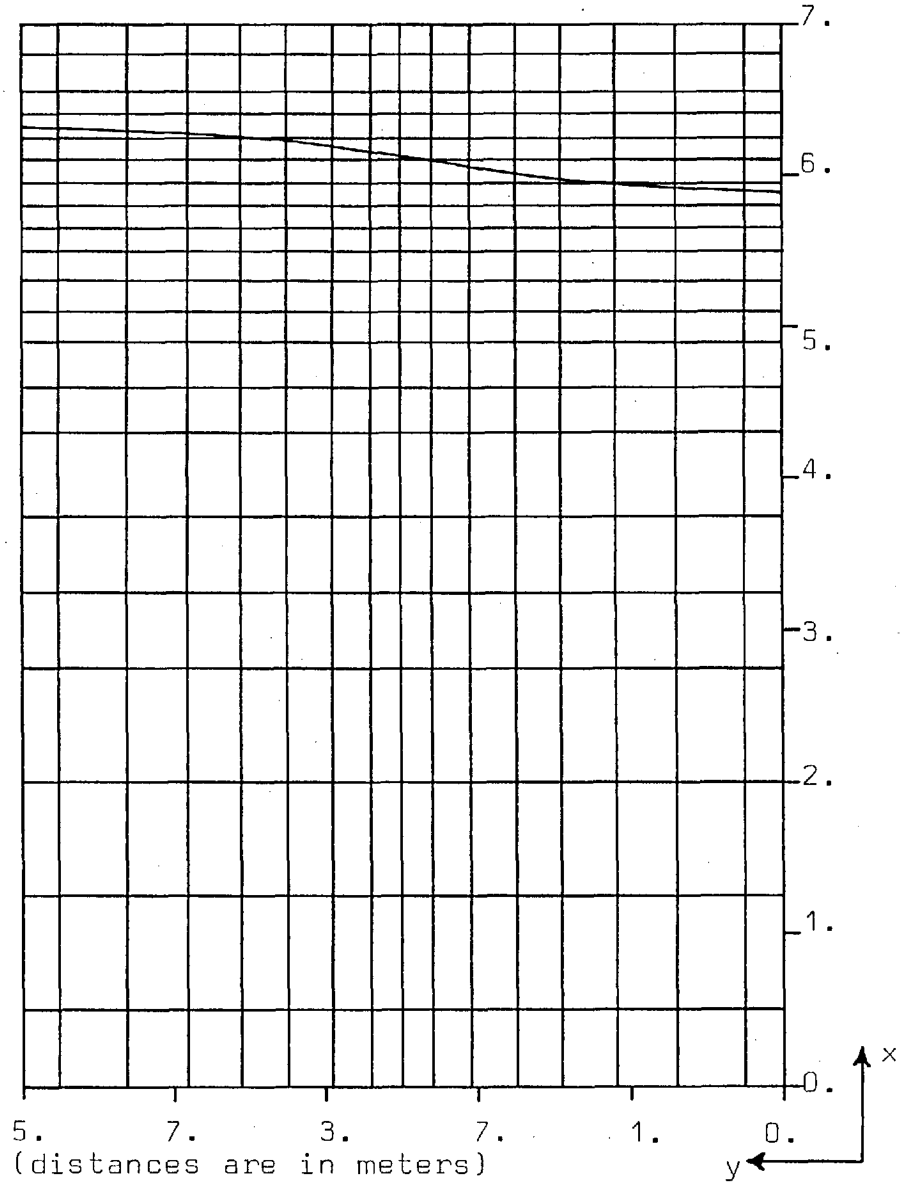

I	x	I	x	J	y	J	y
1	0.00	12	5.30	1	0.00	12	3.25
2	1.50	13	5.50	2	0.25	13	3.55
3	1.25	14	5.65	3	0.70	14	3.90
4	2.00	15	5.80	4	1.10	15	4.30
5	2.75	16	5.95	5	1.45	16	4.75
6	3.25	17	6.10	6	1.75	17	5.00
7	3.75	18	6.25	7	2.05		
8	4.30	19	6.40	8	2.30		
9	4.60	20	6.55	9	2.50		
10	4.90	21	6.80	10	2.70		
11	5.10	22	7.00	11	2.95		

FIGURE 5-12 : GRID USED TO PREDICT PERIODIC WAVE MOTION

Figure 5-13. In Figure 5-14 the surface elevations at $y = 0$ and at $y = 2L$ are plotted versus time. The linear solution (equation 5-8) is also shown in Figure 5-14.

Discussion

The sequence of computed wave shapes in Figure 5-13 shows the wave oscillating through one complete period. On the whole the wave maintains a sinusoidal shape; however, a small irregularity appears on the last "frame" of Figure 5-13. At about $y = L$, there is a small bump on the wave surface. The fluid should rotate about the point $(x = H, y = L)$ and the velocity at (H, L) should be zero. However, because the finite-difference procedure is concerned with quantities averaged over finite regions of space, the velocities computed for the point (H, L) will not necessarily be exactly zero. This error is insignificant to the overall flow, but it does cause the free-surface particles near $y = L$ to "drift" about slightly. The automatic particle-deletion procedure will remove particles that drift too far out of line with respect to their neighbours.

The analytical solution given in equation (5-8) is based on linearised free-surface boundary conditions; however, a real wave exhibits a non-linear behaviour. The non-linearities, which are included in the numerical procedure, cause the crests of the wave to be higher

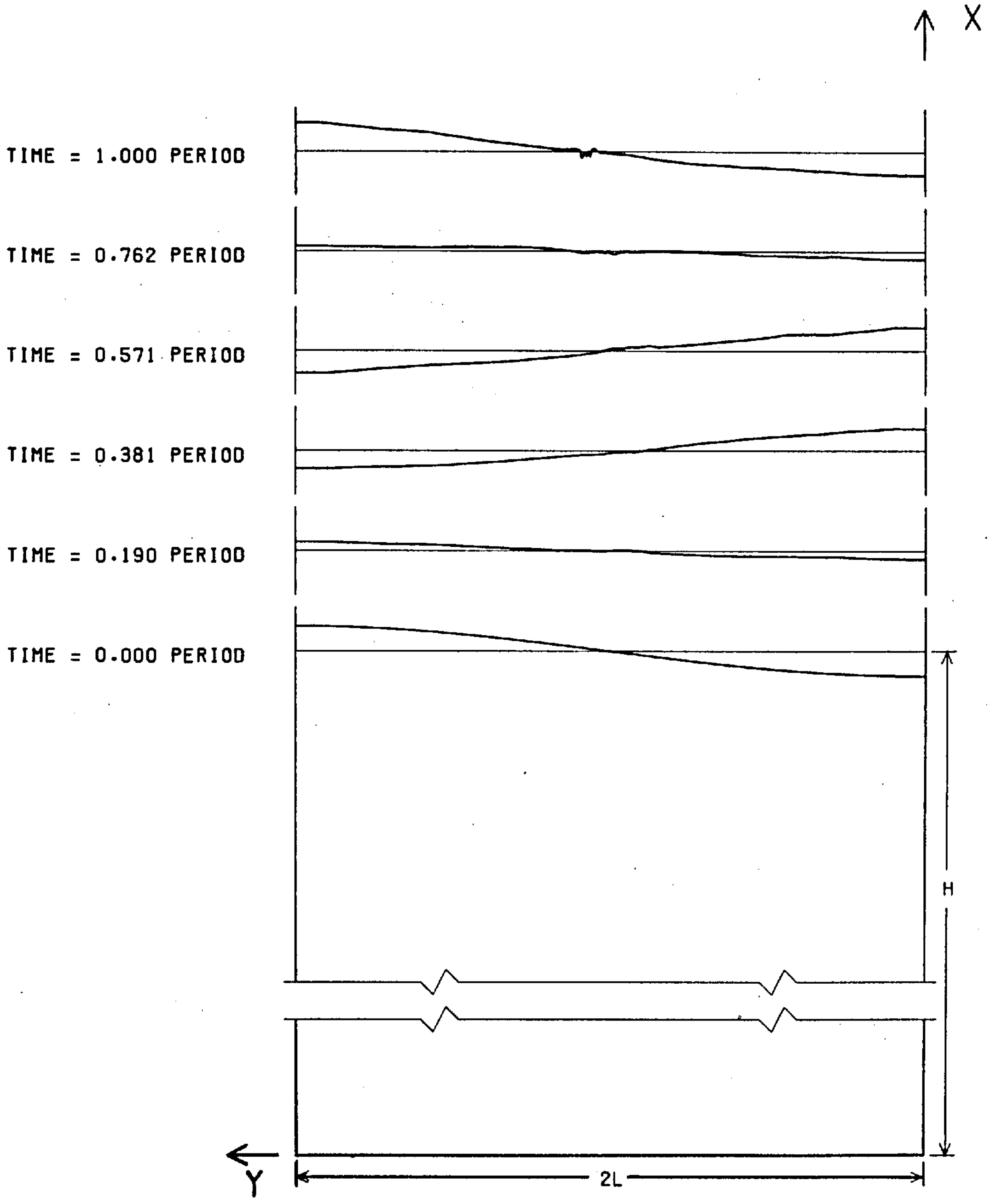

FIGURE 5-13 : FREE-SURFACE SHAPES FOR PERIODIC WAVE MOTION

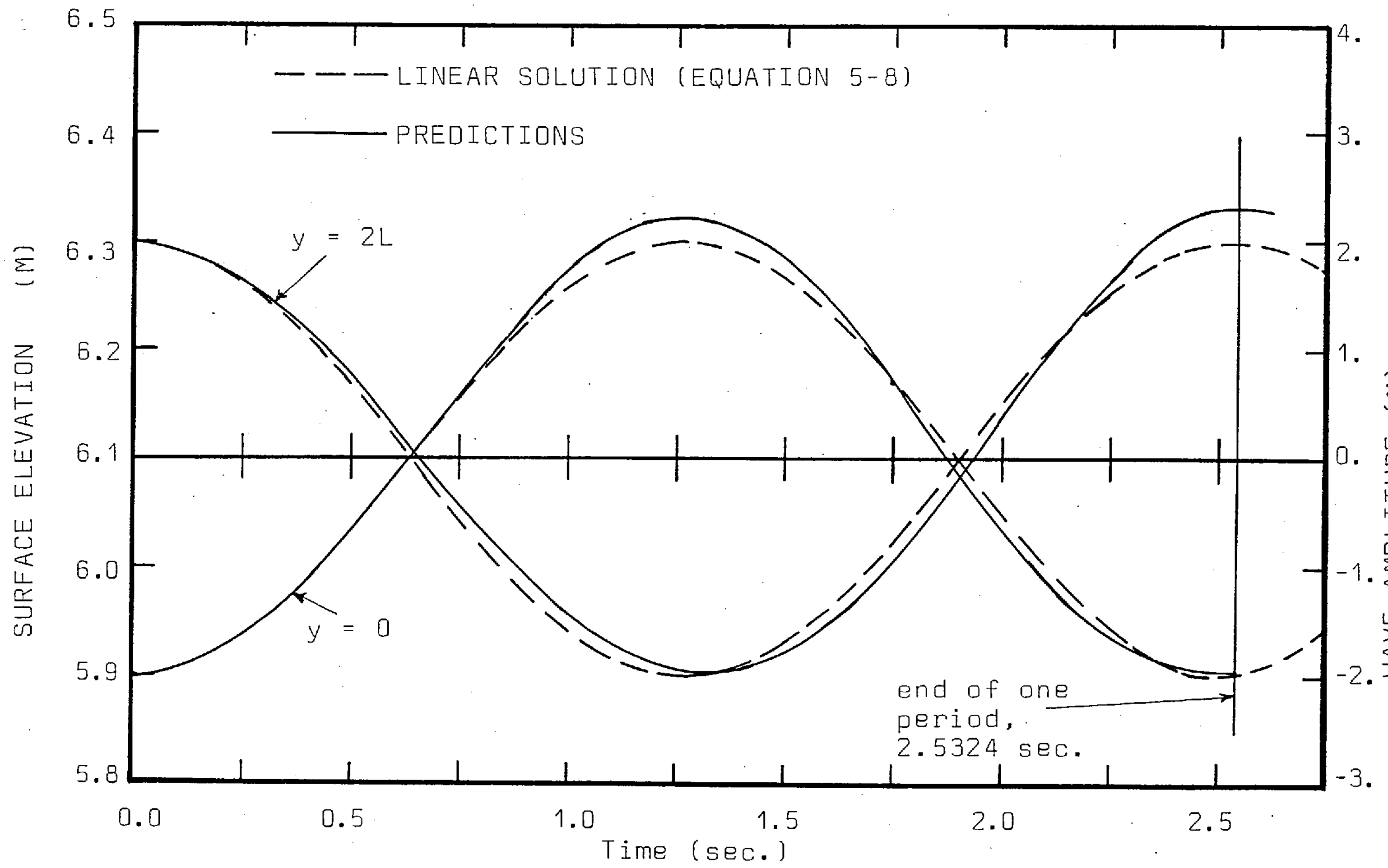

FIGURE 5-14 : SURFACE ELEVATION AT y=0 AND y=2L FOR THE PERIODIC WAVE than those of the linear counterpart and the trough to be shallower. Figure 5-14 shows these effects. It also shows that the frequency of the computed wave is quite accurately predicted.

5.6 SUMMARY

In this chapter predictions of four problems have been compared with analytical solutions. These comparisons verify the model and solution procedure in three ways. First, the accurate predictions for the water plug, the U-tube and the periodic wave demonstrate the ability to correctly solve the basic equations of motion. Secondly, the computations for all four problems, but especially the spherical bubble problem, show that the particle-tracking procedure moves the free-surface correctly. Finally, the results of the U-tube and the periodic wave calculations verify that the solution procedure can properly predict periodic motion and maintain the correct time scale.

CHAPTER 6

PREDICTIONS TO COMPARE WITH EXPERIMENTAL RESULTS

6.1 INTRODUCTION

In this chapter predictions of wave motions are compared with experimental results. First, predictions for the movement of the wave-front produced by a collapsing column of liquid and the impact of a solitary wave on a vertical wall are compared with data taken from the literature. Finally, the experimental results presented in Chapter 4 are compared with calculations. Details of the computations are tabulated in Table 6-1.

6.2 COLLAPSE OF A LIQUID COLUMN

Presentation

Gravitational acceleration causes a liquid to seek the lowest possible level or position of minimum potential energy; hence, a "column" of water will not "stand up" on a flat surface. Instead the column will collapse and form a thin layer. The reduction in column height and the outward movement of the liquid front have been measured by Martin and Moyce (1952) for several columns of different initial shapes. Figure 6-1 shows a typical collapsing column and defines several dimensionless quantities that Martin and Moyce used to present the data. The liquid columns are identified by the initial section shape (rectangular or semi-

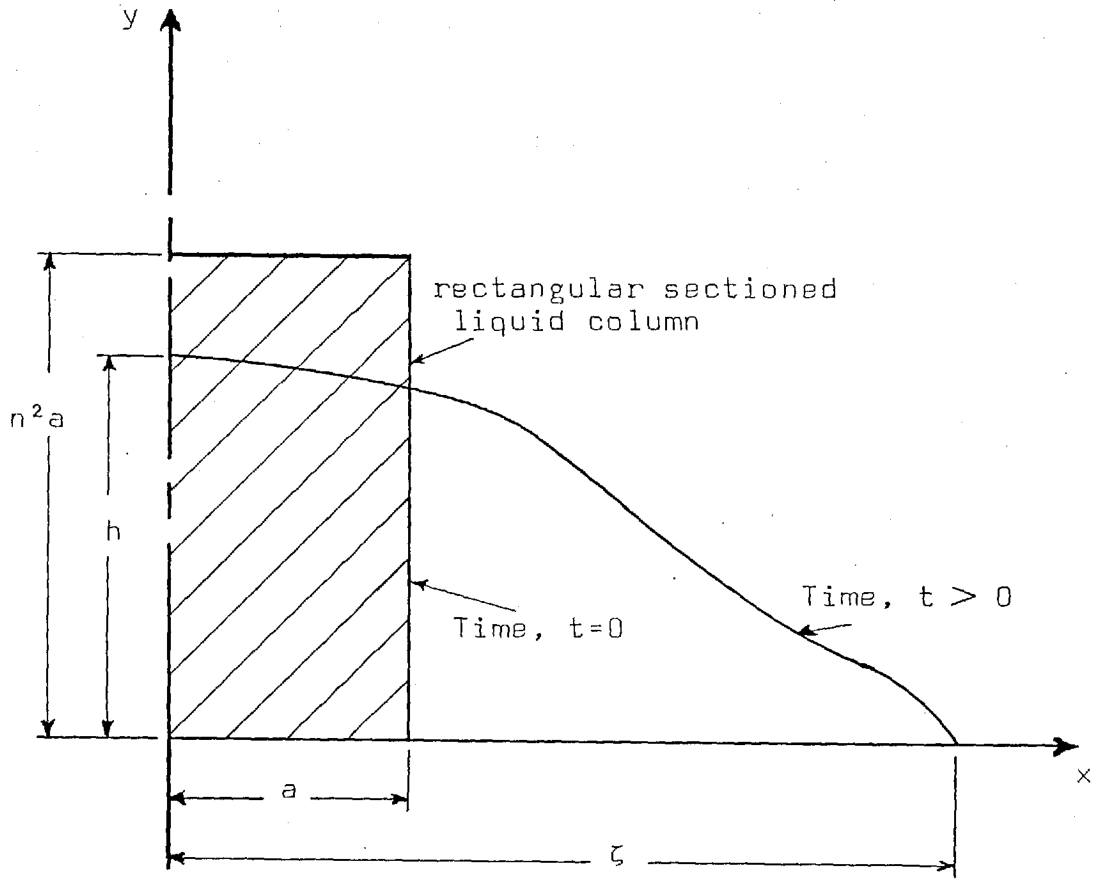

$Z \equiv \zeta/a$

$H \equiv h/n^2a$

$T \equiv nt\ (g/a)^{\frac{1}{2}}$

$\Upsilon \equiv t\ (g/a)^{\frac{1}{2}}$

FIGURE 6-1 : DEFINITION SKETCH FOR COLLAPSING-COLUMN PROBLEM

	COLLAPSING COLUMNS			
	$n^2=1$ a=0.05715	$n^2=1$ a=0.8	$n^2=4$ a=0.028575	semi-circular a=0.0508
Coordinate System	Cartesian	Cartesian	Cartesian	Cartesian
Grid	22 × 17	37 × 22	37 × 22	22 × 17
Type of Grid Spacing	Non-Uniform	Non-Uniform	Non-Uniform	Non-Uniform
Number of Particle Strings	1	1	1	1
Number of Particles at Start	257	65	161	100
Number of Particles at Finish	500	500	500	402
Maximum Time Sec	2.05	0.8	0.66	0.3
Time Step (Δt) Sec	0.025	0.01	0.005	0.005
Number of Time Steps	82	80	132	60
Number of Iterations per Time Step	10	8	5	8
Direction of Gravitational Acceleration	Y	Y	Y	Y
Density of Gas Kg/m^3	1.198	1.198	1.198	1.198
Density of Liquid Kg/m^3	1000.0	1000.0	1000.0	1000.0
Viscosity of Gas Nt Sec/m^2	1×10^{-5}	1×10^{-5}	1×10^{-5}	1×10^{-5}
Viscosity of Liquid Nt Sec/m^2	1×10^{-3}	1×10^{-3}	1×10^{-3}	1×10^{-3}
Computational Time CDC 6600 Sec	700	365	800	215

TABLE 6-1 : PERTINENT DATA FOR THE PREDICTIONS PRESENTED IN CHAPTER 6 (contd. overleaf)

	SOLITARY WAVES			EXPERIMENTAL WAVES			
	h_o/d_o .25	h_o/d_o .4	h_o/d_o .6	Run No 4	Run No 11	Run No 8	Run No 13
Coordinate System	Cartesian	Cartesian	Cartesian	Cartesian	Cartesian	Cartesian	Cartesian
Grid	37 × 22	37 × 22	37 × 22	37 × 22	37 × 22	37 × 22	37 × 22
Type of Grid Spacing	Non-Uniform	Non-Uniform	Non-Uniform	Non-Uniform	Non-Uniform	Non-Uniform	Non-Uniform
Number of Particle Strings	1	1	1	1	1	1	1
Number of Particles at Start	125	125	125	177	209	177	209
Number of Particles at Finish	149	164	213	288	259	447	320
Maximum Time Sec	4.0	4.0	2.8	1.5	1.5	1.3	1.5
Time Step (Δt) Sec	0.02	0.02	0.02	0.01	0.01	0.01	0.01
Number of Time Steps	200	200	140	150	150	130	150
Number of Iterations per time step	10	10	10	10	12	10	10
Direction of Gravitational Acceleration	Y	Y	Y	Y	Y	Y	Y
Density of Gas Kg/m^3	1.198	1.198	1.198	1.198	1.198	1.198	1.198
Density of Liquid Kg/m^3	1000.0	1000.0	1000.0	1000.0	1000.0	1000.0	1000.0
Viscosity of Gas Nt Sec/m^2	1×10^{-5}	1×10^{-5}	1×10^{-5}	1×10^{-5}	1×10^{-5}	1×10^{-5}	1×10^{-5}
Viscosity of Liquid Nt Sec/m^2	1×10^{-3}	1×10^{-3}	1×10^{-3}	1×10^{-3}	1×10^{-3}	1×10^{-3}	1×10^{-3}
Computational Time CDC 6600 Sec	1890	1876	1300	1600	1725	1300	1540

TABLE 6-1 : PERTINENT DATA FOR THE PREDICTIONS PRESENTED IN CHAPTER 6

circular) and size (2a × n^2a, where a is the semi-base length).

Predictions were made for four column configurations:

rectangular sectioned columns,

RSC1 $n^2 = 1$, $a = 0.05715$ m ,
RSC2 $n^2 = 1$, $a = 0.08$ m ,
RSC3 $n^2 = 4$, $a = 0.028575$ m ,

semi-circular sectioned column,

SSC1 $n^2 = 1$, $a = 0.0508$ m.

Non-uniform grids were used in computing each of the four collapsing columns. The grid point locations are tabulated in Tables 6-2, 6-3, 6-4 and 6-5. In the x-direction the grid points are concentrated near the initial location of the liquid column and in the y-direction they are concentrated near the bottom (y=0) portion of the flow domain. The calculations were run, either until all of the liquid was contained in the bottom row of main "cells" or control volumes, or until the wave-front reached the end of the grid. Computational times in CDC 6600 minutes were approximately 11.6 minutes for RSC1, 6.0 minutes for RSC2, 13.3 minutes for RSC3 and 3.6 minutes for SSC1.

A sequence of section profiles for a square column RSC1, is shown in Figure 6-2 and a similar sequence for the semi-circular column, SSC1, is shown in Figure 6-3. The velocity vectors are also included in Figures 6-2

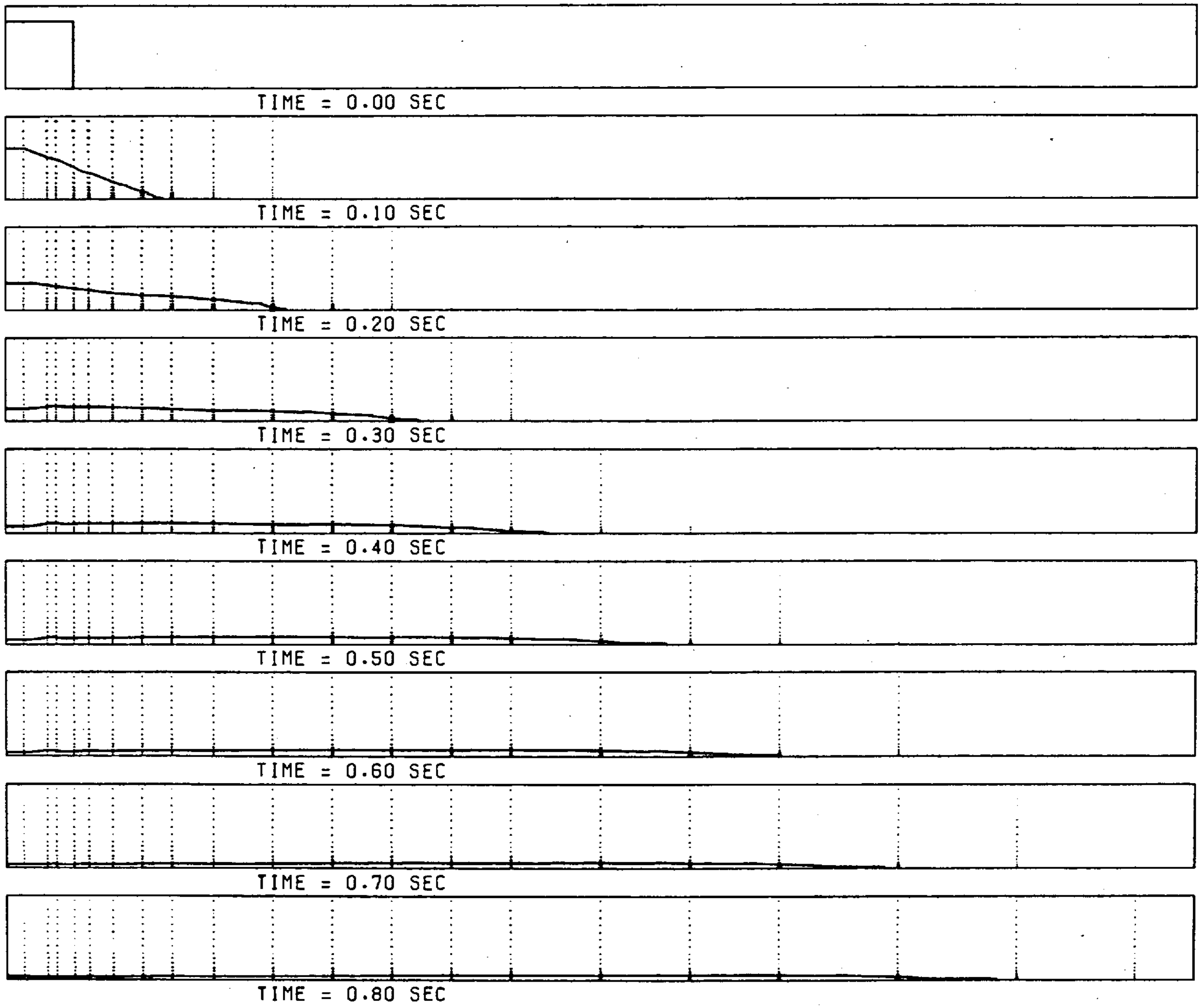

FIGURE 6-2 : PREDICTED SECTION PROFILES AND VELOCITY VECTORS FOR RECTANGULAR COLLAPSING COLUMN,

$n^2 = 1$, $a = 0.05715$ M

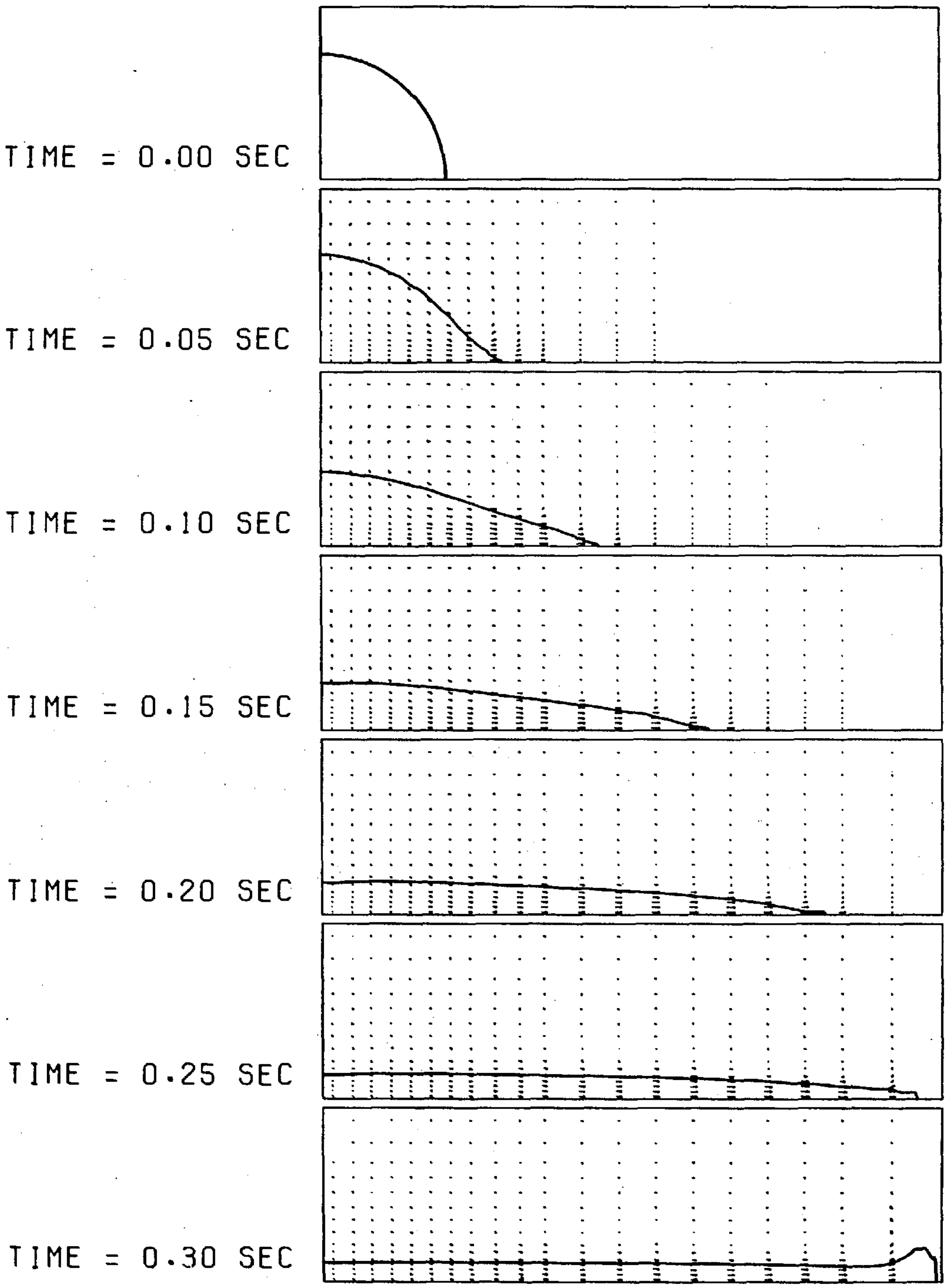

FIGURE 6-3 : PREDICTED SECTION PROFILES AND VELOCITY VECTORS FOR SEMI-CIRCULAR COLLAPSING COLUMN,

$n^2 = 1$, $a = 0.0508$ M

I	x	I	y	J	y	J	y
1	0.000	12	0.275	1	0.00	12	0.040
2	0.015	13	0.325	2	0.001	13	0.046
3	0.035	14	0.375	3	0.003	14	0.052
4	0.0425	15	0.425	4	0.005	15	0.058
5	0.0575	16	0.500	5	0.075	16	0.066
6	0.070	17	0.575	6	0.010	17	0.070
7	0.090	18	0.650	7	0.014		
8	0.115	19	0.750	8	0.018		
9	0.140	20	0.850	9	0.022		
10	0.175	21	0.950	10	0.028		
11	0.225	22	1.000	11	0.034		

TABLE 6-2 : GRID USED TO PREDICT RECTANGULAR COLLAPSING COLUMN, $n^2 = 1$, $a = 0.05715$ meters (RSC1)

I	x	I	x	J	y
1	0.0	21	5.0	1	0.0
2	0.05	22	5.3	2	0.02
3	0.20	23	5.6	3	0.05
4	0.40	24	5.9	4	0.08
5	0.60	25	6.2	5	0.12
6	0.80	26	6.5	6	0.20
7	1.00	27	6.8	7	0.28
8	1.20	28	7.1	8	0.36
9	1.4	29	7.4	9	0.44
10	1.7	30	7.7	10	0.52
11	2.0	31	8.0	11	0.60
12	2.3	32	8.3	12	0.68
13	2.6	33	8.6	13	0.76
14	2.9	34	8.9	14	0.82
15	3.2	35	9.2	15	0.88
16	3.5	36	9.5	16	0.94
17	3.8	37	10.0	17	1.0
18	4.1				
19	4.4				
20	4.7				

TABLE 6-3 : GRID USED TO PREDICT RECTANGULAR COLLAPSING COLUMN, $n^2 = 1$, $a = 0.8$ meter (RSC2)

I	x	I	x	J	y
1	0.0	23	0.3	1	0.0
2	0.005	24	0.325	2	0.003
3	0.01	25	0.35	3	0.006
4	0.015	26	0.375	4	0.009
5	0.02	27	0.4	5	0.012
6	0.025	28	0.45	6	0.015
7	0.03	29	0.5	7	0.02
8	0.035	30	0.55	8	0.025
9	0.04	31	0.6	9	0.03
10	0.045	32	0.65	10	0.035
11	0.05	33	0.7	11	0.04
12	0.06	34	0.75	12	0.05
13	0.07	35	0.85	13	0.06
14	0.09	36	0.95	14	0.07
15	0.11	37	1.0	15	0.08
16	0.13			16	0.09
17	0.15			17	0.10
18	0.175			18	0.11
19	0.2			19	0.12
21	0.225			21	0.13
21	0.25			21	0.14
22	0.275			22	0.15

TABLE 6-4 : GRID USED TO PREDICT RECTANGULAR COLLAPSING COLUMN, n^2 = 4, a - 0.023575 meter (RSC3)

I	x	J	y
1	0.0	1	0.0
2	0.004	2	0.001
3	0.012	3	0.003
4	0.020	4	0.005
5	0.028	5	0.007
6	0.036	6	0.009
7	0.044	7	0.012
8	0.052	8	0.015
9	0.060	9	0.02
10	0.070	10	0.025
11	0.080	11	0.03
12	0.090	12	0.036
13	0.105	13	0.042
14	0.12	14	0.048
15	0.135	15	0.056
16	0.15	16	0.065
17	0.165	17	0.070
18	0.18		
19	0.195		
20	0.21		
21	0.23		
22	0.25		

TABLE 6-5 : GRID USED TO PREDICT SEMI-CIRCULAR COLLAPSING COLUMN, $n^2 = 1$, a = 0.0508 meter (SSC1) and 6.3. Comparisons of the predictions with the experimental results of Martin and Moyce for the non-dimensional wave-front location, Z, and column height, H (see Figure 6-1), are presented in Figures 6-4 through 6-9. The zero times for the experimental results were adjusted, before presentation, to agree with the zero times of the computed results. This adjustment, which did not exceed 0.02 seconds, is reasonable because of the uncertainty about the zero times expressed by Martin and Moyce.

Discussion

The results shown in Figures 6-4 through 6-9 demonstrate that the numerical procedure can accurately predict the collapse of a liquid column. The computed values for both the wave-front location and the height of the column top compare very well with the experimental results of Martin and Moyce. Not until the liquid has spread into a thin film occupying only one or two rows of control volumes along the "bottom" of the grid (for example RSC1 after T = 7, and RSC2 after T = 9) or until the wave front has entered the last grid cell in the x-direction and is approaching the end of the grid (SSC1 after T = 3), do the predictions differ significantly from the experimental results. The "long time" solution for the dam-break or collapsing-column problem (Stoker, 1957), yields 2. as the asymptotic value for the non-dimensional wave-front velocity, $\frac{dZ}{dT}$. Martin and Moyce reported the maximum

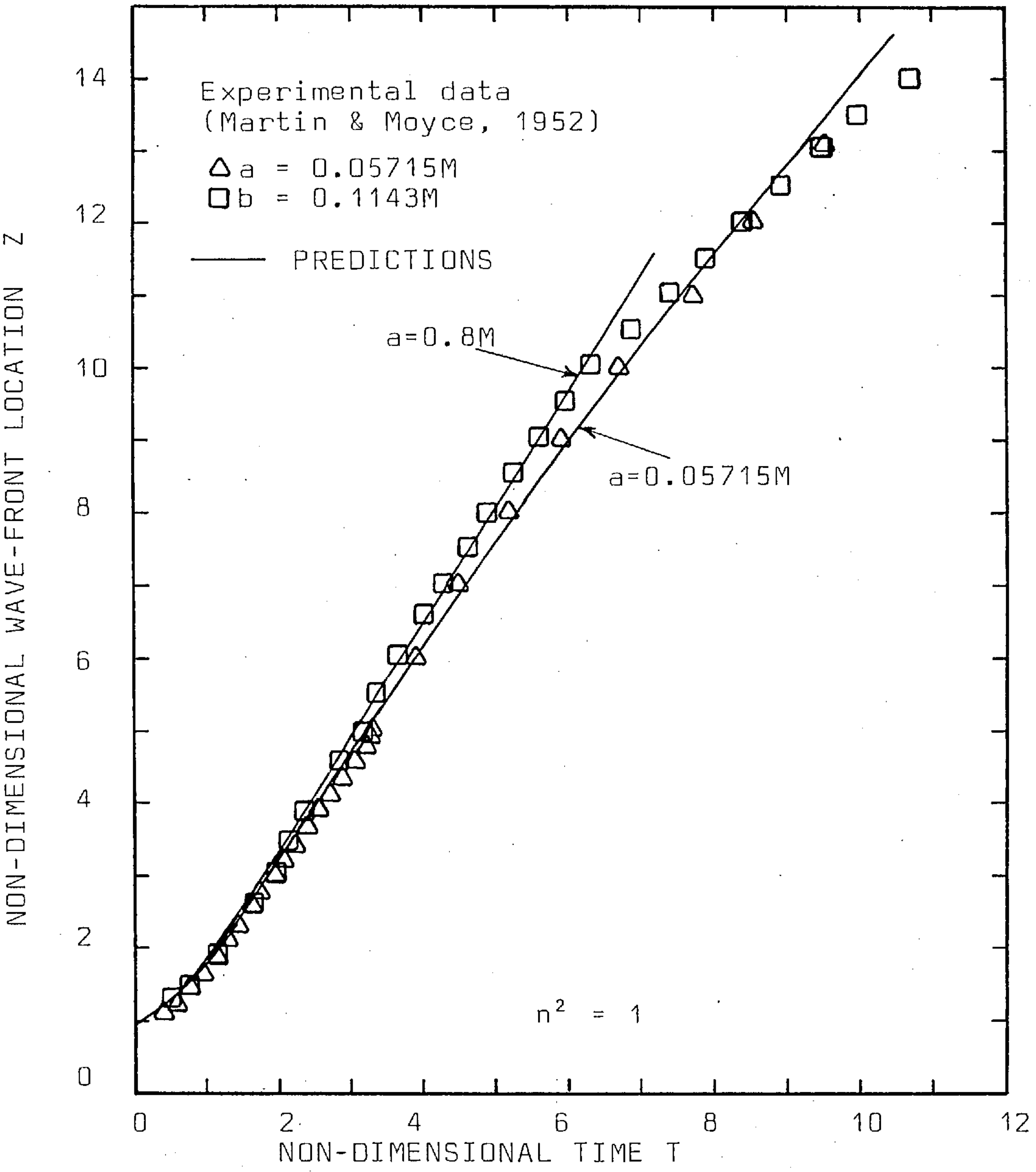

FIGURE 6-4 : Z VERSUS T FOR RECTANGULAR COLLAPSING COLUMN, $n^2 = 1$.

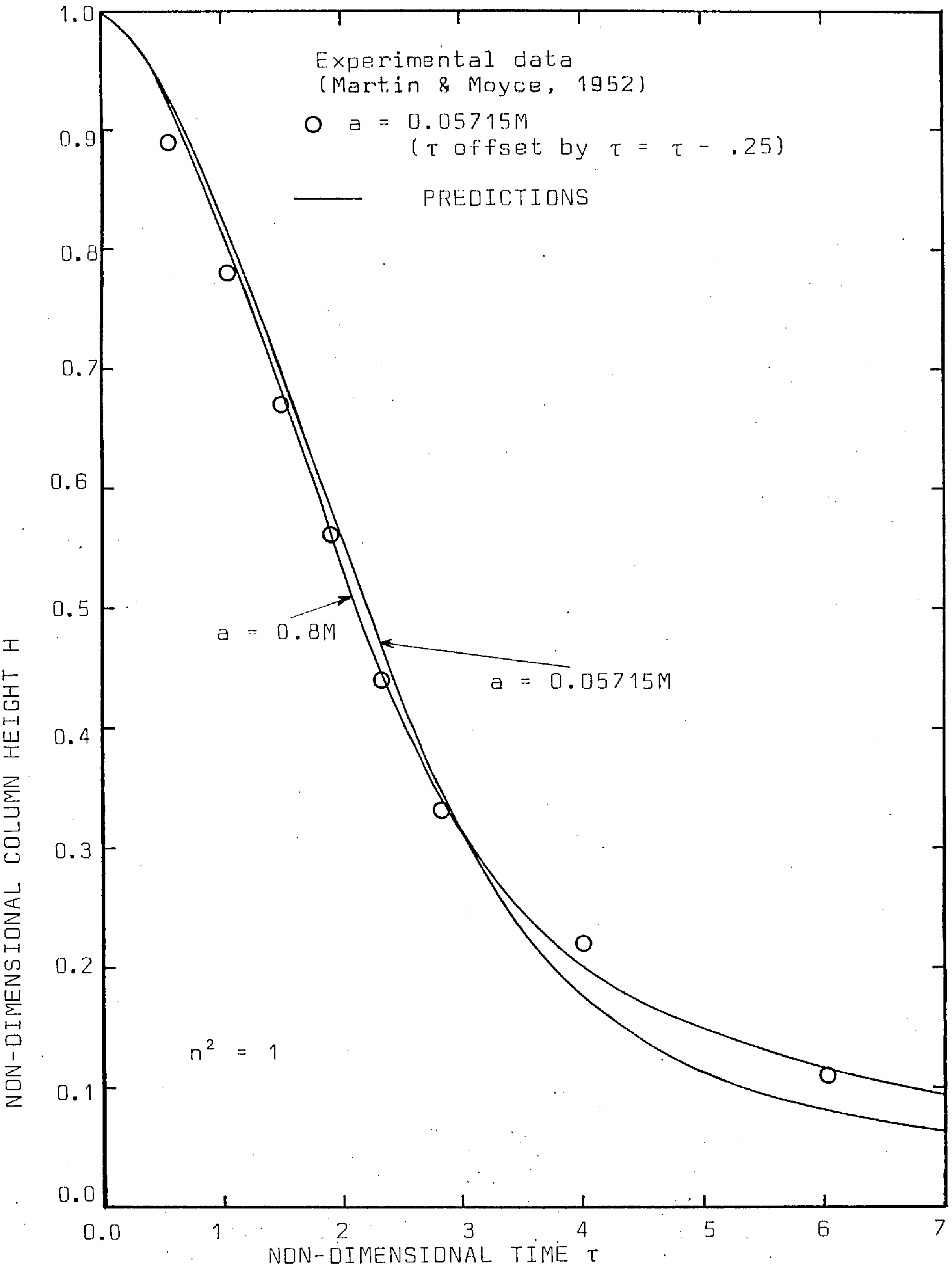

FIGURE 6-5 : H VERSUS τ FOR RECTANGULAR COLLAPSING COLUMN, $n^2 = 1$.

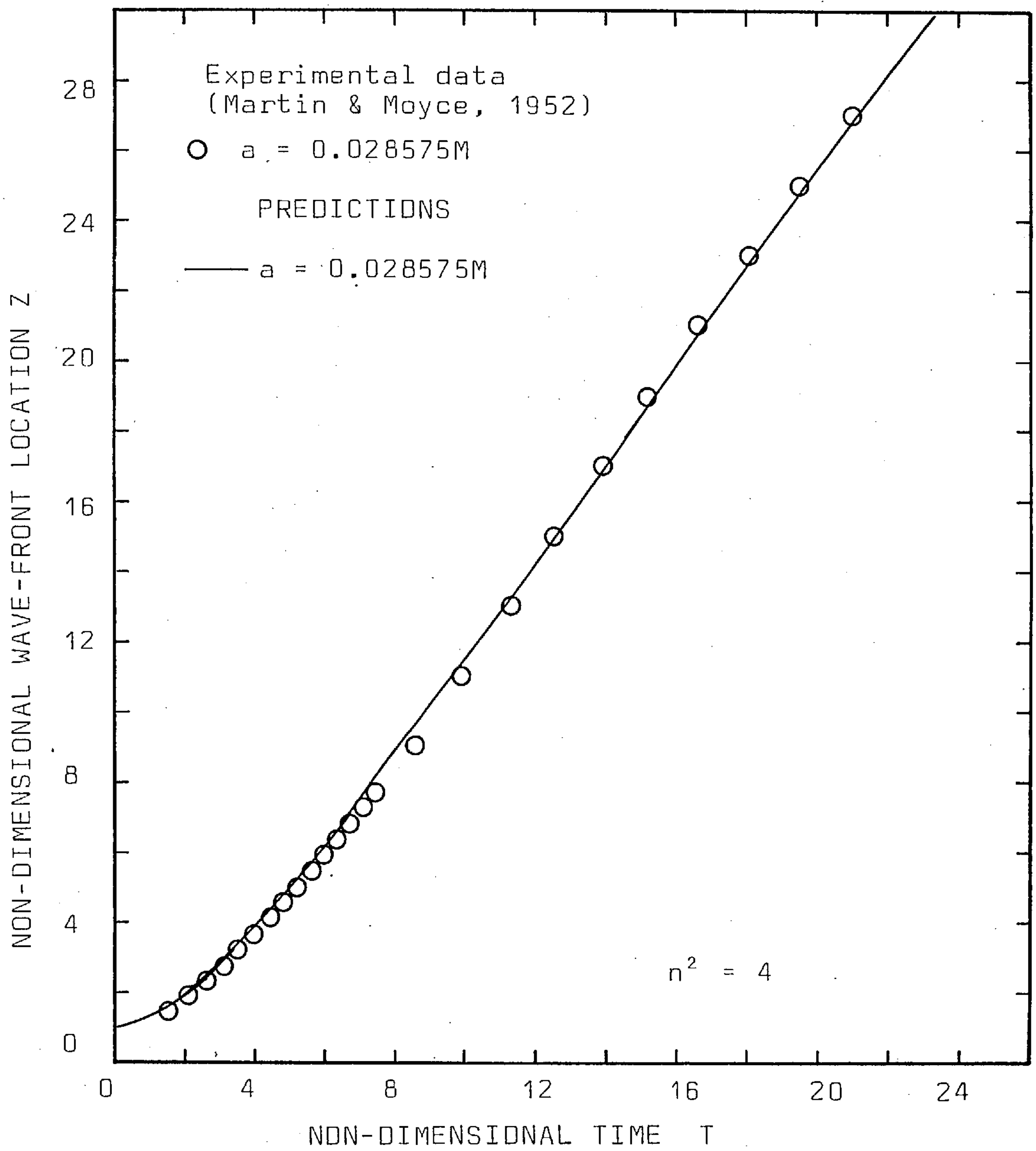

FIGURE 6-6 : Z VERSUS T FOR RECTANGULAR COLLAPSING COLUMN, $n^2 = 4$.

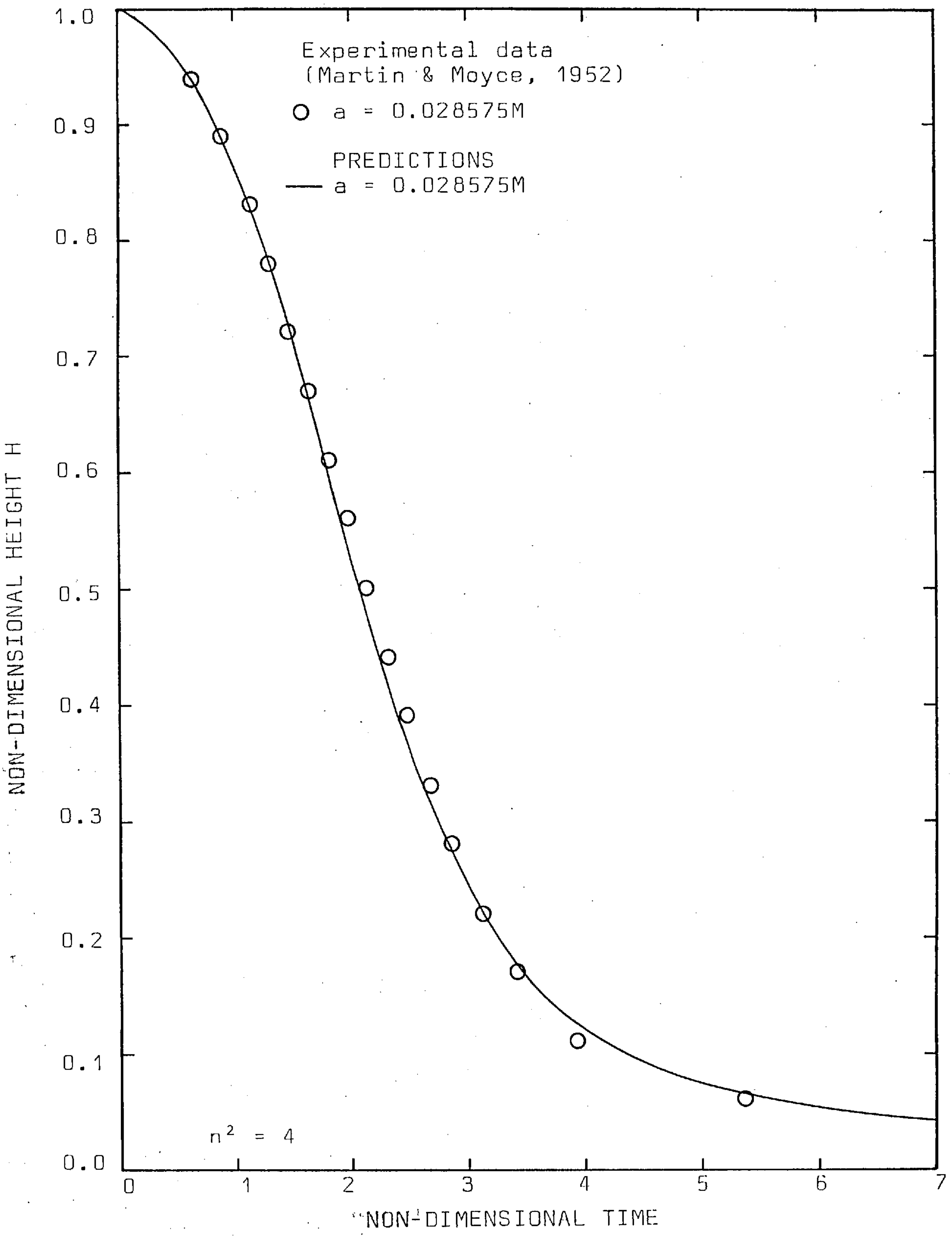

FIGURE 6-7 : H VERSUS τ FOR RECTANGULAR COLLAPSING COLUMN, $n^2 = 4$.

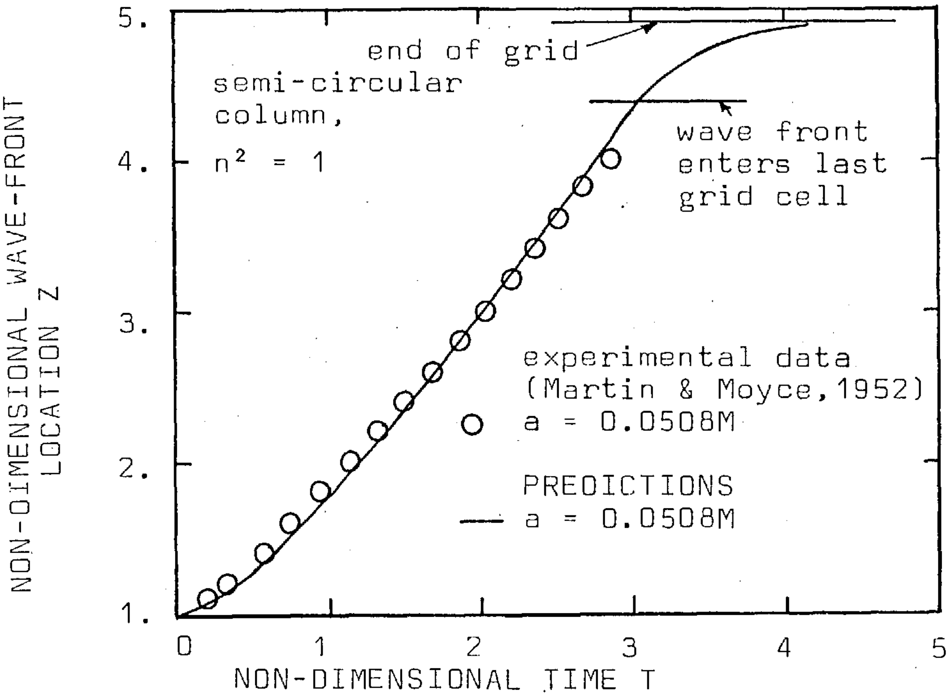

FIGURE 6-8 : Z VERSUS T FOR SEMI-CIRCULAR COLLAPSING COLUMN, $n^2 = 1$.

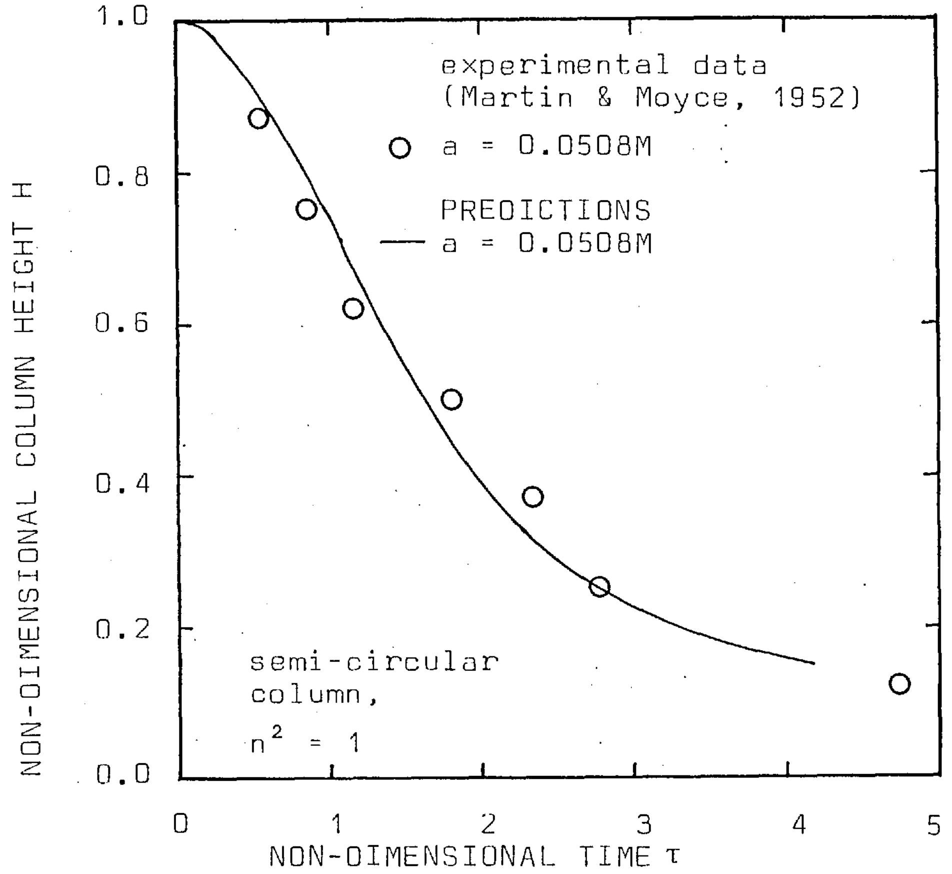

FIGURE 6-9 : H VERSUS τ FOR SEMI-CIRCULAR COLLAPSING COLUMN, $n^2 = 1$.

surge velocities for the rectangular sectioned columns as follows:

n^2	a (m)	$\frac{dZ}{dT}$ (max.)
1	0.05715	1.62
1	0.1143	1.66
4	0.028575	1.62

The values obtained from the present computations are:

	n^2	a (m)	$\frac{dZ}{dT}$ (max.)
RSC1	1	0.05715	1.61
RSC2	1	0.08	1.68
RSC3	4	0.028575	1.55
SSC1	1	0.0508	1.39

Thus the wave-front velocity is also predicted quite accurately. Overall, the predictions agree very well with the experimental data reported by Martin and Moyce. However, as is always the case with numerical computations, the results could be enhanced by employing a finer grid, especially in the lower, right-hand portion of the flow domain.

Very little can be asserted to validate the predicted free-surface shape for the collapsing columns. Martin and Moyce presented four photographs for a rectangular $n^2 = 1$ column; however, they did not specify the times to which the photographs relate. These four surface shapes are shown in Figure 6-10 along with several surface profiles from the predictions. Even though

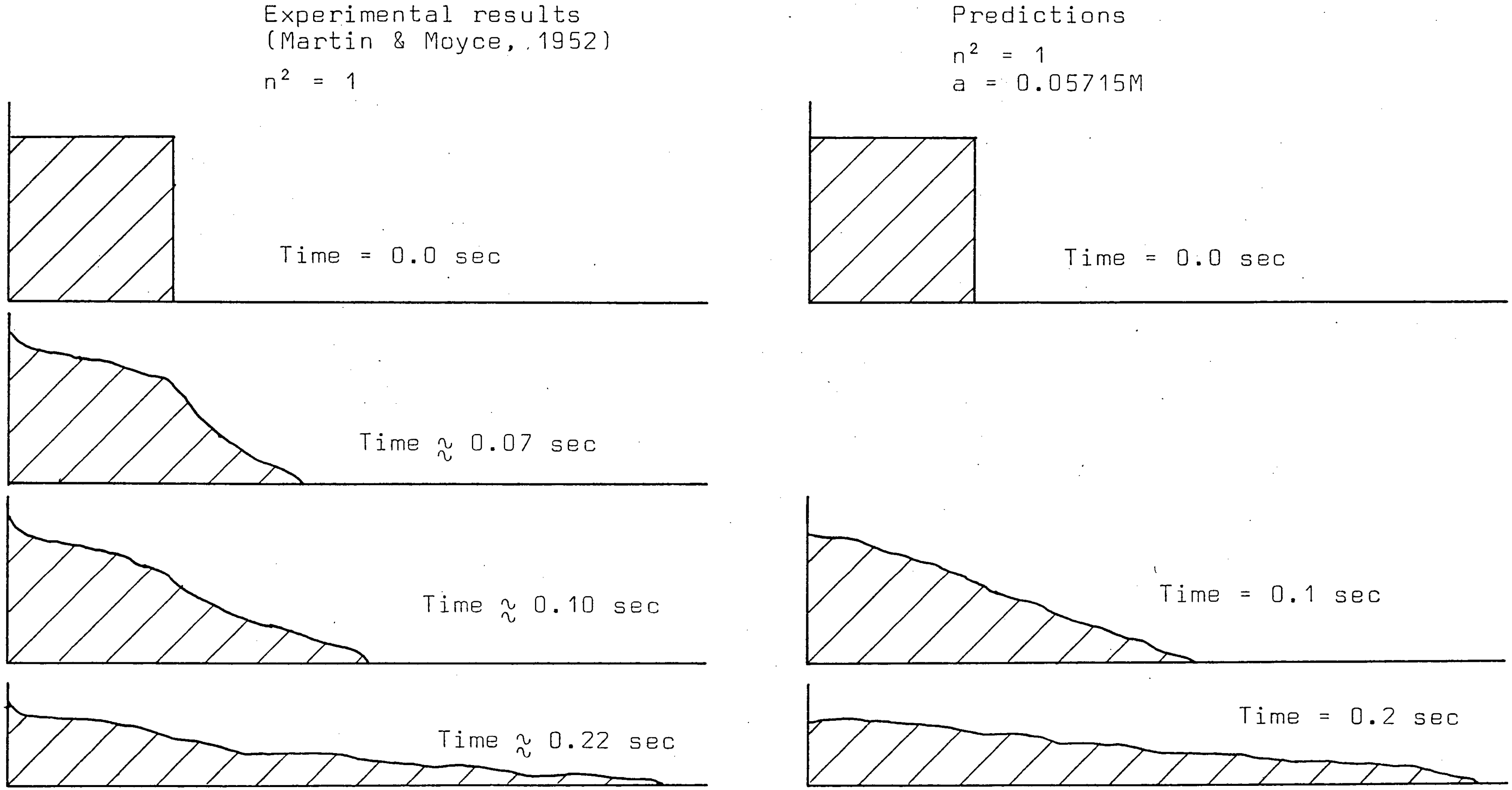

FIGURE 6-10 : QUALITATIVE COMPARISON OF FREE-SURFACE SHAPES FOR RECTANGULAR COLLAPSING COLUMN the illustrations in Figure 6-10 can only be compared qualitatively, they do suggest that the free-surface shape is predicted reasonably well.

6.3 SOLITARY-WAVE RUN-UP ON A VERTICAL WALL

Presentation

Shallow water waves can be approximated analytically as solitary waves. The solitary wave stands entirely above the nominal liquid level and the wave height is not necessarily small in relation to the total liquid depth. A solitary wave can travel for a considerable distance along a uniform channel with little or no distortion (Lamb, 1975). Laitone's second approximation for the solitary wave, as reported by Wiegel (1964), is given below.

Wave speed:

$$\frac{C}{\sqrt{gd_o}} = \left[1 + \frac{1}{2} \frac{h_o}{d_o} - \frac{3}{20} \left(\frac{h_o}{d_o}\right)^2 \right] \qquad (6\text{-}1)$$

Wave profile:

$$y_s = d_o + h_o \,\mathrm{sech}^2\,(Awx - ct) -$$

$$\frac{3}{4} h_o \left(\frac{h_o}{d_o}\right) \mathrm{sech}^2\,(Awx - ct)\left[1 - \mathrm{sech}^2\,(Awx - ct)\right] \qquad (6\text{-}2)$$

where $Awx = \frac{x}{d_o} \sqrt{\frac{3}{4} \frac{h_o}{d_o}} \left(1 - \frac{5}{8} \frac{h_o}{d_o}\right)$

Liquid velocities:

$$\frac{u}{\sqrt{gd_o}} = \frac{h_o}{d_o}\left[1 + \frac{1}{4}\frac{h_o}{d_o} - \frac{3}{2}\frac{h_o}{d_o}\frac{y^2}{{d_o}^2}\right] \text{sech}^2\ (Awx - ct)$$

$$+ {\frac{h_o}{d_o}}^{2}\left[- 1 + \frac{9}{4}\frac{y^3}{{d_o}^2}\right] \text{sech}^4\ (Awx - ct) \qquad (6\text{-}3)$$

$$\frac{v}{\sqrt{gd_o}} = \sqrt{3}\ \left(\frac{h_o}{d_o}\right)^{3/2}\ \frac{y}{d_o}\ \text{sech}^2\ (Awx - ct)$$

$$\cdot\ \tanh\ (Awx - ct)\left[1 - \frac{3}{8}\frac{h_o}{d_o} - \frac{1}{2}\frac{h_o}{d_o}\left(\frac{y}{d_o}\right)^2\right|$$

$$+ \frac{h_o}{d_o}\left[-2 + \frac{3}{2}\left(\frac{y}{d_o}\right)^2 \text{sech}^2\ (Awx - ct)\right] \qquad (6\text{-}4)$$

Figure 6-11 shows a sketch of a solitary wave and defines the free water level, d_o, the wave height, h_o, and the wave run-up, R.

The movement of a solitary wave and its impact on a vertical wall were simulated with the numerical procedure. Equations (6-1, 6-2, 6-3 and 6-4) were used to define the initial conditions for the wave. Three runs were made for the h_o/d_o ratios of .25, .4 and .6. A 37 by 22 grid was used for each run. The grid used for the h_o/d_o = .4 run is shown in Figure 6-12; the grids for the other runs had the same relative spacings, but the overall grid dimensions were adjusted with respect to the size of each wave. Time steps of 0.02 second were used and each run consumed approximately 31 minutes of CDC 6600 time.

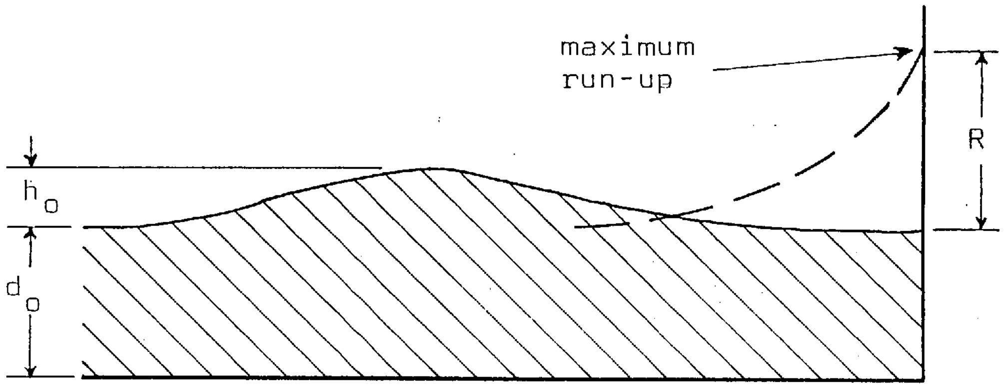

FIGURE 6-11 : DEFINITION SKETCH FOR SOLITARY WAVE RUN-UP PROBLEM

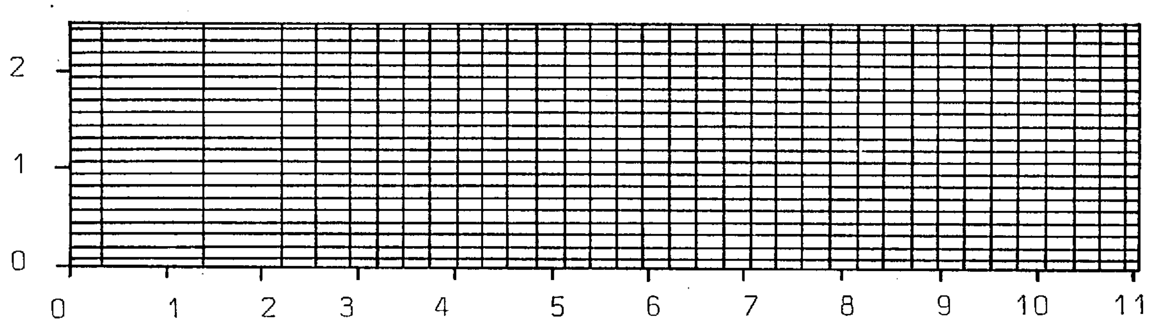

I	x	I	x	I	x	J	y	J	y
1	0.0	13	4.842	25	8.163	1	0.0	12	1.323
2	0.277	14	5.119	26	8.439	2	0.063	13	1.449
3	1.383	15	5.396	27	8.716	3	0.189	14	1.575
4	2.214	16	5.672	28	8.993	4	0.315	15	1.701
5	2.546	17	5.949	29	9.269	5	0.441	16	1.827
6	2.905	18	6.226	30	9.546	6	0.507	17	1.953
7	3.182	19	6.502	31	9.823	7	0.693	18	2.079
8	3.459	20	6.779	32	10.10	8	0.819	19	2.205
9	3.735	21	7.056	33	10.38	9	0.945	20	2.331
10	4.012	22	7.333	34	10.65	10	1.071	21	2.457
11	4.289	23	7.609	35	10.79	11	1.197	22	2.502
12	4.566	24	7.886	36	10.92				
				37	11.07				

FIGURE 6-12 : GRID USED TO PREDICT SOLITARY WAVE MOTION, h_o/d_o = 0.4

The movement of the h_o/d_o = .4 wave is illustrated in Figure 6-13, which shows the predicted free-surface shapes and velocity vectors for several time steps. The predicted wave run-up is compared with the experimental results of Maxworthy (1976) and Street and Camfield (1966) in Figure 6-14. The phase shift of the reflected wave is shown in Figure 6-15 along with results measured by Maxworthy. Figure 6-16 shows the computed velocity profile under the wave crest before and after the wave impacts the wall. Also shown on Figure 6-16 are the analytical velocity profiles of McCowan and Laitone (from Wiegel, 1966) and the experimental results of Daily and Stephan (from Chan Street and Strelkoff, 1969).

Discussion

The predictions for the solitary wave agree very well with the available experimental results. Figure 6-14 shows that the maximum wave run-up is predicted accurately. The results presented in Figure 6-15 indicate that the predicted wave moves with the correct celerity, and that it is reflected from the wall with a negative phase shift. The magnitude of the predicted phase shift is somewhat smaller than that measured by Maxworthy. There are two possible reasons for this discrepancy. First, the time step size, Δt, used for the computations may have been too large. Hence, even though the calculations were quite stable, the predicted wave motion during the impact with the wall

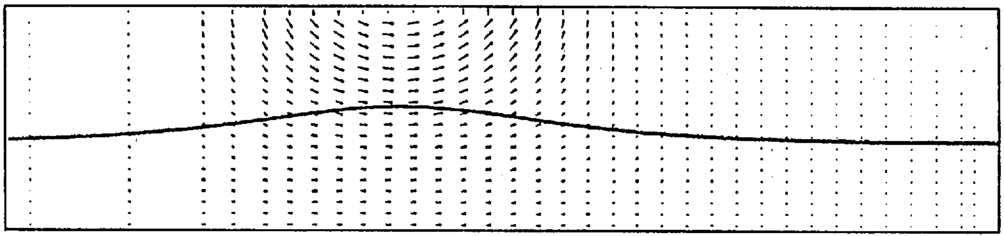

TIME = 0.00 SEC

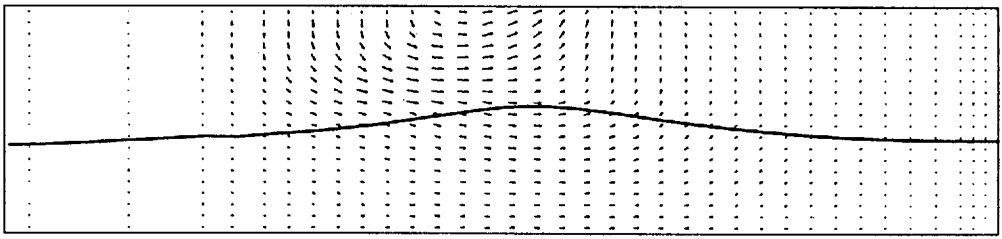

TIME = 0.40 SEC

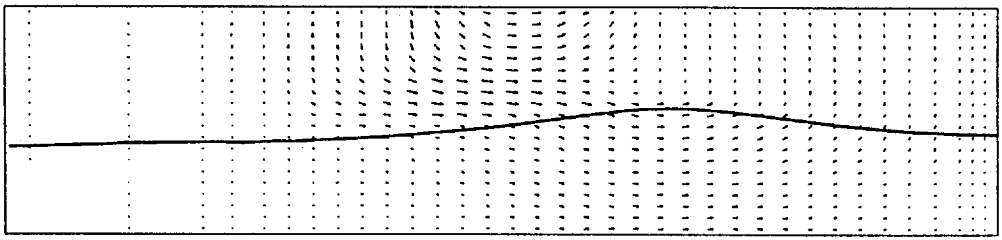

TIME = 0.80 SEC

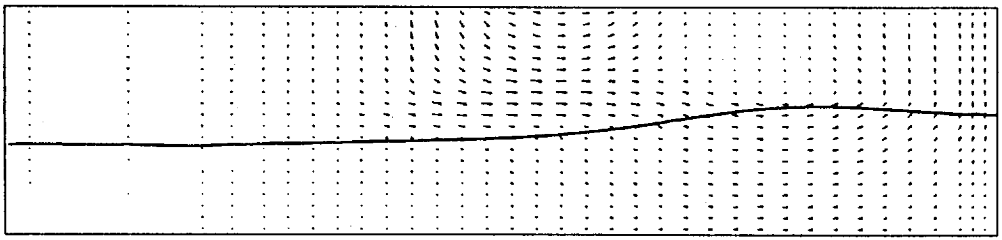

TIME = 1.20 SEC

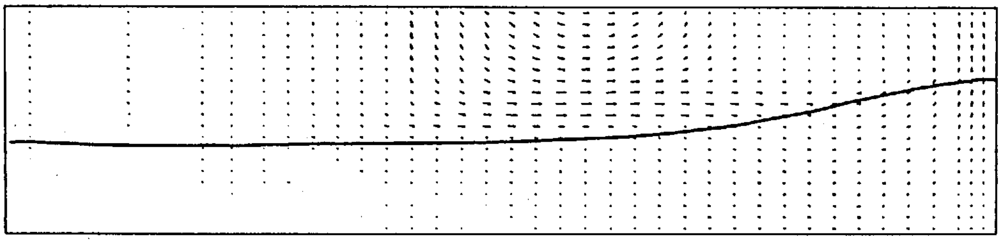

TIME = 1.60 SEC

FIGURE 6-13 : PROFILES AND VELOCITY VECTORS FOR SOLITARY WAVE IMPACTING WALL, $h_o/d_o = 0.4$

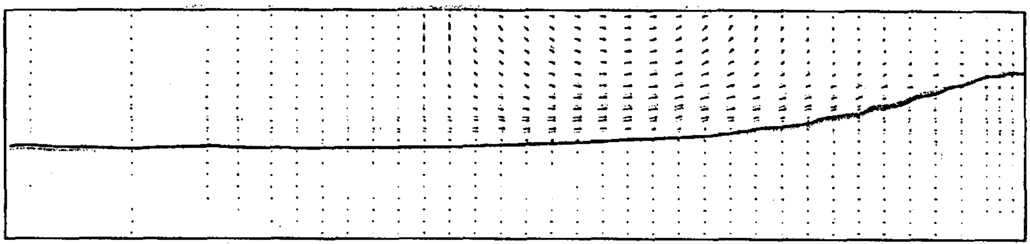

TIME = 2.00 SEC

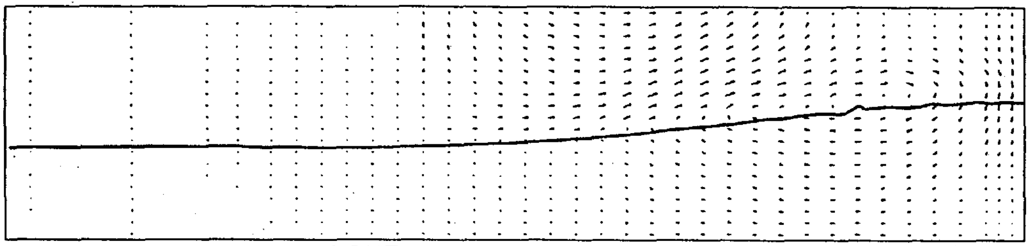

TIME = 2.40 SEC

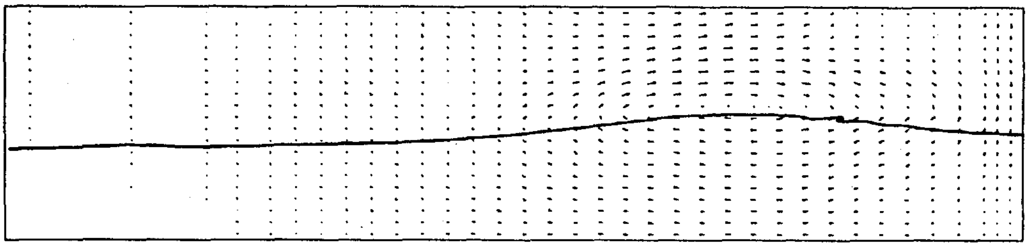

TIME = 2.80 SEC

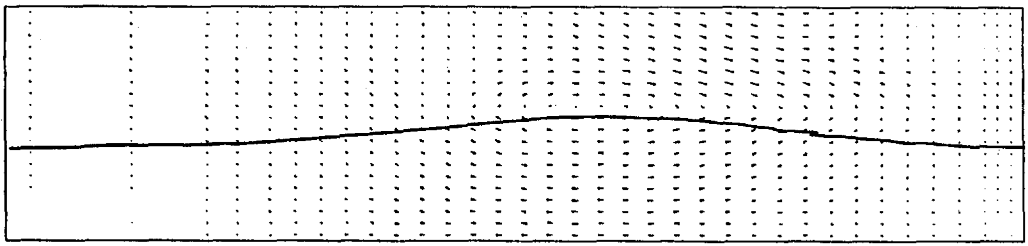

TIME = 3.20 SEC

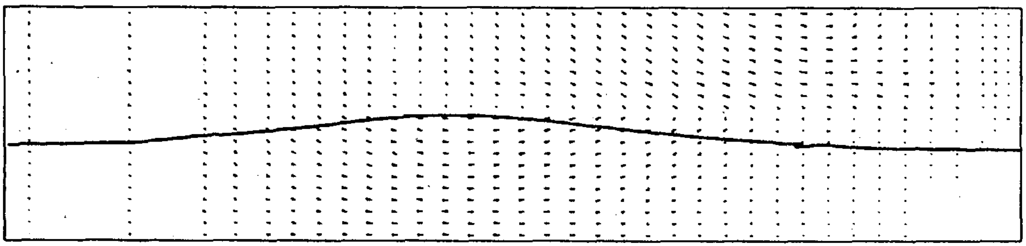

TIME = 3.60 SEC

FIGURE 6-13 : (CONTINUED)

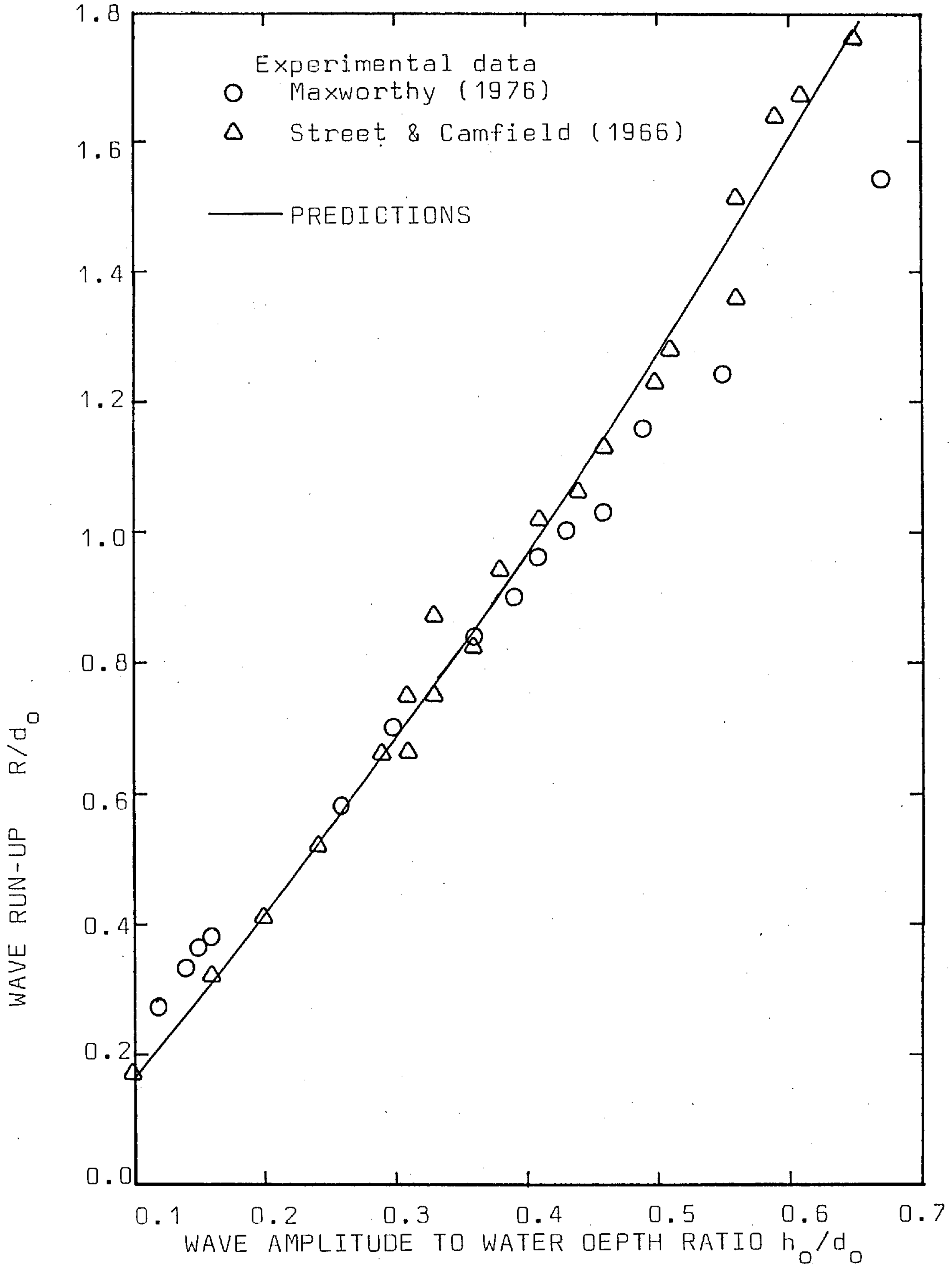

FIGURE 6-14 : MAXIMUM RUN-UP FOR SOLITARY WAVES

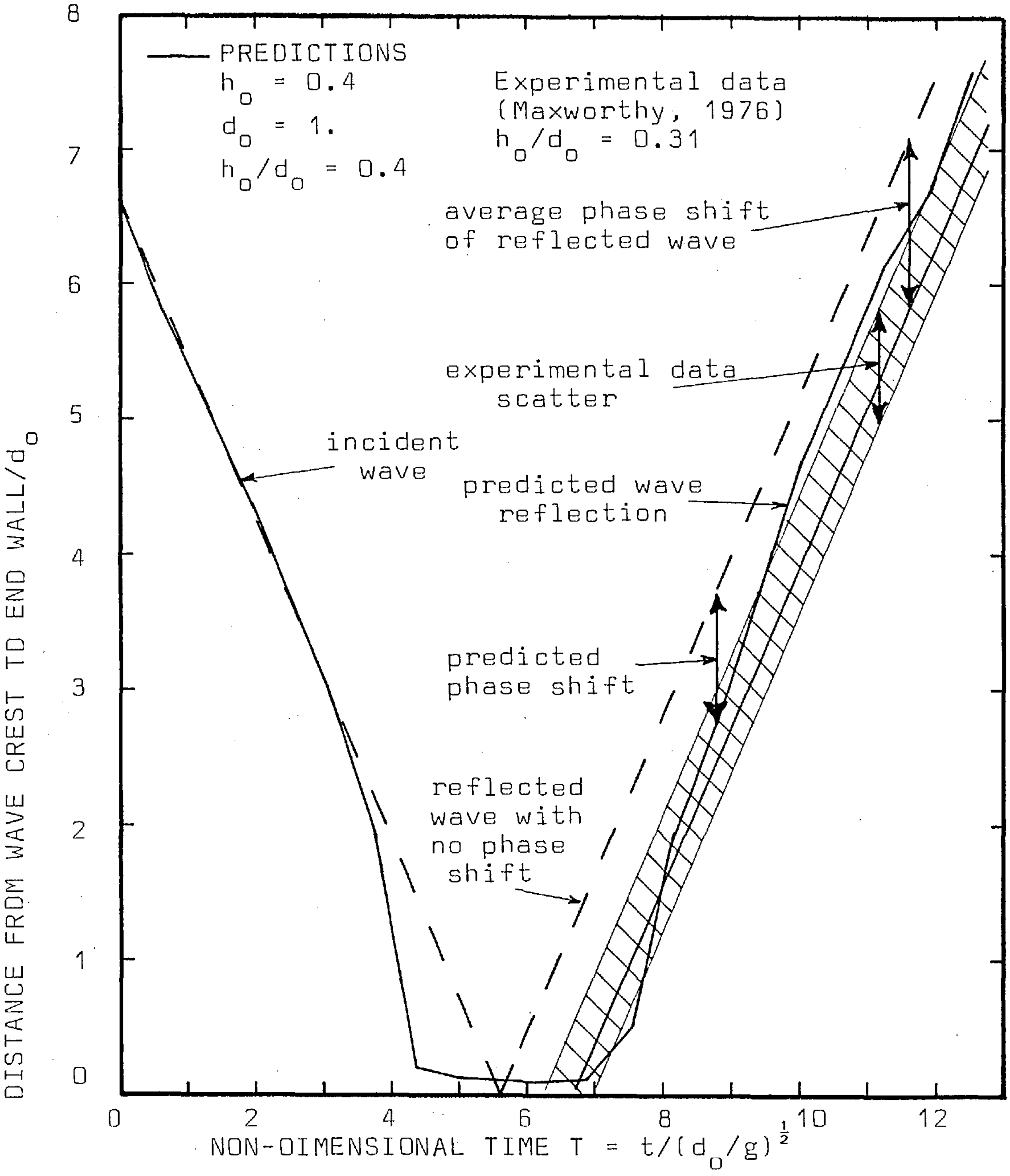

FIGURE 6-15 : PHASE SHIFT OF SOLITARY WAVE DURING INTERACTION WITH VERTICAL WALL

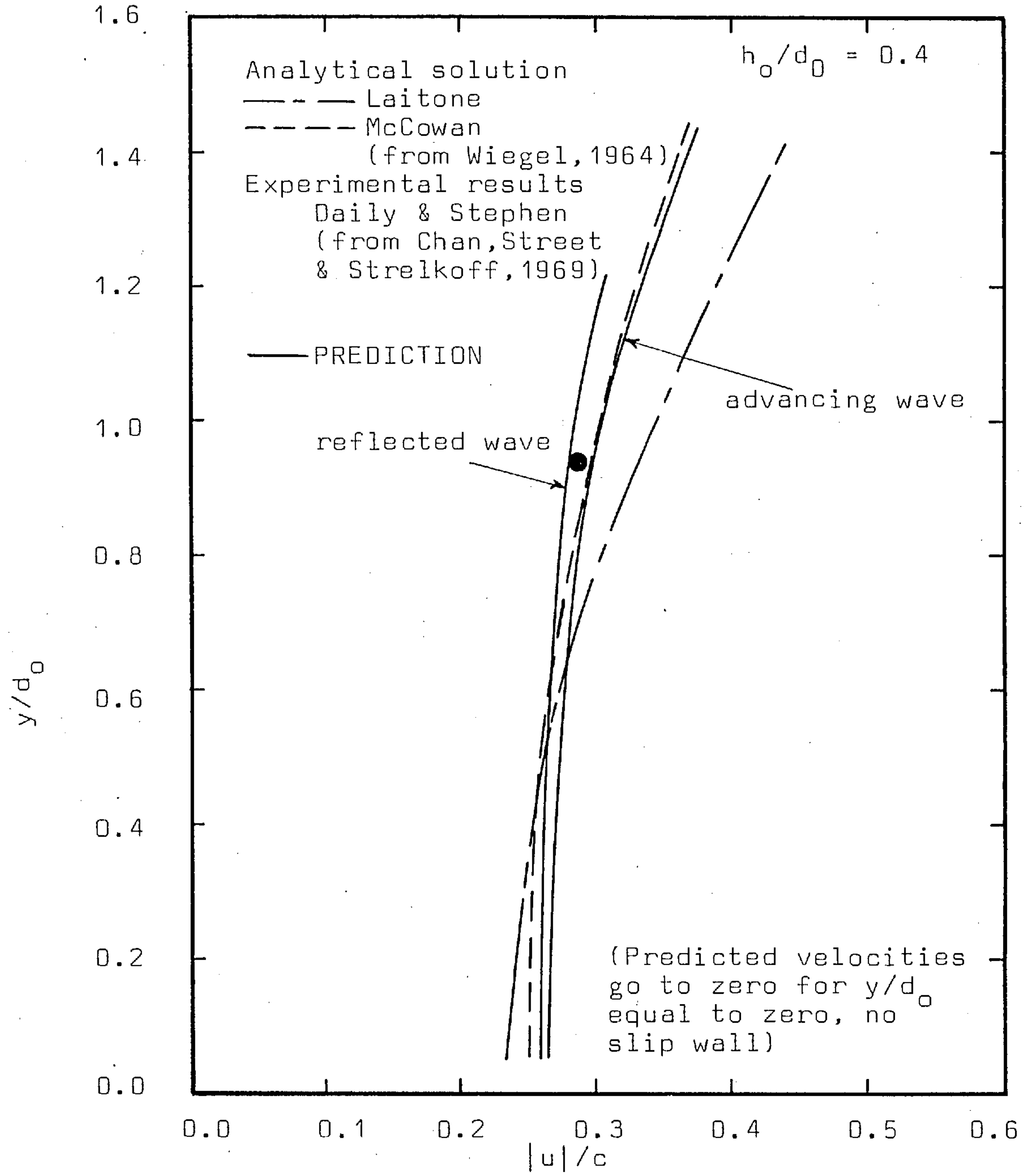

FIGURE 6-16 : VELOCITY PROFILES UNDER WAVE CREST could have been falsely accelerated. Secondly, as Maxworthy indicates, it is difficult to generate single, solitary waves, thus, his results could have been affected by the presence of secondary waves. The horizontal velocity beneath the crest of the predicted wave (Figure 6-16) has the same magnitude as the experimental measurement of Daily and Stephan (from Wiegel, 1964). Further, the analytical solution of McCowan (which, according to Wiegel, best describes the velocity profile beneath the crest of a solitary wave) agrees well with the computed profiles for both the advancing wave and the reflected wave. Note that the initial velocity profile is identical to that of Laitone. Finally, the wave profiles presented in Figure 6-13 show that the simulated wave moves smoothly and that the advancing and reflected waves possess the characteristic shape of a solitary wave.

6.4 WAVE GENERATION: EXPERIMENTAL RESULTS OF THE PRESENT STUDY

Presentation

Predictions were made for the four experimental waves presented in Chapter 4. The computations were performed with a 37 by 22, non-uniform grid (see Figure 6-17). Each computation was run until the wave had reflected from the end wall of the tank. This required 150 0.01 second time steps and approximately 29 minutes of CDC 6600 time. Atmospheric pressure was maintained in the top row of main control volumes by making the air in

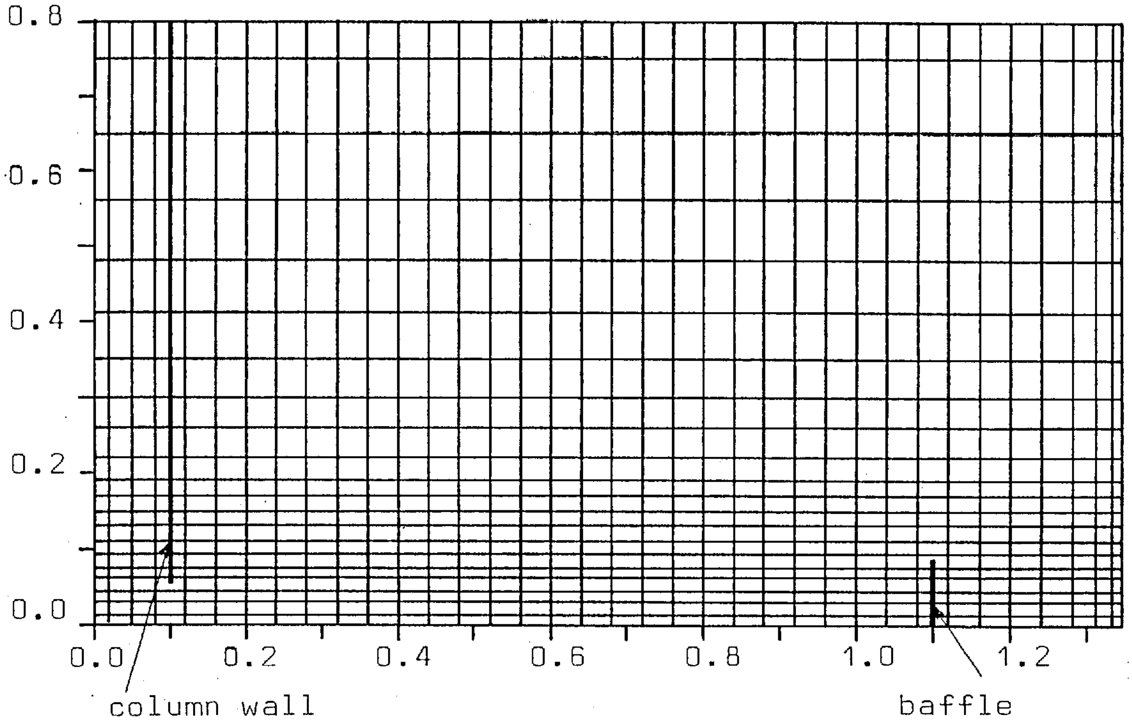

I	x	I	x	J	y
1	0.00	21	0.76	1	0.0000
2	0.02	22	0.80	2	0.0125
3	0.05	23	0.84	3	0.0300
4	0.08	24	0.88	4	0.0450
5	0.12	25	0.92	5	0.0600
6	0.16	26	0.96	6	0.0775
7	0.20	27	1.00	7	0.0925
8	0.24	28	1.04	8	0.1100
9	0.28	29	1.08	9	0.1300
10	0.32	30	1.12	10	0.1500
11	0.36	31	1.16	11	0.1700
12	0.40	32	1.20	12	0.1900
13	0.44	33	1.24	13	0.2200
14	0.48	34	1.28	14	0.2600
15	0.52	35	1.31	15	0.3000
16	0.56	36	1.33	16	0.3500
17	0.60	37	1.346	17	0.4100
18	0.64			18	0.4800
19	0.68			19	0.5600
20	0.72			20	0.6500
				21	0.7500
				22	0.8000

FIGURE 6-17 : GRID USED TO PREDICT EXPERIMENTAL WAVES these cells infinitely compressible. The wall separating the column from the remainder of the tank and the baffles in Runs No. 8 and 13 were simulated by zeroing the appropriate normal velocities and accounting for the wall friction via the source terms for the velocities parallel to the wall.

The "measured data", defined in Chapter 4, for the wave amplitude, wave-crest location and liquid height in the column are compared with the predictions in Figures 6-18 through 6-21. The computed wave profiles and velocity vectors are shown for Runs No. 4, 11, 8 and 13 in Figures 6-22, 6-23, 6-24 and 6-25 respectively. Finally, the predicted wave forces exerted on the end wall of the tank are presented in Figure 6-26.

Discussion

Overall, the predictions of wave amplitude, wave-crest location and liquid height in the column agree with the experimental results (Figures 6-18 through 6-21). The decrease of liquid height in the column is predicted very well for all four runs. The computed wave amplitude during the impact of the wave on the end wall is too small, especially for Runs No. 11 and 13. This results because the grid near the end of the tank is not fine enough to "see" the thin sheet of water which runs up the end wall. Because the wave in Run No. 4 is smaller, it does not form a thin sheet of water up the end wall of the tank; and hence, the wave amplitude is

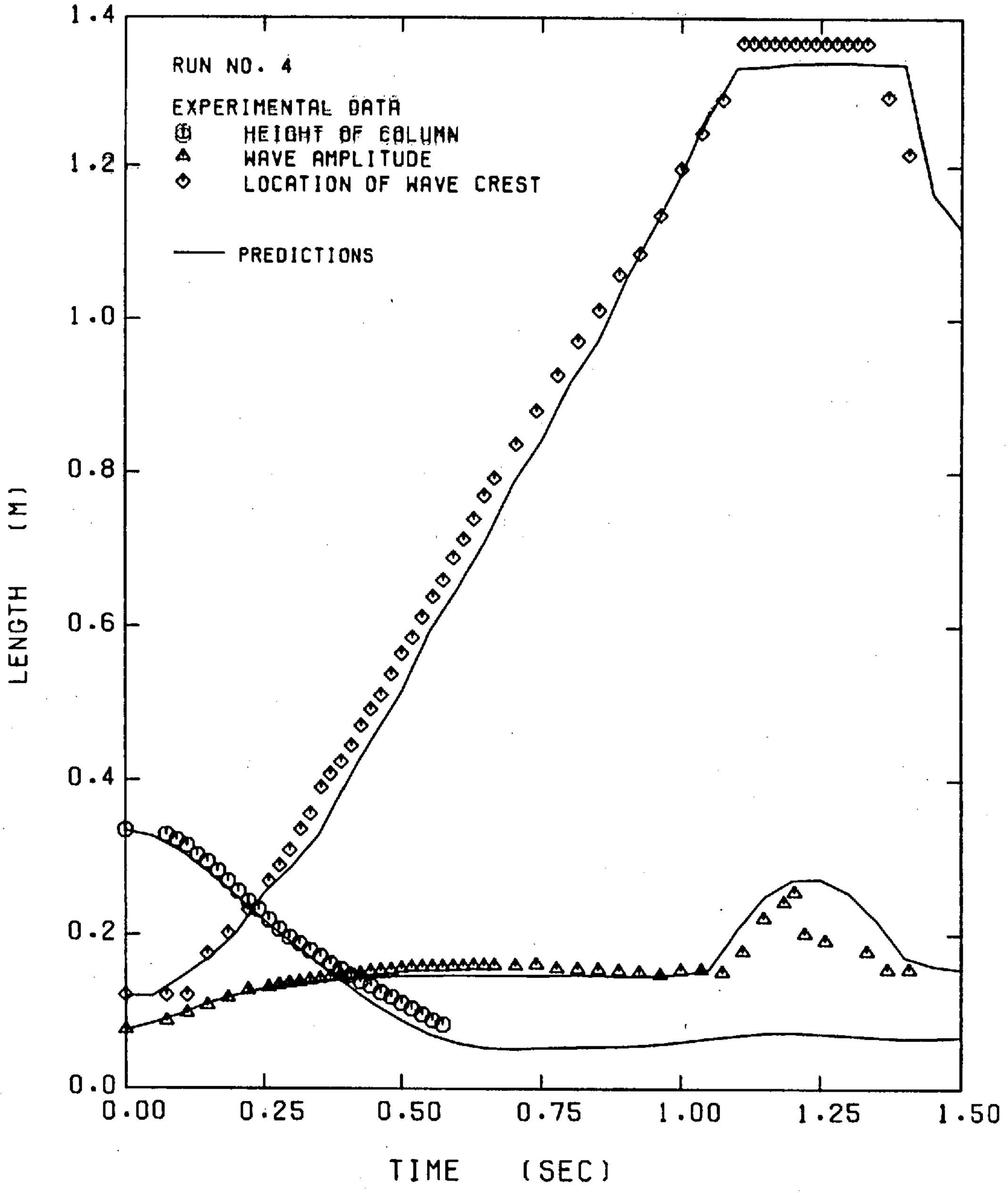

FIGURE 6-18 : MEASURED DATA FOR RUN NO. 4 VERSUS PREDICTIONS

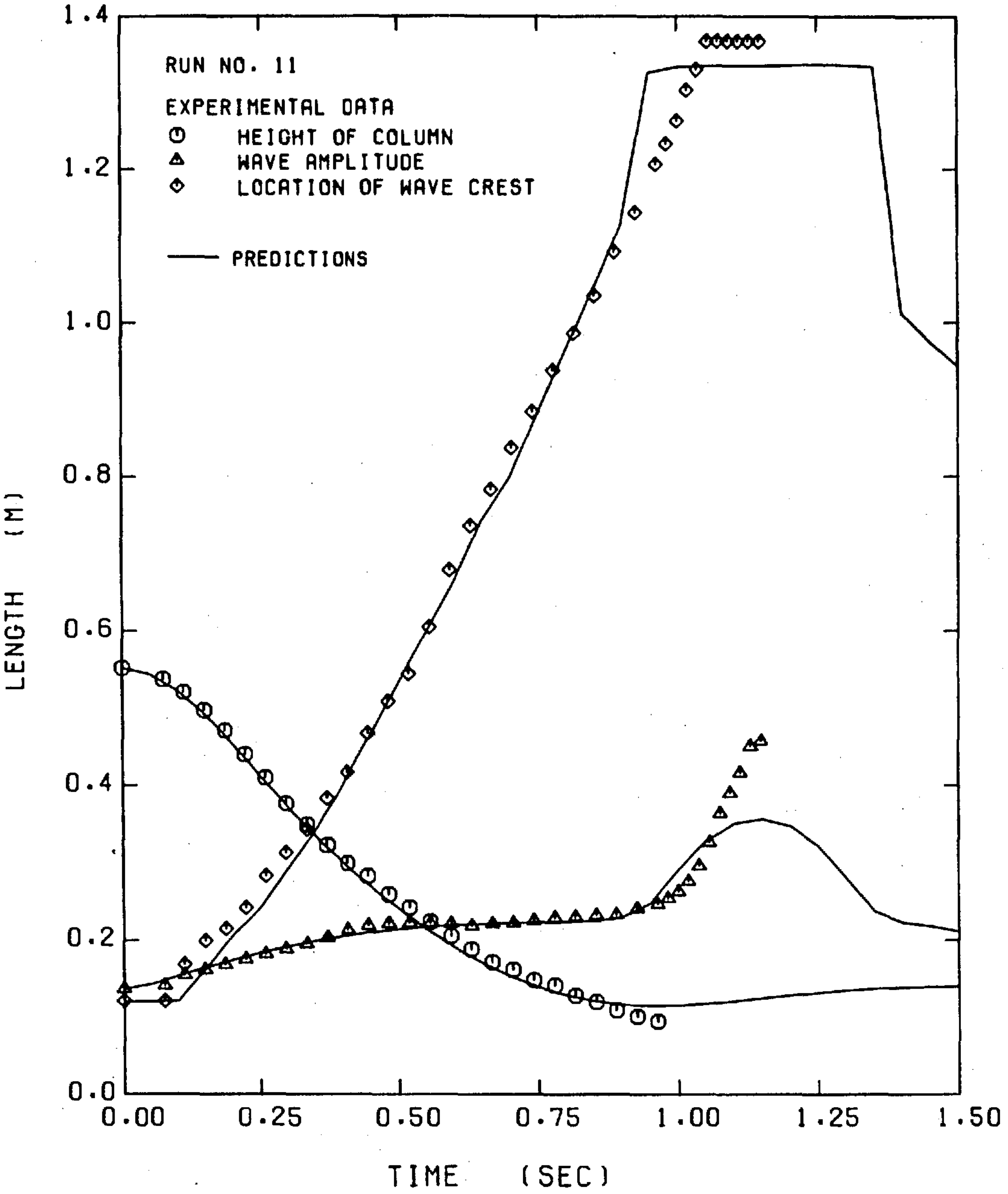

FIGURE 6-19 : MEASURED DATA FOR RUN NO. 11 VERSUS PREDICTIONS

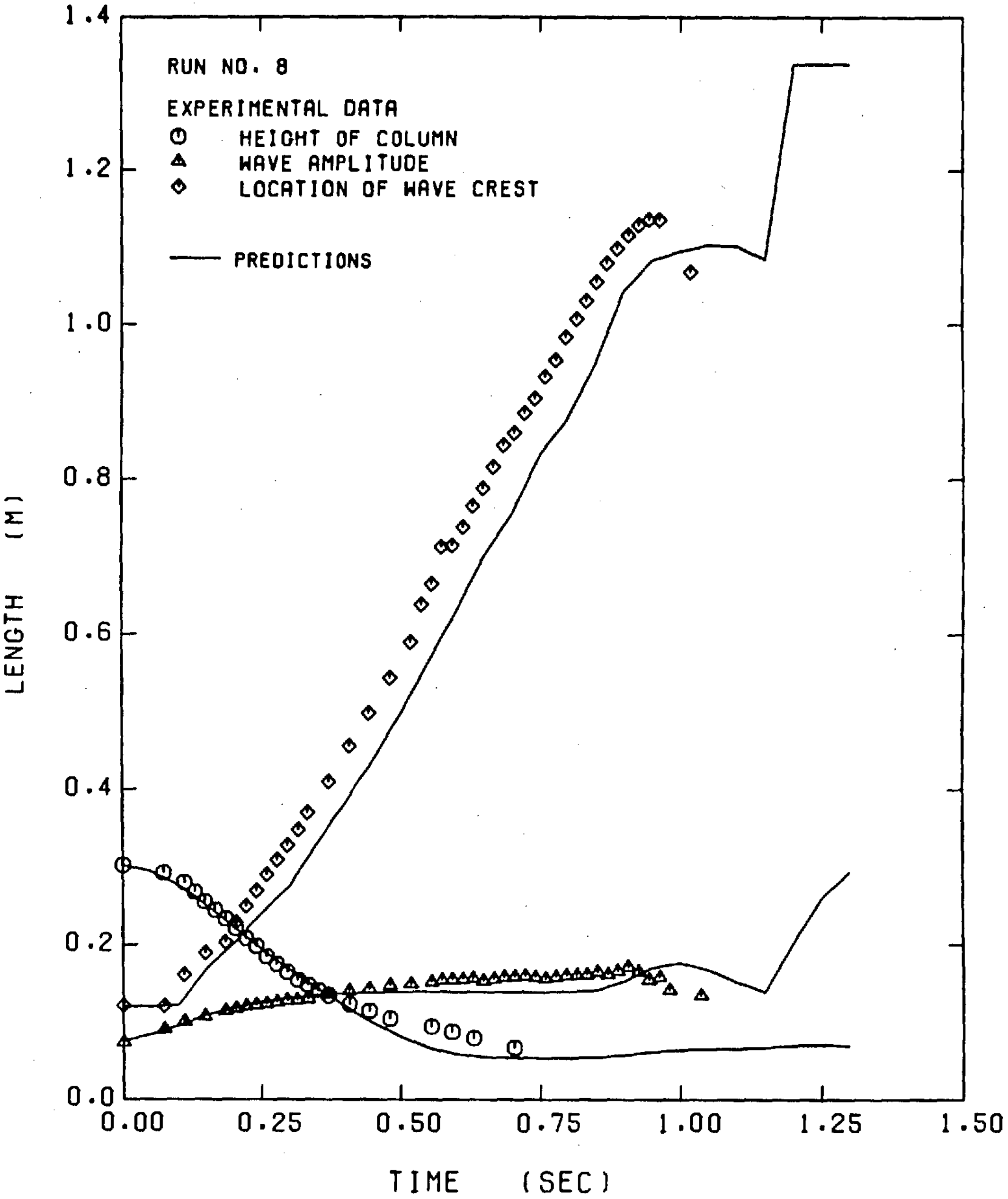

FIGURE 6-20 : MEASURED DATA FOR RUN NO. 8 VERSUS PREDICTIONS

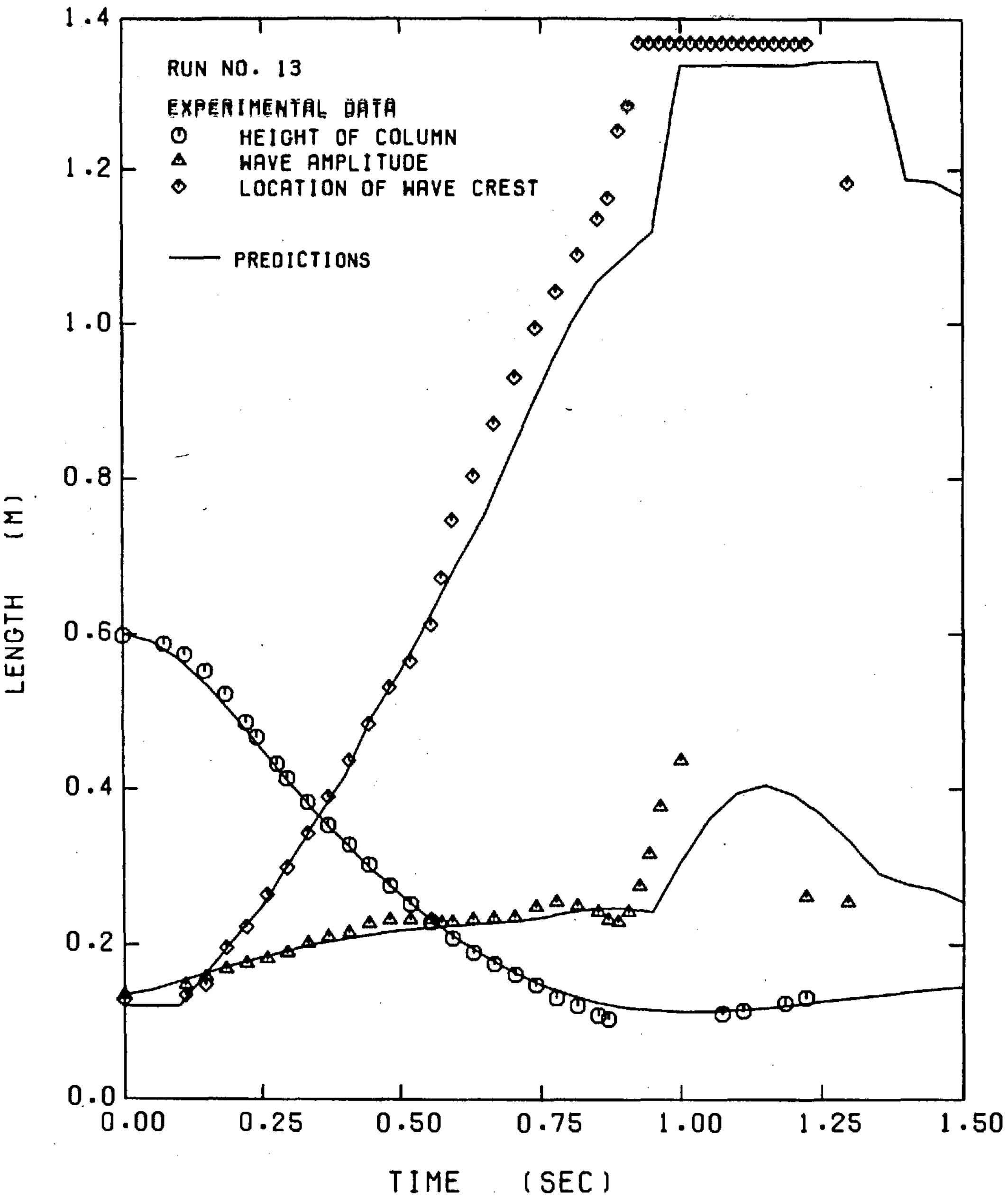

FIGURE 6-21 : MEASURED DATA FOR RUN NO. 13 VERSUS PREDICTIONS

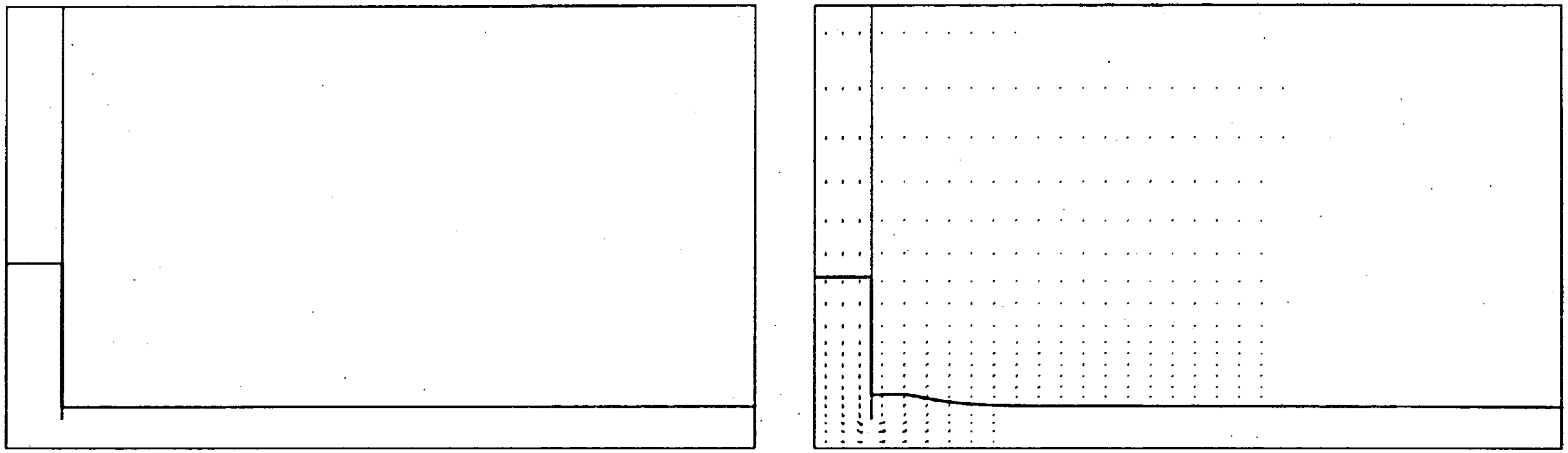

TIME = 0.00 SEC

TIME = 0.10 SEC

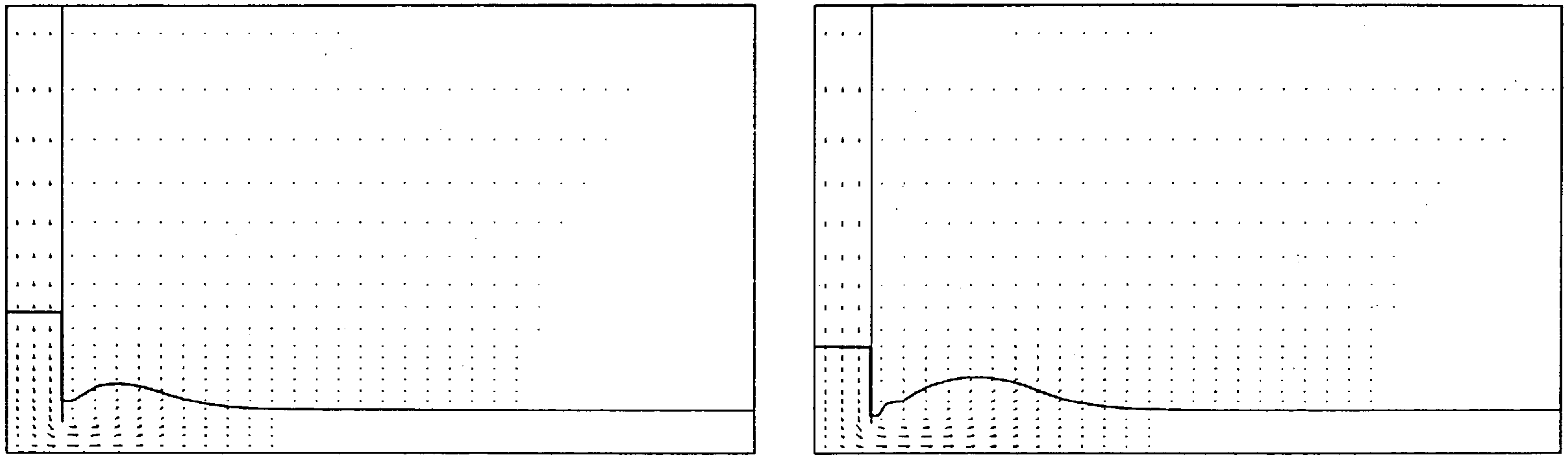

TIME = 0.20 SEC

TIME = 0.30 SEC

FIGURE 6-22 : PREDICTED WAVE PROFILES AND VELOCITY VECTORS FOR RUN NO. 4

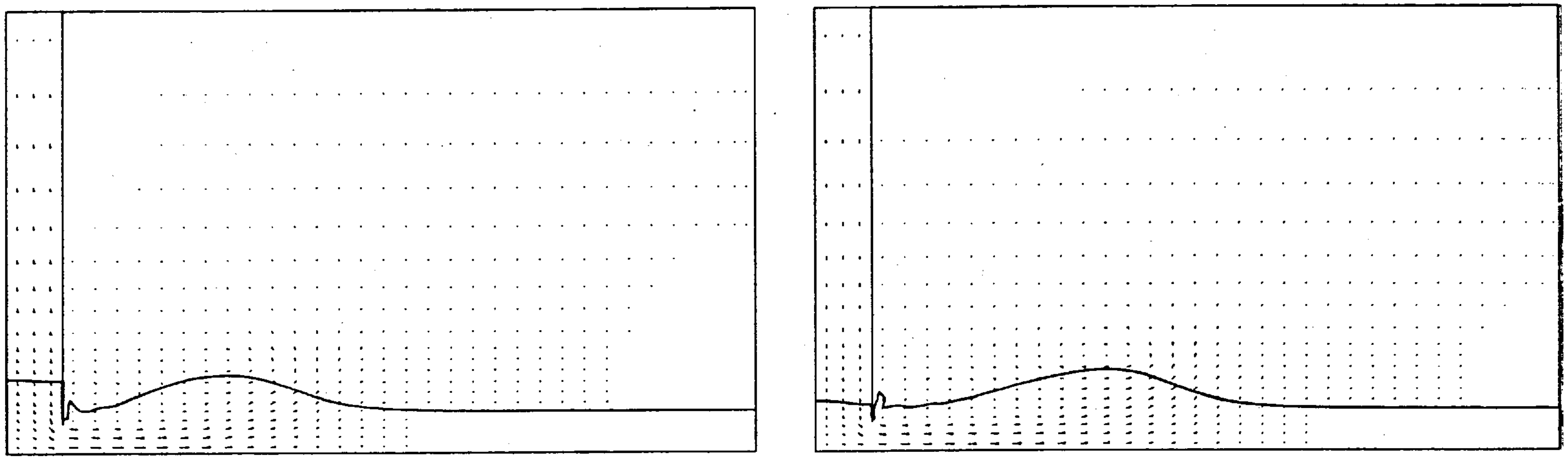

TIME = 0.40 SEC

TIME = 0.50 SEC

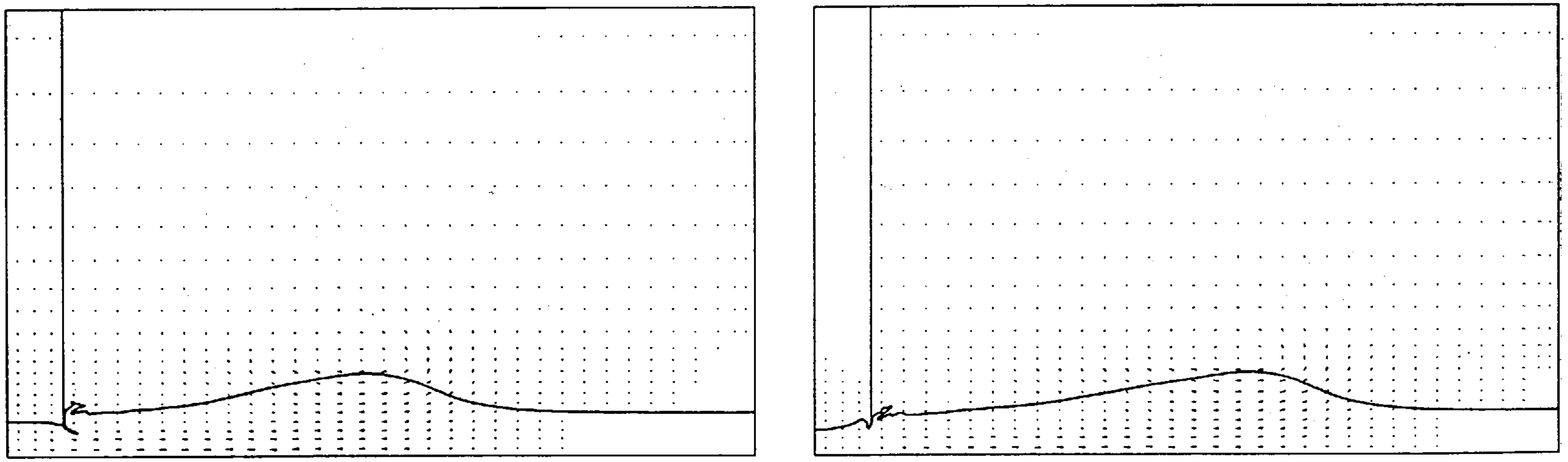

TIME = 0.60 SEC

TIME = 0.70 SEC

FIGURE 6-22 : (CONTINUED)

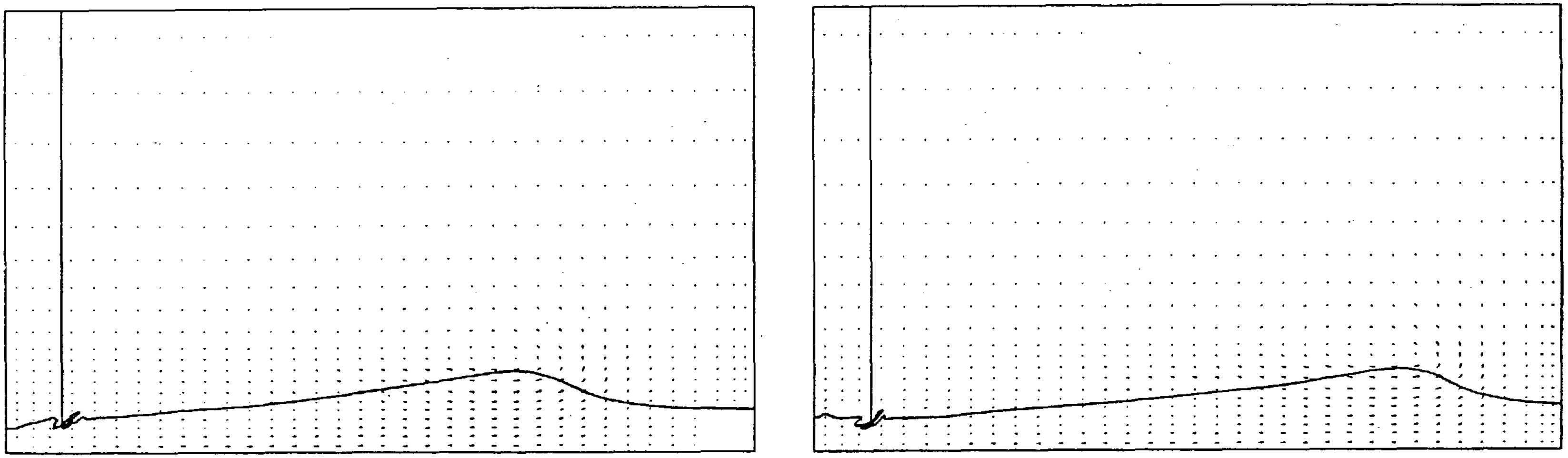

TIME = 0.80 SEC

TIME = 0.90 SEC

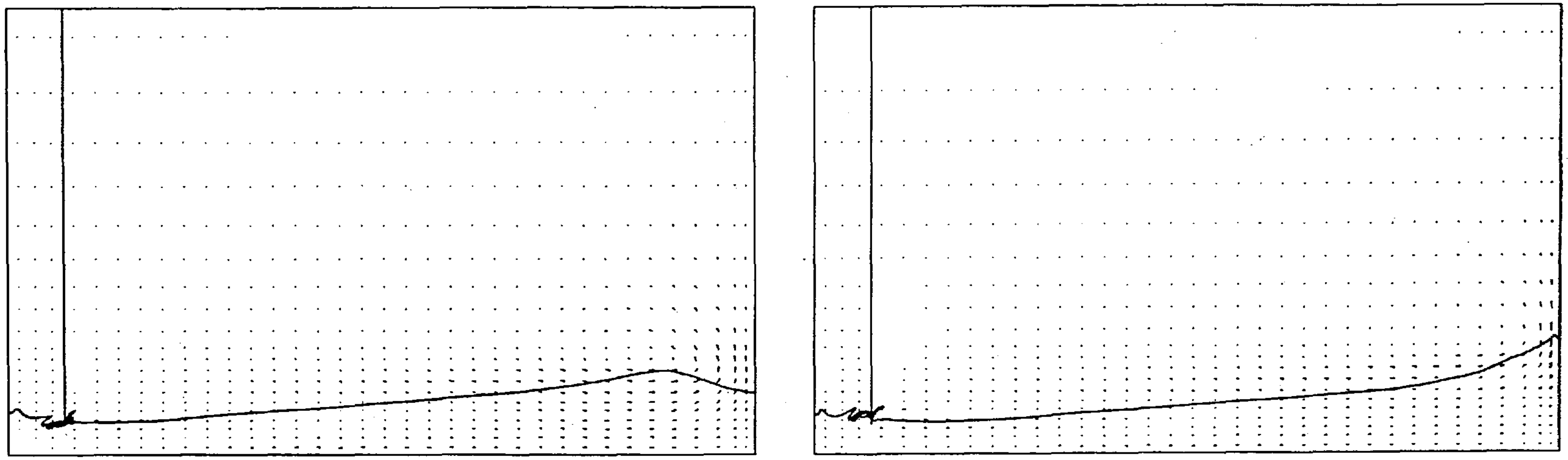

TIME = 1.00 SEC

TIME = 1.10 SEC

FIGURE 6-22 : (CONTINUED)

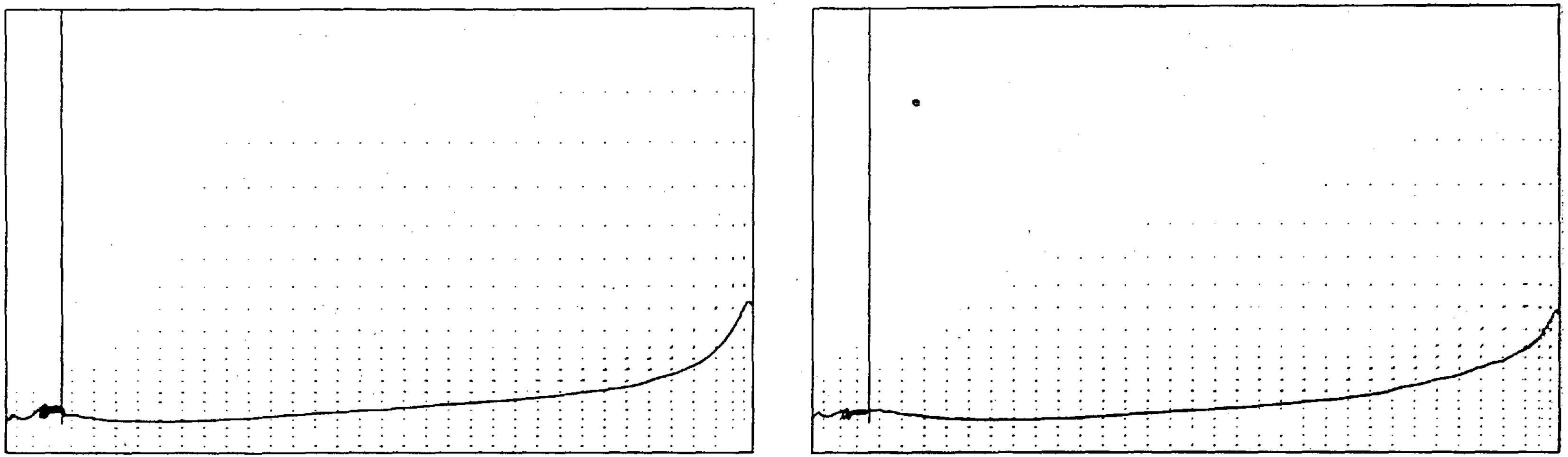

TIME = 1.20 SEC

TIME = 1.30 SEC

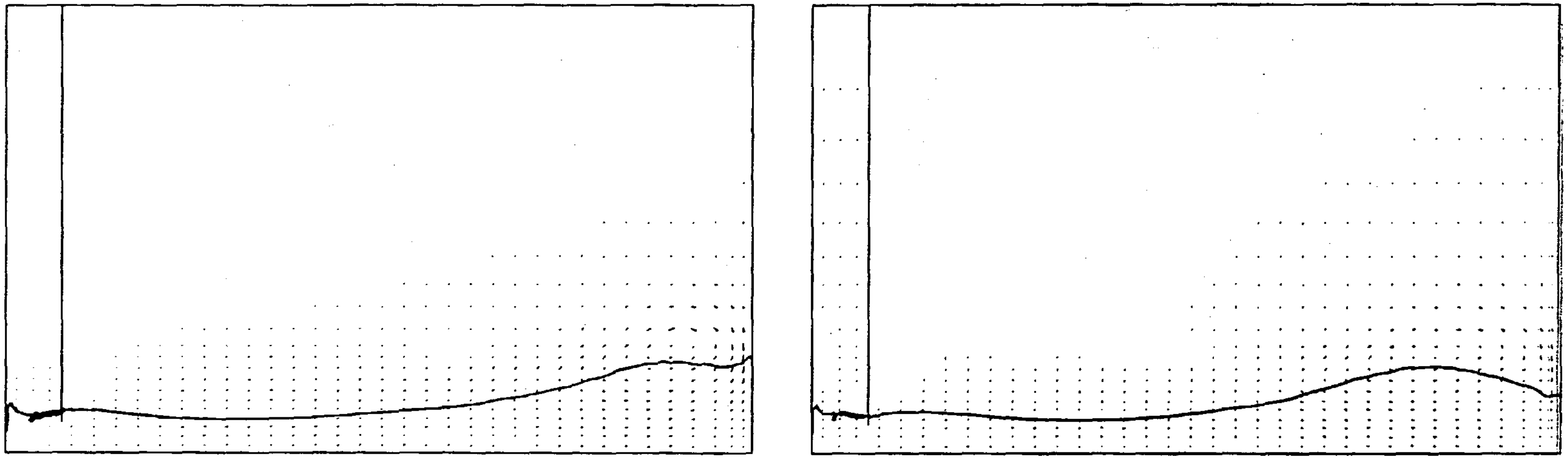

TIME = 1.40 SEC

TIME = 1.50 SEC

FIGURE 6-22 : (CONTINUED)

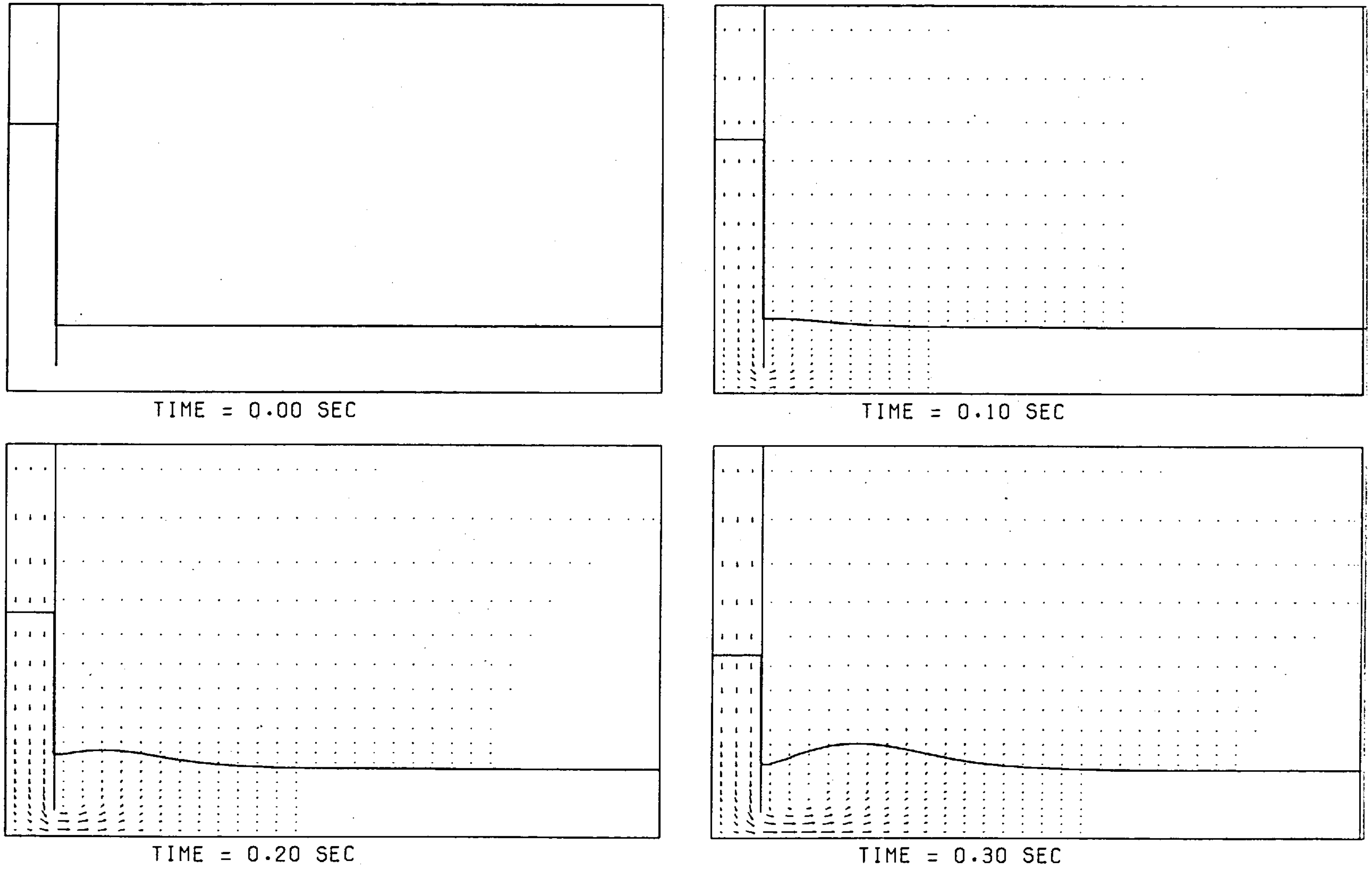
TIME = 0.00 SEC

TIME = 0.10 SEC

TIME = 0.20 SEC

TIME = 0.30 SEC

FIGURE 6-23 : PREDICTED WAVE PROFILES AND VELOCITY VECTORS FOR RUN NO. 11

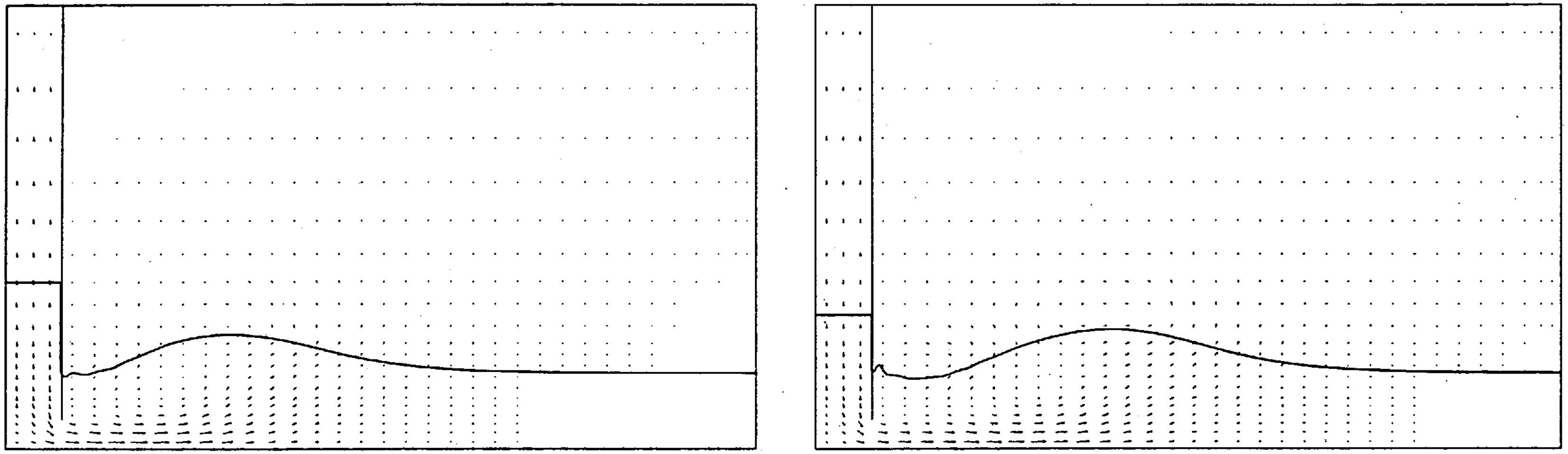

TIME = 0.40 SEC

TIME = 0.50 SEC

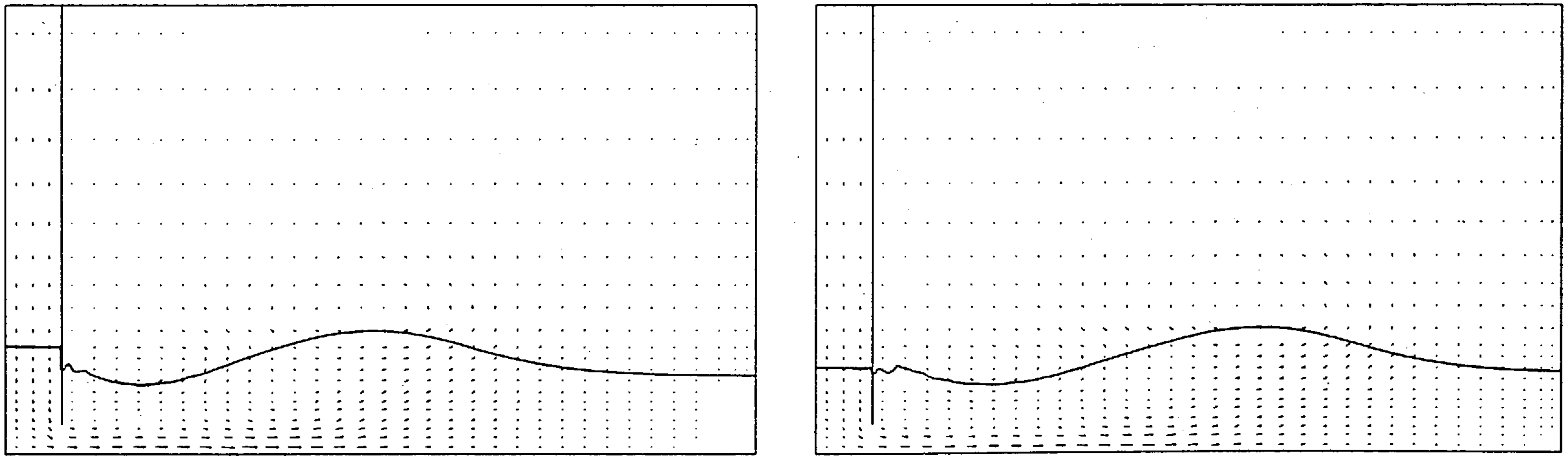

TIME = 0.60 SEC

TIME = 0.70 SEC

FIGURE 6-23 : (CONTINUED)

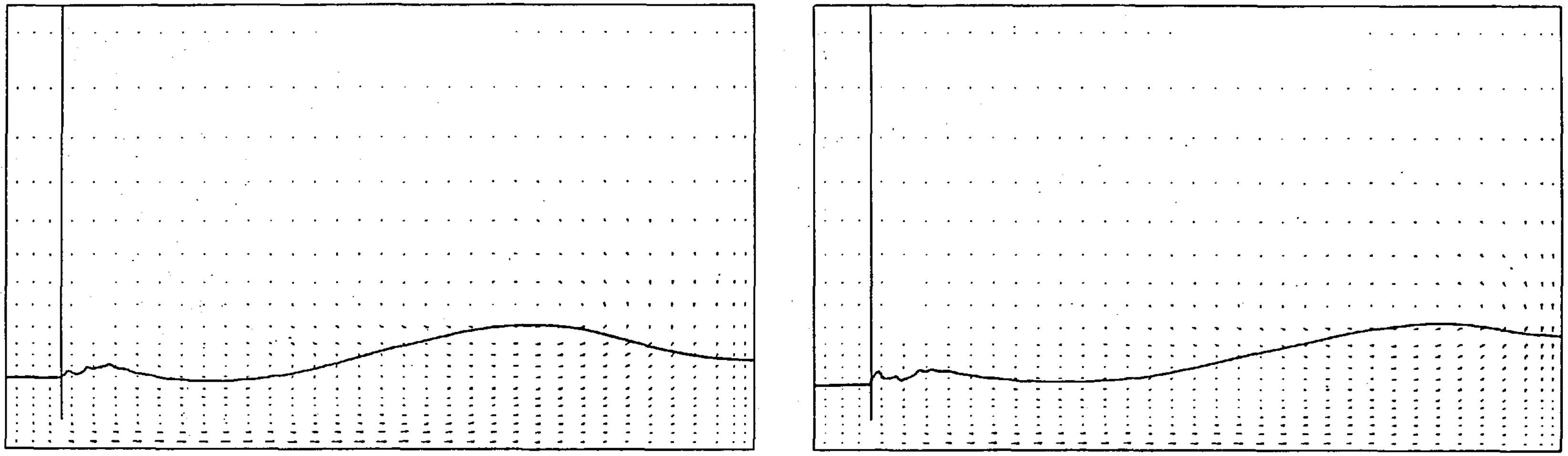

TIME = 0.80 SEC

TIME = 0.90 SEC

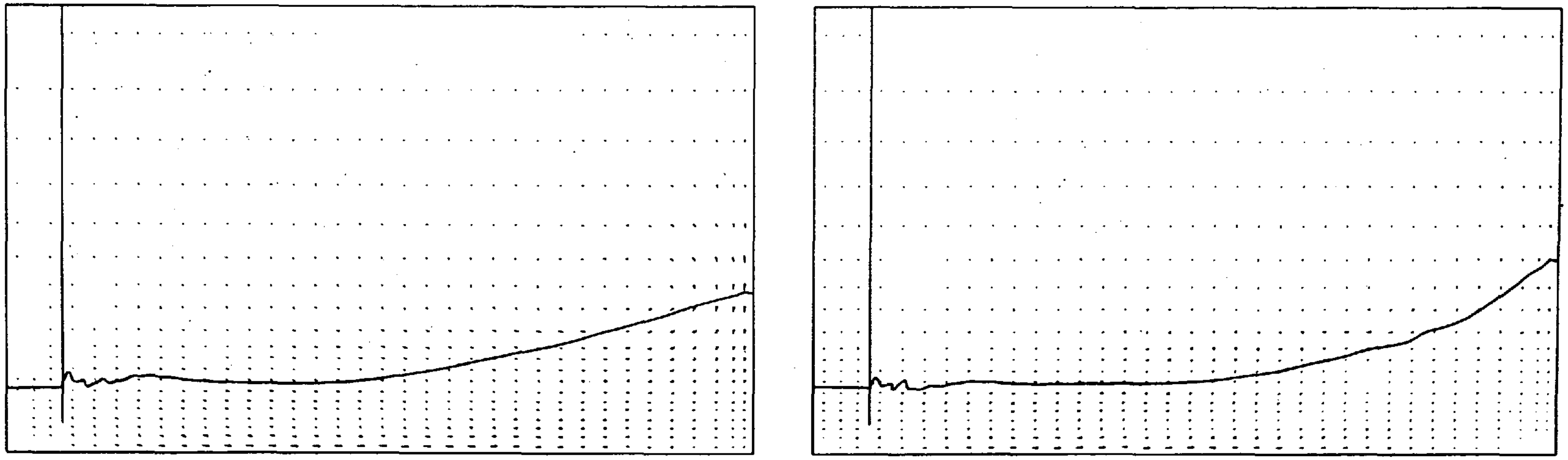

TIME = 1.00 SEC

TIME = 1.10 SEC

FIGURE 6-23 : (CONTINED)

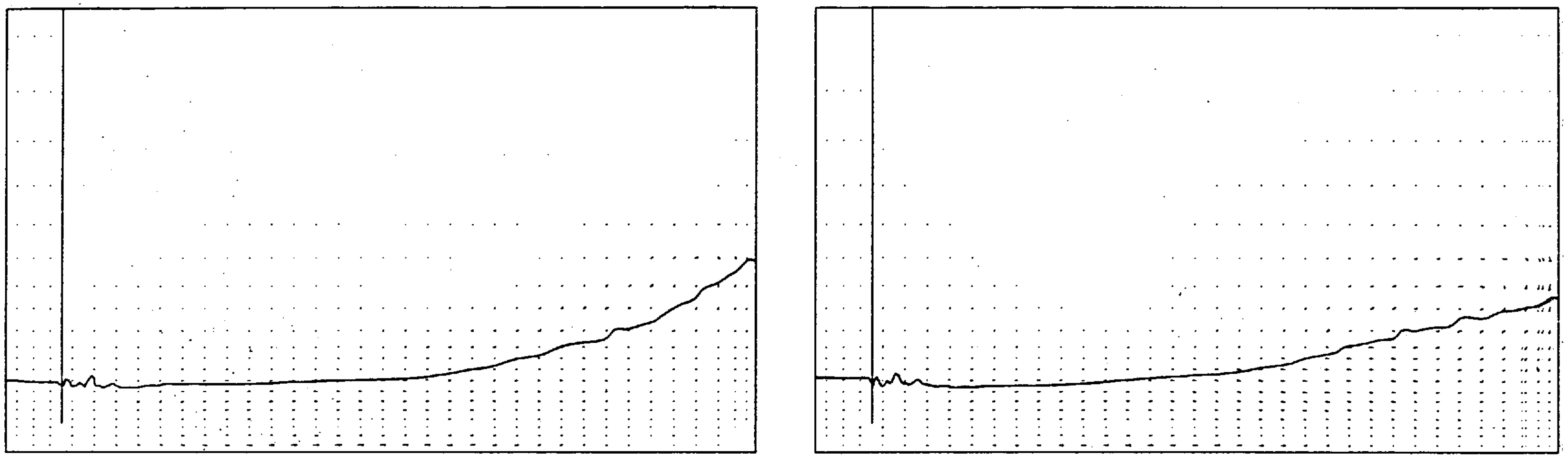

TIME = 1.20 SEC

TIME = 1.30 SEC

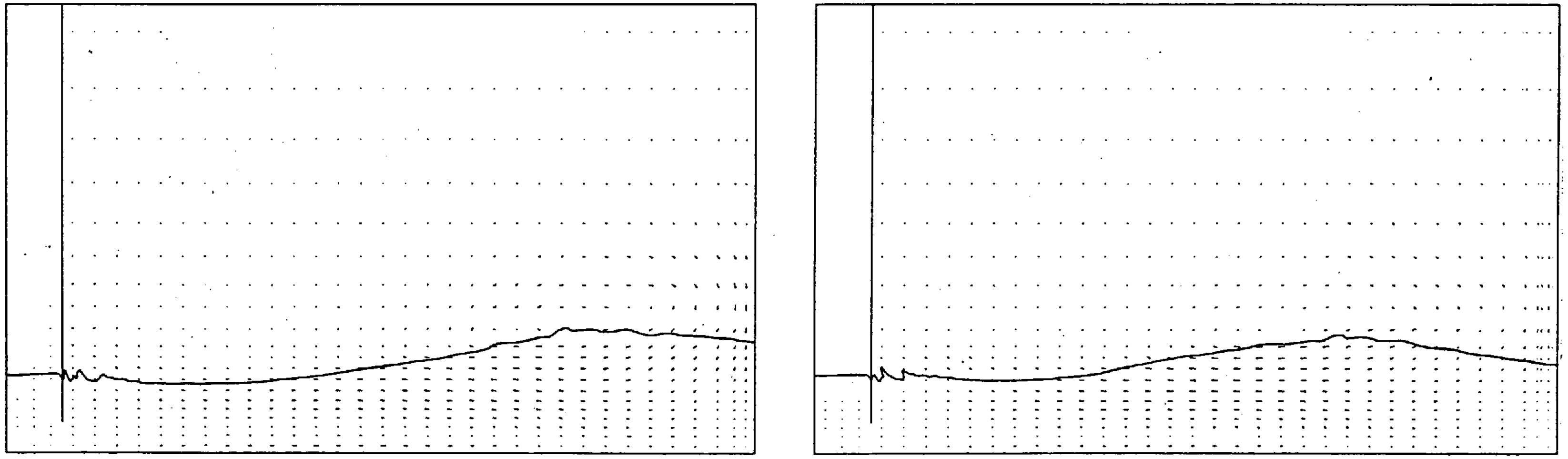

TIME = 1.40 SEC

TIME = 1.50 SEC

FIGURE 6-23 : (CONTINUED)

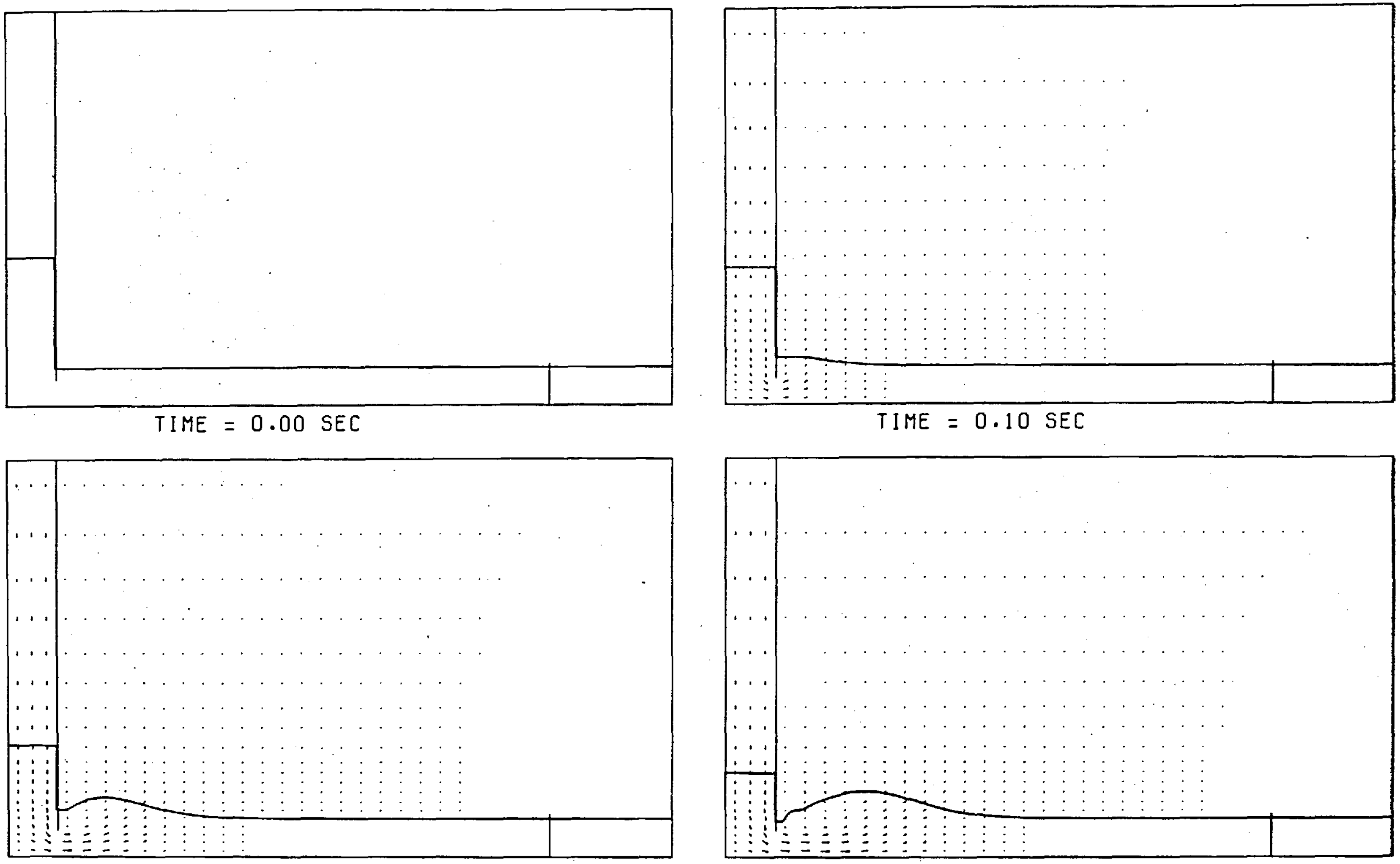

TIME = 0.00 SEC

TIME = 0.10 SEC

TIME = 0.20 SEC

TIME = 0.30 SEC

FIGURE 6-24 : PREDICTED WAVE PROFILES AND VELOCITY VECTORS FOR RUN NO. 8

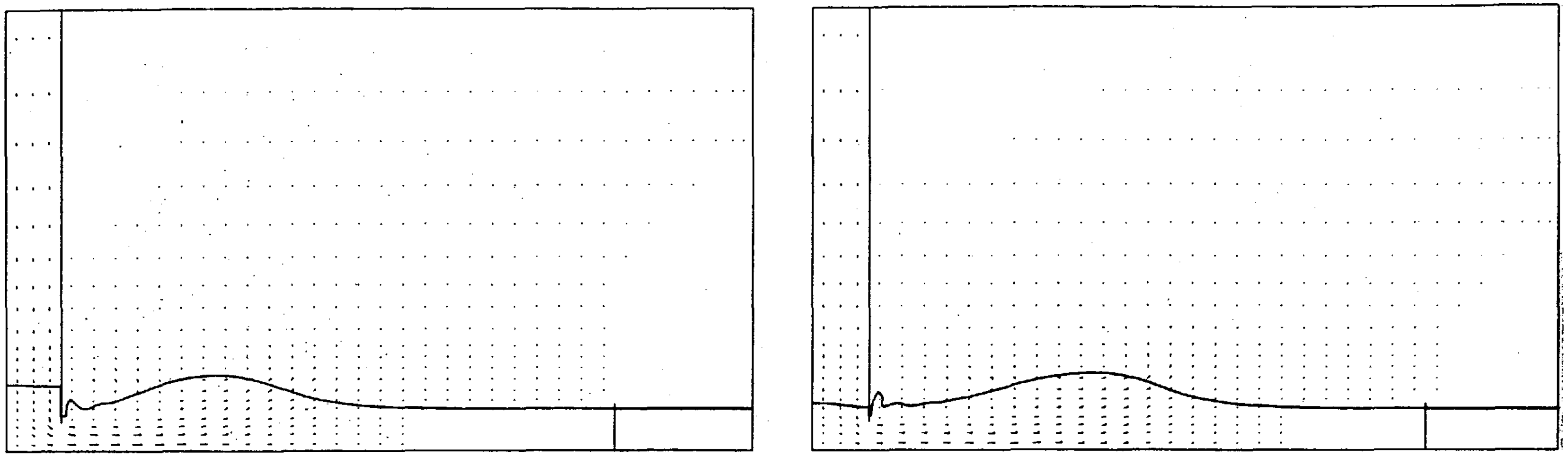

TIME = 0.40 SEC

TIME = 0.50 SEC

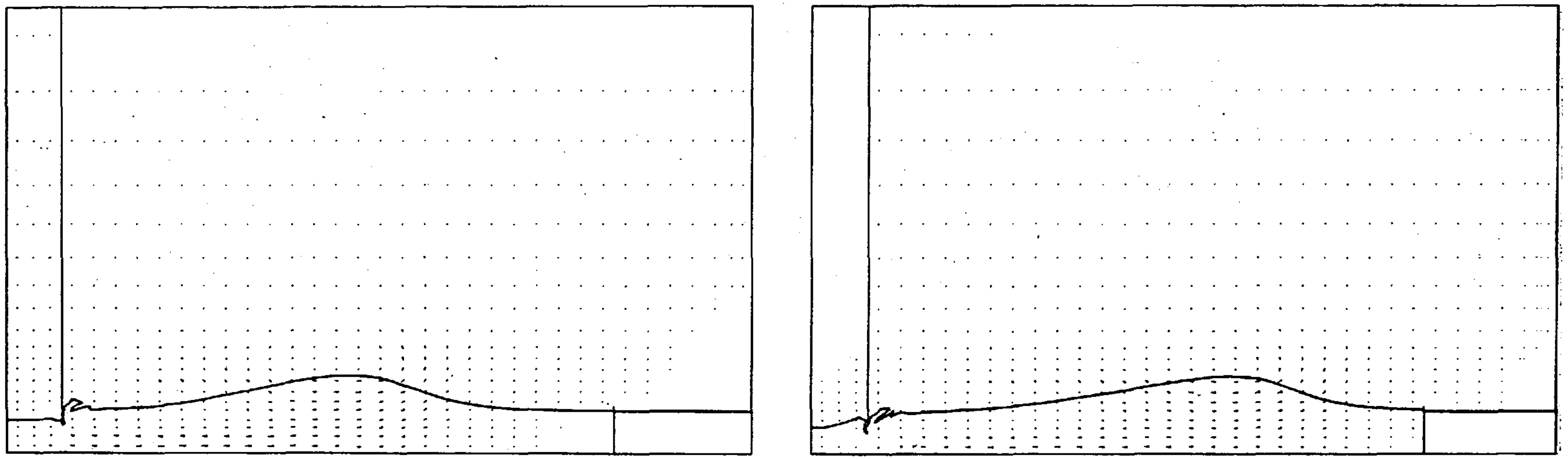

TIME = 0.60 SEC

TIME = 0.70 SEC

FIGURE 6-24 : (CONTINUED)

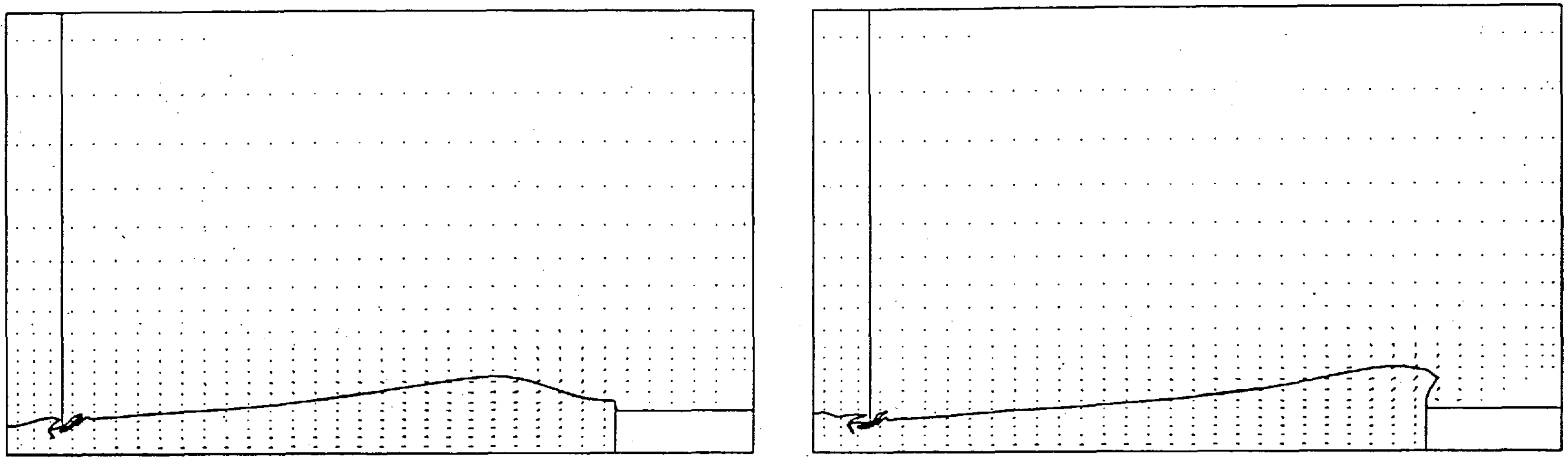

TIME = 0.80 SEC

TIME = 0.90 SEC

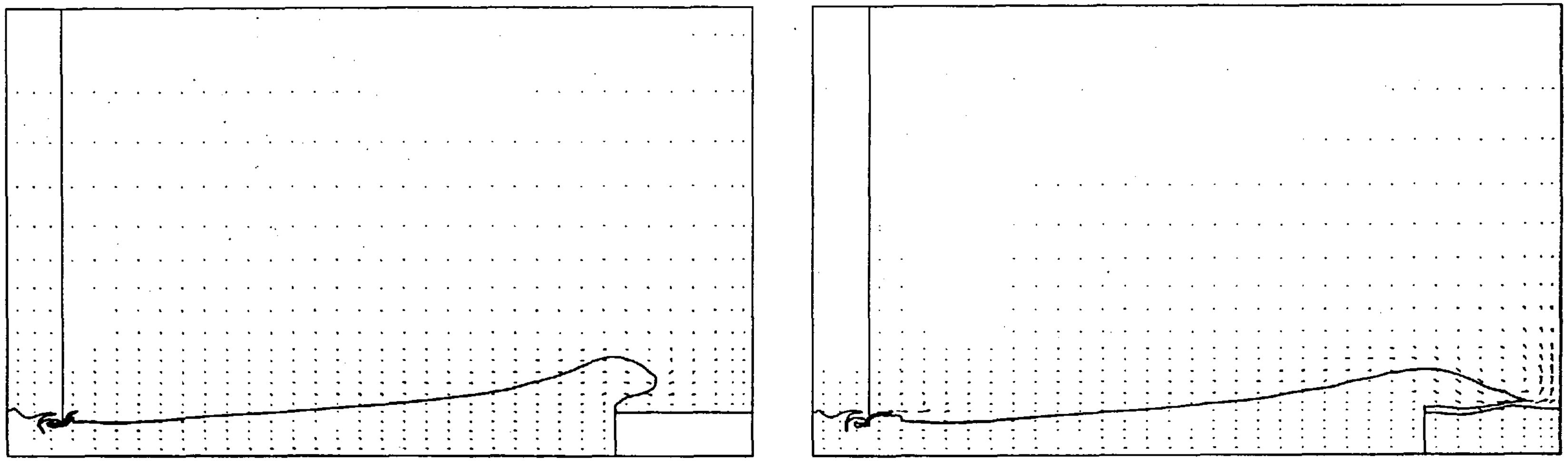

TIME = 1.00 SEC

TIME = 1.10 SEC

FIGURE 6-24 : (CONTINUED)

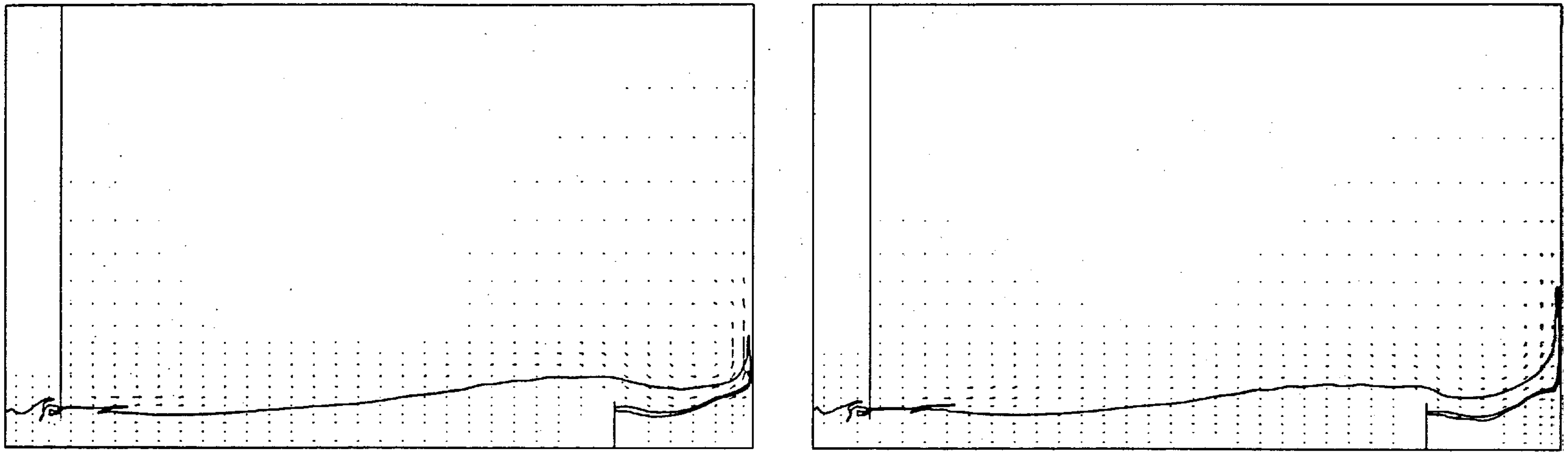

TIME = 1.20 SEC

TIME = 1.30 SEC

FIGURE 6-24 : (CONTINUED)

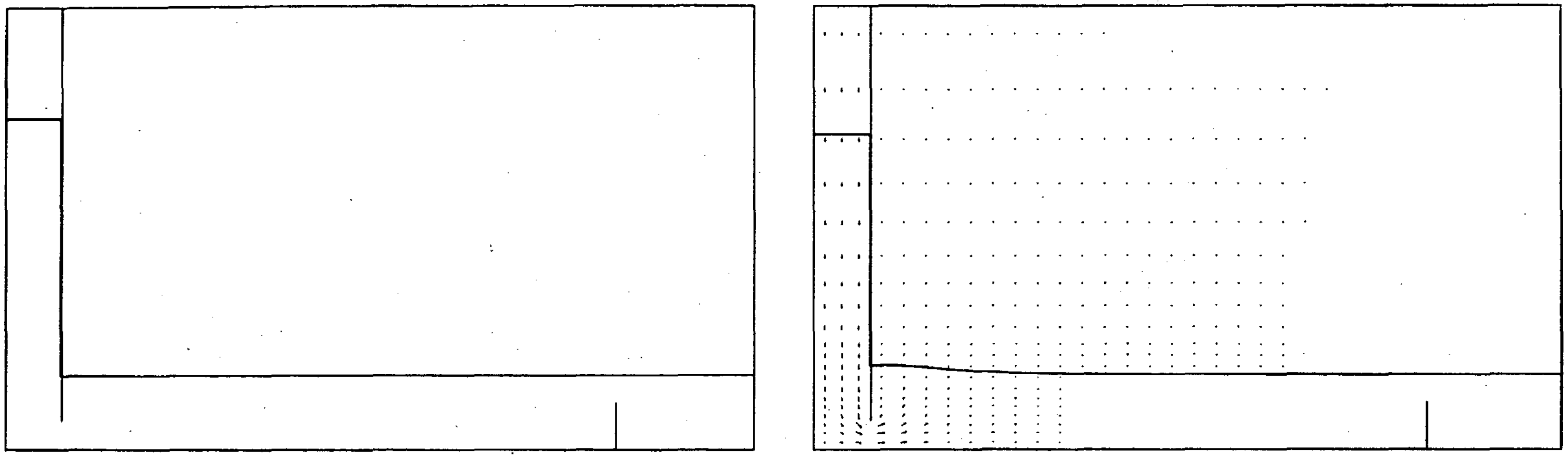

TIME = 0.00 SEC

TIME = 0.10 SEC

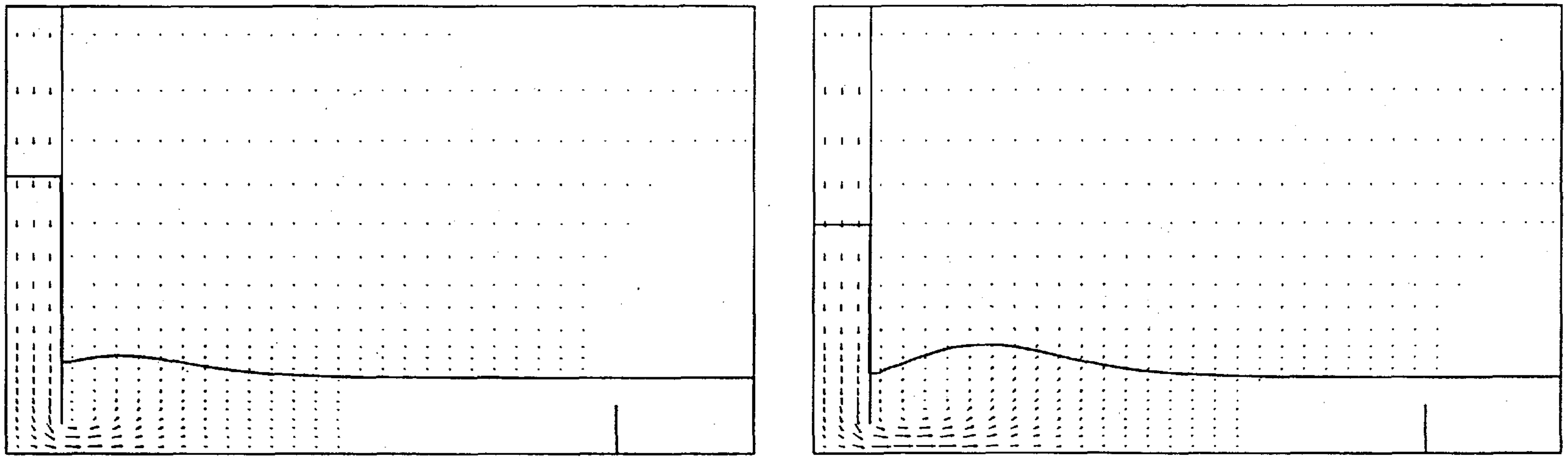

TIME = 0.20 SEC

TIME = 0.30 SEC

FIGURE 6-25 : PREDICTED WAVE PROFILES AND VELOCITY VECTORS FOR RUN NO. 13

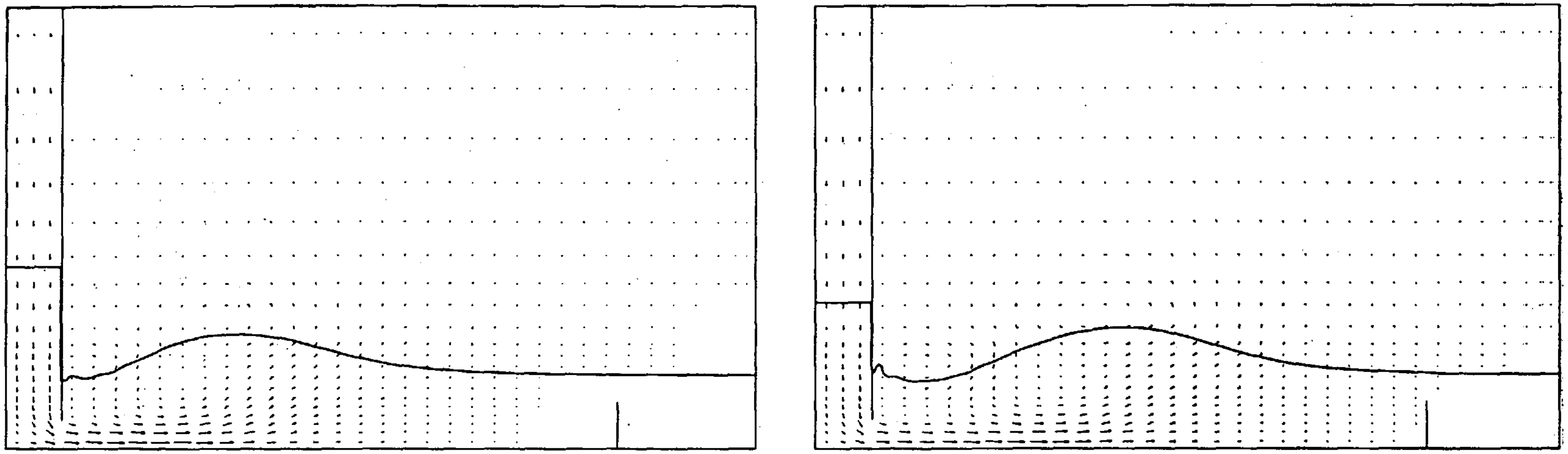

TIME = 0.40 SEC

TIME = 0.50 SEC

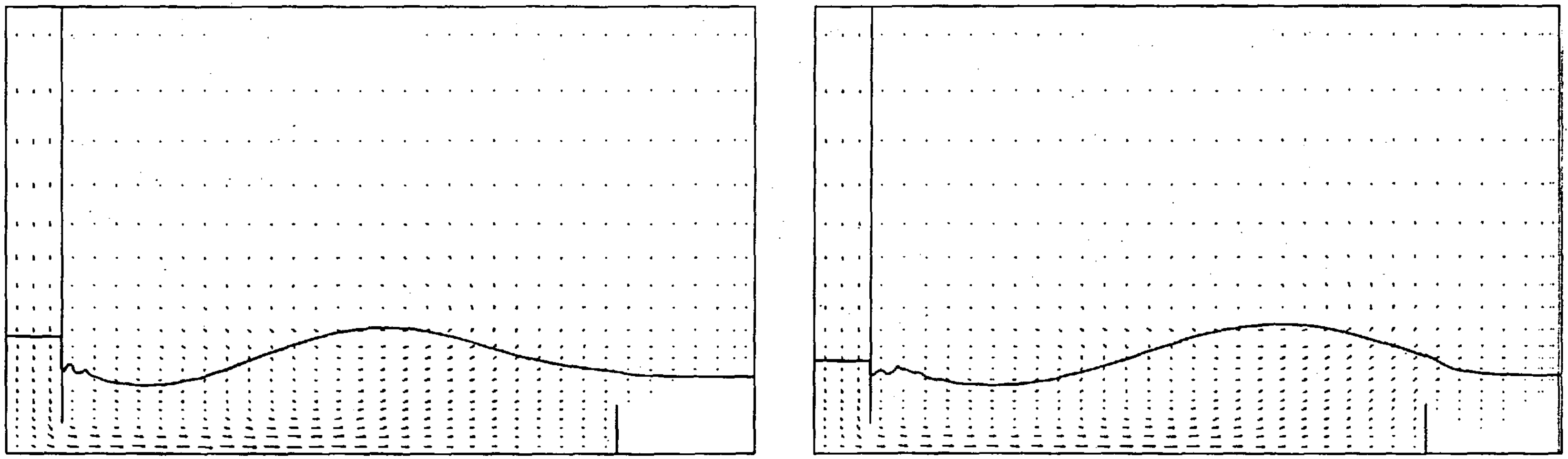

TIME = 0.60 SEC

TIME = 0.70 SEC

FIGURE 6-25 : (CONTINUED)

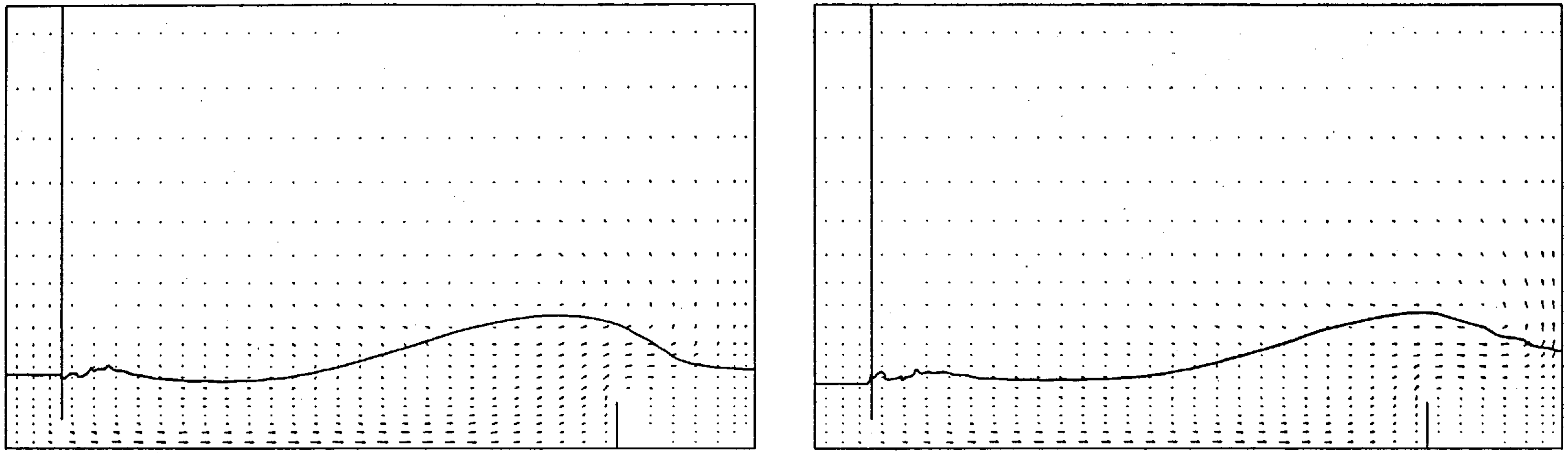

TIME = 0.80 SEC

TIME = 0.90 SEC

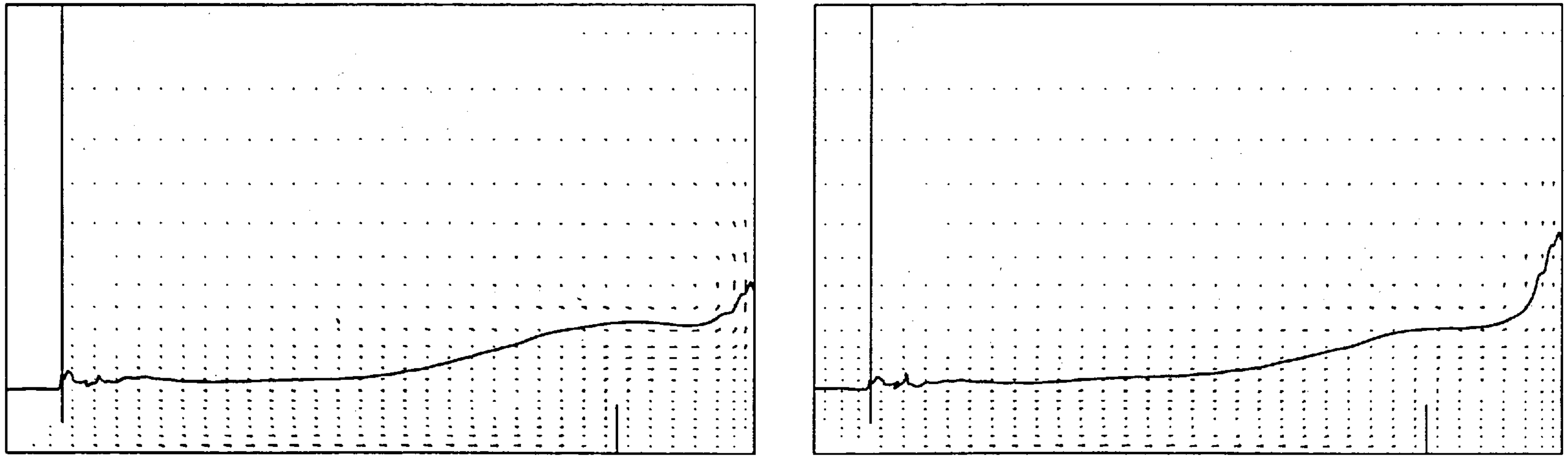

TIME = 1.00 SEC

TIME = 1.10 SEC

FIGURE 6-25 : (CONTINUED)

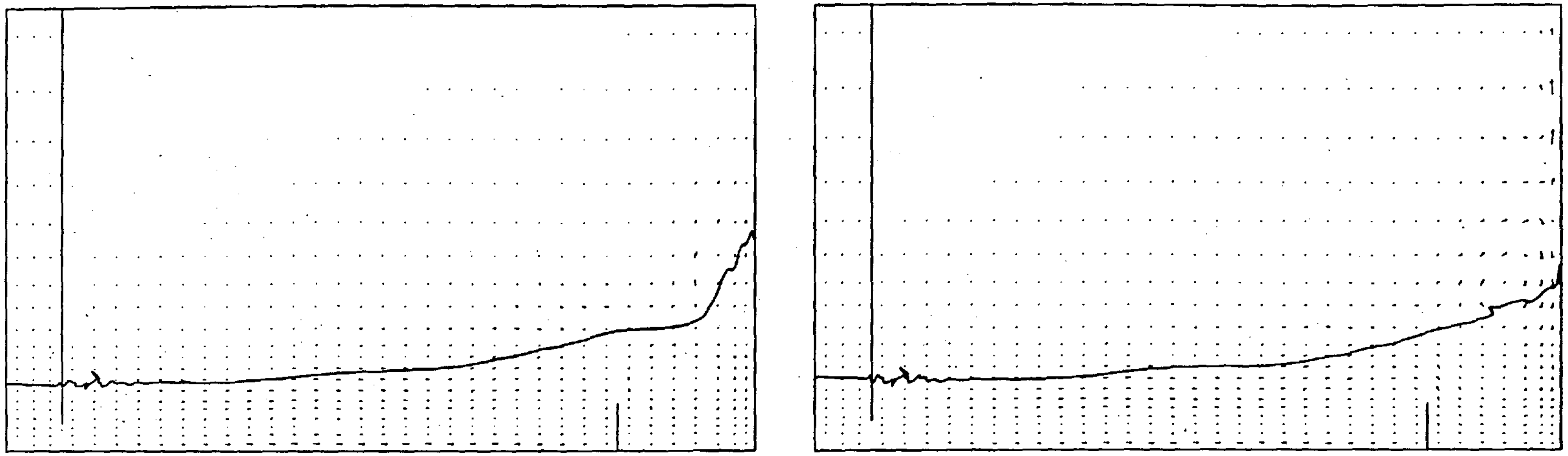

TIME = 1.20 SEC

TIME = 1.30 SEC

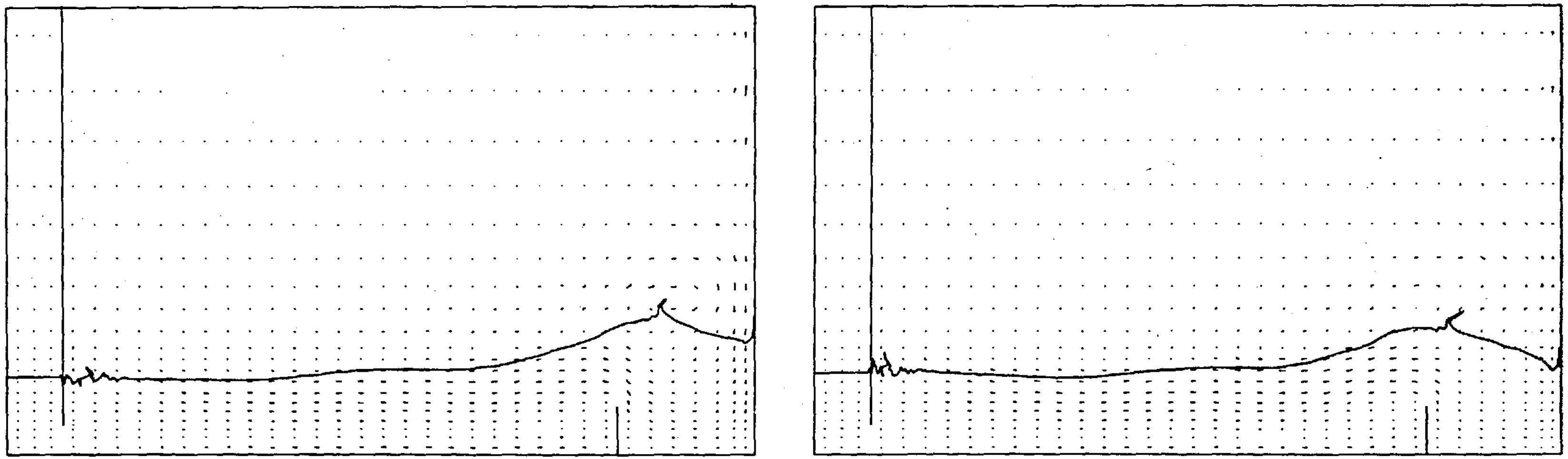

TIME = 1.40 SEC

TIME = 1.50 SEC

FIGURE 6-25 : (CONTINUED)

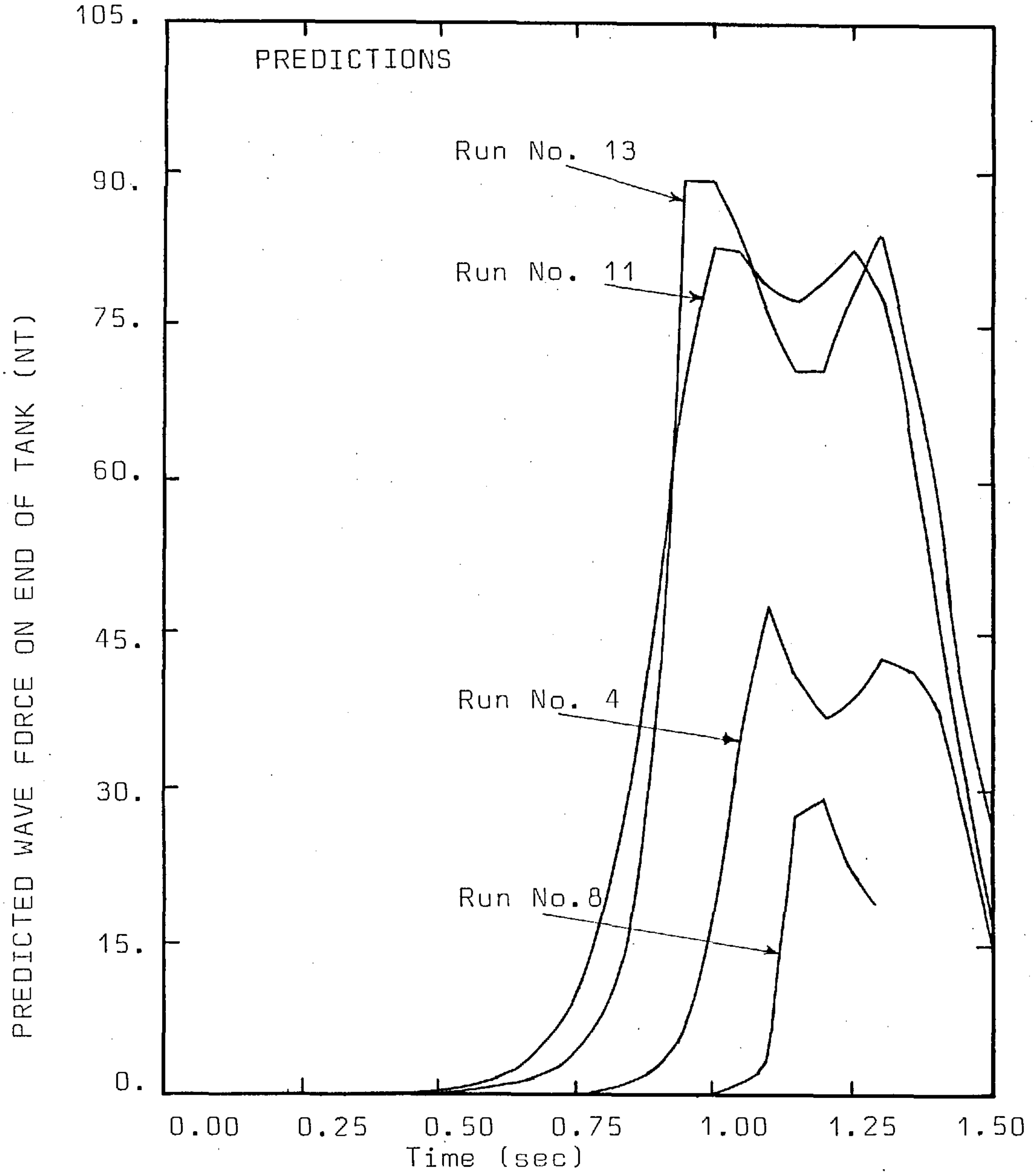

FIGURE 6-26 : PREDICTED WAVE FORCES ON THE END WALL OF THE TANK predicted more accurately. The increase of amplitude caused by the waves moving over the baffle can clearly be seen in the predictions of Runs No. 8 and 13. The proper movement of the wave crests indicates that the wave speeds are predicted correctly. The time scale of the predicted results, particularly for Runs No. 8 and 13, differs somewhat from that of the experimental results. This is due to the difficulty of defining zero time for the experimental results and to the inconsistency in the film speed of the ciné camera. It should also be noted that obtaining the data from the ciné film, especially for the motion near the end wall, was quite tedious; hence, the experimental results are subject to at least 5 per cent error.

The predicted wave shapes (Figures 6-22 through 6-25) exhibit the same basic characteristics as do the photographs of the experimental waves (Figures 4-4, 4-6, 4-8 and 4-10). However, there are some significant discrepancies. Consider first Run No. 4 (Figures 4-4 and 6-22). During the first quarter of a second, the predicted wave shapes match the data quite well; however, after a time of 0.3 second the computed wave appears to have a smoother surface than the real wave. As time progresses, the real wave develops a steep front, a flat top and a sharp dip in the trailing edge and breaks forward slightly as it moves across the tank. The predicted wave maintains a more rounded shape and does not break. The predicted and experimental results show better agreement as the waves approach and impact the end of the tank. The frames TIME = 1.111 (Figure 4-6) and TIME = 1.10 (Figure 6-22) agree very well. Also, the run-up which occurs during the following three frames is predicted correctly. Similar observations can be made for Run No. 11 (Figures 4-6 and 6-23). However, because the initial water levels in both the tank and the column are higher than for Run No. 4, a larger wave is formed and the impact on the end wall of the tank produces a thin "tongue" of water which runs up the end wall. This tongue or sheet of water is not predicted correctly because the grid spacing near the end of the tank is too coarse. In Run No. 8 (Figures 4-8 and 6-24) there is a baffle located at slot G in Figure 4-1. The baffle extends slightly above the initial water level in the tank. Since the initial water levels in Run No. 8 are approximately the same as for Run No. 4, the two waves are similar during the early stages. However, as the wave in Run No. 8 approaches the baffle, the amplitude increases. This increase in amplitude is predicted and can be seen in Figure 6-24 and Figure 6-20. Finally, both the real wave and the simulated wave leap over the baffle and plunge into the quiescent water behind. Run No. 13 (Figures 4-10 and 6-25) also has a baffle; however, the initial water depth in the tank is sufficient to cover the baffle. As with the other runs, the predictions for Run No. 13 are smoothed and rounded in comparison to the real wave. Run No. 13 produces the thin tongue of water on impact with the end wall of the tank as does Run No. 11; thus the maximum wave amplitude is not predicted correctly. Qualitatively, agreement between the predicted wave shapes and the real wave shapes is quite good; however, some details of the wave shapes have been smoothed out in the predictions.

The smoother, more rounded shapes of the predicted waves are a result of neglecting turbulence phenomena. The flow of water issuing from the bottom of the column forms a turbulent wall jet along the bottom of the tank; however the mathematical model only accounts for <u>laminar</u> diffusion. This neglect of turbulence produces two errors. First, without the turbulent diffusion of momentum, the jet does not spread upward as rapidly as it should. Thus, not enough momentum is transferred to the <u>upper</u> part of the wave, and this portion of the wave cannot accelerate properly. Secondly, because the jet does not lose its momentum, it penetrates too far underneath the wave. This overpenetration of the jet acclerates the water in <u>front</u> of the wave and further distorts the wave shape. The bulk motion of the wave is determined primarily by the inertial and gravitational forces; but, the turbulence generated by the flow of liquid from the column does influence the shape of the wave.

Frequently, the main objective in studying wave motions is to determine the forces which are exerted on a structure by the wave. Some examples include the wave loading on bridges, oil platforms or sea walls. To demonstrate that this type of information is readily available from the computations, the predicted force exerted by the waves on the end wall of the tank was calculated and is presented in Figure 6-26. The forces are calculated by, first, multiplying the pressures stored along the end wall of the tank by the surface areas over which they act on the wall to obtain the local forces, and then summing these products to obtain the total force on the wall. The initial hydrostatic load is subtracted from the total force. Run No. 13 produces the largest force because it has the largest difference between initial water height in the column and water height in the tank. Run No. 11 produces almost as large a force as Run No. 13. Figure 6-26 shows clearly that the baffle in Run No. 13 causes a delay in the initiation of the load, but the force then increases more rapidly than that of Run No. 11. Run No. 4 produces a much smaller force than Runs No. 11 and 13. Also, the slower speed of the wave due to the lower water level in the tank delays the impact. Run No. 8 is affected by its baffle more than Run No. 13. All of the runs exhibit a double peak in the force versus time curve. The first peak is produced by the initial wave impact. After the initial impact, water is piled up against the end wall. When the vertical acceleration of this "piled-up" water diminishes, its mass produces an additional hydrostatic load and, thus, creates the second peak in the force curve.

6.5 SUMMARY

In this chapter computations have been compared with experimental results. These comparisons show that the numerical procedure can accurately simulate the physics of wave motions. For the collapsing columns and the solitary waves, both the bulk motions of the fluids and the free-surface shapes were predicted well. Predictions of the experimental waves presented in Chapter 4 were very good; however, it was noted that the turbulence present in the experimental flow was not modelled in the computations. This neglect of turbulence produced some discrepancies between the actual and predicted wave shapes.

CHAPTER 7

PREDICTIONS FOR OTHER FLOWS OF ENGINEERING INTEREST

7.1 INTRODUCTION

In the last two chapters predictions have been compared with analytical results and experimental data to test the credibility of the model and solution procedure. The predictions presented in this chapter demonstrate the flexibility of the model and solution procedure to handle various flows of interest. The problems to be discussed are listed in Table 7-1.

7.2 FILLING AND EMPTYING OF TANKS

Presentation

Tanks and containers frequently have to be filled with a liquid or emptied. In some instances it is necessary for these processes to be carried out in a low or zero gravity environment. Thus, several computations were made for a tank being filled and emptied. An axi-symmetric tank 0.6 meters high and 0.5 meters in diameter was considered. The initial water level in the tanks being drained was 0.47 meters, and the liquid was removed at a constant volumetric flow rate through a 0.1 meter diameter hole in the centre of the tank bottom. The tanks being filled, initially contained water to a depth of 0.22 meters. The computations were made on a 14   12 uniform grid. Time steps of 0.1 second for the emptying tanks and 0.005 second for

	DRAINING TANK WITH GRAVITY	DRAINING TANK NO GRAVITY	DRAINING TANK WITH GRAVITY AND BAFFLE	DRAINING TANK WITH BAFFLE BUT NO GRAVITY
Coordinate System	Cylindrical	Cylindrical	Cylindrical	Cylindrical
Grid	14 × 12	14 × 12	14 × 12	14 × 12
Type of Grid Spacing	Uniform	Uniform	Uniform	Uniform
Number of Particle Strings	1	1	1	1
Number of Particles at Start	33	33	33	33
Number of Particles at Finish	32	43	74	74
Maximum Time Sec	12.0	5.0	9.0	9.0
Time Step (Δt) Sec	0.05	0.1	0.1	0.1
Number of Time Steps	240	50	90	90
Number of Iterations per Time Step	8	10	10	12
Direction of Gravitational Acceleration	X	X	X	X
Density of Gas Kg/m^3	1.198	1.198	1.198	1.198
Density of Liquid Kg/m^3	1000.0	1000.0	1000.0	1000.0
Viscosity of Gas Nt Sec/m^2	1×10^{-5}	1×10^{-5}	1×10^{-5}	1×10^{-5}
Viscosity of Liquid Nt Sec/m^2	1×10^{-3}	1×10^{-3}	1×10^{-3}	1×10^{-3}
Computational Time CDC 6600 Sec	300	80	160	160

TABLE 7-1 : PERTINENT DATA FOR THE PREDICTIONS PRESENTED IN CHAPTER 7 (contd. overleaf)

	FILLING TANK WITH GRAVITY	FILLING TANK NO GRAVITY	SLOSHING TANK	RISING BUBBLE	HIGH PRESSURE BUBBLE
Coordinate System	Cylindrical	Cylindrical	Cartesian	Cylindrical	Cylindrical
Grid	14 × 12	14 × 12	14 × 14	22 × 17	22 × 17
Type of Grid Spacing	Uniform	Uniform	Uniform	Uniform	Uniform
Number of Particle Strings	1	1	1	2	2
Number of Particles at Start	33	33	65	98	229
Number of Particles at Finish	43	43	110	133	281
Maximum Time Sec	0.8	0.8	1.6	0.275	0.12
Time Step (Δt) Sec	0.005	0.005	0.001	0.025	0.001
Number of Time Steps	160	160	160	110	120
Number of Iterations per Time Step	8	8	8	6	10
Direction of Gravitional Acceleration	X	X	Y	X	X
Density of Gas Kg/m^3	1.198	1.198	1.198	1.198	1.198
Density of Liquid Kg/m^3	1000.0	1000.0	1000.0	1000.0	1000.0
Viscosity of Gas Nt Sec/m^2	1×10^{-5}	1×10^{-5}	1×10^{-5}	1×10^{-5}	1×10^{-5}
Viscosity of Liquid Nt Sec/m^2	1×10^{-3}	1×10^{-3}	1×10^{-3}	1×01^{-3}	1×10^{-3}
Computational Time CDC 6600 Sec	200	280	290	300	620

TABLE 7-1 : PERTINENT DATA FOR THE PREDICTIONS PRESENTED IN CHAPTER 7

the filling tanks were used. The calculations required approximately 1.5 CDC 6600 seconds per time step.

Six runs were made: (1) a draining tank with normal gravity, (2) a draining tank with zero gravity, (3) a draining tank with an internal baffle and normal gravity, (4) a draining tank with an internal baffle and zero gravity, (5) a filling tank with normal gravity and (6) a filling tank with zero gravity. The surface profiles and velocity vectors are shown in Figures 7-1 through 7-6.

Discussion

Figure 7-1 shows that the liquid drains from the tank in a reasonable manner. The gravitational force keeps the liquid surface flat until a time of about 9.0 seconds. At 9.0 seconds, near the centreline the free-surface begins to dip down and by 10.0 seconds a gas core has extended into the drain hole. Essentially all of the liquid is removed from the tank. In contrast, Figure 7-2 shows that the absence of gravity causes the central gas core to form very quickly. Indeed, after only 5.0 seconds the outflow from the tank is almost completely gas while a "pile" of liquid is left in the outer portion of the tank. This results because, without the influence of gravity, the liquid does not seek its lowest level.

The effect of an internal baffle on the flow of liquid from the tank is illustrated in Figures 7-3 and 7-4.

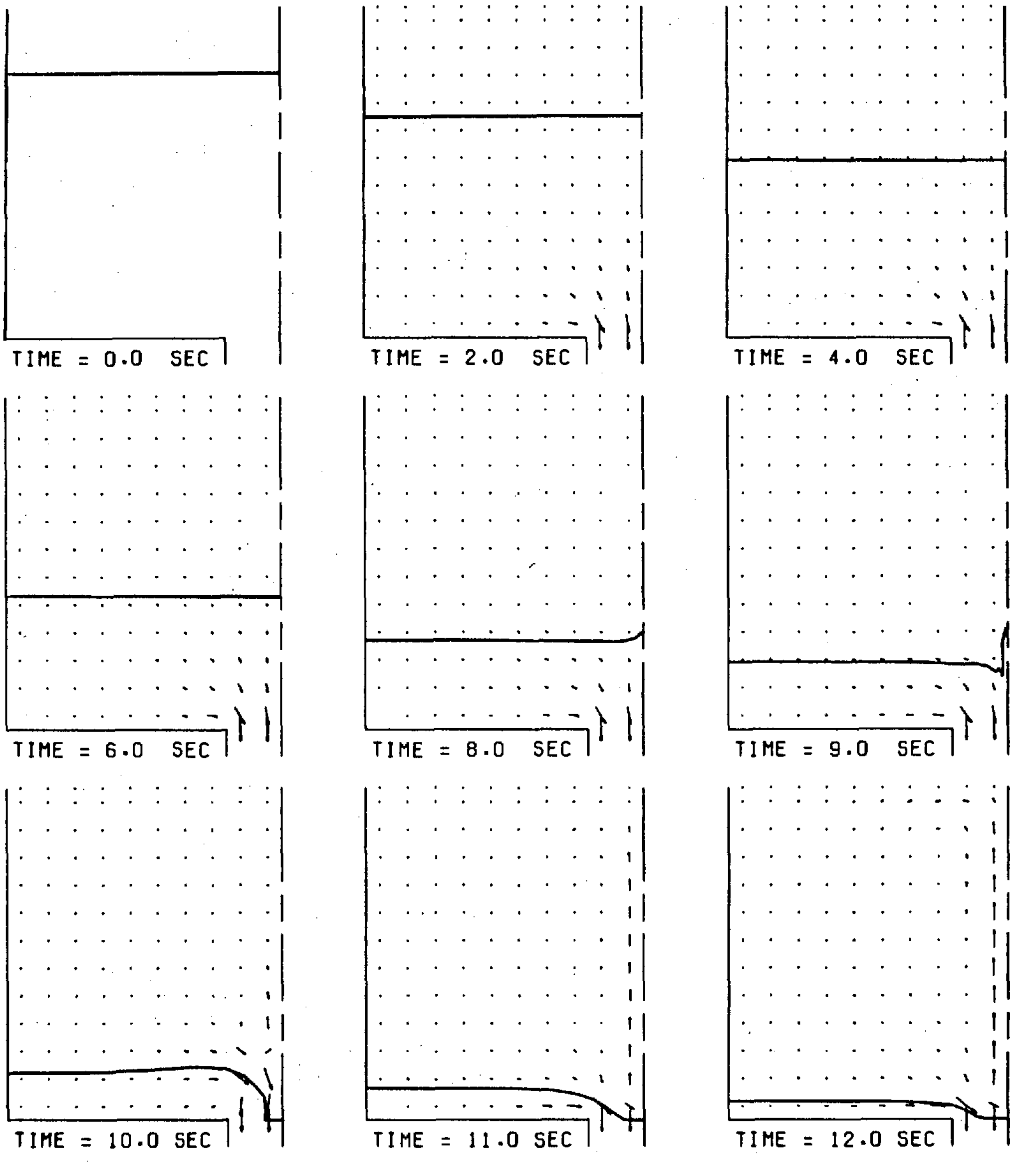

FIGURE 7-1 : DRAINING TANK IN NORMAL GRAVITY ENVIRONMENT

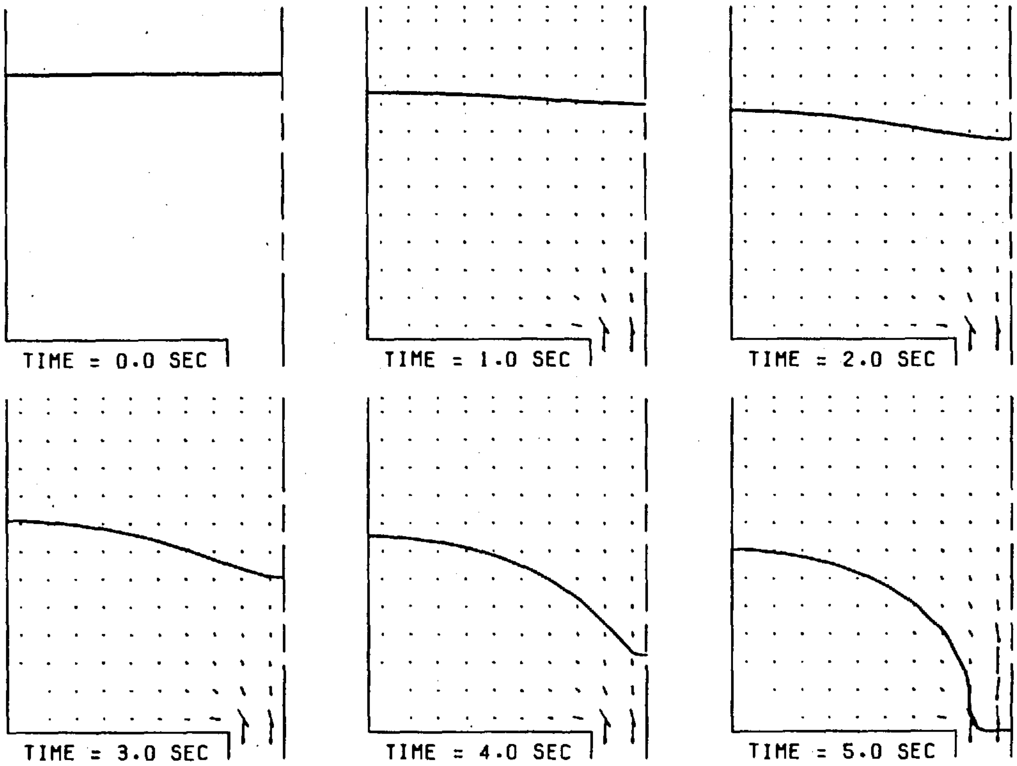

FIGURE 7-2 : DRAINING TANK IN ZERO GRAVITY ENVIRONMENT

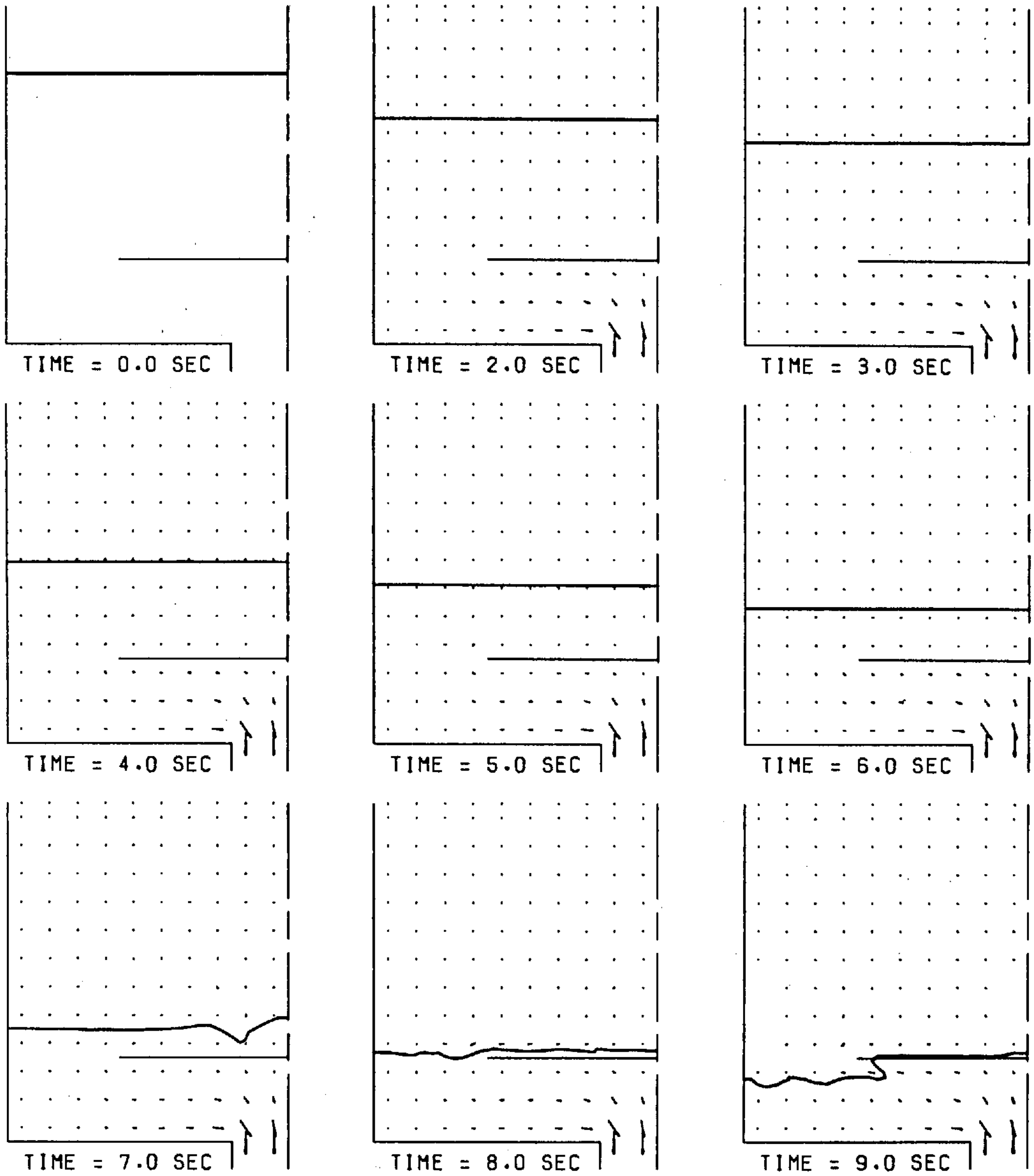

FIGURE 7-3 : DRAINING TANK WITH INTERNAL BAFFLE IN NORMAL GRAVITY ENVIRONMENT

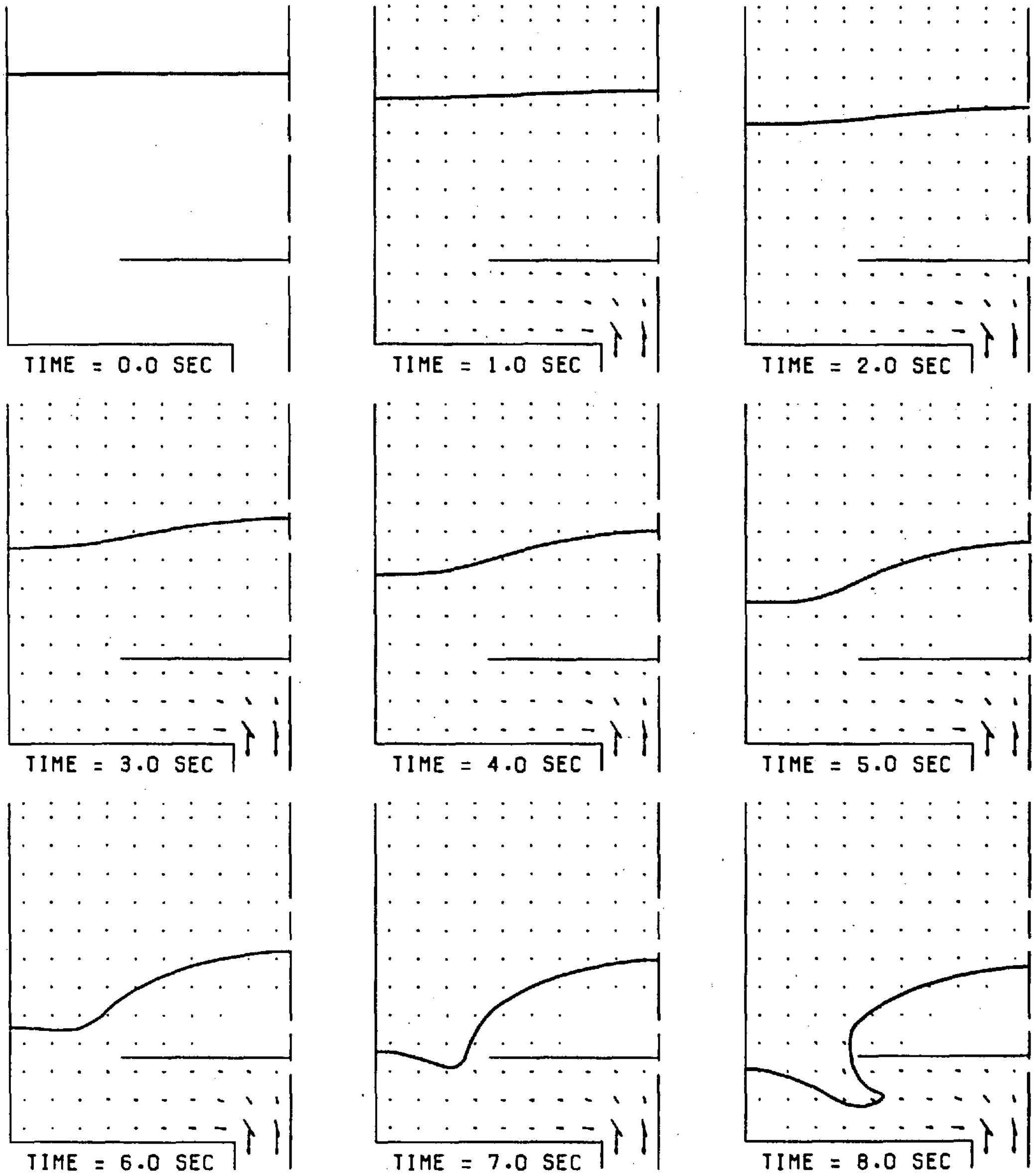

FIGURE 7-4 : DRAINING TANK WITH INTERNAL BAFFLE IN ZERO GRAVITY ENVIRONMENT

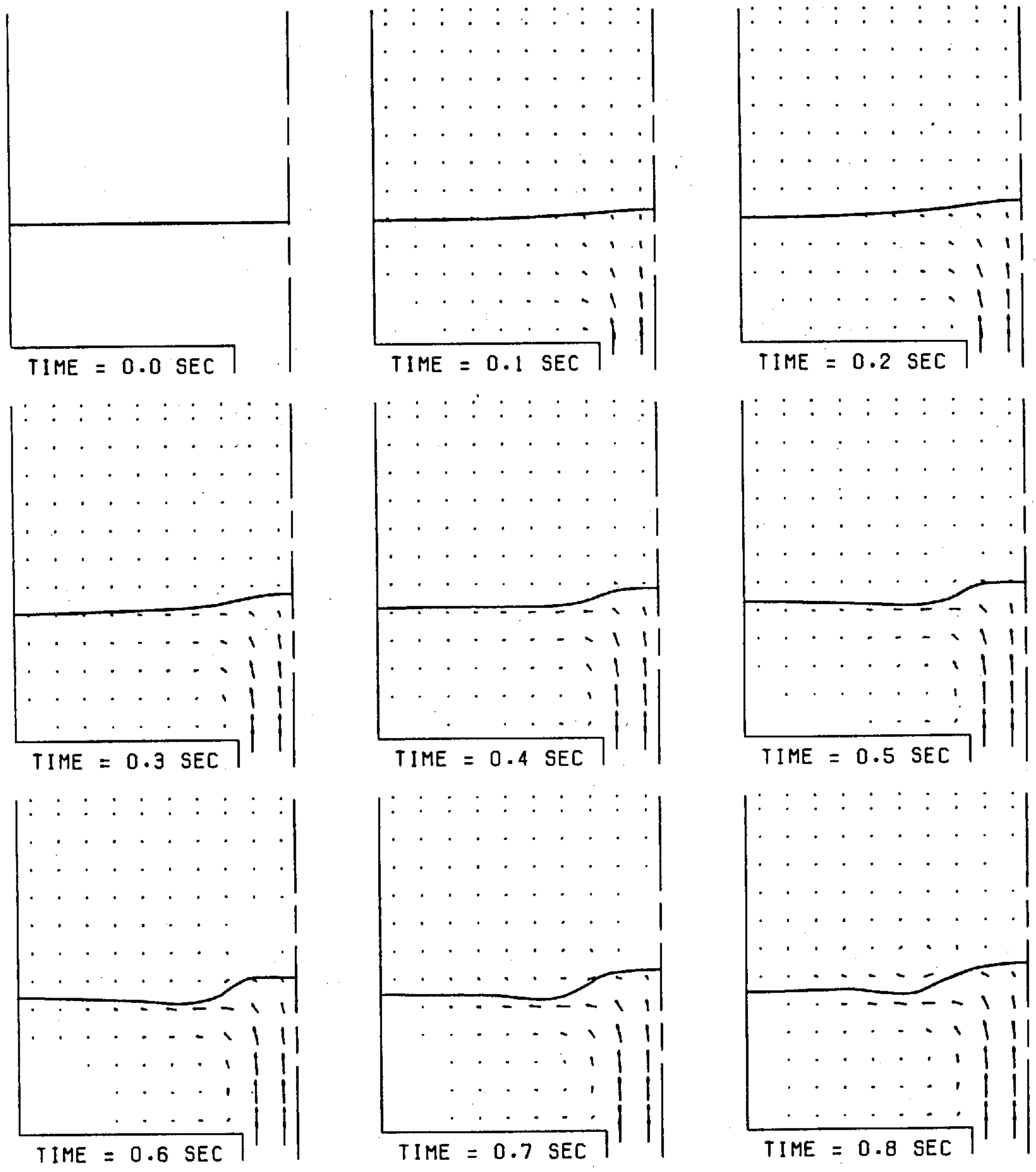

FIGURE 7-5 : FILLING TANK IN NORMAL GRAVITY ENVIRONMENT

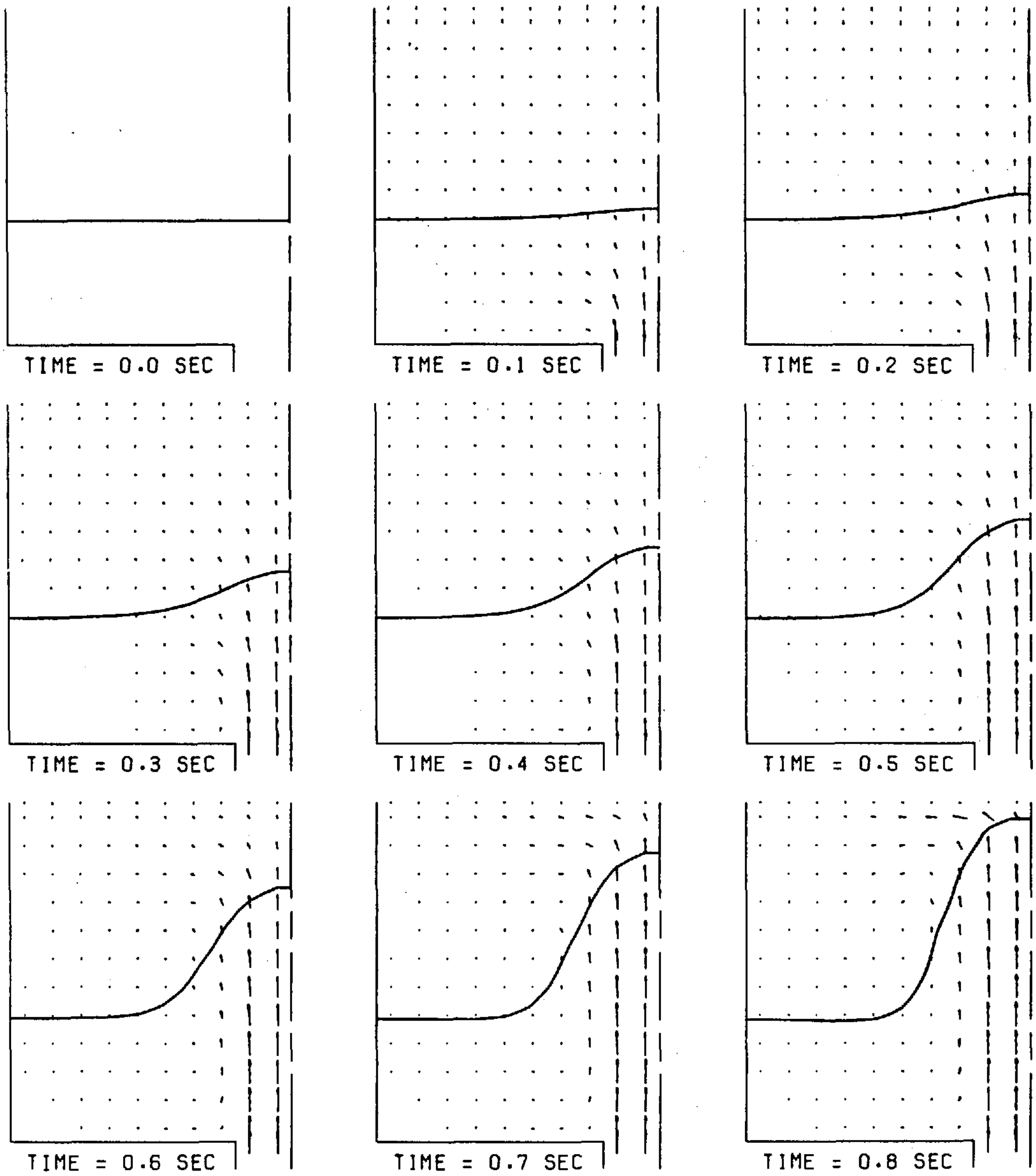

FIGURE 7-6 : FILLING TANK IN ZERO GRAVITY ENVIRONMENT

Comparing Figures 7-1 and 7-3 shows that in the presence of gravity, the baffle has little effect on the liquid surface until the surface actually reaches the baffle. However, in the absence of gravity the behaviour of the free surface is changed completely by the presence of the baffle (compare Figures 7-2 and 7-4). Thus, the presence of the baffle allows much more liquid to be removed from the tank before gas is ingested into the outlet. It is obvious that the liquid behaviour in a zero gravity environment can be influenced tremendously by the presence of baffles or other obstacles. Such obstacles, whether they are impermeable or porous, can easily be simulated by the present numerical procedure.

Finally, Figures 7-5 and 7-6 illustrate the process of filling a tank with liquid. The results presented in Figure 7-5 show that ripples form on the liquid surface and move radially outward, but overall, the surface remains relatively flat. However, Figure 7-6 indicates that, in the absence of gravity, the incoming liquid produces a "pile" over the inlet.

It should be noted that surface tension, which is not included in computations presented in this thesis, becomes a very significant force in zero gravity systems. However, if the characteristic dimensions of the free surface are large (as in these tank flows) and the gravitational acceleration is small, but finite, the importance of surface tension is minimized.

7.3 LIQUID SLOSHING IN A TANK

Presentation

When tanks containing liquids are bumped or undergo sudden acceleration, the liquid sloshes back and forth. Computations were performed to simulate the sloshing of liquid 0.47 meters deep in 1.2 meter wide by 1.2 meter high tank which was suddenly decelerated from a constant velocity of one meter per second to rest at zero time. A 14 by 14 uniform grid was used for the calculations and 160, 0.01 second, time steps were carried out. The computations required 290 seconds of CDC 6600 time. Figure 7-7 presents the free-surface profiles and velocity vectors for the sloshing liquid.

Discussion

The sudden deceleration of the tank causes the liquid to rush, first to the right side of the tank and then back to the left side. Of course, the sloshing will continue until the energy transferred to the liquid by the sudden deceleration of the container is dissipated. The free-surface distortions shown in Figure 7-7 appear to be reasonable. In this example a simple step function was used to define the lateral velocity of the tank; however, any continuous function could be employed.

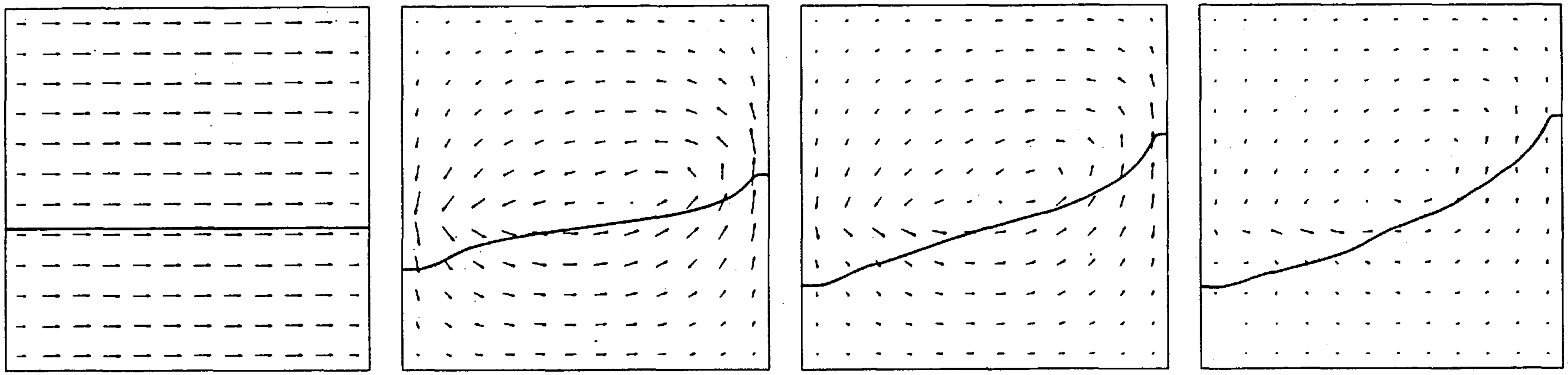

TIME = 0.0 SEC

TIME = 0.1 SEC

TIME = 0.2 SEC

TIME = 0.3 SEC

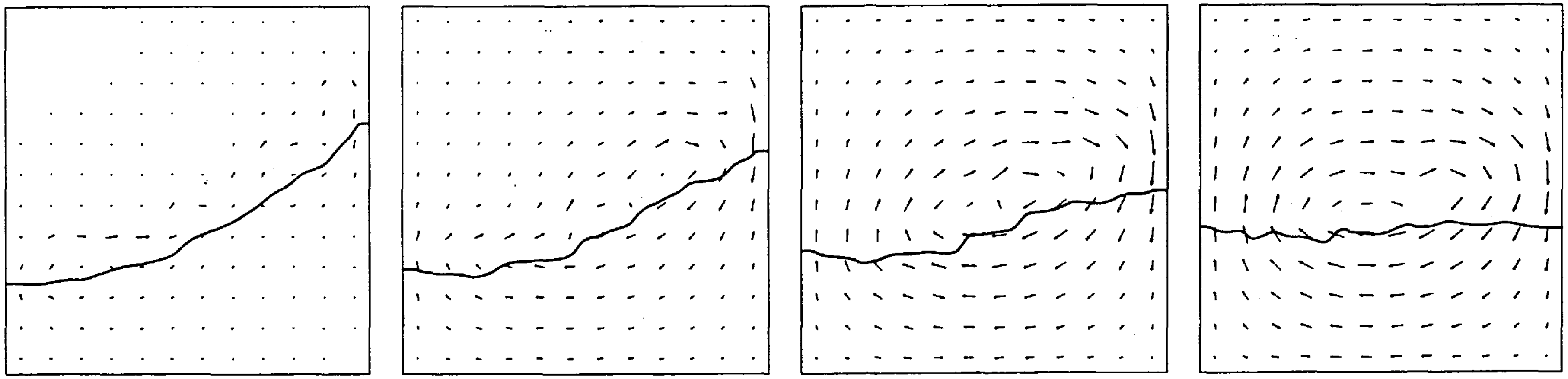

TIME = 0.4 SEC

TIME = 0.5 SEC

TIME = 0.6 SEC

TIME = 0.7 SEC

FIGURE 7-7 : LIQUID SLOSHING IN A TANK

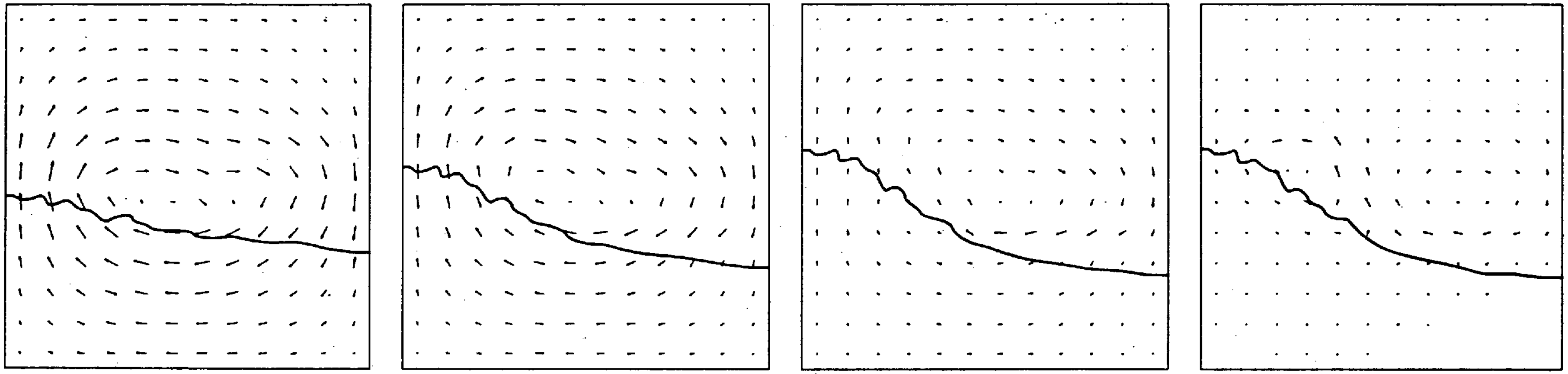

TIME = 0.8 SEC

TIME = 0.9 SEC

TIME = 1.0 SEC

TIME = 1.1 SEC

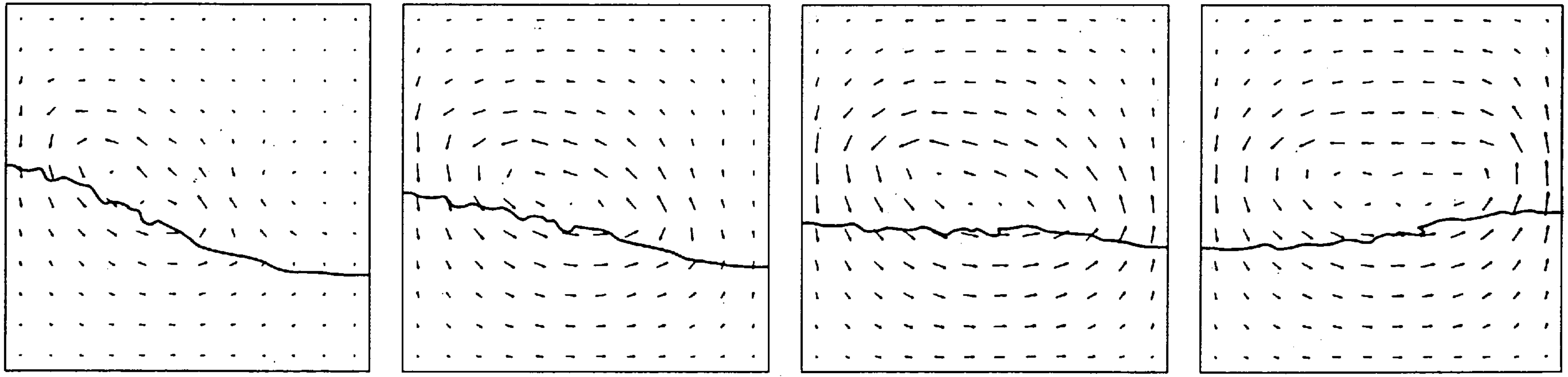

TIME = 1.2 SEC

TIME = 1.3 SEC

TIME = 1.4 SEC

TIME = 1.5 SEC

FIGURE 7-7 : (CONTINUED)

7.4 DISTORTION OF A SUBMERGED BUBBLE

Presentation

The motion of an air bubble rising in a tank of water was simulated. The 0.07 meter diameter bubble was initially spherical and its centre was 0.078 meters from the bottom of a 0.3 meter diameter tank. The tank was 0.3 meters high and filled with water to a depth of 0.26 meters. The initial velocity fields were taken to be zero.

The computations were performed with a 22 by 17 uniformly-distributed grid. Two strings of particles were necessary, one to define the bubble and one to define the liquid free-surface near the top of the tank. The calculations were run for 100 time steps of 0.0025 seconds, and consumed 300 seconds of CDC 6600 time.

A special feature of the bubble calculations is the allowance for compressibility of the gas. This is accomplished by using equation (2-5) to define the volumetric sources (R in equation 2-6) for each main control volume containing gas. The compressibility of the gas causes the bubble volume to increase as the bubble rises through the decreasing hydrostatic pressure field.

The bubble shapes and velocity vectors are shown in Figure 7-8.

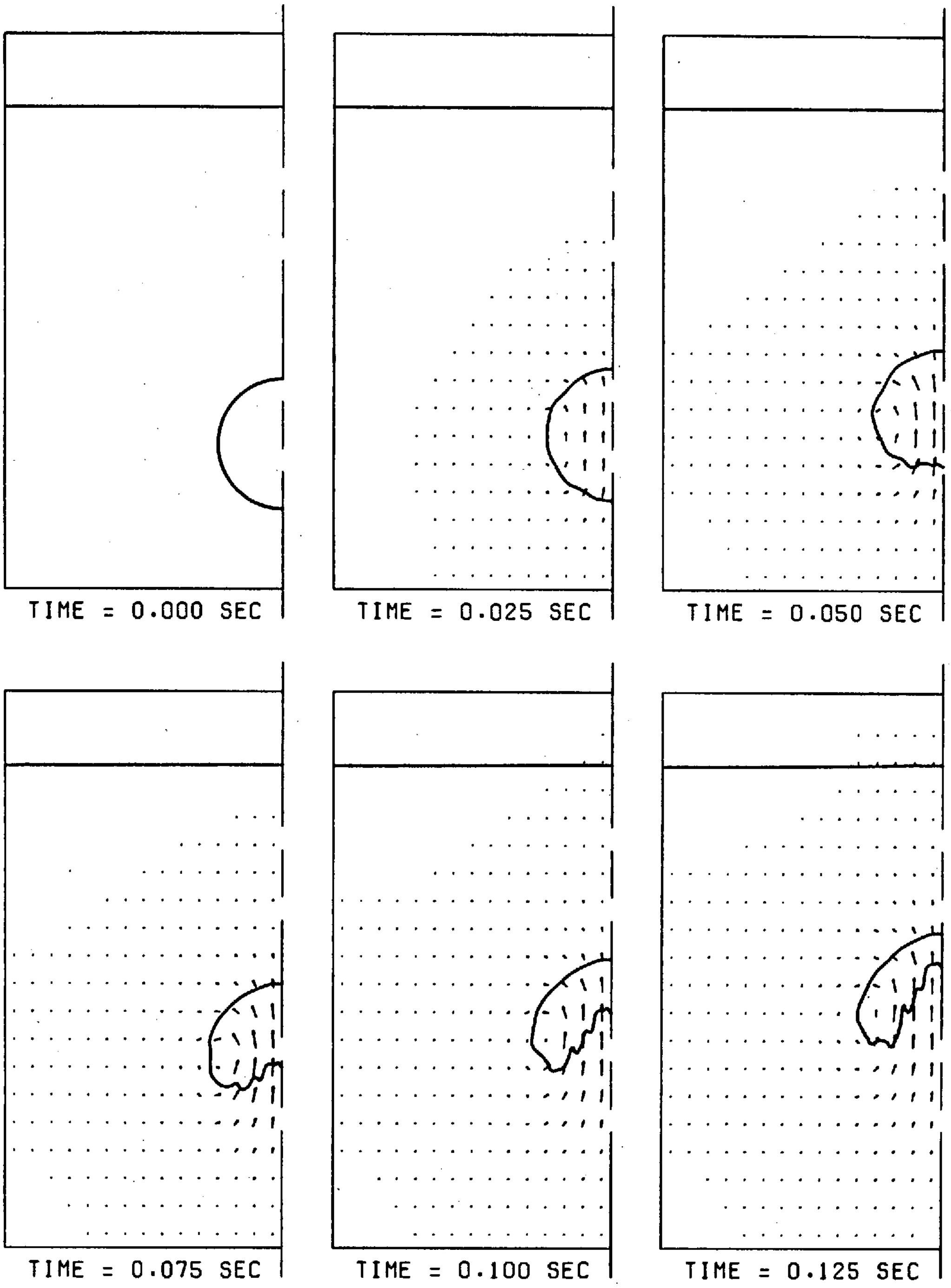

TIME = 0.000 SEC

TIME = 0.025 SEC

TIME = 0.050 SEC

TIME = 0.075 SEC

TIME = 0.100 SEC

TIME = 0.125 SEC

FIGURE 7-8 : BUBBLE RISING THROUGH A LIQUID

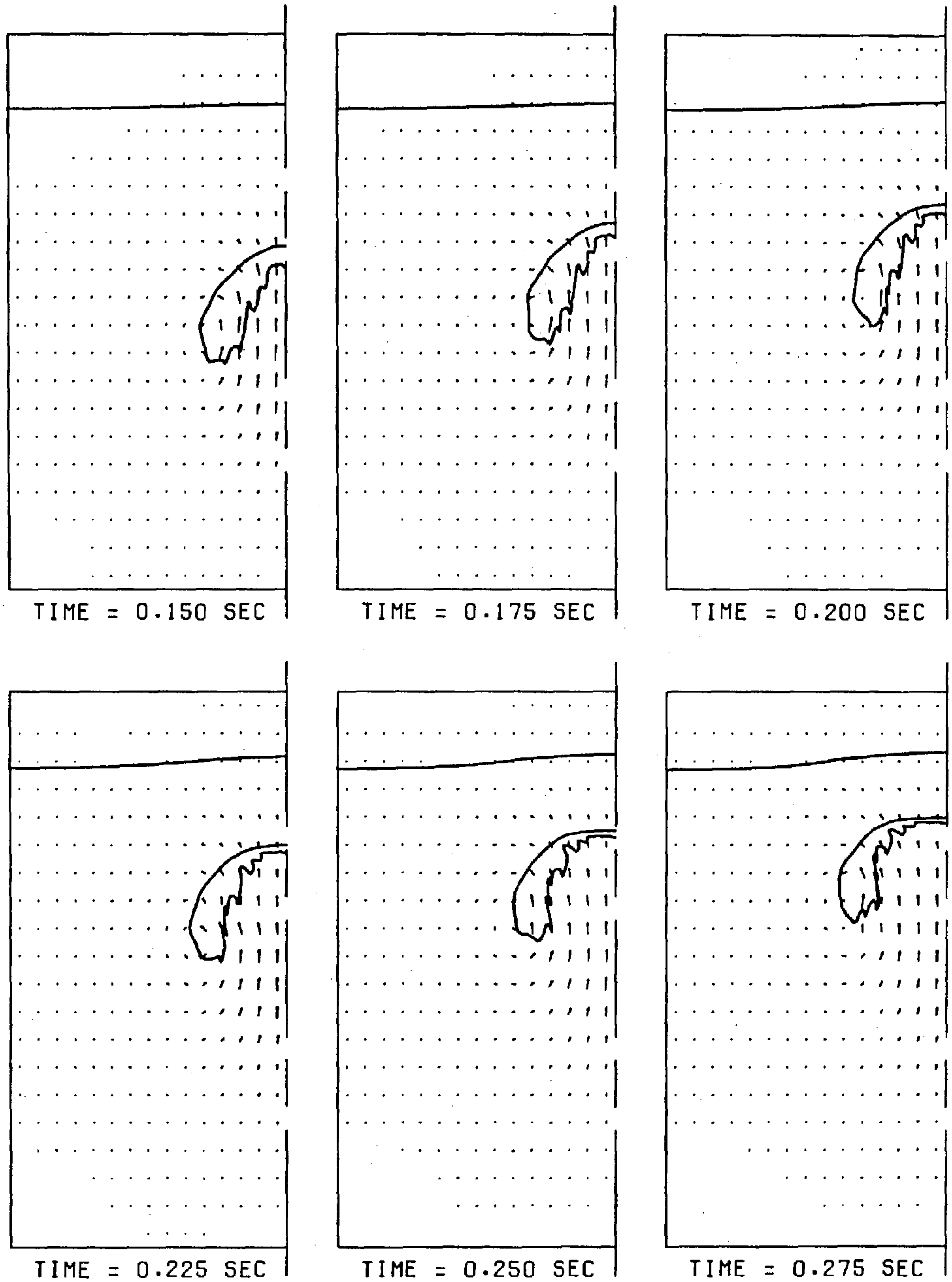

TIME = 0.150 SEC

TIME = 0.175 SEC

TIME = 0.200 SEC

TIME = 0.225 SEC

TIME = 0.250 SEC

TIME = 0.275 SEC

FIGURE 7-8 : (CONTINUED)

Discussion

As the bubble rises through the liquid it rapidly distorts from its initial spherical shape. First the bottom flattens, and then, a tongue of liquid cuts into the bottom of the bubble. In the last frame of Figure 7-8 the bubble is almost toroidal with most of the volume contained in the toroidal portion. According to Walters and Davidson (1963) this toroidal portion should separate from the top part of the bubble and then break into several small bubbles. The top part of the bubble then forms the familiar "spherical cap" bubble. However, because the solution procedure does not consider surface tension, the bubble cannot separate. Qualitatively, the predicted movement and distortion of the bubble agree with the description given by Walters and Davidson. Figure 7-9 compares the calculated movement of the bubble centroid with experimental data presented by Walters and Davidson. The bubble rise velocity is predicted accurately. The predicted height of the bubble along the centre-line is compared to data from Walters and Davidson in Figure 7-10. The agreement between the predictions and the experiments does not match well at later times. This is due to the coarseness of the grid; there are not enough control volumes between the top and bottom of the bubble to correctly simulate the relative motion of these points. Overall, considering the coarseness of the grid, the behaviour

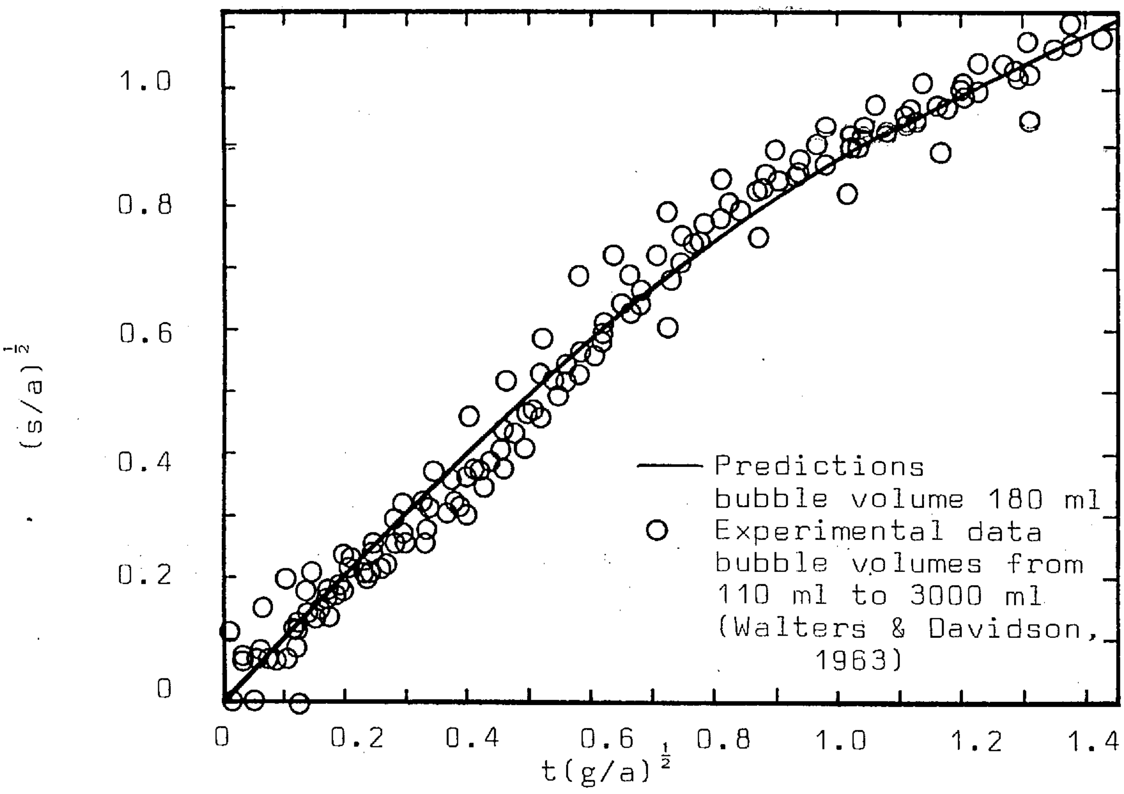

FIGURE 7-9 : MOVEMENT OF THE CENTROID OF THE RISING BUBBLE

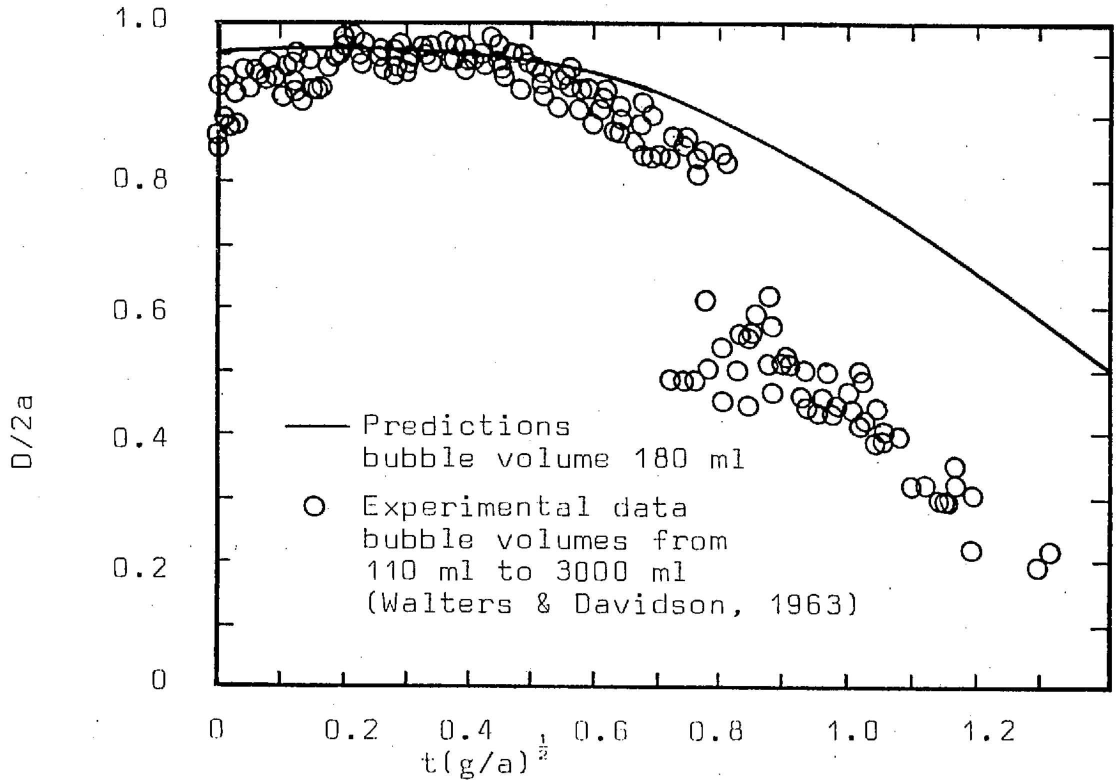

FIGURE 7-10 : VERTICAL THICKNESS OF THE RISING BUBBLE of the bubble is simulated well.

7.5 RAPID EXPANSION OF A HIGH-PRESSURE BUBBLE

Presentation

The final computation to be presented is the rapid expansion of a high-pressure bubble, such as a vapour explosion in a nuclear reactor core. A 4.8 meter diameter bubble, at an initial pressure of 200 atmospheres, was allowed to expand in a pool of water 15 meters in diameter and 17.3 meters deep. The air above the free surface was maintained at atmospheric pressure.

The computations were made on a 22 by 17 uniformly-spread grid. Approximately 670 seconds of CDC 6600 time were necessary to perform 120 time steps of 0.001 second each. Gas compressibility is handled in the same way as for the bubble in Section 7.4. The bubble shapes and velocity vectors are shown in Figure 7-11. Figure 7-12 shows the increase in bubble volume and decrease in bubble pressure versus time.

Discussion

The early growth of the bubble is essentially radial; however, in the later stages the bubble assumes an egg shape. The egg shape results because the bubble can push the liquid upward easier than outward or down toward the bottom of the tank. The free surface begins to erupt above the bubble as the bubble continues

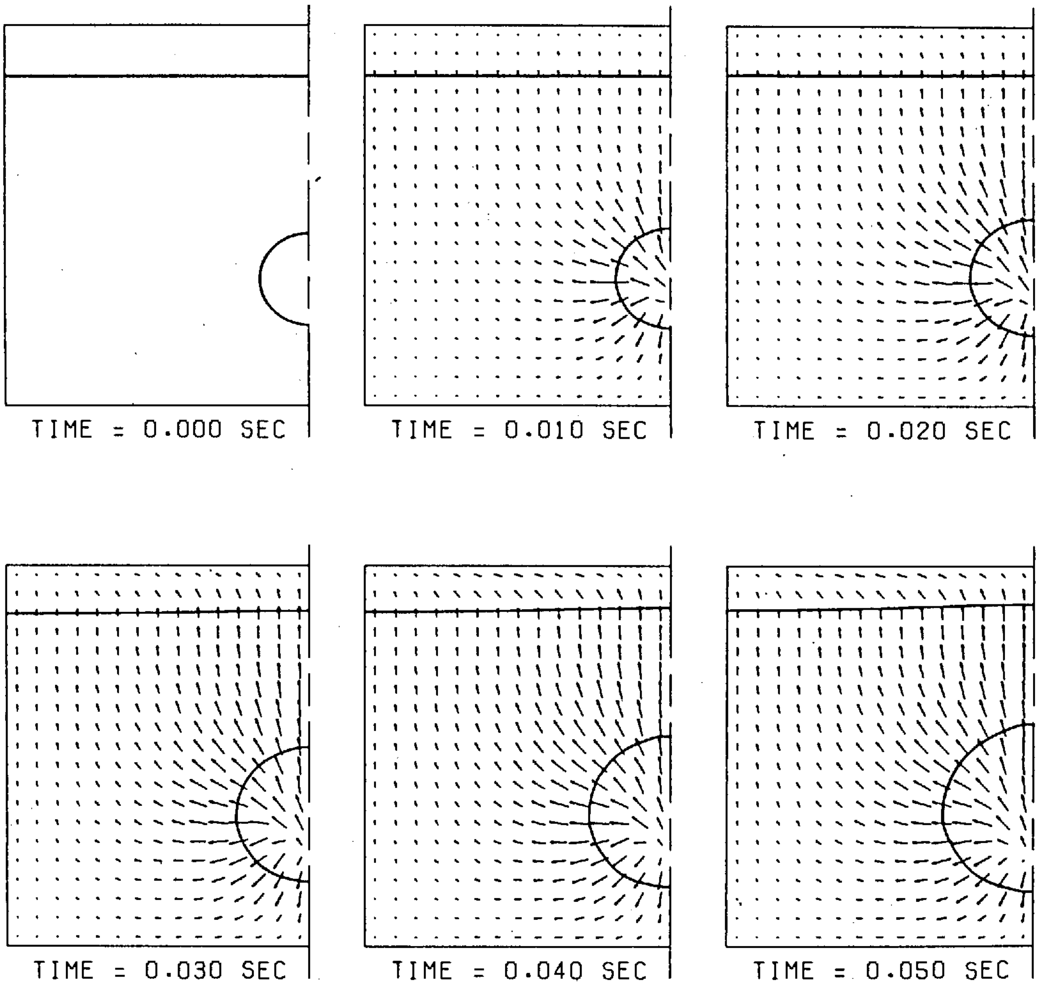
TIME = 0.000 SEC
TIME = 0.010 SEC
TIME = 0.020 SEC
TIME = 0.030 SEC
TIME = 0.040 SEC
TIME = 0.050 SEC

FIGURE 7-11 : EXPANSION OF A HIGH-PRESSURE GAS BUBBLE

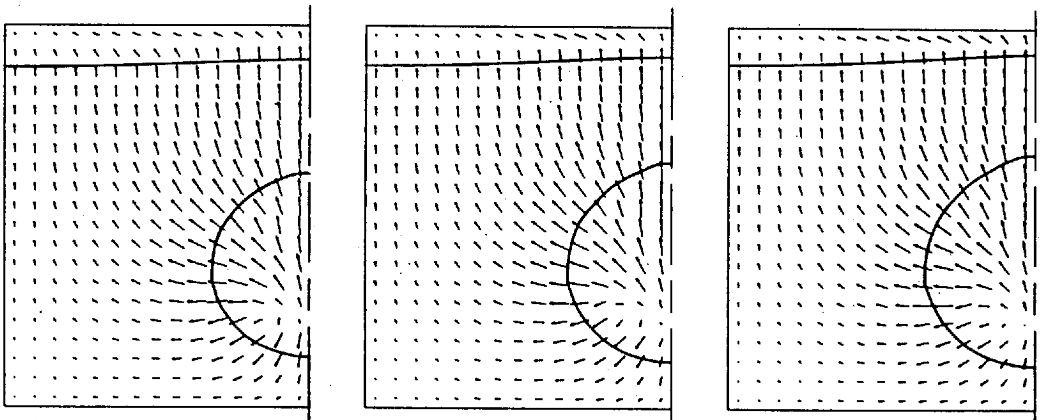

TIME = 0.060 SEC

TIME = 0.070 SEC

TIME = 0.080 SEC

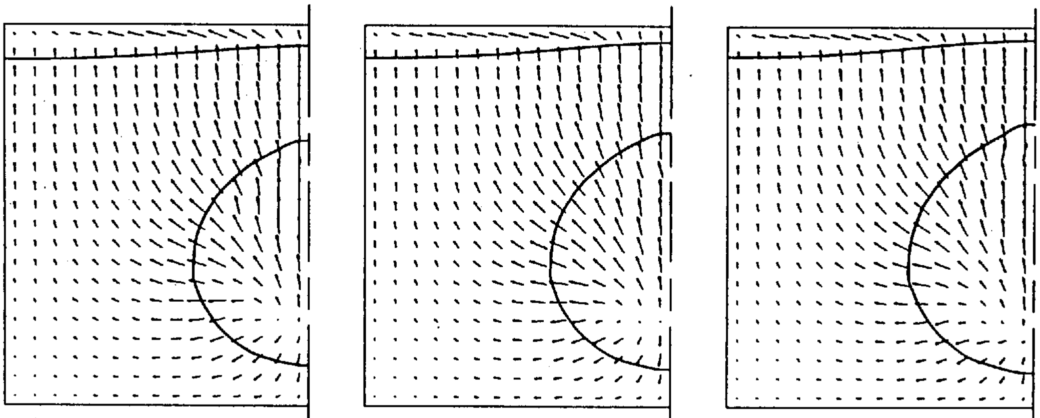

TIME = 0.090 SEC

TIME = 0.100 SEC

TIME = 0.110 SEC

FIGURE 7-11 : (CONTINUED)

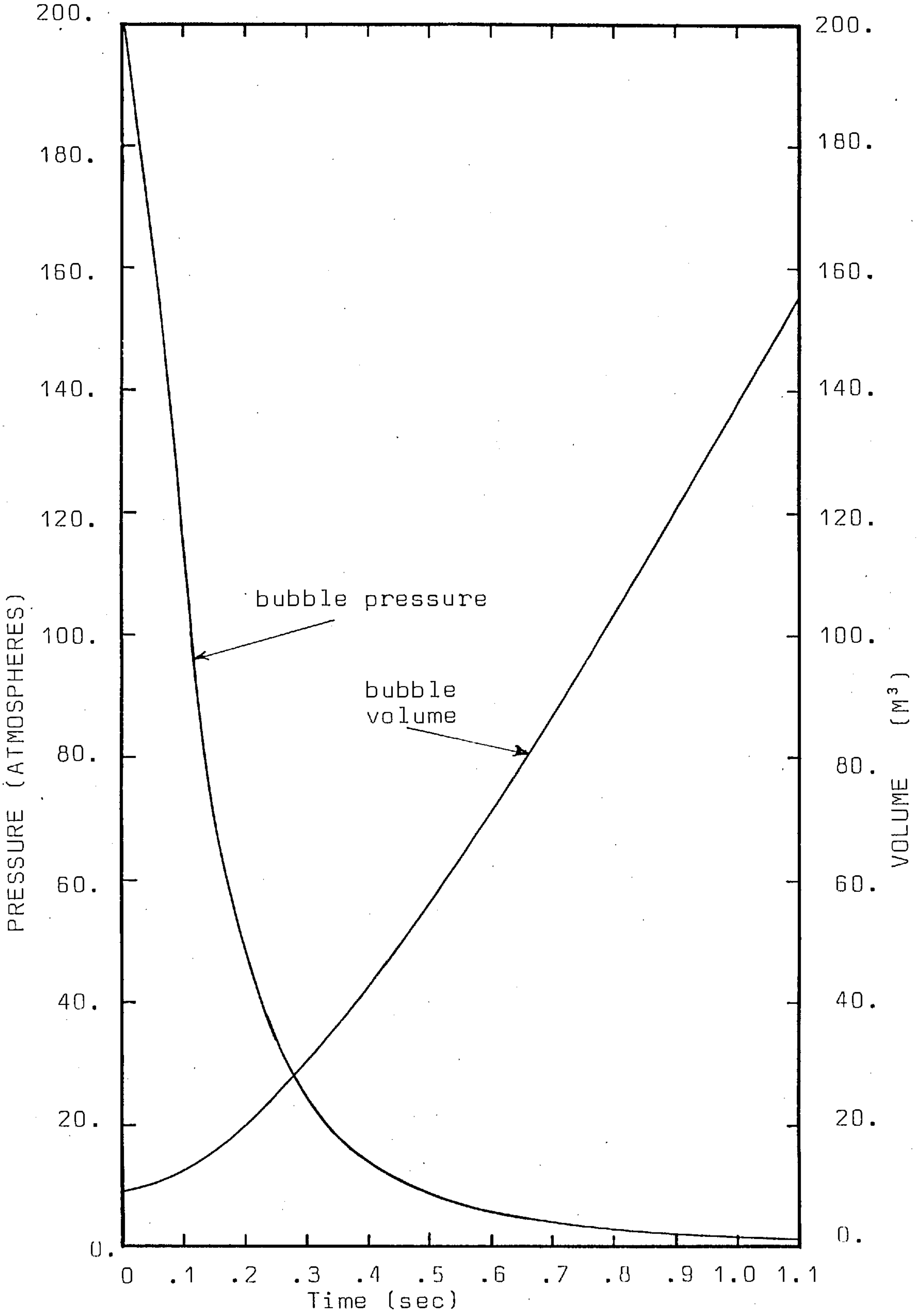

FIGURE 7-12 : BUBBLE PRESSURE AND VOLUME VERSUS TIME FOR HIGH PRESSURE GAS BUBBLE to grow. The predicted growth of the bubble appears to be quite plausible.

7.6 SUMMARY

In this chapter several interesting flows have been presented to demonstrate the scope and flexibility of the numerical procedure. Of particular interest is the ability of the procedure to simulate the gas compressibility and multiple free-surfaces.

CHAPTER 8

CONCLUSIONS

8.1 ACHIEVEMENTS OF THE PRESENT WORK

The achievements of the work presented in this thesis can best be summarised in relation to the objectives stated in Section 1.5.

(a) A mathematical model and solution procedure capable of predicting free-surface flows were developed and are presented in Chapters 2 and 3. Special features of the method include the use of massless particles to define the free-surface and the use of a volumetric, rather than mass, continuity equation. This latter feature allows the free-surface boundary conditions to be handled implicitly.

(b) The comparison of predictions with analytical results presented in Chapter 5 demonstrates the ability of the numerical procedure to accurately solve the finite-difference equations which describe the hydrodynamics. Also, it is verified that the particle-tracking procedure is reliable.

(c) An experimental study of wave motions was carried out and is reported in Chapter 4. The results of the present experimental study and experimental data taken from the literature were compared with predictions. These comparisons showed that the numerical model simulated the physics of free-surface flows very well. However, it was noted that because the numerical procedure does not account for turbulence phenomena, it could not predict the details of the experimental wave profiles accurately.

(d) A wide range of free-surface flow predictions has been presented to demonstrate the versatility of the procedure.

8.2 TOPICS FOR FUTURE CONSIDERATION

Now that the basic numerical procedure for simulating free-surface flows has been developed and validated, attention can be concentrated on extending the capability and flexibility of the method. Several particular areas where more development is needed will be outlined below.

Turbulence

In Section 6.4 it was shown that turbulence phenomena can affect the behaviour of a free-surface flow. Thus, the development of a turbulence model which can adequately describe the turbulent transfer of momentum in a free-surface flow is needed. Perhaps a simple model in which the effective viscosity is merely a function of distance from the tank bottom would suffice for the wave motion in Section 6.4. However, it may be necessary to use a more general turbulence model. In any case, it should be remembered that the computation of transient flows is expensive; and thus, use of the simplest, adequate turbulence model is mandatory.

Surface Tension

To predict the behaviour of a free-surface flow in which the the radius of curvature of the free-surface is small (e.g., the movement of very small bubbles) or in which the body forces are very small (e.g., a zero-gravity environment), it will be necessary to include the effects of surface tension. Surface tension can be added to the numerical procedure by including additional source terms in the momentum equations to represent the forces imposed by the surface tension. Inclusion of surface tension in the procedure should be a straightforward, but tedious, task.

Three-Dimensional Computations

The solution procedure can readily be extended to predict three-dimensional flows. However, there are two serious drawbacks; excessive computer time and computer storage. If the expenses of making transient three-dimensional computations can be justified, the conversion to three-dimensionality is primarily a matter of FORTRAN programming. Indeed, similar programs to predict the three-dimensional hydrodynamics and heat transfer already exist. However, the particle-tracking and density-calculation procedure must be suitably modified to account for the third dimension. Note that the free-surface will become a surface of particles rather than a string of particles.

Mass Transfer between the Fluids

If phase change or mass transfer between the fluids is to be simulated, a relevant equation of state must be employed to compute the volume of fluid which is changing phase. Then, after the surface is moved by the hydrodynamic velocities for each time step, it must be moved again to account for the volume of fluid which has undergone phase change. The primary difficulty will be to prevent the particle strings from crossing each other or themselves as a result of the movements related to the phase change.

REFERENCES

1. ABRAMSON H N (ED.) (1966)
"The Dynamic Behaviour of Liquids in Moving Containers".
NASA SP-106, 1966.

2. AMSDEN A A & HARLOW F H (1970)
"The SMAC Method: A Numerical Technique for Calculating Incompressible Fluid Flows".
Los Alamos Scientific Laboratory Report LA-4370, February 1970.

3. AYDELOTT JOHN C (1976)
"Axial Jet Mixing of Ethanal in Spherical Containers during Weightlessness".
NASA TM X-3380, April 1976.

4. BRADSHAW, KROMIC & ZICH (1976)
"An Analytical Study of Reduced Gravity Flow Dynamics".
NASA-CR-135023, 1976.

5. CARETTO L S, GOSMAN A D, PATANKAR S V & SPALDING D B (1972)
"Two Calculational Procedures for Steady, Three-Dimensional Flows with Recirculation".
Imperial College, London, Mechanical Engineering Department, Heat Transfer Section Report No. HTS/72/5, 1972.

6. CHAN R K C & STREET ROBERT L (1970)
"A Computer Study of Finite-Amplitude Water Waves".
J. of Computational Physics, Vol. 6, pp 68-94, 1970.

7. CHAN R K C, STREET R L & STRELKOFF (1969)
"Computer Studies of Finite-Amplitude Water Waves".
Stanford University, Dept. of Civil Engineering, Technical Report No. 104, 1969.

8. COLLINS R (1967)
"The Effect of a Containing Cylindrical Boundary on the Velocity of a Large Gas Bubble in a Liquid".
J. of Fluid Mechanics, Vol. 28, Part 1, pp 97-112, 1967.

9. GLUCH D F, GILLE J P, SIMKIN D J & ZUKOSKI E E (1966)
"Distortion of the Liquid Surface during Tank Discharge under Low G Conditions".
Chemical Engineering Progress Symposium Series, No. 61, Vol. 62, 1966.

10. IPPEN A T (1966)
Estuary and Coastline Hydrodynamics.
McGraw Hill Book Company, Inc., New York, N.Y. 1966.

11. LAMB H (1975)
Hydrodynamics, 6th Edition, Cambridge University Press, London, England, 1975.

12. MARKATOS N C G (1974)
"The EASI Computer Program", CHAM Technical Report TR/9, October 1974.

13. MARKATOS N C G (1974)
"The TRIC Computer Program", CHAM Technical Report TR/10, May 1974.

14. MARTIN J C & MOYCE W J (1952)
"Part IV An Experimental Study of the Collapse of Liquid Columns on a Rigid Horizontal Plane".
Phil. Trans. Royal Society (London), Vol. 244, p 132, March 1952.

15. MAXWORTHY T (1976)
"Experiments on Collisions between Solitary Waves".
J. of Fluid Mechanics, Vol. 76, Part 1, pp 177-185, 1976.

16. MOODY F J (1970)
"Prediction of Fluid Free Surface Motions under the Influence of Body Force Acceleration and External Pressures".
Ph.D. Thesis, Stanford University, 1970.

17. NUSSLE R C, DERDUL J D & PETRASH D A (1965)
"Photographic Study of Propellant Outflow from a Cylindrical Tank during Weightlessness".
NASA TN D-2572, January 1965.

18. OTTO E W (1966)
"Static and Dynamic Behaviour of the Liquid-Vapour Interface during Weightlessness".
Chemical Engineering Progress Symposium Series No. 61, Vol. 62, 1966.

19. PATANKAR S V & SPALDING D B (1972)
"A Calculation Procedure for Heat, Mass and Momentum Transfer in Three-Dimensional Parabolic Flows".
Int. J. of Heat & Mass Transfer, Vol. 15, pp 1787-1806, 1972.

20. RAMSHAW J D & TRAPP J A (1976)
"A Numerical Technique for Low-Speed Homogenous Two-Phase Flow with Sharp Interfaces".
J. of Computational Physics, Vol. 21, pp 438, 453, August 1976.

21. ROACHE P J (1976)
Computational Fluid Dynamics, Hermosa Publishers, Albuquerque, N.M., 1976.

22. SPALDING D B (1974)
"A Method for Computing Steady and Unsteady Flows Possessing Discontinuities of Density".
CHAM Report 910/2, December 1974.

23. SPALDING D B (1976)
"The Calculation of Free-Convection Phenomena in Gas-Liquid Mixtures".
Imperial College, London, Mechanical Engineering Department, Heat Transfer Section Report No. HTS/76/11, 1976.

24. STOKER (1957)
Water Waves, Interscience Publishers Inc., 1957.

25. STREET & CAMFIELD (1966)
"Observations and Experiments on Solitary-Wave Deformation".
Proceedings of 10th Conference of Coastal Engineering, Tokyo, Japan, ASCE, 1966.

26. SYMONS P & STASKAS J V (1971)
"Interface Stability during Liquid Inflow to Partially Full, Hemispherical Ended Cylinders During Weightlessness" NASA-TM-X-2348, August 1971.

27. WALTERS J K & DAVIDSON J F (1963)
"The Initial Motion of a Gas Bubble formed in an Inviscid Liquid".
Part 2, "The Three-Dimensional Bubble and the Toroidal Bubble", J. of Fluid Mechanics, Vol. 17, Part 3, pp 321-336, 1963.

28. WELCH J E, HARLOW F H, SHANNON J P & DALY B J (1966)
"The MAC Method - A Computing Technique for Solving Viscous, Incompressible, Transient Fluid-Flow Problems involving Free Surfaces".
Los Alamos Scientific Laboratory Report, LA-3425, 1966.

29. WIEGEL R L (1964)
Oceanographic Engineering, Prentice-Hall, Inc., Englewood Cliffs, N.J., 1964.

NOMENCLATURE

SYMBOL	MEANING
a	area of a control volume face, local identifier for a specific particle, wave amplitude, bubble radius, width of collapsing column;
A	finite-difference coefficient, TDMA coefficient;
b	local identifier for a specific particle;
B	TDMA coefficient, body force;
c	wave velocity, local identifier for a particle;
C	TDMA coefficient;
d	nominal liquid depth;
D	coefficient for pressure-gradient term, TDMA coefficient, height of distorted bubble;
E	grid location east of P;
g	gravitational acceleration;
h	instantaneous liquid height, wave height;
H	average height of liquid, non-dimensional height of liquid;
k	ratio of specific heats, wave number, particle index;
l	wave length;
L	length, half width;
m	particle identifier;
M	mass contained in a control volume;

SYMBOL	MEANING
n	used to define initial height of liquid column;
N	grid location north of P;
p	pressure, point used in defining a set of coordinate axes;
P	grid location of current interest;
q	point used in defining a set of coordinate axes, volumetric rate of fluid creation at a point source;
r	radius, radial coordinate, particle position vector;
R	rate of reduction of fluid volume (compressibility term for continuity equation), wave run-up;
s	location of bubble centroid;
S	grid location south of P, source term;
t	time;
T	non-dimensional time;
u	x-direction velocity component;
v	v-direction velocity component,
V	volume, velocity vector when used with overbar;
w	z-direction velocity component;
W	grid location west of P;
x	coordinate direction;
y	coordinate direction;
z	coordinate direction, wave-front location;
Z	non-dimensional location of wave-front;

SYMBOL	MEANING
Greek Symbols	
α	per cent by volume of liquid;
Γ	transport coefficient;
δ	distance related to particle deletion;
ε	angle related to particle deletion;
ζ	coordinate direction, wave-front location;
η	height of wave surface above average liquid depth;
θ	coordinate;
λ	second coefficient of viscosity;
μ	dynamic viscosity;
ρ	density;
T	non-dimensional time;
ϕ	any scalar quantity;
ω	wave frequency.
Subscripts	
avg	average;
B	bottom of control volume (minimum x-dimension of control volume);
e	for east control volume face;
E	for grid location to the east of P;
g	for gas;
l	for liquid;
L	left-hand side;
n	for north control volume face;

SYMBOL	MEANING
Subscripts (contd.)	
N	for grid location to the north of P;
o	initial;
p	relating to a particle;
R	right-hand side;
s	for south control volume face;
S	for grid location to the south of P;
u	relating to the u-velocity;
v	relating to the v-velocity;
w	for the west control volume face;
W	for the grid location to the west of P;
ϕ	relating to the scalar, ϕ;
Superscripts	
$*$	guessed quantities (pressure, p^*) or quantities based on the guessed quantities (u^*, v^*);
$'$	corrections to be added to guessed quantities;
—	overbar indicates the quantity is a vector.